HYDROTHERMAL SYNTHESIS, FORMATION MECHANISMS AND ENVIRONMENTAL APPLICATIONS OF SELECTED FUNCTIONAL OXIDE NANOMATERIALS

Dissertation

zur

Erlangung der naturwissenschaftlichen Doktorwürde

(Dr. sc. nat.)

vorgelegt der

Mathematisch-naturwissenschaftlichen Fakultät

der

Universität Zürich

von

Ying Zhou

aus

V. R. China

Promotionskomitee

Prof. Dr. Greta R. Patzke (Vorsitz, Leitung der Dissertation)

Prof. Dr. Roger Alberto

Zürich, 2010

To my family

CONTENTS

Acknowledgments

More than three years have been passed since I started my PhD studies at the University of Zurich in June 2007. Looking back, I am glad that I made the right decision to pursue my projects here and I am happy that I met so many kind and supporting people along the way. Without their assistance and help, this PhD thesis would not have been accomplished.

I would like to express my sincere gratitude to Prof. Dr. Greta R. Patzke for offering me the opportunity to study here, for her patient guidance, generous support and continuous encouragement. Moreover, I appreciate her support for the attendance of international conferences and workshops that provided a unique opportunity to enhance my knowledge and my abilities.

I am indebted to Prof. Dr. Roger Alberto, to Prof. Dr. Heinz Berke and to Prof. Dr. Roland Sigel as co-referees of this dissertation.

I would like to thank Prof. Dr. Jan-Dierk Grunwaldt (Institute for Chemical Technology and Polymer Chemistry, Karlsruhe Institute of Technology) for the fruitful collaboration concerning in situ XAS measurements and for the interesting discussions. I am also grateful to Prof. Dr. Wolfgang Bensch, Dr. Nicole Pienack and Elena Antonova (Institute of Inorganic Chemistry, University of Kiel) for their great support with in situ EDXRD studies.

I wish to thank Dr. Frank Krumeich (Laboratory of Inorganic Chemistry, ETH Zurich) and Dan Xie (ETH Zurich) for many valuable suggestions and for their support with TEM investigations.

I am grateful to Dr. Andre Heel (Laboratory for High Performance Ceramics, EMPA Dübendorf) for giving us the opportunity perform photocatalytic reactions at EMPA, to Kathrin Vuille for useful discussion concerning photocatalytic experiments, to Benjamin Probst for his introduction to water splitting setups and for experimental support and to Dr. Lichang Yin (Institute of Metal Research, Chinese Academy of Sciences) for his help with DFT calculations.

I truly enjoyed the collaboration with Prof. Guorong Chen, Dr. Kaibo Zheng and Leilei Gu (Department of Materials Science, Fudan University) concerning sensor fabrication and I learned a lot while performing sensing experiments at Fudan University.

I am grateful to Dr. Ferdinand Wild for his kind introduction to the operation of SEM, Raman

and TG, to Dr. Thomas Fox for his great help and support in solid state NMR measurements, and to Heinz Spring for conducting many elemental analyses.

I would like to thank Peter Wägli (Electron Microscopy ETH Zurich, EMEZ) and Hans-Peter Gautschi (Center for Microscopy and Image Analysis, University of Zurich) for training sessions in high resolution electron microscopy and for providing me with a work license.

Special thanks go to Beatrice Spichtig, Susanna Sprokkereef, Nathalie Fichter and Dr. Jae Kyoung Pak for their great help with administrative tasks and to Manfred Jöhri for his support concerning electronics and hardware.

My gratitude goes to all the members of our group: Dr. Firasat Hussain, Franziska Conrad, Roman Kontic, Min Sheng, Lubin Ni and Georg Geisberger for a lot of everyday support and for the friendly working atmosphere.

I would like to thank Yanfeng Jiang, Chunfang Jiang, Yan Li, Xianghua Yang, Xinjun Luan, Yuzheng Zhang, Xia Meng, Hailin Dong, Yunjun Shen, Yu Liu, Xiaoqiong Wan and Kai Zhou for helpful discussions and for the nice leisure activities.

Moreover, I thank the synchrotron facilities (DESY, BESSY, SLS and ESRF) for providing beamtime to perform our experiments, and the Graduate School of Chemical and Molecular Science Zurich for educational and financial support.

It is impossible to end without expressing my appreciation to my mother Yunfang Li and to my father Decheng Zhou for their endless love and support that I can always rely on.

Finally, I wish to express my special thanks to my wife Xiaoxian Yuan. With her love, understanding, company and encouraging, I could even get through the most depressing and hard times.

This work was supported by Swiss National Science Foundation (SNF Professorship PP002-114711/1), by the University of Zurich and by the Sino Swiss Science and Technology Cooperation (SSSTC, EG05-092008), which are gratefully acknowledged.

Abbreviations

AC	alternate current
AMT	ammonium metatungstate
BET	Brunauer-Emmett-Teller
CB	conduction band
CN	coordination number
DFT	density functional theory
EDXRD	energy dispersive X-ray diffraction
EDXS	energy dispersive X-ray spectroscopy
EXAFS	extended X-ray absorption fine structure
FT	Fourier transformation
FWHM	full width at half maximum
HRTEM	high resolution transmission electron microscopy
HTB	hexagonal tungsten bronze
PEEK	polyetheretherketone
LA-ICP-MS	laser ablation inductively coupled mass spectrometry
MAS	magic angle spinning
MB	methylene blue
MS	multiple scattering
NMR	nuclear magnetic resonance
PXRD	powder X-ray diffraction
QEXAFS	quick recording X-ray absorption fine structure
RH	relative humidity
RhB	rhodamine B
SAED	selected area electron diffraction
SAXS	small angle X-ray scattering
SEM	scanning electron microscopy
TEM	transmission electron microscopy
TG	thermogravimetry
TMOs	transition metal oxides
VB	valence band
XAS	X-ray absorption spectroscopy
XANES	X-ray absorption near edge structure
1D	one dimensional
2D	two dimensional

Publications

The following parts of this PhD thesis have been published:

Chapter 1

G. R. Patzke, Y. Zhou, R. Kontic, F. Conrad. Oxide Nanomaterials: Synthetic Developments, Mechanistic Studies and Technological Innovations. *Angew. Chem. Int. Ed.* **2010**, doi: 10.1002/anie.201000235.

Y. Zhou, G. R. Patzke. Targeted Synthesis and Environmental Applications of Oxide Nanomaterials. *Chimia* **2010**, *64*, 252-258.

Chapter 2

Y. Zhou, K. Vuille, A. Heel, B. Probst, R. Kontic, G. R. Patzke. An Inorganic Hydrothermal Route to Photocatalytically Active Bismuth Vanadate. *Appl. Catal. A* **2010**, *375*, 140-148.

Chapter 3

Y. Zhou, E. Antonova, W. Bensch, G. R. Patzke. In Situ X-Ray Diffraction Study of the Hydrothermal Crystallization of Hierarchical Bi_2WO_6 Nanostructures. *Nanoscale* **2010** (accepted)

Y. Zhou, K. Vuille, A. Heel, G. R. Patzke. Studies on Nanostructured Bi_2WO_6: Convenient Hydrothermal and TiO_2 Coating Pathways. *Z. Anorg. Allg. Chem.* **2009**, *635*, 1848-1855.

Chapter 5

Y. Zhou, F. Krumeich, A. Heel, G. R. Patzke. A Flexible Hydrothermal Coating Approach to Photocatalytically Active Oxide Composites. *Dalton Trans.* **2010**, 39, 6043-6048.

Chapter 6

K. Zheng, Y. Zhou, L. Gu, X. Mo, G. R. Patzke, G. R. Chen. Humidity Sensors Based on Aurivillius-Type Bi_2MO_6 (M = W, Mo) Oxide Films. *Sens. Actuators B* **2010,** 148, 240-246.

Chapter 7

Y. Zhou, J.-D. Grunwaldt, F. Krumeich, K. Zheng, G. Chen, J. Stötzel, R. Frahm, G. R. Patzke. Hydrothermal Synthesis of $Bi_6S_2O_{15}$ Nanowires: Structural, In Situ EXAFS and Humidity Sensing Studies. *Small* **2010**, 6, 1173-1179.

Chapter 8

Y. Zhou, N. Pienack, W. Bensch, G. R. Patzke. The Interplay of Crystallization Kinetics and Morphology in Nanostructured W/Mo-Oxide Formation: An In Situ Diffraction Study. *Small* **2009**, *5*, 1978-1983.

Y. Zhou, K. Zheng, J.-D. Grunwaldt, T. Fox, X. Mo, G. Chen, G. R. Patzke. W/Mo-Oxide Nanomaterials: Structural Studies and Ammonia Sensing Applications. *J. Phys. Chem. C* **2010** (submitted)

R. Kiebach, N. Pienack, W. Bensch, J.-D. Grunwaldt, A. Michailovski, A. Baiker, T. Fox, Y. Zhou, G. R. Patzke. Hydrothermal Formation of W/Mo-Oxides: A Multidisciplinary Study of Growth and Shape. *Chem. Mater.* **2008**, *20*, 3022-3033.

1. Introduction

1.1 Challenges of oxide nanomaterials synthesis

The depletion of energy resources and the degradation of the natural environment at a global level have already become the most important and urgent issues of our times.[1-5] The future of our modern society can only be maintained when the key challenges of sustainable energy sources and constant access to clean water resources can be resolved. Interestingly, these major problems may be solved by something very small.[6-16] Nanomaterials, with at least one dimension less than 100 nm, are currently being explored for potential energy and environmental applications. Among the manifold nanomaterials, nanostructured oxides are indispensable for most applications, because they offer an almost infinite variety of structural motifs with equally attractive chemical and physical properties.[17-23] Over the past years, it has been reported that oxide nanomaterials have promising applications in photocatalysts,[24-28] solid oxide fuel cells,[29-31] solar cells,[32-36] electrochemical energy storage,[37-41] miniaturized sensors,[42-46] thermoelectric conversion processes,[47-49] and other crucial areas of energy and environmental technology. However, the performances of oxide materials strongly depend on their size, shape, structure and chemical composition. For example, the photocatalytic reaction process is a complex interplay of band structure, crystal structure, crystallinity and particle size: layered structures are favorable for the separation and transportation of photo-induced charge carriers; a high degree of crystallinity can decrease the amount of defects which operate as trapping and recombination centers and small particle sizes can finally decrease the possibility of recombination.[50-53] This calls for the development and tailoring of synthetic procedures to access oxide nanomaterials in a targeted fashion. Remarkable progress has been achieved in this direction and many different synthesis routes including solid-state synthesis,[54,55] vapor phase routes,[56-58] aerosol flame syntheses,[59,60] sonochemical syntheses,[61-63] hydrothermal routes,[64-66] microwave-assisted strategies,[67-69] or biomolecule-assisted syntheses[70,71] have been reported to provide oxide nanomaterials in a wide variety of phases and different morphologies, such as nanotubes, nanowires, nanorings, nanosheets, hierarchical nanostructures and so on. Nevertheless, the high expectations for nanomaterials

research are now critically reconsidered with respect to methodological progress and technological benefits.[72] Preparative nanochemistry has apparently reached a "turning point", because considerable synthetic challenges still have to be solved:

- Firstly, most of the above-mentioned synthetic routes involve expensive infrastructure, high reaction temperatures and organic solvents which are energy consuming and ecologically harmful, thereby impeding large scale nanomaterials production. This calls for the development of environmentally friendly and energy-saving methodologies for nanomaterial synthesis.[73]
- Secondly, most of the preparative activities are still focused on commercially relevant binary oxide nanomaterials, such as TiO_2, ZnO, SnO_2 and Fe_3O_4. In contrast to this trend, technologically important ternary and higher oxides remain to be transferred onto nanoscale dimensions. This is an urgent incentive to speed up detailed experimental investigations on the size-dependent properties of these oxide materials and of their resulting potential applications.[74]
- Finally, the structural analysis of oxide materials under real reaction conditions is much more complicated compared with related investigations in organic synthesis. As a consequence, we still do not fully understand the nucleation and growth processes of nanomaterials in general.[72] This lack of quantitative mechanistic knowledge renders the rational design of new functional oxide materials a demanding task.

In summary, difficulties in the synthesis of ternary and higher oxide nanomaterials are largely due to the fact that we still do not understand the formation mechanism of oxide materials on a general level so that insights from mechanistic investigations are highly useful for the large-scale technical production of oxide nanomaterials. Therefore, an essential long-term goal of synthetic endeavours should be the understanding of their reaction mechanisms. For this purpose, the continuous in situ monitoring of nanomaterials formation is the most detailed and accurate approach to obtain quantitative kinetic information and to investigate possible intermediates,[75-77] because there are no generally applicable theoretical concepts available at

the moment. This information is the first step towards developing a model for the reaction mechanism. Furthermore, considering the environmental issues, the most promising large scale production strategy would be the economic fabrication of oxide nanomaterials from readily available inorganic materials with low-resource settings.[72]

1.2 Inorganic hydrothermal routes

In order to optimize the large-scale production of oxide nanomaterials, the following guidelines are important:

1. The precursor materials should be nontoxic and air-stable to avoid the use of special protective atmospheres.
2. The number of precursors should be kept to a minimum.
3. Water is the best choice for the solvent because it is environmentally friendly, low-cost and its polarity leads to its exceptional ability to dissolve mineral salts.
4. The number of reaction steps should be minimized and the reaction temperature should be kept as low as possible.

A pressure and temperature map of the currently available synthetic techniques is shown in Figure 1.1.[78] Among the manifold routes, hydrothermal technology is considered as environmentally benign due to its mild reaction conditions, which is a promising prerequisite for the large scale production of nanomaterials. The hydrothermal process is purely of geological origin which was first discovered by the British geologist *Sir R. Murchison* (1792-1871).[79] Recently, *K. Byrappa* and *T. Adschiri* defined hydrothermal processing in a wider sense as any heterogeneous reaction in the presence of aqueous solvents or mineralizers under high pressure and temperature conditions to dissolve and recrystallize materials which are relatively insoluble under standard conditions.[79] A detailed introduction to hydrothermal techniques can be found in the comprehensive reviews published by *K. Byrappa*, *T. Adschiri*[80] and by *R. I. Walton*.[81] Over the past years, the hydrothermal technique has

become one of the most important tools for oxide nanomaterials synthesis,[19, 64, 66] because hydrothermal syntheses offer manifold advantages: they can be operated as "green" one-step and waste-free reactions without organic solvents involved. Moreover, hydrothermal reactions permit the adjustment of a wide range of experimental parameters and they are operated at low temperatures well below the melting point of the precursors, thereby offering infinite opportunities to synthesize high surface area oxide nanomaterials with a variety of compositions as well as metastable phases which are difficult to access with conventional solid state reactions.[79]

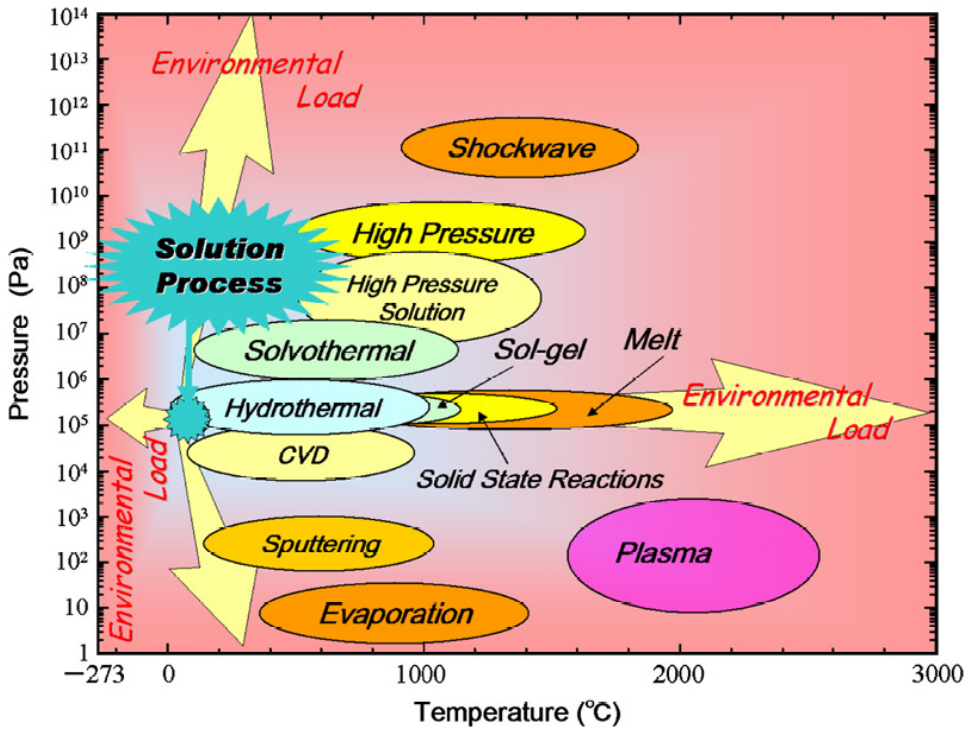

Figure 1.1. Pressure and temperature map of materials processing techniques.[78]

From the viewpoint of large-scale production, hydrothermal syntheses of anisotropic oxide nanomaterials that are based on the inherent structural features of the target materials are a promising strategy, because they can be operated in a facile, one-step and surfactant-free manner. The presence of anisotropic chain-like structural elements, for example, can lead to the growth of one-dimensional (1D) morphologies of the desired products.[83,84] Layered precursor materials would consequently support the formation of 2D morphologies such as

sheet-like or platelet shapes.[85,86] Nevertheless, the anisotropic growth of oxide nanomaterials based on their crystal structures only covers a limited number of oxide materials. Furthermore, modifying the morphology of oxide materials with anisotropic structural elements into another direction is also a general challenge. To overcome these problems, organic surfactants or hard templates, which can block certain surfaces of the growing crystals and turn them into various anisotropic morphologies, have been widely used as "growth modifiers" in hydrothermal synthesis.[87-89] However, the presence of templates may lead to impurities in the final products and their use and subsequent removal can also increase the overall production costs. In addition, the thermal instability of organic components can give rise to decomposition processes and side reactions.[90]

On the other hand, low cost and flexible inorganic salt additives could be an elegant way to exert morphology and structure control over nanoscale products. Recent results have clearly demonstrated that inorganic salts in a hydrothermal reaction system can play an equally powerful role as organic surfactants or hard templates in controlling the morphology and structure of the emerging oxide materials. A survey of typical examples illustrating the hydrothermal synthesis of oxide nanomaterials with inorganic additives is given in Table 1.1.

In fact, the implementation of inorganic salt additives in hydrothermal reactions already has a long history and is common practice in other areas. Traditionally, inorganic salts were used as mineralizers to increase the solubility of the precursors and to furthermore change the temperature coefficients of their solubility.[80] Therefore, the use of various salts can render the pressure and temperature conditions of hydrothermal syntheses more convenient, which in turn simplifies the experimental setups.[79] However, the most recent insights into hydrothermal processes revealed that inorganic additives play a much more complex role than that of simple mineralizers. It was found that inorganic additives can strongly influence and adjust the morphology and structure of the hydrothermal products emerging from different oxide systems. Among them, MnO_2 is an illustrative example of highly efficient morphology and structure control through the combination of inorganic additives with a structurally flexible target oxide that occurs in different polymorphs, such as α-, β-, γ-, and δ- and ε-MnO_2. They contain edge- or corner-sharing MnO_6 octahedra in different connectivity

schemes, thereby offering a wide variety of possibilities to adjust the structure and morphology of MnO_2. Through the careful selection of versatile inorganic additives, MnO_2 nanotubes,[94] nanowires,[91] hierarchical nanostructures[92] and nanoplates[93] of different MnO_2 phases have been obtained under hydrothermal conditions. These results clearly demonstrate that the steering of hydrothermal processes through the use of readily available inorganic additives provides particularly elegant approaches to control the structure and morphology of key oxide materials. However, this raises another question: how and why can inorganic additives influence the structure and morphology of the oxide materials so strongly? Generally, several roles of inorganic additives in hydrothermal reactions can be proposed:

1. The solubility of the precursors is increased by additives working in the sense of mineralizers.
2. Inorganic additives can enhance the reactivity of precursors to form intermediates, thereby changing the reaction pathway.
3. They can interact with special crystallographic planes to change their surface energy. This can promote or inhibit the growth of a specific plane, resulting in different final morphologies. The stabilizing effect of NO_3^- ions on the {100} planes of Cu_2O is an instructive example.[105, 106]
4. Inorganic ions may be incorporated into the crystal structure of the final products to stabilize metastable phases or to form an entirely new structure motif.
5. Inorganic additives can finally influence the formation of seeds and the growth rates of the oxide materials as well as the resulting reaction kinetics.

As a result, hydrothermal reactions that are assisted by inorganic additives involve a complex multitude of steps, such as the dissolution equilibria of the starting materials, the possible formation of intermediates, the surface interactions of the additive ions with the growing nuclei, and the resulting reaction kinetics. Due to these manifold factors, their mechanistic principles are little understood to date. As expected, the majority of the according investigations on oxides are focused on binary systems as illustrated in Table 1.1. Mechanistic and morphological studies on ternary and higher oxide systems are quite limited due to their much more complex reaction pathways.

Table 1.1. Selected examples for hydrothermal syntheses of oxide nanomaterials with inorganic additives.

Oxide	Inorganic additive	Specific features	Ref.
MnO_2	KCl, NH_4Cl, NaCl	Cationic effect on MnO_2 crystallization	[91]
MnO_2	$Fe(NO_3)_3 \cdot 9H_2O$, $Al(NO_3)_3 \cdot 9H_2O$	Influence of metal ions on the structure and morphology of MnO_2	[92]
MnO_2	NH_4Cl, NH_4NO_3, $(NH_4)_2SO_4$, $(NH_4)_3PO_4$	Influence of anions on the morphology and phase of MnO_2	[93]
MnO_2	NaF, Na_2SO_4, NaCl, $NaNO_3$, NH_4F	Effect of inorganic salts on polymorphs and morphology of MnO_2	[94]
CeO_2	$NaNO_3$, Na_2SO_4, $NaBrO_3$, NaI, NaBr	Anion-induced growth of CeO_2 nanorods and nanocubes	[95]
CeO_2	$Na_3PO_4 \cdot 6H_2O$	Selective synthesis of CeO_2 nano-octahedrons and nanorods	[96]
Fe_2O_3	$NH_4H_2PO_4$	Synthesis of Fe_2O_3 nanotubes	[97]
Fe_2O_3	NaCl, NaAc	Selective synthesis of Fe_2O_3 with different morphologies	[98]
ZnO	Na_2SO_4, NaCl	Effects of inorganic salts on the morphologies of ZnO	[99]
MoO_3	KNO_3, $Ca(NO_3)_2$, $La(NO_3)_3$	Morphology-controlled synthesis of MoO_3	[100]
SnO_2	Na_2SO_4	Synthesis of SnO_2 nanocrystals	[101]
$W_{18}O_{49}$	Na_2SO_4	Fabrication of $W_{18}O_{49}$ nanorods	[102]
M_xWO_3 (M= Li~Cs)	Li_2SO_4, Na_2SO_4, Rb_2SO_4, K_2SO_4, LiCl, NaCl, KCl, RbCl, CsCl	Hexagonal alkali tungsten bronzes (M_xWO_3) with different morphologies	[103]
$BiFeO_3$	KNO_3	Synthesis of $BiFeO_3$ nanoparticles	[104]

All in all, we believe that inorganic hydrothermal routes are very promising for the large-scale production of oxide nanomaterials due to their manifold options for optimization and their facile technical handling. This calls for a systematic investigation of the role of inorganic

additives and of the according hydrothermal formation mechanisms taking place in oxide systems. In the following, key in situ methods for this purpose are briefly introduced.

1.3 In situ methods

In principle, the reaction pathways of hydrothermal reactions can be determined by ex situ methods, where autoclaves are quenched to interrupt the reaction after various time intervals. Consequently, the phase, compositions, morphology and the degree of crystallization can be investigated for different stages of the reaction. However, these indirect strategies always bear the risk of isolating artefacts that lead to false conclusions. Furthermore, ex situ experiments can only provide limited data, which renders a more detailed kinetic analyses quite difficult. As mentioned in section 1.1, in situ investigations yield the most accurate data to study, for example, how inorganic additives influence nucleation and crystal growth processes. They also provide information about intermediate phases that may occur during the reaction process. Generally, in situ methods offer a good solution when the fundamental understanding of hydrothermal kinetics in a given system is insufficient. Over the past years, considerable progress has been achieved both in the construction of in situ reaction cells and in the use of powerful radiation sources, instrumentation and detectors. A great variety of in situ methods, including in situ XRD,[107] in situ XAS,[108] in situ NMR,[109] in situ SAXS,[110] in situ IR,[111] in situ UV/Vis[112] and in situ Raman,[113] has been developed to monitor the formation pathways of oxide materials. Nevertheless, it is important to know that all these in situ techniques have their inherent limitations and are only capable of monitoring a selective aspect of the complex reaction process. Detailed introductions to different in situ techniques are given in recent reviews.[114,115] Furthermore, one should keep in mind that hydrothermal reactions are performed under non-ambient temperatures and pressures in sealed cells so that high energy radiation sources which can penetrate the reaction vessel walls are indispensable. For this purpose, synchrotron X-ray sources with very high intensity and brilliance (number of photons per volume unit) are most suitable in terms of intensity, time resolution (far below the minute scale) and accuracy. Hence, the following discussion is focused on diffraction and

spectroscopic techniques based on synchrotron X-ray sources.

1.3.1 In situ EDXRD techniques

Synchrotron X-ray diffraction experiments can be performed using two different techniques: angular or energy dispersive diffraction. In the case of angular dispersive XRD, a monochromatic X-ray beam is selected with a monochromator to obtain high resolution data that are suitable for Rietveld refinements that yield detailed structural information.[116] On the other hand, the use of monochromators significantly decreases the intensity of the employed X-rays. Consequently, in situ studies of hydrothermal reactions with angular dispersive XRD techniques are limited to quite small reaction cells.[117] *P. Norby* et al. have developed an in situ cell based on a quartz capillary to study the hydrothermal crystallization of inorganic materials.[118] However, the obvious drawback of this method is the downscaling of the synthesis reactor to minimize absorption effects in comparison with laboratory experiments. As hydrothermal reactions are generally sensitive towards changes in the experimental conditions, in situ results always have to be critically compared to their laboratory-scale analogues. On the other hand, in the course of energy dispersive X-ray diffraction (EDXRD) techniques, data are collected with a fixed angle solid state photon counting and energy discriminating detector and the Bragg diffraction is recorded as a function of the energy which is dependent on the angle of the detector.[119] Since no monochromator is employed, the X-ray with high flux and intensity permits the probing of large volume samples in thick-walled reaction vessels. Hence, the reaction cells used for in situ EDXRD can be very similar to standard laboratory autoclaves which render the results obtained from in situ EDXRD more realistic. Furthermore, EDXRD techniques utilizing a polychromatic beam offer a high time resolution which is very important to monitor the reaction pathways. Some of the first experiments involving in situ EDXRD to study the hydrothermal synthesis of solid state materials were reported by *H. He* et al. in 1992.[120] Since then, in situ EDXRD techniques have become increasingly popular to investigate the hydrothermal crystallization processes of inorganic materials.[121-125] *P. Barnes* and coworkers in particular have made pioneering efforts

in the use of EDXRD for monitoring hydrothermal syntheses of inorganic materials at the Daresbury Synchrotron Radiation Source (SRS).[126] *D. O'Hare* et al. have further developed this technique and a large number of in situ studies of chemical reactions has been published by this group.[119,124,127] Figure 1.2 shows a typical hydrothermal autoclave for in situ EDXRD experiments developed by *D. O'Hare* et al. with three energy discriminating detectors.[119] This setup permits three *d*-spacing regions of the diffraction pattern to be measured at the same time.

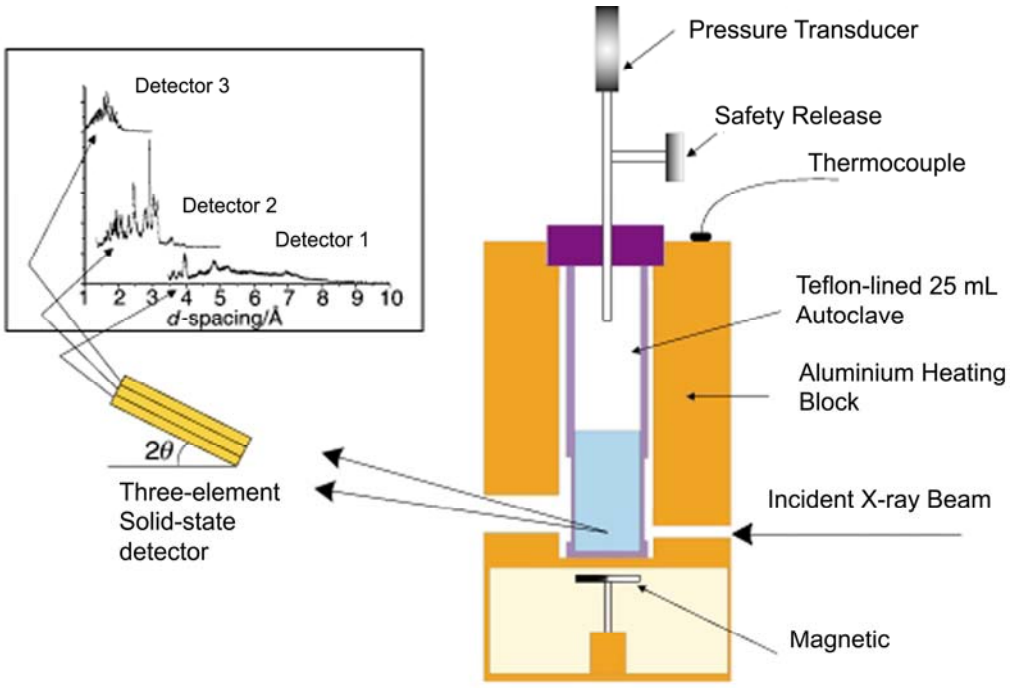

Figure 1.2. Schematic representation of the Oxford/Daresbury hydrothermal autoclave used for in situ EDXRD studies.[119]

The data obtained from in situ diffraction can be used to evaluate the reaction kinetics, because the intensity of a Bragg reflection is directly proportional to the amount of diffracting solid. The first step of the in situ data analysis is the integration of the peak intensity in the individual spectra using a Gaussian function. Next, the integrated intensities of the product reflections are normalized against the intensity of the related element resonance. The value of the extent of reaction α at a given time, *t*, can be calculated from the growth of a newly emerging Bragg reflection (*hkl*) using

$\alpha(t)=I_{hkl}(t)/I_{hkl}(t_\infty)$, where $I_{hkl}(t)$ is the normalized intensity of a reflection (*hkl*) with time *t*, and $I_{hkl}(t_\infty)$ represents the normalized intensity when the reaction is finished ($\alpha=1$). To obtain detailed information on the kinetics of the crystallization process, the kinetic evaluation is performed after subtracting the induction time t_{ind} (defined as the time interval until the first reflections are observed) from the measured time *t*, using the well-known Avrami-Erofe'ev equation, which takes the form:[127-129]

$$\alpha=1-\exp\{-[k(t-t_{ind})]^m\} \qquad (Eq.\ 1.1)$$

here, *k* represents a rate constant and the exponent *m* is often used to distinguish between different reaction mechanisms.[130] The value of *m* is most easily visualized with the aid of a Sharp-Hancock (SH) plot using the following equation:[131]

$$\ln[-\ln(1-\alpha)]=m\ln(t-t_{ind})+m\ln k \qquad (Eq.\ 1.2)$$

When $\ln[-\ln(1-\alpha)]$ is plotted vs. $\ln(t-t_{ind})$, a straight line is obtained if the given period of the reaction proceeds according to a single mechanism. A change of the mechanism consequently results in a change of the slope of the curve. The exponent *m* can be evaluated from the slope of the linear part of the curve. Furthermore, *k* can be obtained from the intercept with the *y* axis. Although this method has been widely used to study the reaction kinetics of zeolites,[117] oxides[121,123] and metal-organic frameworks,[122] it should be kept in mind that the value of *m* is strongly dependent on the data analysis, especially on the choice of the induction time. Moreover, the Avrami-Erofe'ev equation was developed to simulate nucleation and growth of crystalline solids using ideal conditions like spherical particles of identical size, no impinge of the particles, and related conditions. These criteria are seldom fulfilled in real systems. Therefore, it is important not to over-interpret the kinetic data.

The main disadvantage of EDXRD compared with angular dispersive XRD is the low resolution of the obtained data due to the limited energy resolution of the detectors. This often renders the extraction of structure information from energy dispersive data, e.g. via Rietveld refinement, impossible. Nevertheless, for the present research goals of our current work, in situ EDXRD was often the method of choice.

1.3.2 In situ XAS methods

As mentioned above, a selected in situ technique can only provide a part of the comprehensive information that is required to fully understand hydrothermal processes. Bragg diffraction, for example, does not permit the direct observation of particles smaller than ca. 5 nm and of potential amorphous phases. As a consequence, no information about rearrangements in liquid and amorphous phases can be obtained, which is very important to understand the decisive nucleation stages. X-ray absorption spectroscopy (XAS) refers to the oscillatory structure in the X-ray absorption coefficient just above an X-ray absorption edge which can provide information about the local atomic structure and the oxidation state of the absorber atom regardless of its crystallinity. Obviously, their combination with in situ EDXRD is a very far-reaching and comprehensive strategy: whereas diffraction techniques can track the kinetics, growth processes and phase changes of solids, XAS can overcome the detection limits of Bragg diffraction to monitor the crucial nucleation steps and to obtain structural information from amorphous and liquid phases. A detailed introduction to the history, theory and data evaluation of XAS can be found in a review published by *J. J. Rehr* and *R. C. Albers*.[132] XAS spectra at a specific absorption edge can be divided into two major regions (X-ray absorption near edge structure, XANES, and extended X-ray absorption fine structure, EXAFS): XANES includes the pre-edge region and extends from a few eV to about 50 eV above the edge, whereas EXAFS extends from energies about 50 eV up to more than 1000 eV higher than the absorption edge. The XANES region contains peaks corresponding to electronic transitions, which are sensitive to the electronic structure of the absorber and its chemical bonding environments, thereby providing a “fingerprint” of the local coordination geometry. EXAFS oscillations are a result of the backscattering of the ejected photoelectron with the neighboring atoms which contains information about the interatomic distances and coordination numbers.[133] Furthermore, the edge position is influenced by the oxidation state of the absorber atom. However, the theory of XANES is not as yet fully self-consistent so that the evaluation of XANES data normally requires a comparison to references with known structure motifs. Moreover, the evaluation of EXAFS data is not straightforward either and the detailed analytic procedures can be found in the literature.[132] In general, the recorded

EXAFS data need to be transformed into *k*-space after background subtraction and normalization. The EXAFS oscillation, $\chi_i(k)$, is defined as the sum of modified sine waves with different frequencies and phases from each backscattering coordination shell *j*, around the central atom *i* as shown in the following equation:

$$\chi_i(k) = \sum_j A_j(k) \sin[\varphi_{ij}(k)] \qquad (Eq.\ 1.3)$$

where $A_j(k)$ is the total backscattering amplitude of the *j*th shell and $\varphi_{ij}(k)$ is the corresponding total phase function. The curved wave scattering theory including contributions from multiple scattering has been developed by *E. A. Stern* et al.[134] Hence, the phase shift and scattering amplitude factors can be calculated on the basis of a theoretical model using the FEFF-code.[135] After least squares curve fitting between the experimental data and a calculated XAFS function, the interatomic distances, the coordination number and the Debye-Waller factor of the absorber atom can be evaluated.

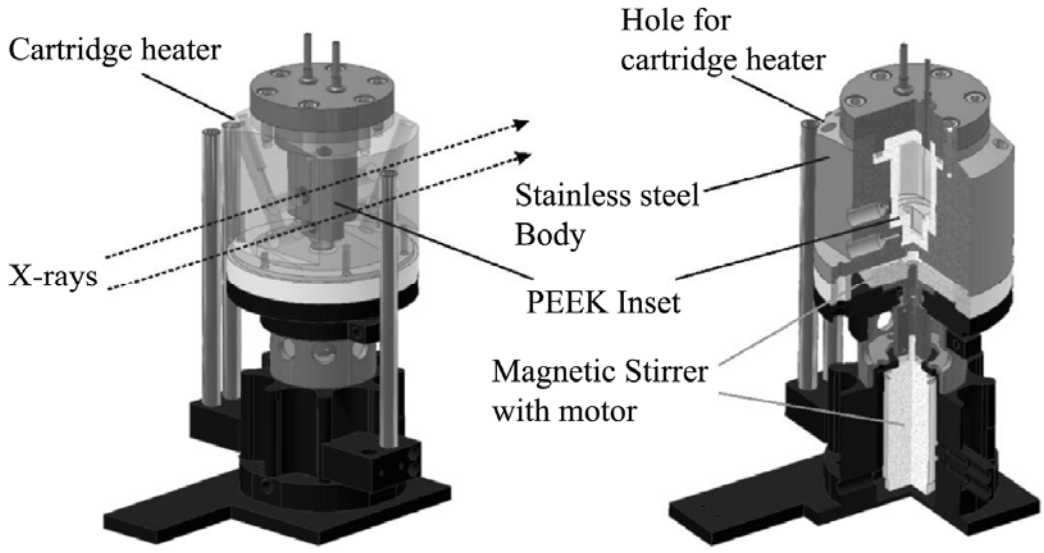

Figure 1.3. 3D views of the batch reactor cell with PEEK container and magnetic stirrer.[136]

To date, the acquisition of high quality data for in situ EXAFS investigations of hydrothermal reactions with a high time resolution remains a difficult task. Most often, only XANES data are used to investigate the local environment and the oxidation state of the absorber. Figure 1.3 shows an in situ XAS cell designed by *J.-D. Grunwaldt* et al. which allows the

simultaneous monitoring of the liquid phase and the liquid/solid interface.[136] *G. R. Patzke*, *J.-D. Grunwaldt* and coworkers have successfully used this apparatus to elucidate the hydrothermal transformation of $MoO_3 \cdot 2H_2O$ into MoO_3 fibers and their results demonstrate how different hydrothermal pathways can be from the initial "chemical intuition".[108] As the precursors and products bear close structural resemblance, it was reasonable to propose a reaction mechanism involving a topotactic transformation of $MoO_3 \cdot 2H_2O$ in the first place. However, in situ XAS studies of both the liquid and solid phase during the conversion process in combination with in situ EDXRD measurements demonstrated that a quick dissolution-precipitation mechanism without a crystalline intermediate phase leads to MoO_3 instead. This example clearly proved that the combination of in situ EDXRD and in situ XAS is a very powerful approach to understand the hydrothermal formation mechanisms of oxide nanomaterials. Nevertheless, such insights into the crystallization pathways of oxide nanomaterials are still limited to selected systems and most of them are focused on binary oxides. Therefore, in the present study, we investigate the hydrothermal formation mechanisms of ternary and higher oxides with a high tuning potential for technological applications.

1.4 Environmental applications of oxide nanomaterials

Energy and environmental issues at a global level are the most important and urgent research topics these days. They will not be solved without the development of renewable energy systems and constant access to clean water resources.[2,3] Since the discovery of photoelectrochemical splitting of water on n-TiO_2 electrodes,[24] semiconductor-based photocatalysis has attracted increasing attention and it is regarded as a promising strategy to alleviate both problems through splitting water for hydrogen and oxygen production and by degrading toxic pollutants in waste water. In addition, the continuous monitoring of environmental conditions on all levels from daily processes to industrial productions is another important step to ensure a constant quality of life.[137] Recently, great progress has been achieved to construct novel miniaturized sensors based on oxide nanomaterials that can

be applied almost everywhere with minimum energy supply. [42] Starting from new insights based on in situ investigations, it is now possible to synthesize oxide nanomaterials with controllable composition, structure, particle size and morphology through hydrothermal reactions. Therefore, the environmental applications of the obtained oxide nanomaterials are investigated accordingly in the present thesis.

1.4.1 Photocatalytic reactions

The main processes in a photocatalytic reaction involve several individual steps as shown in Figure 1.4.[3] Electron (e^-)-hole (h^+) pairs are generated when a semiconductor is irradiated by photons with an energy that exceeds or equals the band gap energy. Most of these electron-hole pairs recombine and release the absorbed energy as light or heat. However, a small percentage of these carriers can migrate to the surface of the material where they can be captured by adsorbed molecules to initiate various redox reactions. Consequently, to design highly active photocatalysts, several factors need to be considered:

- ✧ The band gap of the involved semiconductors should match the solar spectrum so that the energy of the incident sunlight can be effectively used.
- ✧ The bottom level of the conduction band of semiconductors has to be lower than the redox potential of H^+/H_2 (0 V *vs.* NHE), while the top level of the valence band must exceed the redox potential of O_2/H_2O (1.23 V).
- ✧ As only the electrons and holes on the surface are involved in the catalytic reactions, it is extremely important to decrease the recombination chance of photo-induced electrons and holes on their way through the crystal: several factors, especially, crystal structure, crystallinity and particle size strongly affect this process. Layered structures are favorable for the separation and transportation of charge carriers, because they can provide sufficient space to polarize the related atoms and orbitals. The induced dipoles can separate hole-electron pairs efficiently. A high degree of crystallinity can minimize the amount of defects which operate as trapping and recombination centers. Small particle sizes can furthermore decrease the recombination possibility by shortening the migration

distances of electrons and holes to the surface.

✧ The catalysts should be nontoxic and stable for practical recycling processes.

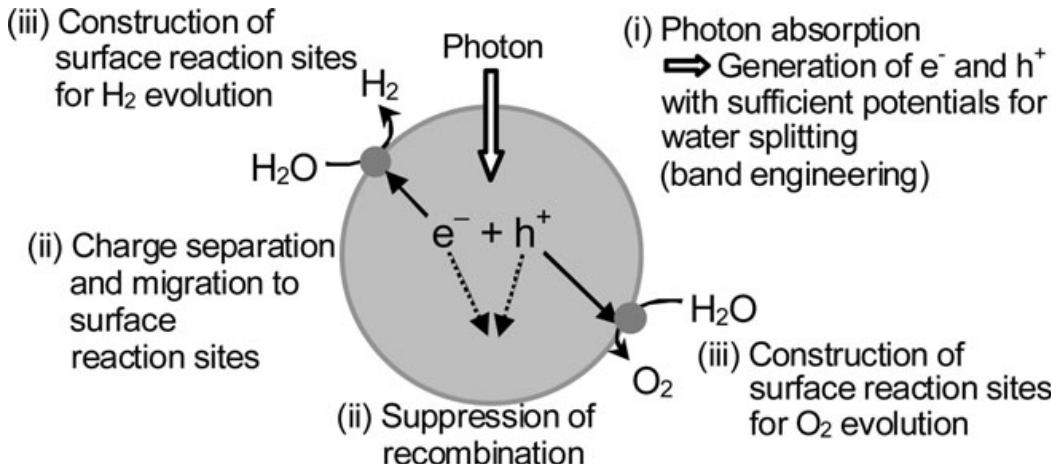

Figure 1.4. Key steps of photocatalytic reactions.[3]

Therefore, the overall process is a complex interplay of individual factors including band structure, crystal structure, crystallinity and particle size. The general requirements for the targeted synthesis of photocatalysts can be summarized as follows: appropriate band structure, high crystallinity and high surface area.

TiO_2 is by far the most widely used and investigated photocatalyst due to its high efficiency, good photostability, non-toxicity and its low price. Despite these remarkable advantages, the wide band gap of TiO_2 (3.2 eV, $\lambda < 387$ nm) limits its activation to UV irradiation, which represents only 4 % of the sunlight arriving on the surface of the earth. Hence, its potential for sustainable technologies can not be entirely implemented in an economic fashion.[26] Therefore, intensive research efforts are focused on the modification of TiO_2 by doping with metallic or nonmetallic elements such as V and Cr, or N, S, and C, respectively, to render photocatalysis under visible light irradiation possible.[138] However, the doped TiO_2 materials often suffer from lower absorbance than undoped TiO_2 and from fast e^-/h^+ recombination rates, which limit their photocatalytic activity. Another strategy is the development of entirely new photocatalytic materials as visible light driven alternatives to TiO_2. Currently, it is becoming increasingly clear that the development of functionalized ternary and higher oxides

is an efficient strategy to overcome the intrinsic band structure limitations of binary oxides.[139] Among the multitude of complex oxides that have been investigated for the development of photocatalysts, bismuth-containing oxides have proven especially promising under visible light irradiation.[140] The electronic structure of many Bi-based oxides resembles the model shown in Figure 1.5. The Bi 6s and O 2p levels of these oxides can form a hybridized valence band (VB) that is largely dispersed. Thus, the band gaps are narrowed and the mobility of photoholes in the VB is enhanced,[139, 140] which favors the visible light driven photocatalytic process. Moreover, these oxide systems have manifold structural motifs that offer the great opportunity to adjust their properties according to the desired applications. Therefore, the present work is focused on the synthesis of Bi-containing oxide nanomaterials and on their photocatalytic activities.

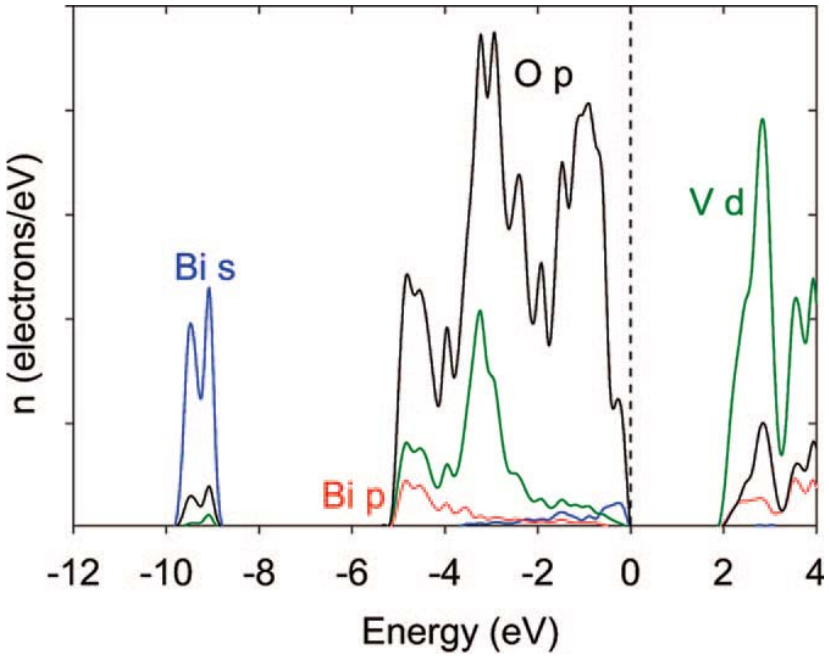

Figure 1.5. Total and partial electronic density of states of $BiVO_4$.[139]

1.4.2 Gas sensing applications

Monitoring and controlling environmental conditions has become more important than ever before in the areas of air quality control, environmental protection and healthcare as well as

for industrial process control.[141] For example, the humidity conditions around a membrane electrode assembly can strongly affect proton exchange performance. At low humidity values, it can not be easily traversed by protons, resulting in high ohmic voltage losses which in turn reduce the cell performance. However, excess water can lead to local water flooding that affects gas transport and distribution, which deteriorates the cell performance significantly.[142,143] Since *T. Seiyama* et al. discovered that the electrical conductivity of ZnO could be dramatically changed in the presence of gases in the air,[144] semiconducting metal oxides have attracted much attention in the field of gas sensors due to their low cost and flexibility in production.[145] Until now, a wide variety of oxides, especially binary oxides such as SnO_2, ZnO, In_2O_3, TiO_2 and WO_3, has been studied as sensing elements in gas sensors and they have also been used for commercial devices.[146, 147] Nevertheless, the choice of a suitable material is still rather difficult, because gas sensing mechanisms in general are still not well understood. The gas adsorption process which is responsible for the sensor signal is strongly influenced by the presence of the pre-adsorbed species such as ionosorbed oxygen, hydroxyl groups and carbonates.[145] Therefore, the measuring of the resistance changes of the sensing materials upon exposure to the target gas can only record the overall electrical effect in contrast to the complex surface reactions. Hence, it is difficult to correlate individual surface species with their electrical effects. Furthermore, it has been demonstrated that the gas sensing properties of oxide materials are strongly related to their adsorption abilities, electronic, electro-physical and chemical properties, catalytic activities, thermodynamic stabilities, crystallographic structures and interface states.[149] Therefore, very few oxides can excel in all of these requirements. The present strategy in this field is to measure all sensing properties including sensitivity, selectivity and stability to discover suitable sensing materials.

So far, many different material types have been studied in the gas sensor field and many companies such as Figaro, MICS, UST and Applied Sensors can already offer tailored commercial sensors for different applications. However, the search for new materials with quick response/recovery to fabricate sensitive and stable sensors is still an ongoing demand. As oxides offer an almost endless spectrum of structural motifs and properties that can be tuned through substitution reactions and nanomaterials formation, there are numerous ternary,

quaternary and complex metal oxides which are of interest for gas sensing applications. We therefore studied the gas sensing properties of our obtained oxide nanomaterials to screen them for potential sensing applications.

1.5 Goals and strategy of the present thesis

1.5.1 Goals

In this work, we focus on the hydrothermal synthesis of functional oxide nanomaterials and on the understanding of their formation mechanisms using in situ EDXRD/XAS techniques. We aim for facile inorganic hydrothermal routes to nanostructured ternary oxides with a high environmental application potential, such as in photocatalysis and gas sensing.

1.5.2 Research strategy

Figure 1.6 provides a detailed flow-chart illustrating our approach. The strategy towards the development of novel materials with potential applications in environmentally relevant areas includes the definition of the property requirements and of the target materials (step 1). The band structure, crystal structure, crystallinity and particle size of materials significantly influence their performances in most applications. This requires the development or tailoring of adaptable synthetic procedures. In this work, hydrothermal methods are the preferred technique (step 2) and for the targeted synthesis of oxide nanomaterials, the combination of two different approaches (“top-down” vs. “bottom-up”) will be compared. Firstly, the target hydrothermal systems can be screened through adjusting the preparation parameters (empirical “top-down” strategy). Next, they are studied from the “bottom-up” by in situ monitoring of their reaction kinetics to elucidate the reaction mechanisms. Subsequently, the thorough characterization of the materials properties (e.g. structure, morphology, composition, surface area, stability and optical properties) is crucial to understand the complex relationships between compositions, structure, properties and applications (step 3). Finally, the environmental applications of the synthesized materials are investigated and novel strategies for improving their applications are furthermore developed (steps 4 and 5).

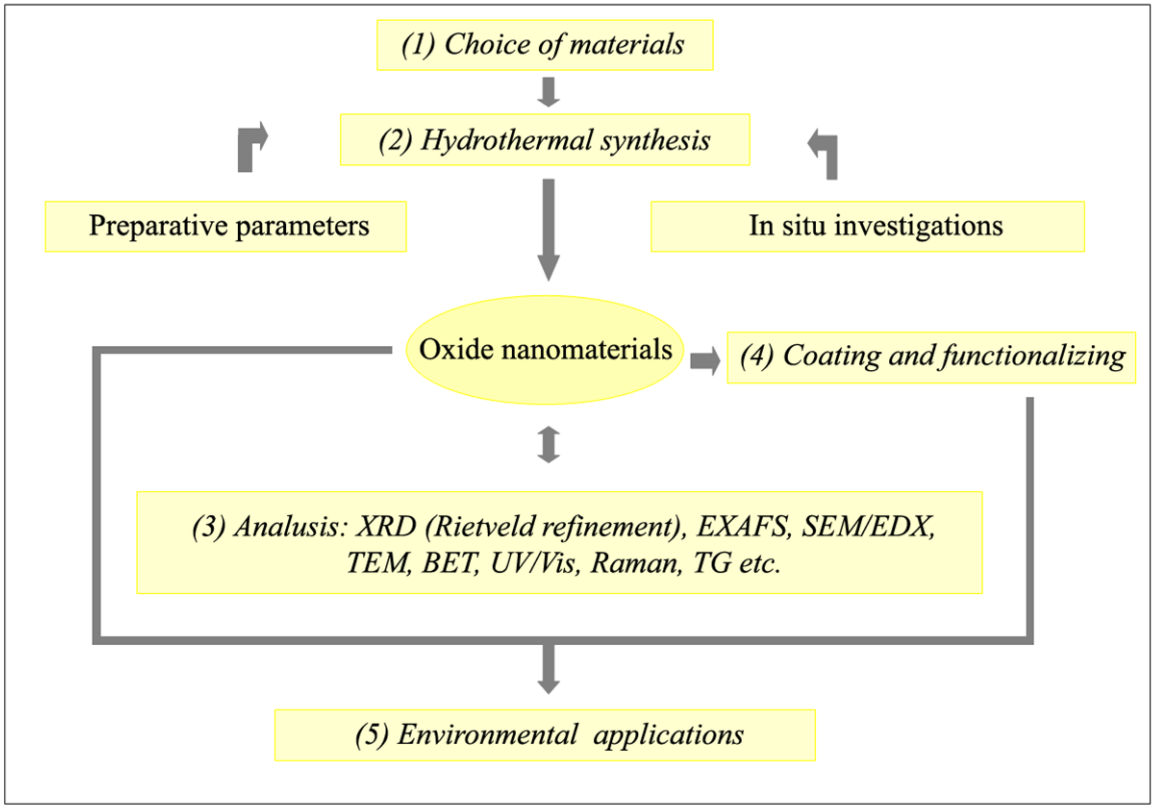

Figure 1.6. Flowchart of the experimental approaches and methods employed in the present thesis.

The course of the investigations for the present study is shown in Figure 1.7. Part I is focused on the development of Bi-containing oxides for visible light driven photocatalytic applications. In this part, different preparative strategies are applied to improve the activity of oxide materials. Chapter 2 demonstrates that the photocatalytic activities of $BiVO_4$ particles can be significantly enhanced through decreasing the particle size and increasing the surface area via an additive-assisted hydrothermal approach. In chapter 3, the photocatalytic activities of hierarchical Bi_2WO_6 nanostructures are investigated. The activity of such materials can be further enhanced through modifying the electronic structure (chapter 4) and through the formation of heterojunctions (cf. chapter 5). The sensing applications of selected oxide nanomaterials are investigated in Part II. Chapter 6 illustrates that hierarchical Bi_2WO_6 nanostructures are not only good candidates for photocatalytic applications but that they also exhibit a promising application potential for the fabrication of effective, stable and low-cost humidity sensors. In chapter 7, we report on the humidity sensing properties of $Bi_6S_2O_{15}$

nanowires that furthermore represent a novel bismuth oxysulfate type. In the final chapter, the NH_3 sensing properties of W/Mo-oxides are investigated. Moreover, several examples for the successsful investigation of hydrothermal formation mechanisms of complex oxide nanomaterials with the help of in situ methods are reported in the course of the present work.

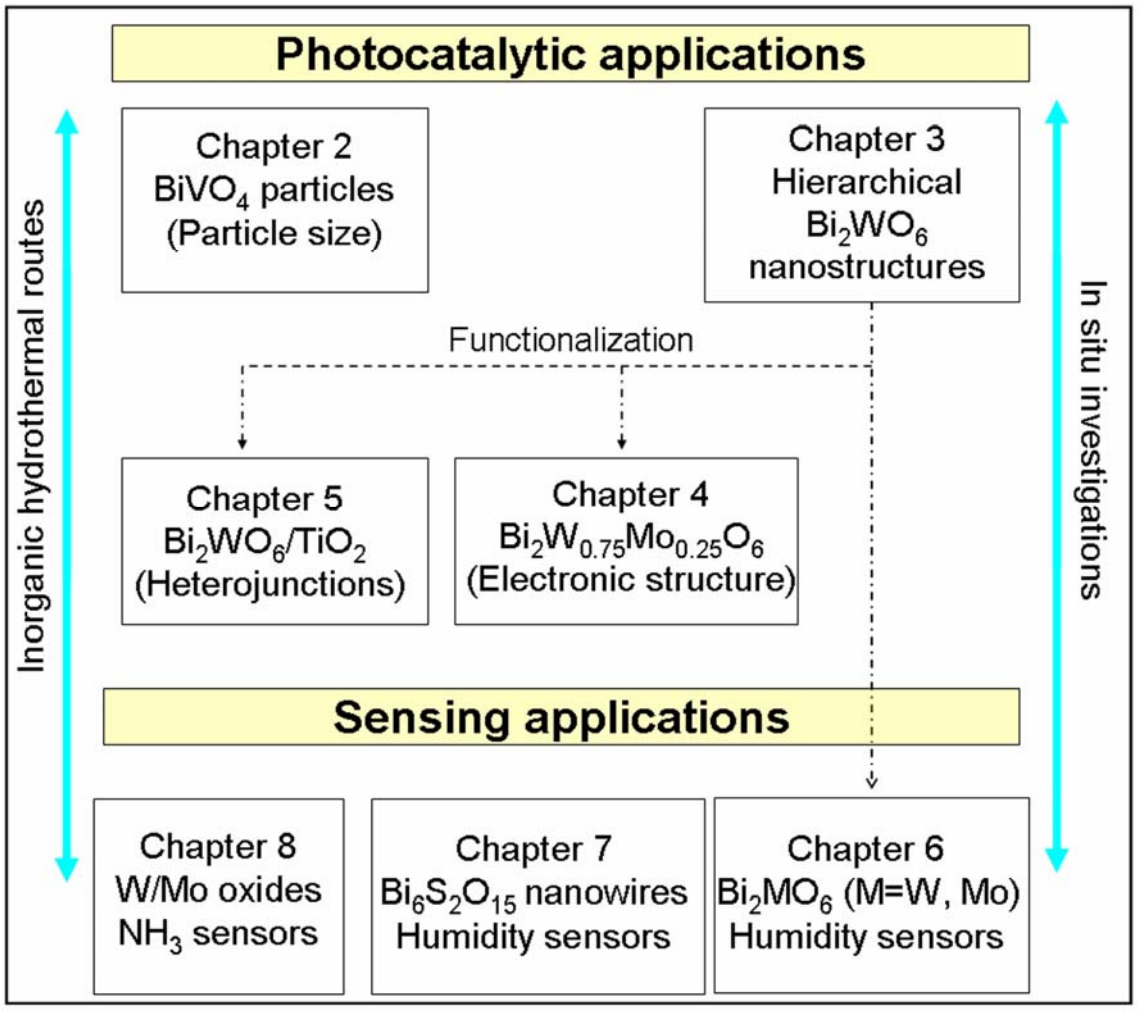

Figure 1.7. Strategic flowchart of the present work.

References

[1] A. Hochbaum, P. Yang, *Chem. Rev.* **2010**, *110*, 527.

[2] M. R. Hoffmann, S. T. Martin, W. Choi, D. W. Bahnemann, *Chem. Rev.* **1995**, *95*, 69.

[3] A. Kudo, Y. Miseki, *Chem. Soc. Rev.* **2009**, *38*, 253.

[4] C. Liu, F. Li, L. Ma, H. Cheng, *Adv. Mater.* **2010**, *22*, E28.

[5] Q. Zhang, C. S. Dandeneau, X. Zhou, G. Cao, *Adv. Mater.* **2009**, *21*, 4087.

[6] X. Hu, G. Li, J. C. Yu, *Langmuir* **2010**, *26*, 3031.

[7] X. Xie, Y. Li, Z. Liu, M. Haruta, W. Shen, *Nature* **2009**, *458*, 746.

[8] Y. Qin, X. D. Wang, Z. L. Wang, *Nature* **2008**, *451*, 809.

[9] X. D. Wang, J. H. Song, J. Liu, Z. L. Wang, *Science* **2007**, *316*, 102.

[10] H. Goesmann, C. Feldmann, *Angew. Chem. Int. Ed.* **2010**, *49*, 1362.

[11] E. Roduner, *Chem. Soc. Rev.* **2006**, *35*, 583.

[12] T. Trindade, P. O'Brien, N. L. Pickett, *Chem. Mater.* **2001**, *13*, 3843.

[13] X. Wang, Y. Li, *Chem. Commun.* **2007**, 2901.

[14] A. N. Shipway, E. Katz, I. Willner, *ChemPhysChem* **2000**, *1*, 18.

[15] P. V. Kamat, *J. Phys. Chem. C* **2007**, *111*, 2834.

[16] D. R. Kauffman, A. Star, *Angew. Chem. Int. Ed.* **2008**, *47*, 6550.

[17] M. Fernández-García, A. Martínez-Arias, J.C. Hanson, J. A. Rodriguez, *Chem. Rev.* **2004**, *104*, 4063.

[18] G. Shen, P. Chen, K. Ryu, C. Zhou, *J. Mater. Chem.* **2009**, *19*, 828.

[19] G. R. Patzke, F. Krumeich, R. Nesper, *Angew. Chem. Int. Ed.* **2002**, *41*, 2446.

[20] K. S. Shankar, A. K. Raychaudhuri, *Mater. Sci. Eng. C* **2005**, *25*, 738.

[21] N. A. Chernova, M. Roppolo, A. C. Dillon, M. S. Whittingham, *J. Mater. Chem.* **2009**, *19*, 2526.

[22] C. N. R. Rao, F. L. Deepak, G. Gundiah, A. Govindaraj, *Prog. Solid State Chem.* **2003**, *31*, 5.

[23] J. A. Rodriguez, M. Fernandez-Garcia, *Synthesis, Properties and Applications of Oxide Nanomaterials*, Wiley InterScience, **2007**.

[24] A. Fujishima, K. Honda, *Nature* **1972**, *238*, 37.

[25] F. E. Osterloh, *Chem. Mater.* **2008**, *20*, 35.

[26] M. D. Hernandez-Alonso, F. Fresno, S. Suarez, J. M. Coronado, *Energy Environ. Sci.* **2009**, *2*, 1231.

[27] Z. Zou, J. Ye, K. Sayama, H. Arakawa, *Nature* **2001**, *414*, 625.

[28] J. Zhang, Q. Xu, Z. Feng, M. Li, C. Li, *Angew. Chem. Int. Ed.* **2008**, *47*, 1766.

[29] D. J. L. Brett, A. Atkinson, N. P. Brandon, S. J. Skinner, *Chem. Soc. Rev.* **2008**, *37*, 1568.

[30] J. M. Vohs, R. J. Gorte, *Adv. Mater.* **2009**, *21*, 943.

[31] L. Yang, C. Zuo, S. Wang, Z. Cheng, M. Liu, *Adv. Mater.* **2008**, *20*, 3280.

[32] Y. Luo, D. Li, Q. Meng, *Adv. Mater.* **2009**, *21*, 4647.

[33] M. Law, L. E. Greene, J. C. Johnson, R. Saykally, P. Yang, *Nature Mater.* **2005**, *4*, 455.

[34] J. Qian, P. Liu, Y. Xiao, Y. Jiang, Y. Cao, X. Ai, H. Yang, *Adv. Mater.* **2009**, *21*, 3663.

[35] P. Falaras, T. Stergiopoulos, D. S. Tsoukleris, *Small* **2008**, *4*, 770.

[36] Z. Yin, S. Wu, X. Zhou, X. Huang, Q. Zhang, F. Boey, H. Zhang, *Small* **2010**, *6*, 307.

[37] A. S. Aricò, P. Bruce, B. Scrosati, J. Tarascon, W. V. Schalkwijk, *Nature Mater.* **2005**, *4*, 366.

[38] Y. G. Guo, J. S. Hu, L. J. Wan, *Adv. Mater.* **2008**, *20*, 2878.

[39] Z. Chen, Y. Qin, D. Weng, Q. Xiao, Y. Peng, X. Wang, H. Li, F. Wei, Y. Lu, *Adv. Funct. Mater.* **2009**, *19*, 3420.

[40] A. Manthiram, A. V. Murugan, A. Sarkar, T. Muraliganth, *Energy Environ. Sci.* **2008**, *1*, 621.

[41] P. Kurzweil, *J. Power Sources* **2009**, *190*, 189.

[42] Z. Fan, J. C. Ho, T. Takahashi, R. Yerushalmi, K. Takei, A. C. Ford, Y. Chueh, A. Javey, *Adv. Mater.* **2009**, *21*, 3730.

[43] Q. Kuang, C. Lao, Z. L. Wang, Z. Xie, L. Zheng, *J. Am. Chem. Soc.* **2007**, *129*, 6070.

[44] Q. H. Li, Y. X. Liang, Q. Wan, T. H. Wang, *Appl. Phys. Lett.* **2004**, *85*, 6389.

[45] J. Liu, X. Wang, Q. Peng, Y. Li, *Adv. Mater.* **2005**, *17*, 764.

[46] X. Hu, J. Gong, L. Zhang, J. C. Yu, *Adv. Mater.* **2008**, *20*, 4845.

[47] H. Ohta, K. Sugiura, K. Koumoto, *Inorg. Chem.* **2008**, *47*, 8429.

[48] S. Li, R. Funahashi, I. Matsubara, K. Ueno, S. Sodeka, H. Yamada, *Chem. Mater.* **2000**, *12*, 2424.

[49] W. Kobayashi, S. Hebert, D. Pelloquin, O. Perez, A. Maigan, *Phys. Rev. B* **2007**, *76*, 245102.

[50] Y. Zhou, K. Vuille, A. Heel, B. Probst, R. Kontic, G. R. Patzke, *Appl. Catal. A* **2010**, *375*, 140.

[51] T. Tachikawa, M. Fujitsuka, T. Majima, *J. Phys. Chem. C* **2007**, *111*, 5259.

[52] D. Chen, L. Gao, A. Yasumori, K. Kuroda, Y. Sugahara, *Small* **2008**, *4*, 1813.

[53] L. Zhang, W. Wang, L. Zhou, H. Xu, *Small* **2007**, *3*, 1618.

[54] M. Jansen, *Angew. Chem. Int. Ed.* **2002**, *41*, 3747.

[55] P. Bowen, C. Carry, *Powder Technol.* **2002**, *128*, 248.

[56] Z. W. Pan, Z. R. Dai, Z. L. Wang, *Science* **2001**, *291*, 1947.

[57] Y. Qiu, D. Liu, J. Yang, S. Yang, *Adv. Mater.* **2006**, *18,* 2604.

[58] K. C. Patil, S. T. Aruna, S. Ekambaram, *Curr. Opin. Solid State Mater. Sci.* **1997**, *2*, 158.

[59] R. Strobel, A. Baiker, S. E. Pratsinis, *Adv. Powder Technol.* **2006**, *17*, 457.

[60] N. C. Castillo, A. Heel, T. Graule, C. Pulgarin, *Appl. Catal. B* **2010**, *95*, 335.

[61] U. T. Gonzenbach, A. R. Studart, E. Tervoort, L. J. Gauckler, *Angew. Chem. Int. Ed.* **2006**, *45*, 3526.

[62] J. H. Bang, K. S. Suslick, *J. Am. Chem. Soc.* **2007**, *129*, 2242.

[63] L. Zhu, Q. Li, J. Y. Li, X. D. Liu, J. Meng, X. Q. Cao, *J. Nanopart. Res.* **2007**, *9*, 261.

[64] X. Wang, Y. Li, *Pure. Appl. Chem.* **2006**, *78*, 45.

[65] X. Wang, Y. Li, *Inorg. Chem.* **2006**, *45*, 7522.

[66] W. Yao, S. Yu, *Int. J. Nanotechnology* **2007**, *4*, 129.

[67] I. Bilecka, P. Elser, M. Niederberger, *ACS Nano* **2009**, *3*, 467.

[68] I. Bilecka, I. Djerdj, M. Niederberger, *Chem. Commun.* **2008**, 886.

[69] X. L. Hu, J. C. Yu, J. M. Gong, Q. Li, G. S. Li, *Adv. Mater.* **2007**, *19*, 2324.

[70] D. P. Dutta, V. Sudarsan, P. Srinivasu, A. Vinu, A. K. Tyagi, *J. Phys. Chem. C* **2008**, *112*, 6781.

[71] F. Gao, Q. Lu, S. Komarneni, *Chem. Commun.* **2005**, 531.

[72] G. A. Ozin, L. Cademartiri, *Small* **2009**, *5*, 1240.

[73] Y. Mao, T. Park, F. Zhang, H. Zhou, S. S. Wong, *Small* **2007**, *3*, 1122.

[74] Y. Mao, T. Park, S. S. Wong, *Chem. Commun.* **2005**, 5721.

[75] R. I. Walton, F. Millange, R. I. Smith, T. C. Hansen, D. O'Hare, *J. Am. Chem. Soc.* **2001**, *123*, 12547.

[76] A. K. Cheetham, C. F. Mellot, *Chem. Mater.* **1997**, *9*, 2269.

[77] R. J. Francis, S. J. Price, J. S. O. Evans, S. O'Brien, D. O'Hare, *Chem. Mater.* **1996**, *8*, 2102.

[78] M. Yoshimura, W. Suchanek, K. Byrappa*, MRS Bull.* **2000**, *25*, 17.

[79] K. Byrappa, T. Adschiri, *Prog. Cryst. Growth Charact. Mater.* **2007**, *53*, 117.

[80] K. Byrappa, T. Adschiri, *Handbook of Hydrothermal Technologies*, William Andrew Publishing, New Jersey, **2001**.

[81] R. I. Walton, *Chem. Soc. Rev.* **2002**, *31*, 230.

[82] C. Wu, Y. Xie, *Chem. Commun.* **2009**, 5943.

[83] G. R. Patzke, A. Michailovski, F. Krumeich, R. Nesper, J.-D. Grunwaldt, A. Baiker, *Chem. Mater.* **2004**, *16*, 1126.

[84] Y. Fang, A. Xu, R. Song, H. Zhang, L. You, J. C. Yu, H. Liu, *J. Am. Chem. Soc.* **2003**, *125*, 16025.

[85] L. M. Liz Marzán, *J. Mater. Chem.* **2006**, *16*, 3891.

[86] C. Zhang, Y. F. Zhu, *Chem. Mater.* **2005**, *17*, 3537.

[87] M. P. Pileni, *Nature. Mater.* **2003**, *2*, 145.

[88] K. Biswas, B. Das, C. N. R. Rao, *J. Phys. Chem. C* **2008**, *112*, 2404.

[89] C. Bae, H. Yoo, S. Kim, K. Lee, J. Kim, M. A. Sung, H. Shin, *Chem. Mater.* **2008**, *20*, 756.

[90] G. R. Patzke, *Angew. Chem. Int. Ed.* **2003**, *42*, 972.

[91] X. K. Huang, D. P. Lv, H. J. Yue, A. Attia, Y. Yang, *Nanotechnology* **2008**, *19*, 225606.

[92] P. Yu, X. Zhang, D. L. Wang, L. Wang, Y. W. Ma, *Cryst. Growth Des.* **2009**, *9*, 528.

[93] Y. Q. Gao, Z. H. Wang, S. L. Xiong, Y. Liu, Y. T. Qian, *J. Nanosci. Nanotechnol.* **2006**, *6*, 2576.

[94] Y. C. Gui, L. W. Qian, X. F. Qian, *Chin. J. Inorg. Chem.* **2009**, *25*, 668.

[95] Q. Wu, F. Zhang, P. Xiao, H. S. Tao, X. Z. Wang, Z. Hu, Y. N. Lu, *J. Phys. Chem. C* **2008**, *112*, 17076.

[96] L. Yan, R. B. Yu, J. Chen, X. R. Xing, *Cryst. Growth Des.* **2008**, *8*, 1474.

[97] C. J. Jia, L. D. Sun, Z. G. Yan, L. P. You, F. Luo, X. D. Han, Y. C. Pang, Z. Zhang, C. H. Yan, *Angew. Chem. Int. Ed.* **2005**, *44*, 4328.

[98] X. L. Wu, Y. G. Guo, L. J. Wan, C. W. Hu, *J. Phys. Chem. C* **2008**, *112*, 16824.

[99] R. Yi, H. F. Zhou, N. Zhang, G. Z. Qiu, X. H. Liu, *J. Alloys Compd.* **2009**, *479*, L50.

[100] T. A. Xia, Q. Li, X. D. Liu, J. A. Meng, X. Q. Cao, *J. Phys. Chem. B* **2006**, *110*, 2006.

[101] S. M. Gao, W. Yang, W. Jiang, Z. X. Yu, Y. Dai, B. B. Huang, *Chin. J. Inorg. Chem.* **2006**, *22*, 673.

[102] X. W. Lou, H. C. Zeng, *Inorg. Chem.* **2003**, *42*, 6169.

[103] A. Michailovski, R. Kiebach, W. Bensch, J.-D. Grunwaldt, A. Baiker, S. Komarneni, G. R. Patzke, *Chem. Mater.* **2007**, *19*, 185.

[104] Y. G. Wang, G. Xu, Z. H. Ren, X. Wei, W. J. Weng, P. Du, G. Shen, G. R. Han, *J. Am. Ceram. Soc.* **2007**, *90*, 2615.

[105] M. J. Siegfried, K. S. Choi, *J. Am. Chem. Soc.* **2006**, *128*, 10356.

[106] M. J. Siegfried, K. S. Choi, *Angew. Chem. Int. Ed.* **2005**, *44*, 3218.

[107] M. Bremholm, J. Becker-Christensen, B. Iversen, *Adv. Mater.* **2009**, *21*, 3572.

[108] A. Michailovski, J.-D. Grunwaldt, A. Baiker, R. Kiebach, W. Bensch, G. R. Patzke, *Angew. Chem. Int. Ed.* **2005**, *44*, 5643.

[109] J. D. Epping, B. F. Chmelka, *Curr. Opin. Colloid Interface Sci.* **2006**, *11*, 81.

[110] M. Bremholm, M. Felicissimo, B. B. Iversen, *Angew. Chem. Int. Ed.* **2009**, *48*, 4788.

[111] G. Garnweitner, C. Grote, *Phys. Chem. Chem. Phys.* **2009**, *11*, 3767.

[112] R. Viswanatha, P. K. Santra, C. Dasgupta, D. D. Sarma, *Phys. Rev. Lett.* **2007**, *98*.

[113] F. Fan, Z. Feng, K. Sun, M. Guo, Q. Guo, Y. Song, W. Li, C. Li, *Angew. Chem. Int. Ed.* **2009**, *48*, 8743.

[114] A. Dey, G. de With, N. A. J. M. Sommerdijk, *Chem. Soc. Rev.* **2010**, *39*, 397.

[115] G. R. Patzke, Y. Zhou, R. Kontic, F. Conrad, *Angew. Chem. Int. Ed.* **2010**, doi:10.1002/anie.201000235.

[116] C. Kongmark, V. Martis, A. Rubbens, C. Pirovano, A. Löfberg, G. Sanker, E. Bordes-Richard, R. Vannier, W. V. Beek, *Chem. Commun.* **2009**, 4850.

[117] P. Norby, *Curr. Opin. Colloid Interface Sci.* **2006**, *11*, 118.

[118] P. Norby, A. N. Christensen, J. C. Hanson, *Stud. Surf. Sci. Catal.* **1994**, *84*, 179.

[119] R. I. Walton, D. O'Hare, *Chem. Commun.* **2000**, 2283.

[120] H. He, P. Barnes, J. Munn, X. Turrillas, J. Klinowski, *Chem. Phys. Lett.* **1992**, *196*, 267.

[121] A. M. Beale, G. Sankar, *Chem. Mater.* **2006**, *18*, 263.

[122] F. Millange, C. Serre, N. Guillou, G. Férey, R. I. Walton, *Angew. Chem. Int. Ed.* **2008**, *47*, 4100.

[123] Y. Zhou, N. Pienack, W. Bensch, G. R. Patzke, *Small* **2009**, *5*, 1978.

[124] Y. Du, K. M. Ok, D. O'Hare, *J. Mater. Chem.* **2008**, *18*, 4450.

[125] L. Engelke, M. Schaefer, M. Schur, W. Bensch, *Chem. Mater.* **2001**, *13*, 1383.

[126] P. Barnes, S. M. Clark, D. Hausermann, E. Henderson, C. H. Fentiman, M. N. Muhamad, S. Rashid, *Phase Transitions* **1992**, *39*, 117.

[127] M. J. Avrami, *J. Chem. Phys.* **1939**, *7*, 1103.

[128] M. J. Avrami, *J. Chem. Phys.* **1940**, *8*, 212.

[129] M. J. Avrami, *J. Chem. Phys.* **1941**, *9*, 177.

[130] S. F. Hulbert, *J. Br. Ceram. Soc.* **1969**, *6*, 11.

[131] J. D. Hancock, J. H. Sharp, *J. Am. Ceram. Soc.* **1972**, *55*, 74.

[132] J. J. Rehr, *Rev. Mod. Phys.* **2000**, *72*, 621.

[133] M. A. Newton, A. J. Dent, J. Evans, *Chem. Soc. Rev.* **2002**, *31*, 83.

[134] E. A. Stern, D. E. Sayers, F. W. Lytle, *Phys. Rev. B* **1975**, *11*, 4836.

[135] M. Newville, M. *J. Synchrot. Radiat.* **2000**, *8*, 322.

[136] J.-D. Grunwaldt, M. Ramin, M. Rohr, A. Michailovski, G. R. Patzke, A. Baiker, *Rev. Sci. Instrum.* **2005**, *76*, 054104.

[137] N. Barsan, D. Koziej, U. Weimar, *Sens. Actuators B* **2007**, *121*, 18.

[138] T. Kako, Z. Zou, M. Katagiri, J. Ye, *Chem. Mater.* **2007**, *19*, 198.

[139] A. Walsh, Y. F. Yan, M. N. Huda, M. M. Al-Jassim, S. H. Wei, *Chem. Mater.* **2009**, *21*,

547.

[140] J. Tang, Z. Zou, J. Ye, *Angew. Chem. Int. Ed.* **2004**, *43*, 4463.

[141] B. Timmer, W. Olthuis, A. Berg, *Sens. Actuators B* **2005**, *107*, 666.

[142] C. Lee, W. Hsieh, G. Wu, *J. Power Sources* **2008**, *181*, 237.

[143] Z. Wang, C. Chang, X. Zhao, W. Qian, X. Zhang, Z. Xie, B. Hwang, C. Hu, J. Shen, R. Hui, *J. Power Sources* **2009**, *190*, 351.

[144] T. Seiyama, A. Kato, K. Fulishi, M. Nagatani, *Anal. Chem.* **1962**, *34*, 1502.

[145] C. Wang, L. Yin, L. Zhang, D. Xiang, R. Gao, *Sensors* **2010**, *10*, 2088.

[146] E. Traversa, *Sens. Actuators B* **1995**, *23*, 135.

[147] K. J. Choi, H. W. Jang, *Sensors* **2010**, *10*, 4083.

[148] N. Barsan, D. Koziej, U. Weimar, *Sens. Actuators B* **2007**, *121*, 18.

[149] G. Korotcenkov, *Mater. Sci. Eng. B* **2007**, *139*, 1.

Part I

Visible Light Driven Photocatalysts

2. Photocatalytically active $BiVO_4$: an inorganic hydrothermal route

2.1 Introduction

The layered vanadate $BiVO_4$ has attracted increasing research interest as a photocatalyst and it exists in three modifications: the monoclinic scheelite type and the tetragonal zircon and scheelite types, respectively. Monoclinic $BiVO_4$ with a band gap of 2.4 eV is one of the most promising visible light driven photocatalysts[1] so that it has been synthesized with a variety of methods, such as solid state reactions,[2] co-precipitation,[3] metal-organic decomposition,[4] sonochemical[5] and hydrothermal reactions.[6] However, most of these synthetic pathways have only brought forward $BiVO_4$ materials with large crystal sizes and low surface areas (typical range from 0.3 - 4.2 m^2/g), probably due to the rapid crystal growth kinetics of this material.[7, 8] This impedes its photocatalytic applications, because a high surface area is required to speed up the adsorption/desorption kinetics of organic pollutants on the surface of $BiVO_4$ catalyst particles. Therefore, the search for $BiVO_4$ photocatalysts with high surface area and activity remains a challenging topic.

Recently, progress in this direction has been achieved through template-assisted approaches, e.g. 2D $BiVO_4$ nanosheets have been synthesized in the presence of sodium dodecyl benzene sulfonate (SDBS)[9] or 1D $BiVO_4$ nanofibers were hydrothermally prepared using cetyltrimethylammonium bromide (CTAB).[10] The photocatalytic performance of mesoporous $BiVO_4$ could also be enhanced through increasing the surface via silica (KIT-6) as a hard template.[11] However, all present strategies to improve the morphology and surface area of $BiVO_4$ materials are less favorable from the technological point of view, because they require either “soft” (i.e. organic additives) or “hard” templates. Their use may leave the final product with impurities, increase the overall costs and finally render the large-scale technical production difficult. As has been outlined in the introduction, inorganic salt additives could be an elegant way to circumvent these problems and to benefit from morphology control options that are equally versatile as those provided by organic substances. This is demonstrated by recent studies and previous activities of our group.[12-14]

In this chapter, we report on a facile and straightforward hydrothermal route to synthesize

monoclinic $BiVO_4$ particles with an enhanced surface area in the presence of K_2SO_4 as an inorganic morphology-directing agent. Firstly, we outline the synthetic optimization process, followed by an evaluation of the visible light driven photocatalytic activity of the obtained $BiVO_4$ particles with respect to MB photodegradation and water oxidation. Furthermore, the advantages and drawbacks of inorganic additives are critically discussed.

2.2 Experimental

2.2.1 Synthesis

In a typical procedure, 97 mg (0.2 mmol) of $Bi(NO_3)_3 \cdot 5H_2O$, 37 mg (0.2 mmol) V_2O_5 and 1 g (5.7 mmol) K_2SO_4 were suspended in 10 mL of water at room temperature and stirred magnetically for 10 min. The resulting precursor suspension was transferred into a Teflon-lined stainless steel autoclave with a capacity of 23 mL, maintained at 200 °C for 24 h, and subsequently cooled to room temperature naturally. The precipitate was collected after filtration, washed with distilled water and dried in air (we refer to this sample as $BiVO_4$(5) in the text). In order to compare the photocatalytic activity of $BiVO_4$ with different morphologies and surface areas, several hydrothermal parameters were varied accordingly (cf. Table 2.1) whilst the reaction time was kept constant at 24 h.

2.2.2 Analytical characterization

PXRD was performed on a STOE STADI P diffractometer in transmission mode (flat sample holders, Ge monochromator and Cu $K_{\alpha 1}$ radiation) equipped with a position sensitive detector. For SEM analyses, obtained with a LEO 1530 (FEG) microscope with 2 keV electrons, samples were dispersed in ethanol and subsequently deposited on a silicon wafer. EDXS investigations were performed on a Zeiss SUPRA 50 VP microscope equipped with an EDAX detector. TEM investigations were performed on a Philips CM30/ST microscope operated at 300 kV (LaB_6 cathode). The material was deposited on a perforated carbon foil supported on a copper grid. The BET surface area measurements were performed on a Coulter SA 3100 in

N_2-adsorption mode. The sample was degassed at 180 °C for 2-3 h under N_2 atmosphere before the nitrogen adsorption measurement. The optical absorption spectrum was recorded on a Cary 500 UV-VIS-NIR spectrophotometer.

Table 2.1. Preparative parameters of representative pathways to $BiVO_4$.

Sample	Reactants	Temperature / °C
$BiVO_4$ (1)	0.2 mmol $Bi(NO_3)_3 \cdot 5H_2O$ 0.2 mmol NH_4VO_3 10 mL 20 vol.% acetic acid	160
$BiVO_4$ (2)	0.2 mmol $Bi(NO_3)_3 \cdot 5H_2O$ 0.2 mmol NH_4VO_3 4 mmol K_2SO_4 10 mL 20 vol.% acetic acid	160
$BiVO_4$ (3)	0.2 mmol $Bi(NO_3)_3 \cdot 5H_2O$ 0.2 mmol V_2O_5 10 mL 20 vol.% acetic acid	200
$BiVO_4$ (4)	0.2 mmol $Bi(NO_3)_3 \cdot 5H_2O$ 0.2 mmol V_2O_5 10 mL H_2O	200
$BiVO_4$ (5)	0.2 mmol $Bi(NO_3)_3 \cdot 5H_2O$ 0.2 mmol V_2O_5 5.7 mmol K_2SO_4 10 mL H_2O	200
$BiVO_4$ (6)	0.2 mmol $Bi(NO_3)_3 \cdot 5H_2O$ 0.2 mmol $VOSO_4 \cdot xH_2O$ 5.7 mmol K_2SO_4 10 mL H_2O	200

2.2.3 Photocatalytic activity measurements

The photocatalytic degradation of organic pollutants was evaluated through the decomposition of MB (cf. Figure 2.1) as a reference compound in a LIDAM photoreactor equipped with 12 bulbs of either blue light (Hg bulbs LCD M2-6S-01, max. intensity at 450

nm), UV-light (Sylvana blacklight F8W/BLB T5, max. intensity at 355-360 nm) or simulated daylight (Philips TL8W Aquarelle). The bulb spectra of blue light and simulated daylight are shown in Figure 2.2. The bulbs were arranged in a circular fashion around the reaction vessel that was thermostated at 30 °C. Before the illumination was started, 50 mg of the photocatalyst powder was dispersed in an ultrasound bath in the dark for 10 min. in a MB solution (125 mL, 10 ppm) to ensure the equilibration of the investigated solution. These initial ratios are in line with the recommended ranges as outlined in representative publications in the field.[15, 16] The suspension was transferred into the reaction vessel and put under a constant air flow of dry air (100 mL/min). At given time intervals, 3 mL of the suspension was collected through a filter to remove the photocatalyst powder. The filtrates were analyzed by recording the variations of the absorption peak at 664 nm in a Varian Cary 50 Scan UV-Vis spectrometer.

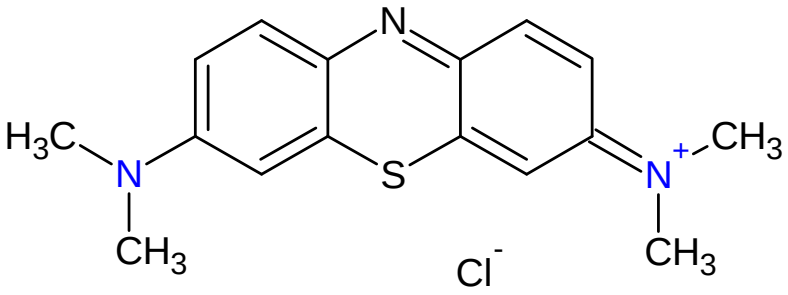

Figure 2.1. Molecular structure of methylene blue (MB).

Photocatalytic O_2 evolution was carried out in a 50 mL Schlenk flask equipped with a stirring bar and filled with 10 mL of 1 mol/L $AgNO_3$ or $FeCl_3$ solution. 10 mg of the $BiVO_4$ catalyst and the required electron acceptor were flushed with N_2 to remove all the remaining oxygen from the solvent. The light source was a 300 W Xe arc lamp (LOT Oriel) in line with a cut off filter ($\lambda \geq 400$ nm). The distance of the sample to the light source was varied to obtain a constant light intensity of 200000 lux. In regular intervals 100 µL of the reaction headspace were sampled with a gas tight microliter syringe (Hamilton 1825 RN) using a gas chromatograph (Varian CP-3800) with He as carrier gas and a 3 m × 2 mm column packed with molecular sieve 13X 80-100. The gas flow was set to 20 mL/min. The oven was operated isothermally at 100 °C. The gases were detected using a thermal conductivity detector (Varian)

operated at 150 °C. Calibrations were performed by the injection of known quantities of pure oxygen diluted in the same Schlenk tube containing the same volume of solvent as used for measurements.

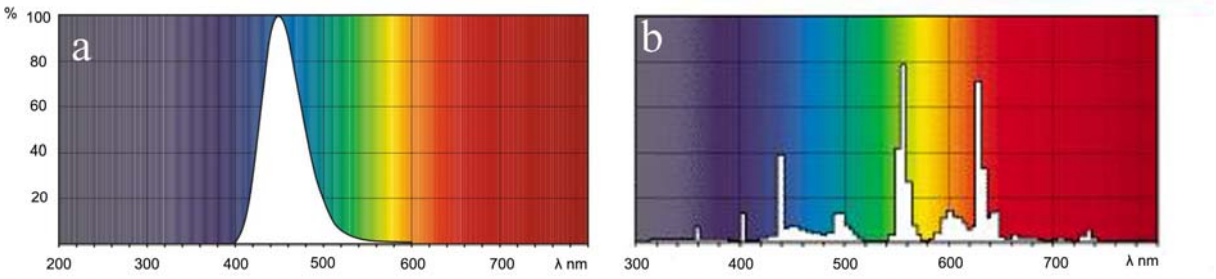

Figure 2.2. Bulb-spectra of (a) blue light and (b) simulated daylight (UV/Vis).

2.3 Results and discussion

2.3.1 Hydrothermal synthesis of monoclinic $BiVO_4$ particles

Whereas the general hydrothermal formation of monoclinic $BiVO_4$ is rather robust towards parameter variations, the fine-tuning of the product morphology can be quite difficult as it responds quickly to small changes in the reaction conditions.

Parameter optimization: We have thus performed an extensive parameter screening of the hydrothermal $BiVO_4$ synthesis and representative trends concerning phase and morphology of the products are summed up in the following. Regarding the pH value, previous studies have revealed that an increase of pH during $BiVO_4$ synthesis exerts a negative influence on the photocatalytic performance of the emerging materials.[17] We have observed a related effect, because syntheses at pH values of 7 and above led to the formation of amorphous side products in significant quantities or even to the formation of impure product mixtures. Therefore, the pH was generally adjusted to 1 with 20 vol.% acetic acid for all of the synthetic procedures mentioned in the following. $Bi(NO_3)_3 \cdot 5H_2O$ was chosen as a bismuth source throughout, because the use of $BiCl_3$ can lead to the formation of VCl_2 as a side product and $NaBiO_3$ frequently generates products with an irregular morphology. Furthermore, K_2SO_4

was selected as an inorganic morphology control agent through screening experiments with various inorganic additives.

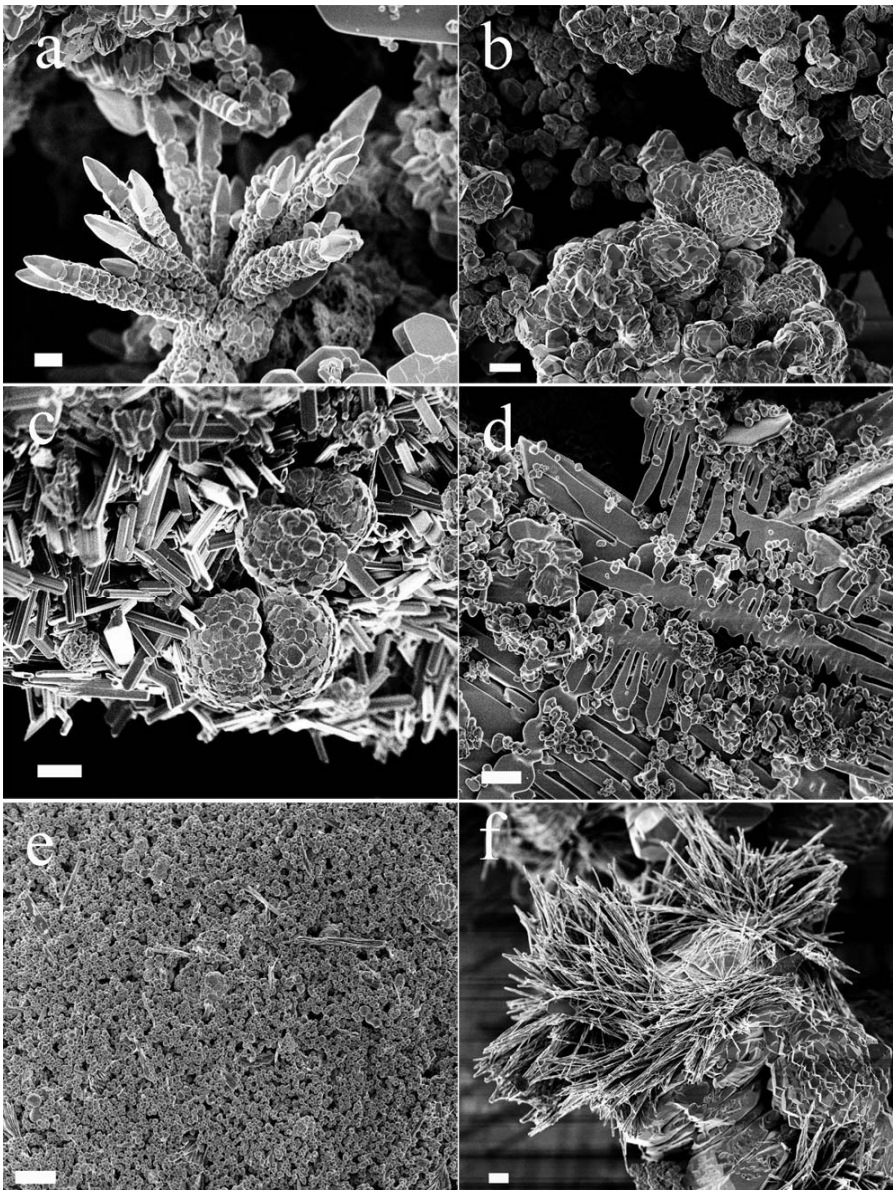

Figure 2.3. Representative SEM images of $BiVO_4$ samples obtained from different hydrothermal parameters: (a) $BiVO_4$(1); (b) $BiVO_4$(2); (c) $BiVO_4$(3); (d) $BiVO_4$(4); (e) $BiVO_4$(5); (f) $BiVO_4$(6); scale bar = 2 μm.

The products obtained from NH_4VO_3 as a vanadium source (denoted as $BiVO_4$(1) in the absence of K_2SO_4 and $BiVO_4$(2) in the presence of K_2SO_4) are phase pure and their XRD patterns are in good agreement with pure monoclinic scheelite $BiVO_4$ (JCPDS 75-2480). In principle, the addition of K_2SO_4 exerts a productive effect on the synthesis. $BiVO_4$(2)

displays not only a more regular morphology (cf. Figure 2.3b) but also a higher surface area and a better photocatalytic performance (cf. section 2.3.3): $BiVO_4$(2) furthermore has a higher BET surface area (1.3 m^2/g) than $BiVO_4$(1) with 0.9 m^2/g. However, continued parameter adjustments in the $Bi(NO_3)_3 \cdot 5H_2O/NH_4VO_3/K_2SO_4$ system failed to generate more enhanced morphologies so that the vanadium source was changed to V_2O_5. $BiVO_4$(3) was obtained from the $Bi(NO_3)_3 \cdot 5H_2O/V_2O_5$ system under acidic conditions and the sample displays a mixed morphology of microscale rods and larger crystallites with an overall BET surface area of 1.2 m^2/g. $BiVO_4$(4) represents the analogous product generated from aqueous conditions (pH ca. 3) and it exhibits smaller particles and hierarchical growth patterns, thereby leading to a further increase in surface area to 3.5 m^2/g. However, these improved surface areas and morphologies came with the disadvantage of side products (V_2O_5) as can be seen from the XRD patterns of all samples in Figure 2.4.

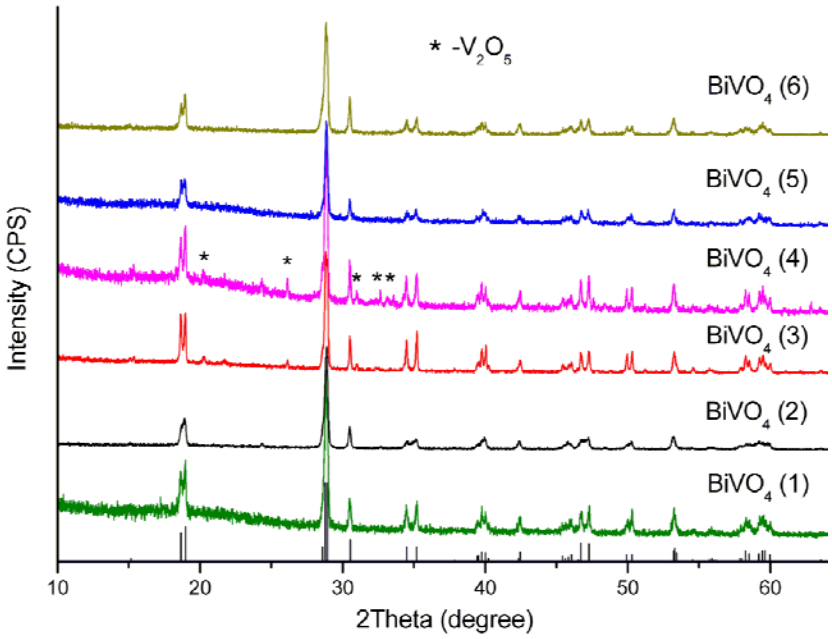

Figure 2.4. XRD patterns of $BiVO_4$ samples obtained from different preparation conditions (cf. Table 2.1). The reference pattern of monoclinic $BiVO_4$ (JCPDS No. 75-2480) is shown at the bottom.

The addition of K_2SO_4 to the $Bi(NO_3)_3 \cdot 5H_2O/V_2O_5$ hydrothermal system clearly enhanced the particle morphology so that two species were formed: Particles with an average diameter

of 150 nm and a fibrous product. Both phases could be separated by means of filtration and centrifugation and the XRD pattern of the purified particles ($BiVO_4$(5)) corresponds to phase pure monoclinic $BiVO_4$. The formation of homogeneous $BiVO_4$ particles strongly depends on the vanadium source so that replacing V_2O_5 with $VOSO_4 \cdot xH_2O$, for example, led to deteriorated morphologies although the product still consisted of phase pure $BiVO_4$ ($BiVO_4$(6), cf. Figures 2.3 and 2.4). Furthermore, the influence of acidic and basic additives on the phase and morphology of the products was investigated and HCl as well as H_3PO_4 were found to generate unwanted side products, such as VCl_2 and $BiPO_4$. The combination of K_2SO_4 with H_2SO_4 brought forward phase mixtures of $K_3Bi_2(VO_4)_3$ and $BiVO_4$, whereas tetragonal $BiVO_4$ emerged as another side product when the pH was raised to 6. Whilst formiate additives, H_2O_2 and HNO_3 favor the formation of phase pure $BiVO_4$, these additives do not exert an interesting influence on the product morphology and the average crystallite sizes are larger than 10 µm with no special features.

Phase relationships in the hydrothermal system: As outlined above, the $Bi(NO_3)_3 \cdot 5H_2O/V_2O_5/K_2SO_4$ hydrothermal system affords two structurally different product types and the mechanically separated fibres and $BiVO_4$ particles both display homogeneous morphologies (cf. Figure 2.5 a - b). The $BiVO_4$ crystals exhibit average dimensions around 150 nm according to SEM investigations (Figures 2.3 and 2.5). Their surface area was determined as 15.6 m^2/g. In addition, the well-developed crystal facets of the $BiVO_4$ particles indicate their high crystallinity (Figure 2.5 a). The color of the products is bright yellow and this corresponds with a band gap of 2.47 eV that has been derived from UV/Vis spectra (cf. Table 2.2). According to EDXS investigations (Figure 2.6 a), the particles mainly consist of Bi, V and O - the Si and C peaks arise from the substrate and the weak K peak is caused by small residual amounts due to the excess of K_2SO_4 in the starting material. TEM investigations (Figure 2.5 c) confirm the particle diameter range of 100 – 300 nm (cf. also Figure 2.5 a) and the SAED patterns indicate that they are polycrystalline and can be indexed to monoclinic $BiVO_4$ (JCPDS 75-2480, cf. also XRD pattern in Figure 2.4).

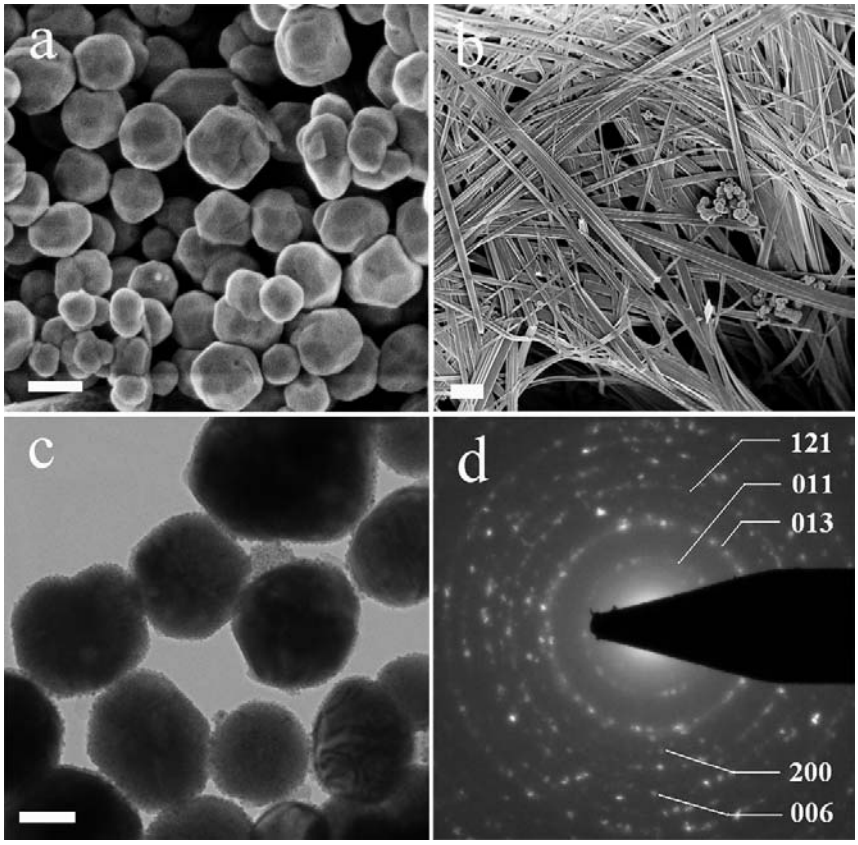

Figure 2.5. SEM images of (a) $BiVO_4$ particles (scale bar = 200 nm) and of (b) potassium vanadate fibers, scale bar = 2 μm; (c) TEM image of $BiVO_4$ particles (scale bar = 100 nm) and (d) the corresponding SAED patterns.

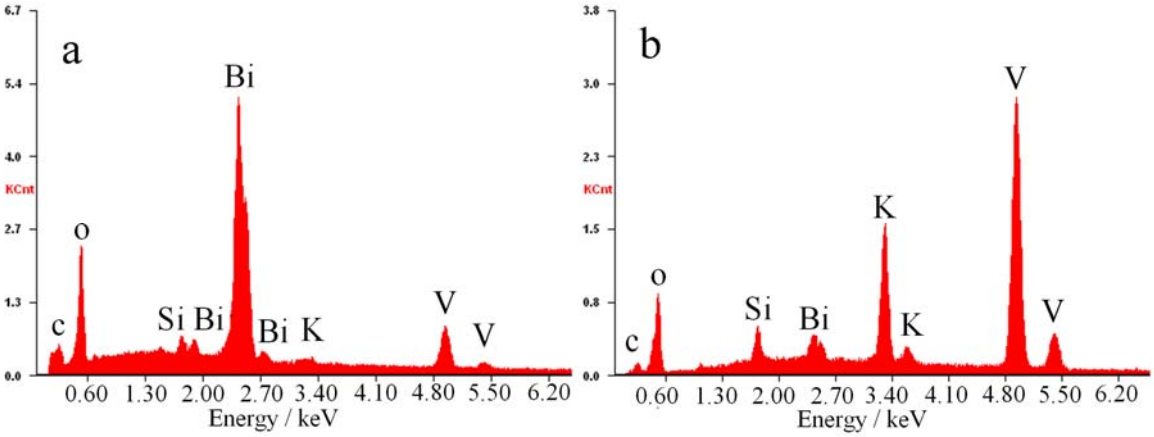

Figure 2.6. EDXS spectra of $BiVO_4$ particles (a) and potassium vanadate fibers (b).

The deep brown fibrous product has larger dimensions than the $BiVO_4$ particles (diameters around 1 μm and 50 nm, and lengths up to several tens of micrometers) so that the fibers exhibit a surface area of 8.8 m^2/g. The band gap of the fibrous material could be lowered to

2 eV compared to 2.47 eV the $BiVO_4$ particles (for details cf. section 2.3.2). The EDXS investigations (cf. Figure 2.6) clearly demonstrate that the $BiVO_4$ particles and fibers display different compositions, because the latter mainly contain K, V and O together with small amounts of Bi arising from residual $BiVO_4$ particles that could not be removed through mechanical separation (cf. TEM image in Figure 2.7). SAED patterns of the fibrous product reveal the presence of a single crystalline phase with two *d* values of 0.62 nm and 0.36 nm with a perpendicular orientation (Figure 2.7 b). As they do not correspond to any lattice parameters of the known $BiVO_4$ polymorphs and the Bi contents are probably due to side products, we refer to the rod-shaped products as potassium vanadate fibers in the following. However, the adherent $BiVO_4$ crystals still outperform the potassium vanadate fibers in terms of scattering intensity so that the XRD patterns of the less crystalline potassium fibers are often superposed by the reflections of the $BiVO_4$ side products. As we have frequently observed a low degree of crystallinity in hydrothermally synthesized potassium vanadates, this effect is not very surprising.[18] However, it renders the structural characterization of the potassium vanadate fibers from XRD data challenging and assigning a structural motif to anisotropic nanostructured materials is a rather common problem in the hydrothermal synthesis of alkali vanadates.[18]

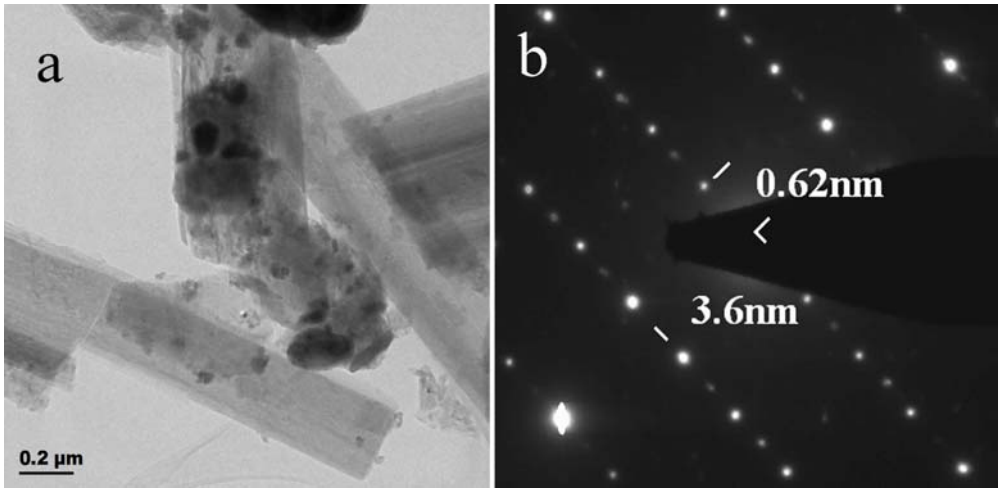

Figure 2.7. TEM images (a) as well as the SAED patterns (b) of fibrous products.

Second phase of parameter optimization: We then performed another series of optimization experiments that shed light on the sensitive response of the $Bi(NO_3)_3{\cdot}5H_2O/V_2O_5/K_2SO_4$ hydrothermal system towards parameter changes. Neither prolonged reaction times (62 h or above) nor increased amounts of K_2SO_4 significantly changed the ratio between fibers and $BiVO_4$ particles. Only elevated reaction temperatures around 220 °C slightly favored the formation of potassium vanadate fibers. As the $BiVO_4$ particles and the potassium vanadate fibers can be easily differentiated through their color, we concluded from the as-synthesized arrangement of the products in the Teflon liner that the deposition of the $BiVO_4$ particles on the fiber surface might be energetically favored. This hypothesis is backed by a reference experiment performed under stirring that completely prevented fiber formation and exclusively afforded orange $BiVO_4$ particles with sizes in the 500 nm range. Further experiments were performed to investigate the influence of ready-made substrates on the product deposition process, such as glass and sea sand, for example. Whilst the sea sand promoted fiber growth, the glass substrate inhibited the formation of fibers. In the course of another optimization approach, the amount of water was varied: The reaction was performed in 5, 10 and 15 mL of water (30, 65 and 90 % autoclave filling height, respectively) for 24 h. For the experiment starting from 5 mL of water, the concentration of the reactants was decreased to 50 mol % of the original value and for the 15 mL experiment an increase of 1/3 precursors was chosen to keep the reactant concentration constant and to avoid an oversaturation with K_2SO_4. The reaction proved to depend strongly on the initial volume of the reactants: while the reaction in 5 mL H_2O brought forward pure fibers, the amount of $BiVO_4$ particles increased with the degree of filling.

All in all, the formation of $BiVO_4$(5) particles is limited to a narrow parameter window and it depends on the presence of K_2SO_4, because the additive-free hydrothermal reaction leads to the formation of irregular microcrystals that has frequently been reported in the literature.[17]

Critical discussion: The $Bi(NO_3)_3{\cdot}5H_2O/V_2O_5/K_2SO_4$ system illustrates the complex interaction of inorganic additives and transition metal-containing precursors: on the one hand, the K_2SO_4 additive exerts an indispensable surface effect during the formation of monoclinic $BiVO_4$ particles with a high surface area and a homogeneous morphology – on the other hand,

the additive can cause a side reaction of the hydrothermal system that leads to the formation of potassium vanadate fibers which may point to the involvement of a layered vanadate intermediate in the formation pathway of catalytically active $BiVO_4$ particles.[1] As the present hydrothermal system brought forward photocatalytically active monoclinic $BiVO_4$ crystals that can be clearly separated from the fibrous product, however, this side effect of the additive is acceptable and even interesting in this particular case.

2.3.2 Optical properties of $BiVO_4$ catalysts

The UV/Vis spectra of all $BiVO_4$ samples displayed absorption bands in the visible light region which is a characteristic feature of monoclinic $BiVO_4$ (cf. Figure 2.8) as a semiconductor with a direct band gap. The electronic structure of $BiVO_4$ has been investigated with DFT calculations:[1] The valence band of $BiVO_4$ is formed from the hybrid orbitals of Bi 6s and O 2p, and the conduction band is formed from unoccupied V 3d states, resulting in a conduction band minimum at the Brillouin zone edge that maintains favorable low energy direct transitions. The experimentally determined band gaps were calculated according to the equation $(\alpha h\nu)^2 = A\ (h\nu - E_g)$, where α, $h\nu$, A and E_g represent the absorption coefficient, the incident photon energy, a constant and the band gap energy, respectively. The band gaps estimated from the intercept of the plots of $(\alpha h\nu)^2$ versus $h\nu$ (Figure 2.9) are 2.39, 2.42, 2.30, 2.40, 2.47, and 2.41 eV for $BiVO_4$(1), $BiVO_4$(2), $BiVO_4$(3), $BiVO_4$(4), $BiVO_4$(5), and $BiVO_4$(6) respectively (Table 2.2). $BiVO_4$(5) contains the smallest particles among all samples so that its band gap displays a blue shift from ca. 2.40 eV to 2.47 eV. This is in line with the well-known increase in the band gap of semiconductors with decreasing particle size. $BiVO_4$(3) shows the smallest band gap of ca. 2.30 eV that may be caused by the impurities in the sample (cf. Figure 2.4). Furthermore, Figure 2.10 shows the UV/Vis spectra of $BiVO_4$(5) and potassium vanadate fibers. Interestingly, the band gap of the fibrous material could be lowered to 2 eV compared to 2.47 eV the $BiVO_4$(5) particles which is line with the different colors of both materials.

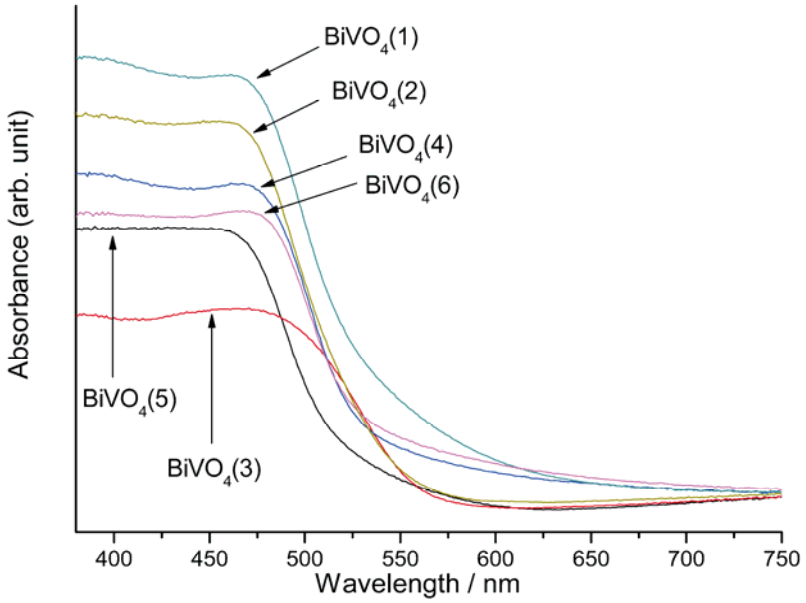

Figure 2.8. UV-Vis absorption spectra of the different $BiVO_4$ samples (cf. Table 2.1).

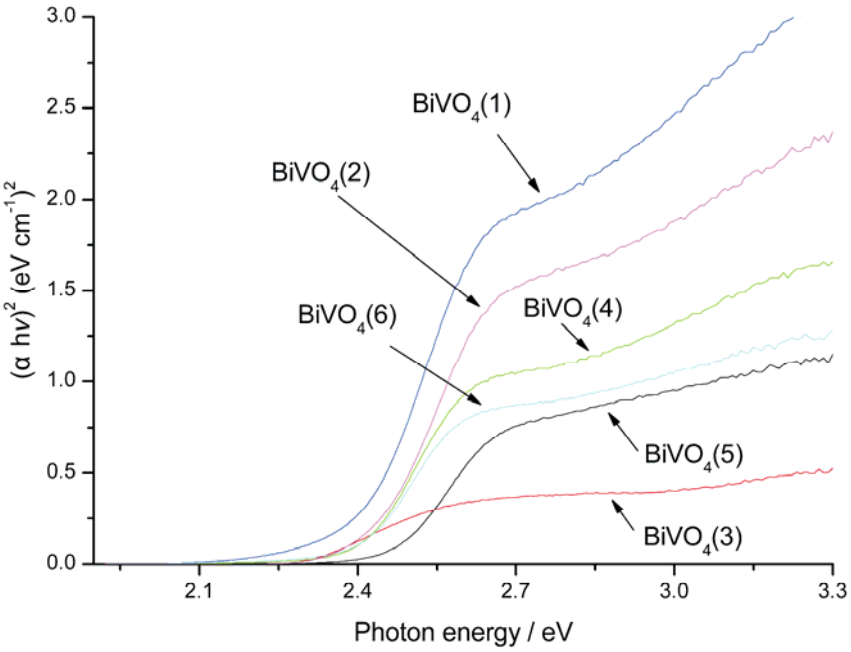

Figure 2.9. Band gap determination of the different $BiVO_4$ samples (cf. Table 2.1).

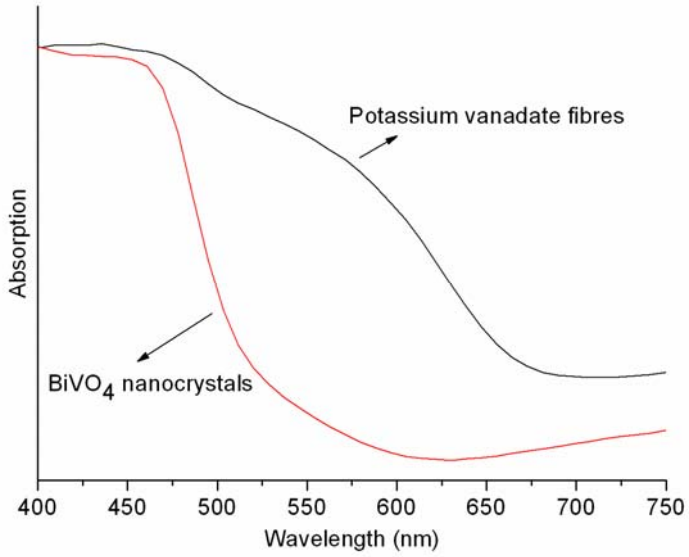

Figure 2.10. UV-vis absorption spectra of $BiVO_4$ (5) and potassium vanadate fibers.

2.3.3 Photocatalytic activity of the obtained $BiVO_4$ samples in the degradation of MB

Visible light driven photocatalytic activity: The photocatalytic degradation process of MB was monitored through the intensity of the characteristic absorption peak at 664 nm against TiO_2 (P25, Degussa, 96% anatase phase) as a reference. The photolysis of MB under visible light irradiation in the absence of a catalyst is negligible and the energy distribution of the blue light bulb (Figure 2.2) excludes self-photosensitized effects from of MB. Figure 2.11 shows the time-dependent MB concentration for the $BiVO_4$ samples compared to P25. The decrease of MB concentration in the presence of P25 is as low as 15 % over a period of 45 min. Obviously, P25 is inactive under visible light irradiation (Figure 2.11 g). The degradation rates of all $BiVO_4$ samples under visible light irradiation are higher than those of P25. Furthermore, the photocatalytic activities of the individual $BiVO_4$ samples are a function of the synthetic parameters and of the resulting surface area, particle size and morphology of the products. The photocatalytic performance of the $BiVO_4$(5) particles exceeded all other samples by far: the main absorption of MB at 664 nm decreased sharply with irradiation time (Figure 2.12) and disappeared almost entirely after only 45 min. of irradiation time. The reaction kinetics of MB degradation was quantitatively described on the basis of a pseudo-

first-order reaction model and the data was fitted with the following equation:

$$\ln (c_0/c) = kt \quad (k = \text{reaction rate constant}). \qquad \textit{Eq. (2.1)}$$

Efficient photocatalysts usually display high values of k. The calculated k values of all $BiVO_4$ samples under visible light irradiation and of P25 under both visible and UV light irradiation are summarized in Table 2.2. The results demonstrate that the visible light driven photocatalytic activity of $BiVO_4$(5) particles outperforms the other samples by a factor of 2-10 and it is 20-fold higher than P 25. Moreover, it is worth noting that the activity of $BiVO_4$(5) crystals under visible light was even higher than that of P25 under UV light irradiation. XRD and SEM analyses of the $BiVO_4$(5) particles after the photocatalytic process showed no structural and morphological changes, thereby suggesting that the material remains intact during the reaction. Note that there is no clear relationship between the BET surface area of the samples under investigation and their degree of MB adsorption on the photocatalysts in the absence of irradiation (Table 2.2).

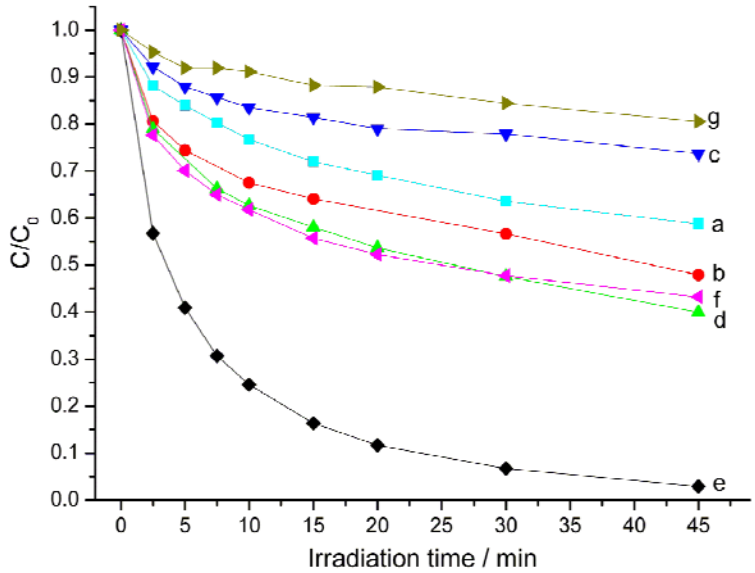

Figure 2.11. Degradation of MB in the presence of different photocatalysts under visible light irradiation: (a) $BiVO_4$(1); (b) $BiVO_4$(2); (c) $BiVO_4$(3); (d) $BiVO_4$(4); (e) $BiVO_4$(5); (f) $BiVO_4$(6); (g) P25 (catalyst: 50 mg; light source: Hg bulbs, max. intensity at 450 nm).

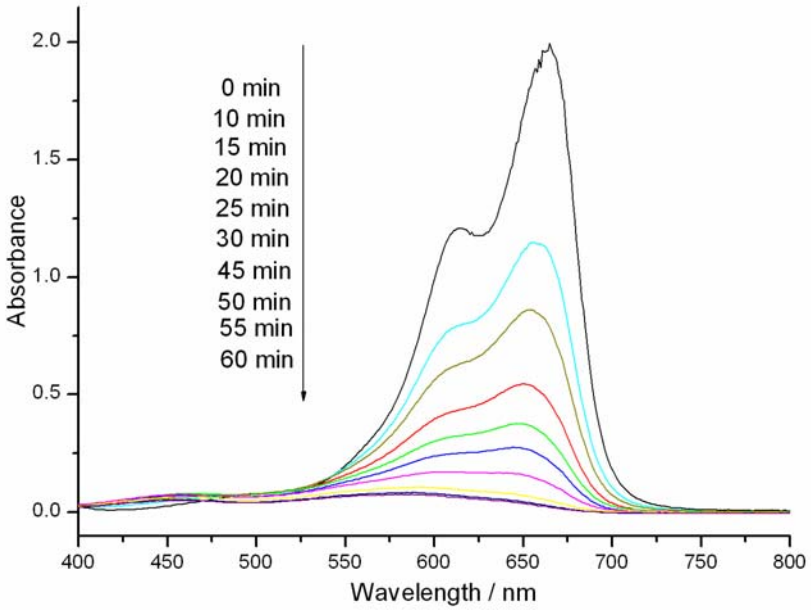

Figure 2.12. UV-vis spectral changes of MB aqueous solution in the presence of $BiVO_4$(5) particles under visible light irradiation.

Table 2.2. Band gap, BET surface area, reaction rate constant *k* and absorption of $BiVO_4$ samples and P25 as a reference.

Sample	**Band gap / eV**	**BET surface / m^2g^{-1}**	***k* / s^{-1}**	**Absorption / %***
$BiVO_4$ (1)	2.39	0.88	4.0×10^{-4}	5%
$BiVO_4$ (2)	2.42	1.25	6.0×10^{-4}	15%
$BiVO_4$ (3)	2.30	1.16	2.0×10^{-4}	10%
$BiVO_4$ (4)	2.40	3.50	9.0×10^{-4}	17%
$BiVO_4$ (5)	2.47	15.58	2.0×10^{-3}	11%
$BiVO_4$ (6)	2.41	1.53	9.0×10^{-4}	20%
P25	3.2	50	1.0×10^{-4} 1.6×10^{-3} (under UV light)	5%

* MB absorption percentages of photocatalyst powders in the dark

Recycling experiments: The reusability of the $BiVO_4$(5) sample was further evaluated in the course of recycling experiments. The photocatalysts were separated by centrifuging and washing with distilled water after the first three runs, respectively. After every run, the

degraded MB was removed and concentrated MB solution was injected to keep the initial concentration of MB and the MB/catalyst ratio unchanged. Figure 2.13 shows that the activity of $BiVO_4$(5) samples decreased with every cycle due to surface contamination. It has been reported in previous studies that the intermediates resulting from MB decomposition can easily be adsorbed on the surface of the oxide particles.[19] Furthermore, the color of the $BiVO_4$(5) samples after the cycling experiments changed from bright yellow to dark green, thereby demonstrating the surface contamination of the particles. For the last cycle, the photocatalysts were irradiated with UV light for ca. 30 min. after centrifuging and washing to remove the surface contamination. These cleaned photocatalysts exhibited higher activity than in the third run. However, it is still lower than in the first two runs (Figure 2.13). As the color of the catalysts only lightened up from dark green to light green after UV irradiation, the surface contamination has probably not been completely removed.

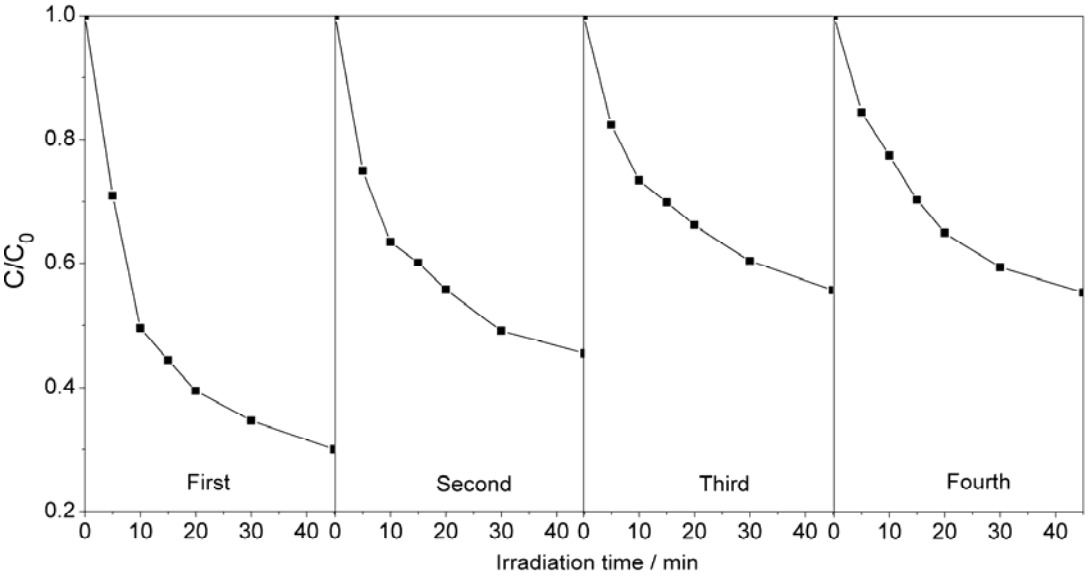

Figure 2.13. Cycling experiments in photocatalytic degradation of MB in the presence of $BiVO_4$(5) particles under visible light irradiation (catalyst: 50 mg; light source: Hg bulbs, max. intensity at 450 nm).

Parameters determining the catalytic activity: It is well known that the crystallinity and the surface area are among the most decisive parameters that influence the activity of a given photocatalyst so that they both have to be optimized for the production of high-performance materials. Although the surface area of $BiVO_4$ powders has been significantly increased in

previous studies, photocatalytic tests revealed that the activity of bulk $BiVO_4$ with a high degree of crystallinity was superior to analogous samples with a high surface area and low crystallinity.[20] This corresponds to previous reports on $BiVO_4$ nanostructured fibers that showed a relatively low photocatalytic activity.[17] As a consequence, the crystallinity of $BiVO_4$ materials appears to be the key to high activities in the photodecomposition of MB. Our newly found route to $BiVO_4$ particles now combines large surface areas with a high degree of crystallinity and thus brings forward materials with superior photocatalytic performance that can be attributed to the following factors:

(1) The high surface area provides more active sites for the degradation reaction of MB in aqueous solution;

(2) The small particle size minimized the sites for the recombination of light-generated electron-hole pairs and permits their more efficient transfer to the surface to degrade the absorbed MB molecules;

(3) In addition, the highly crystalline structure suppresses the recombination process of photogenerated electron-hole pairs.

It is noteworthy that the potassium vanadate fibers also exhibit an unexpectedly high photocatalytic activity. According to the UV/Vis absorption spectrum (Figure 2.10), they display absorption over a wider spectral range than the other substances investigated in this study. Moreover, their absorption maximum is shifted to lower wavelengths at 622 nm (corresponding to a band gap of 2 eV) with respect to the $BiVO_4$ particles (band gap 2.47 eV) so that the potassium vanadate fibers appear even more suitable for catalytic processes under natural light sources. Therefore, the MB degradation rates of potassium vanadate fibers and $BiVO_4$(5) particles under both visible light and simulated daylight irradiation are compared in Figure 2.14. According to the bulb-spectra, the potassium vanadate fibers are expected to exhibit full absorbance under both irradiation conditions (cf. Figure 2.2, note that this does not apply for the $BiVO_4$(5) particles) and indeed their photocatalytic performances under visible light and simulated daylight irradiation are comparable. Although the photocatalytic performance of the $BiVO_4$(5) crystals in visible light with optimum light absorption is superior to the fibers, their band gap limits their use in full daylight, because the entire

spectrum cannot be utilized so that their overall activity decreases. These results render the potassium vanadate fibers promising for applications under ambient conditions so that their demanding structural investigation will be worthwhile.

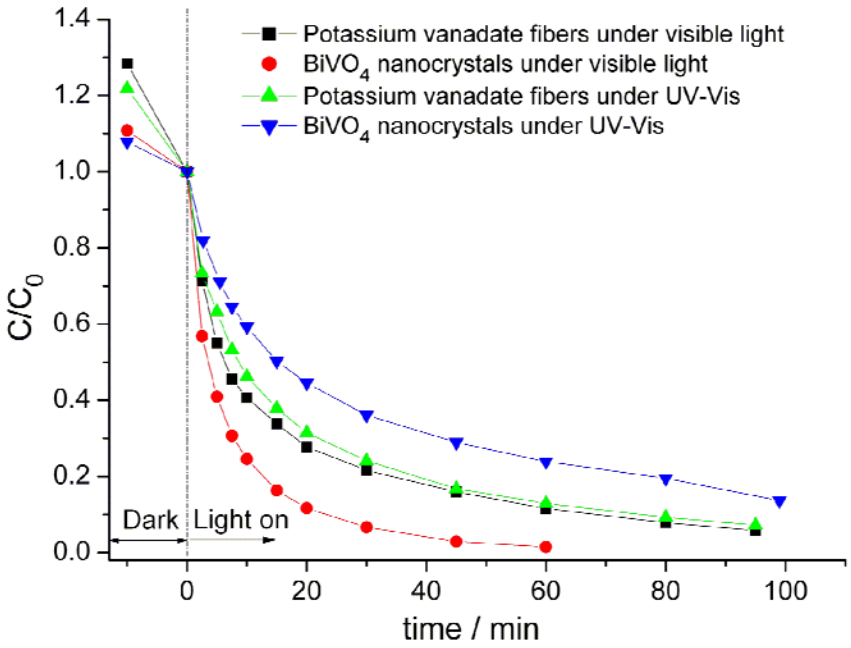

Figure 2.14. Photocatalytic degradation of MB in the presence of $BiVO_4$(5) particles and potassium vanadate fibers under both visible light and simulated daylight irradiation (catalyst: 50 mg; visible light source: Hg bulbs, max. intensity at 450 nm; simulated daylight: Philips TL8W Aquarelle).

2.3.4 Photocatalytic activity with respect to O_2 evolution

Oxygen evolution: The CB of $BiVO_4$ (E_{CB} = 0.33 V vs. NHE) is more positive than the redox potential of H^+/H_2, and the photoexcited electrons in the conduction band can not be captured by H^+. As the redox potentials of both Ag^+/Ag (0.799 V vs. NHE) and Fe^{3+}/Fe^{2+} (0.771 V vs. NHE) are higher than the conduction band potential of $BiVO_4$, they are thermodynamically favorable acceptors for photoexcited electrons. Therefore, the photocatalytic O_2 evolution in the presence of $BiVO_4$(1) and $BiVO_4$(5) particles was investigated in aqueous $AgNO_3$ and $FeCl_3$ solutions, respectively (Figure 2.15). The photocatalytic O_2 evolution rate in $AgNO_3$ solutions of $BiVO_4$(1) and $BiVO_4$(5) samples is 553 µmol/h/g and 428 µmol/h/g and they are higher than the rates observed for the corresponding reactions in $FeCl_3$ solution (239 µmol/h/g

for $BiVO_4$(1) and 221 μmol/h/g for $BiVO_4$(5)). The loading of $BiVO_4$ powders with suitable amounts of a noble metal (e.g. Ag, Pt and Pd) is a general strategy to enhance the photoactivity through the efficient separation of photogenerated carriers at the metal-photocatalyst interfaces and/or via the promotion of catalytic performance on the metal surfaces.[21, 22] The pH value of the $AgNO_3$ solution decreased from 5.1 to 1.6 after $BiVO_4$-assisted O_2 evolution due to the following reaction:

$$2H_2O + 4\,Ag^+ \xrightarrow{h\nu \text{ and } BiVO_4} O_2 \uparrow + 4\,Ag + 4\,H^+ \qquad \textit{(Eq. 2.2)}$$

Furthermore, the XRD patterns of the photocatalysts after the reaction displayed the presence of metallic Ag as a side product. This is a clear proof that Ag^+ ions indeed capture the photoexcited electrons to produce Ag clusters which improve the photoactivity of $BiVO_4$. Nevertheless, the O_2 evolution rate of $BiVO_4$(1) in $AgNO_3$ solution is even higher than that of the $BiVO_4$(5) particles in $AgNO_3$. Here, the deposition of Ag particles on the surface of $BiVO_4$ crystals probably shields the incident light and this counterproductive effect might significantly decrease the light absorption of the photocatalyst.

Recycling options: For reusability experiments of the catalyst material, we focused on the $BiVO_4$(5)/$FeCl_3$ system, because the $BiVO_4$/$AgNO_3$ system is very complicated with respect to recycling.[3] The removal of the side product Ag from the catalysts is extremely difficult in the case of $BiVO_4$/$AgNO_3$. After irradiation for approx. 24 h, the O_2 production from the $BiVO_4$(5)/$FeCl_3$ system stopped. There are two possible explanations in the first place: on the one hand, our catalysts might not be stable during the photocatalytic process – on the other hand, the potential of the system is significantly changed due to the obvious increase in H^+ concentration (pH around 1.8). In order to prove that the termination of O_2 production is not due to an instability of the $BiVO_4$(5) samples, they were separated from the $FeCl_3$ solution after irradiation for 24 h by centrifuging and washing with distilled water, followed by drying at 70 °C. Next, the reused photocatalyst was mixed with a $FeCl_3$ solution of the same concentration. Photocatalytic O_2 evolution over the as-synthesized and reactivated $BiVO_4$(5) samples under visible light irradiation is shown in Figure 2.16. It is evident that the reactivated $BiVO_4$(5) samples showed O_2 production activity again and that the photoactivity

of the reactivated sample decreased only slightly in comparison with the original one (48 µmol O_2 after 24 h in the first cycle and 32 µmol O_2 after recycling), thus indicating the high stability of $BiVO_4$(5) samples. This observed activity decrease is only due to a mechanical loss of catalyst during recollection.

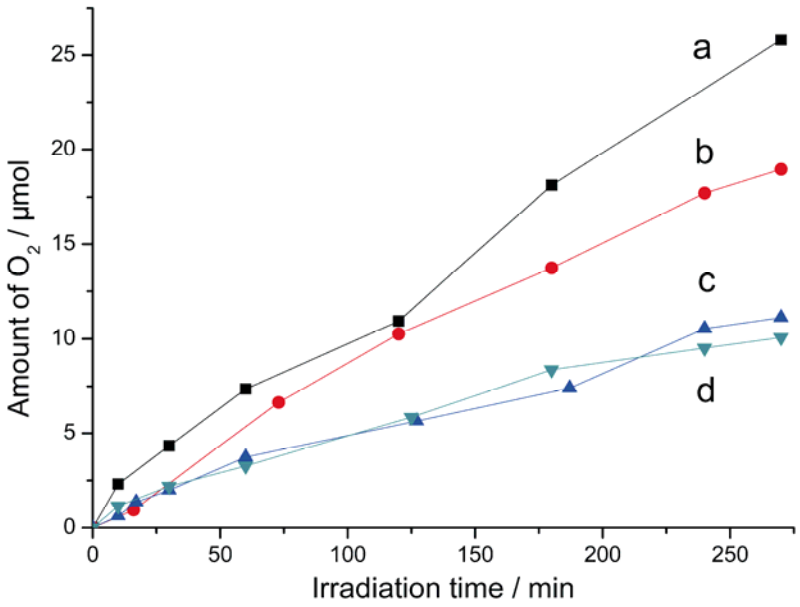

Figure 2.15. Photocatalytic O_2 evolution over different $BiVO_4$ samples under visible light irradiation in $AgNO_3$ solution (a and b) or in $FeCl_3$ solution (c and d); (catalyst: 10 mg $BiVO_4$(1) (a and c); $BiVO_4$(5) (b and d); light source: 300 W Xe arc lamp with a cut off filter ($\lambda \geq 400$ nm)).

Parameter discussion: Although the BET surface are of $BiVO_4$(5) is much higher than that of $BiVO_4$(1) (Table 2.2), both samples display almost equal photocatalytic O_2 evolution rates from $FeCl_3$ solutions (239 µmol/h/g and 221 µmol/h/g, respectively). These results indicate that the surface area and particle size do not significantly influence the activity of the $BiVO_4$ materials in O_2 evolution. We therefore conclude that the optimization of photocatalysts for organic dye photodegradation and for water oxidation require different strategies. For the efficient photodegradation of organic materials, it is necessary to develop new and simple synthetic routes to photocatalysts with high surface areas, small particle sizes and high crystallinity. However, the combination of electronic structure and crystallinity of the photocatalysts is more important for O_2 evolution, because the overall process is a complex

interplay of individual steps that remain to be fully explored. In addition, we also investigated the O_2 evolution over potassium vanadate fibers in $AgNO_3$ solution. O_2 evolution could not be observed: probably, the electron transfer from the conduction band of the potassium vanadate fibers to Ag^+ as an electron acceptor cannot proceed, because the conduction band of the potassium vanadate phase may be located at lower energies as indicated by the lower band gap. Otherwise the energy level of the valence band is less than the oxidation potential of water (+1.23 V vs. NHE). This result points to significant differences in the electronic structures of potassium vanadate fibers and $BiVO_4$.

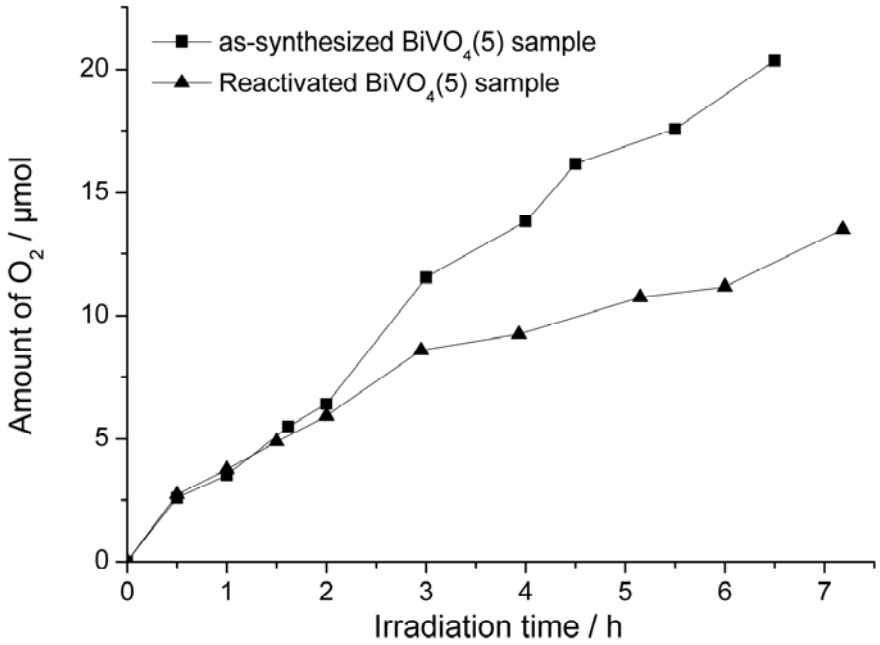

Figure 2.16. Photocatalytic O_2 evolution over the original as-synthesized $BiVO_4(5)$ samples and the reactivated $BiVO_4(5)$ samples under visible light irradiation in $FeCl_3$ solution (catalyst: 10 mg $BiVO_4$; light source: 300 W Xe arc lamp with a cut off filter ($\lambda \geq 400$ nm)).

2.4 Conclusions

In summary, we have established an efficient hydrothermal route to photocatalytically active $BiVO_4$ particles with a homogeneous morphology, high crystallinity and a high surface area. Hydrothermal parameters studies led the way to these enhanced catalytic $BiVO_4$ materials: firstly, we selected appropriate bismuth and vanadium sources and in the next step, the

particle morphology was optimized using K_2SO_4 as a shape-controlling additive in the $Bi(NO_3)_3 \cdot 5H_2O/V_2O_5/K_2SO_4$ hydrothermal system. Generally, the use of low-cost and flexible inorganic additives as a template in nanomaterials fabrication is an attractive option for large-scale processes. In the present system, the use of K_2SO_4 considerably improved the photocatalytic performance of the $BiVO_4$ particles in the decomposition of MB under visible light irradiation in comparison with materials emerging from alternative synthetic routes. Moreover, we compared the performance of $BiVO_4$ materials obtained via different hydrothermal pathways in the O_2 evolution from aqueous $AgNO_3$ and $FeCl_3$ solutions as electron acceptors, respectively. Here, the morphology and surface area are not the only crucial factors for the activity of $BiVO_4$ catalyst particles, but the fine-tuning of their electronic structure and crystallinity has to be pursued with different strategies to optimize the particle surface with respect to the complex redox processes. As this involves a multitude of parameter variations, flexible and straightforward synthetic for quick materials screening are required and hydrothermal methods are among the favorable options here.

Furthermore, the mechanism of the K_2SO_4-assisted $BiVO_4$ nanomaterials formation is an interesting and versatile process, because the $Bi(NO_3)_3 \cdot 5H_2O/V_2O_5/K_2SO_4$ system quickly responds to changes in the hydrothermal parameters. Therefore, it affords nanostructured potassium vanadate fibers as a second product that can be mechanically separated from the $BiVO_4$ particles. The potassium vanadate fibers also display photocatalytic activity due to a band gap that renders them suitable for catalytic reactions under ambient light sources.

All in all, the present results demonstrate that screening procedures in hydrothermal systems with inorganic additives are a powerful search strategy for new materials on the way to clean energy sources and wastewater-treatment catalysts for the future.

References

[1] A. Kudo, K. Omori, H. Kato, *J. Am. Chem. Soc.* **1999**, *121*, 11459.

[2] A. W. Sleight, H. Y. Chen, A. Ferretti, *Mater. Res. Bull.* **1979**, *14*, 1571.

[3] D. N. Ke, T. Y. Peng, L. Ma, P. Cai, P. Jiang, *Appl. Catal. A* **2008**, *350*, 111.

[4] A. Galembeck, O. L. Alves, *Thin Solid Films* **2000**, *365*, 90.

[5] L. Zhou, W. Z. Wang, L. S. Zhang, H. L. Xu, W. Zhu, *J. Phys. Chem. C* **2007**, *111*, 13659.

[6] D. N. Ke, T. Y. Peng, L. Ma, P. Cai, K. Dai, *Inorg. Chem.* **2009**, *48*, 4685.

[7] H. Q. Jiang, H. Endo, H. Natori, M. Nagai, K. Kobayashi, *J. Eur. Ceram. Soc.* **2008**, *28*, 955.

[8] L. Zhou, W. Z. Wang, S. W. Liu, L. S. Zhang, H. L. Xu, W. Zhu, *J. Mol. Catal. A: Chem.* **2006**, *252*, 120.

[9] L. Zhang, D. R. Chen, X. L. Jiao, *J. Phys. Chem. B* **2006**, *110*, 2668.

[10] J. Q. Yu, A. Kudo, *Chem. Lett.* **2005**, *34*, 850.

[11] G. S. Li, D. Q. Zhang, J. C. Yu, *Chem. Mater.* **2008**, *20*, 3983.

[12] R. Kiebach, N. Pienack, W. Bensch, J.-D. Grunwaldt, A. Michailovski, A. Baiker, T. Fox, Y. Zhou, G. R. Patzke, *Chem. Mater.* **2008**, *20*, 3022.

[13] Y. Zhou, N. Pienack, W. Bensch, G. R. Patzke, *Small* **2009**, *5*, 1978.

[14] Z. J. Gu, Y. Ma, W. S. Yang, G. J. Zhang, J. N. Yao, *Chem. Commun.* **2005**, 3597.

[15] S. Lakshmi, R. Renganathan, S. Fujita, *J. Photochem. Photobiol. A* **1995**, *88*, 163.

[16] G. Sivalingam, K. Nagaveni, M. S. Hegde, G. Madras, *Appl. Catal. B* **2003**, *45*, 23.

[17] J. Q. Yu, A. Kudo, *Adv. Funct. Mater.* **2006**, *16*, 2163.

[18] A. Michailovski, M. Wörle, D. Sheptyakov, G. R. Patzke, *J. Mater. Res.* **2007**, *22*, 5.

[19] M. Long, W. Cai, J. Cai, B. Zhou, X. Chai, Y. Wu, *J. Phys. Chem. B* **2006**, *110*, 20211.

[20] J. Q. Yu, Y. Zhang, A. Kudo, *J. Solid State Chem.* **2009**, *182*, 223.

[21] L. Ge, *Mater. Lett.* **2008**, *62*, 926.

[22] L. Ge, *J. Mol. Catal. A: Chem.* **2008**, *282*, 62.

3. Hierarchical Bi_2WO_6 nanostructures

3.1 Introduction

As we have outlined in chapter 2 for the case of $BiVO_4$, the fabrication of small particles with high surface areas is an effective approach to enhance their photocatalytic activity. The particle size of our hydrothermally synthesized $BiVO_4$ particles is between 100 and 200 nm (Figure 2.5 a and c), but the separation of these particles from solutions already turned out to be quite difficult and the activity of the $BiVO_4$ particles decreased with each cycle partly due to a mechanical loss of catalyst during recollection (cf. Figure 2.13), which is a significant drawback for practical applications. These inherent problems of small particle dimensions can be overcome through the formation of hierarchical assemblies of nanostructures into ordered complex architectures. In this way, both micro- and nanostructured features can be maintained.[1-3] Furthermore, such hierarchical nanostructures often benefit from enhanced chemical and physical properties. An instructive example is the use of β-$Ni(OH)_2$ microtubes with hierarchically structured walls as battery materials that are superior to structural analogues based only on a single particle type.[4]

For this purpose, the important family of transition metal oxide-based nanomaterials offers an exceptionally wide range of structural motifs that facilitate the construction of complex nano-architectures. Tungstates represent a considerable fraction of these key building blocks for a future nanotechnology and Bi_2WO_6 excels among them due to its flexible *Aurivillius* structure that is closely related to the perovskite type. The layered 2D structure motif is composed of $[WO_4]_n^{2-}$ sheets consisting of corner-sharing WO_6 octahedra alternating with $[Bi_2O_2]_n^{2+}$ slabs.[5] Bi_2WO_6 has attracted considerable research attention due to its important physical and chemical properties, e.g. ferroelectricity,[6] oxide anion conductivity[7] and nonlinear dielectric susceptibility.[8] Furthermore, Bi_2WO_6 is a highly promising photocatalyst that is capable of O_2 evolution from $AgNO_3$ solution[9] and of the degradation of organic compounds[10] under visible light irradiation.

These environmentally important properties have raised a general interest in the formation of Bi_2WO_6 nano-architectures and it has been found that their catalytic properties are superior to

the bulk material.[11-17] Thus, extraordinary research attention has recently been focused on the fabrication of hierarchically structured Bi_2WO_6 spheres.[18-21] Although their hydrothermal formation has been frequently studied in the presence of organic templates and also via template-free syntheses, each variation of the preparative conditions considerably influences the resulting materials properties and follows a different mechanism.[22-24] This indicates that hierarchically structured Bi_2WO_6 is not only an outstanding multifunctional material, but also an excellent model system to obtain new insights into the general relations between synthesis, morphology and properties in the fabrication of hierarchical nanostructures. However, more detailed studies are required to fully understand these phenomena and they are of general importance: as ternary oxide materials can combine the key features of their binary components into novel synergisms, there is a growing need for the understanding of their nanoscale formation pathways.

Therefore, the present chapter on the development of Bi_2WO_6 nano-architectures from three new perspectives:

- Firstly, we present the most straightforward one-step approach towards hierarchical Bi_2WO_6 microspheres till date as a further step to facilitate their technical production. The photocatalytic properties of the resulting hierarchical Bi_2WO_6 structures were investigated under UV and visible light irradiation.
- Secondly, we have investigated the influence of an inorganic template on the hydrothermal formation of Bi_2WO_6 for the first time. Due to its known productive interaction with the binary oxides, K_2SO_4 was selected as an ideal candidate and it opens up new low-temperature pathways to other bismuth oxide materials (cf. chapter 7).
- Furthermore, the hydrothermal crystallization of hierarchical Bi_2WO_6 nanostructures was studied using in situ EDXRD methods with special emphasis on the influence of the reaction temperatures and the pH value on the crystallization process.

3.2 Experimental

3.2.1 Synthesis

In a typical procedure, 97 mg (0.2 mmol) of $Bi(NO_3)_3 \cdot 5H_2O$ and 33 mg (0.1 mmol) of K_2WO_4 were placed into 10 mL of 20 vol.% acetic acid at room temperature and stirred magnetically for 20 min. to disperse all reagents homogeneously (initial pH 1.3). If required, the pH of the suspension was adjusted to a specific value using 10 M NaOH or 15 M $NH_3 \cdot H_2O$ solution. The resulting precursor suspension was transferred into a Teflon-lined stainless steel autoclave with a capacity of 23 mL, maintained at 160 °C for 24 h, and subsequently cooled to room temperature. The precipitate was collected after filtration, washed with distilled water and dried in air.

3.2.2 Analytical characterization

PXRD was performed on a Bruker D8-Advance X-ray powder diffractometer with CuK_α radiation (λ=1.5418 Å) over a 2θ range from 10 to 65°. For SEM, performed on a LEO 1530 (FEG) microscope with 2 keV electrons, samples were dispersed in ethanol and subsequently deposited on a silicon wafer. The material was deposited on a perforated carbon foil supported on a copper grid. EDXS investigations were performed on a Zeiss SUPRA 50VP microscopy with an EDAX detector. TEM investigations were performed on a Philips CM30/ST microscope operated at 300 kV (LaB_6 cathode). BET surface area measurements were performed on a Coulter SA 3100 in N_2-adsorption mode. The samples were degassed at 180 °C for 2-3 h under N_2 prior to the nitrogen absorption measurements. Raman spectroscopy was performed on a Renishaw Ramascope 1000 with a green SpectraPhysics Argon laser with a wavelength of 524.5 nm and 50 mW capacity. Optical absorption spectra were recorded on a Cary 500 UV/Vis-NIR spectrophotometer.

3.2.3 In situ EDXRD experiments

In situ EDXRD experiments were performed at HASYLAB (Hamburg) bending magnet

beamline F3 that provides an energy range of 13.31-62.54 keV with a maximum intensity at about 26 keV. The *d*-spacing is given by $d = 6.199/E \sin\theta$ (with *d* in Å and *E* in keV). A solid state Ge detector cooled with liquid nitrogen was used for all experiments. With a detector angle of 4.9° the observable *d*-spacing range is 1.16 Å to 5.46 Å. The energy resolution $\Delta d/d$ is about 10^{-2} above 26 keV. The beam was collimated to 0.2 mm for optimum results. For the in situ experiments, autoclaves with glass liners (internal diameter of 10 mm and a volume of 10 mL) were used. In a representative experiment, 97 mg (0.2 mmol) $Bi(NO_3)_3 \cdot 5H_2O$, 33 mg (0.1 mmol) K_2WO_4 and 2 mL 20 vol.-% acetic acid were used as reactants. The reactions were perfomed at 150, 160, 170 and 180 °C, respectively. The pH of the suspension was adjusted to a specific value using 8 M NaOH solution, if required. Data collection was started immediately after the introduction of the autoclave into the oven. The acquisition time per frame for the in situ data measured in these experiments was 120 s. After the in situ experiments, the solid products were filtrated, collected, washed with distilled water and ethanol, and dried in air for further characterizations. It is noteworthy that the reactions have to be performed under rapid stirring to keep the measurement conditions constant by avoiding the sedimentation of the high density product particles.

3.2.4 Photocatalytic activity measurements

Photocatalytic activities were evaluated through the degradation of Rhodamine B (RhB) (cf. Scheme 3.1) under visible light irradiation in a photoreactor equipped with 14 bulbs of blue light (Hg bulbs LCD M2-6S-01, max. intensity at 450 nm) and with UV light, respectively (Sylvana blacklight F8W/BLB T5, max. intensity at 355-360 nm). The bulbs were arranged in a circular fashion around the reaction vessel that was thermostated at 30 °C with a circulating water pump. Prior to illumination, 50 mg of the photocatalyst powder were suspended in an RhB solution (125 mL, 10^{-5} mol/L) through ultrasonication in the dark for 10 min. The suspension was transferred into the reaction vessel and kept under a constant air flow of 100 ml/min. At given time intervals, 3 mL of the suspension were collected through a filter to

remove the photocatalyst powders. The filtrates were analyzed by recording the different intensities of the RhB absorption maximum at 554 nm in a Varian Cary 50 Scan UV/Vis spectrometer.

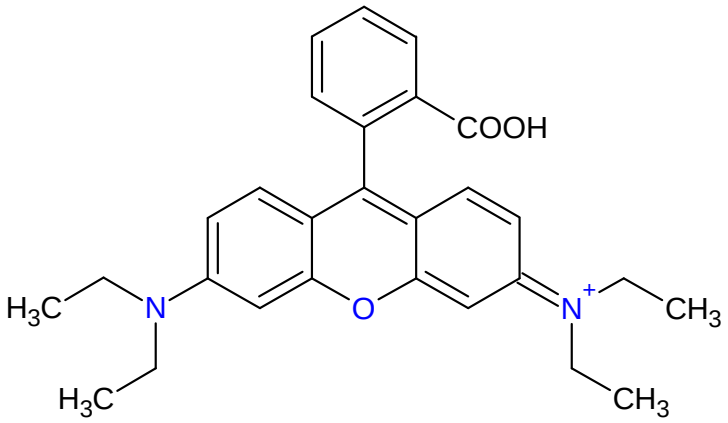

Scheme 3.1. Molecular structure of RhB.

3.3 Results and discussion

3.3.1 Hierarchical assemblies of Bi_2WO_6 nanosheets

The hydrothermal reaction of $Bi(NO_3)_3 \cdot 5H_2O$ and K_2WO_4 at 160 °C for 24 h brings forward Bi_2WO_6 microspheres with diameters between 1 and 5 μm consisting of individual nanoparticles (cf. Figure 3.1 a): in the first place, the spheres are constructed from nanosheets with a thickness of ca. 30 nm. A closer morphological examination reveals that these nanosheets are again composed of numerous nanoplates (cf. Figure 3.1 b). However, the resulting hierarchical microspherical morphology is highly stable, e.g. it withstands 10 min. of ultrasonication. TEM investigations (Figure 3.1 c) show an asymmetric arrangement of the individual nanoparticles and this substructure is also evident from the edges of the microspheres (cf. Figure 3.1 b). A SAED pattern of the microspheres is displayed in Figure 3.1 d and the polycrystalline material can be indexed according to the literature data for Bi_2WO_6 (JCPDS No. 73-1126).

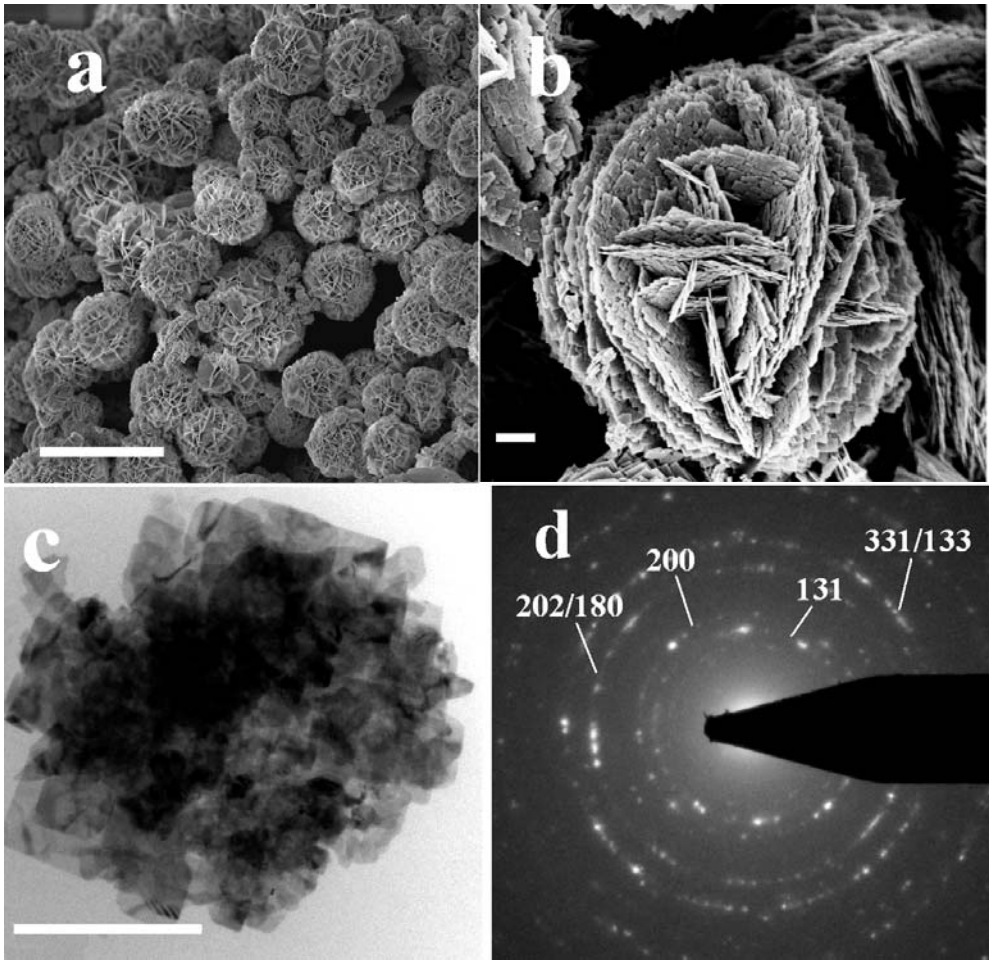

Figure 3.1. (a) Representative SEM image of Bi_2WO_6 microspheres (overview, scale bar = 10 µm); (b) detailed SEM image of an individual Bi_2WO_6 microsphere (scale bar = 300 nm); (c) TEM image of Bi_2WO_6 microspheres (scale bar = 300 nm) and (d) the corresponding SAED pattern.

This is in line with the XRD pattern of the product (cf. Figure 3.2) that can be indexed to pure orthorhombic Bi_2WO_6 (lattice constants a = 5.464(8) Å, b = 5.432(5) Å and c = 16.44(1) Å, cf. JCPDS No. 73-1126). No side products were observed and the increased peak width clearly indicates the nanostructured morphology. As shown in Figure 3.3, the recorded adsorption and desorption isotherm of the hierarchical Bi_2WO_6 nanostructures display a significant hysteresis. The BET surface area of the products calculated from the linear part of the BET plot is 17.4 (+/-1) m^2/g that is due to the internal nanostructure of the Bi_2WO_6 microspheres (cf. Figure 3.1 b).

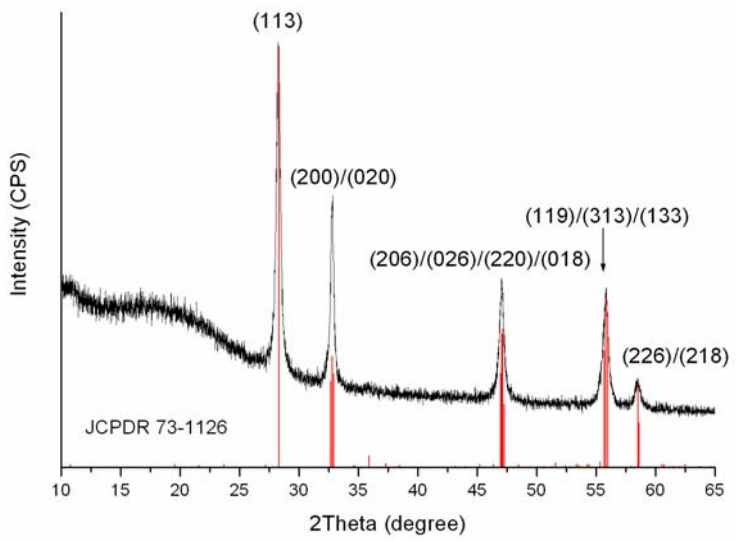

Figure 3.2. XRD pattern of hierarchically structured Bi_2WO_6 microspheres obtained from the standard synthesis route compared to literature data for orthorhombic Bi_2WO_6 (JCPDS 73-1126, bottom).

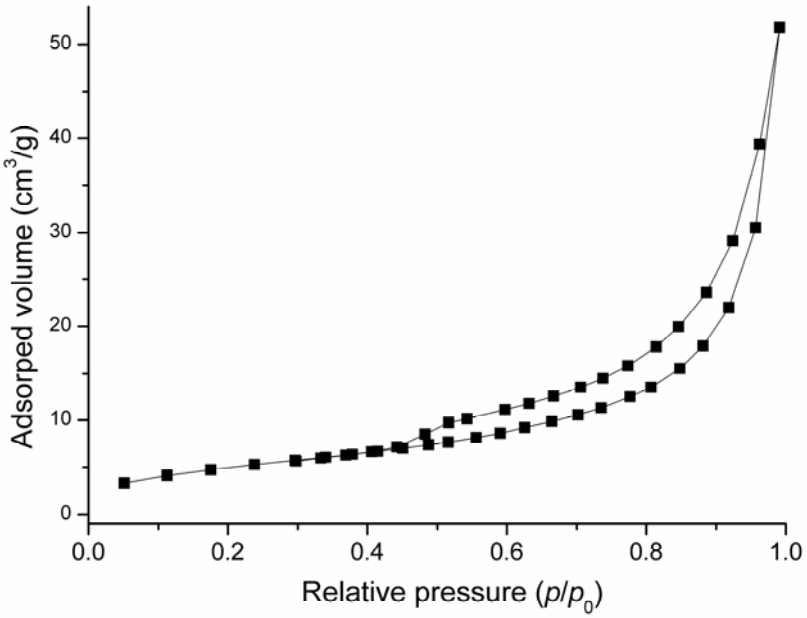

Figure 3.3. Nitrogen adsorption-desorption of the prepared hierarchical Bi_2WO_6 nanostructures.

Our results clearly demonstrate that hierarchical Bi_2WO_6 microspheres can be easily prepared under convenient hydrothermal reaction conditions without any organic additives or additional pre-treatment steps. Similar hierarchical Bi_2WO_6 architectures have been obtained using organic additives including PVP and several block copolymers as templates.[18-21] However, recent studies demonstrated that the presence of a template is not mandatory for

their formation under hydrothermal conditions – but an excess of tungstate precursor and strongly acidic conditions were recommended.[22-24] This raises the question whether all these syntheses of microstructured Bi_2WO_6 materials are based on different mechanistic pathways. Such insights are crucial to establish clear connections between the morphology, the resulting photocatalytic activity and the "preparative history" of bismuth tungstate catalysts – and this represents also a general challenge of nanomaterials research. We thus performed more detailed parameters investigations as outlined in the following section.

3.3.2 Parameter studies on the formation of hierarchical Bi_2WO_6 nanostructures

We have investigated the influence of the hydrothermal key parameters on our one-step route towards hierarchically structured Bi_2WO_6 microspheres in order to optimize their fabrication. The temperature window for their formation is between 120 and 180 °C: lower temperatures lead to amorphous products and impurities occur around 200 °C (cf. Figure 3.4).

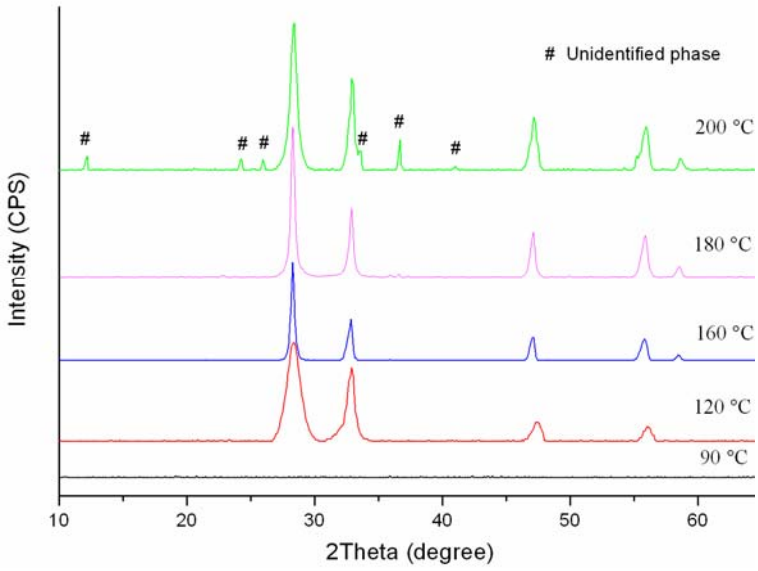

Figure 3.4. XRD patterns of hydrothermal products obtained at different reaction temperatures.

As for the Bi source, $Bi(NO_3)_3 \cdot 5H_2O$ was found to be the only suitable starting material whereas $BiCl_3$ and Bi_2O_3, for example, led to the formation of side products. Interestingly,

the choice of the W source is less decisive and the Bi_2WO_6 microspheres could also be obtained from tungsten precursors with a completely different structure from K_2WO_4, such as the Keggin-type polyoxotungstate $(NH_4)_6[H_2W_{12}O_{40}]\cdot\sim 3H_2O$.

Influence of the pH value: The influence of the pH value on the hydrothermal formation of nanostructured Bi_2WO_6 was investigated by adjusting the original pH (1.3) of the standard route (cf. experimental section 3.2) to the desired value by adding $NH_3\cdot H_2O$ or NaOH solution while keeping all other parameters constant. The XRD patterns of the products obtained at different pH values are summed up in Figure 3.5 (for the reference at pH 1.3 cf. Figure 3.2). The overall pH window for phase pure Bi_2WO_6 formation ranges from 1.3 to 11.8.

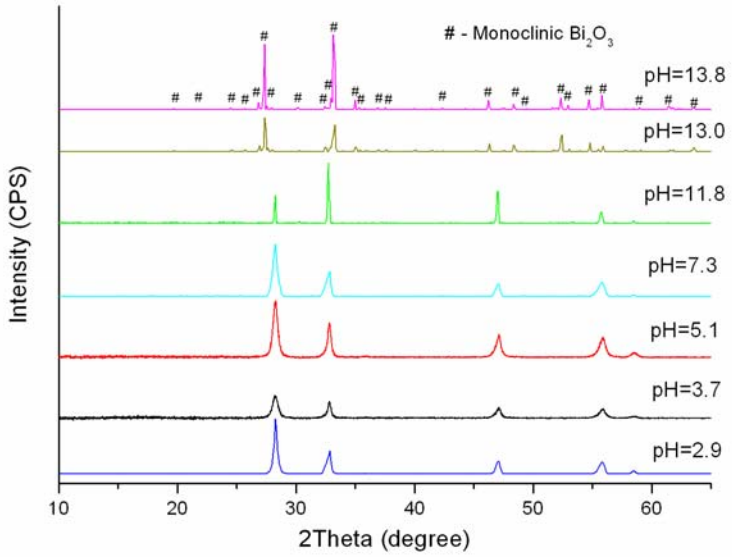

Figure 3.5. XRD patterns of hydrothermal products obtained at different pH values.

Moreover, several pH ranges can be differentiated within the given pH window for Bi_2WO_6 growth (cf. Figure 3.6): The hierarchical Bi_2WO_6 microspheres (cf. Figure 3.1) can be obtained with constant morphology between pH 1.3 and 2.9. At higher pH values (ca. 3.7 – 5.1), the Bi_2WO_6 microspheres start to disintegrate (cf. Figure 3.6 a) and this process continues until the individual nanoplate building blocks appear in an isolated fashion at approx. pH 7.3 (cf. Figure 3.6 b). Finally, even larger micro-platelets are obtained upon further increasing the pH value to an upper limit of 11.8 (cf. Figure 3.6 c). The size of these

particles clearly exceeds that of the original nanosheets present in the hierarchical arrangements. Furthermore, the relative intensity of the (113) reflection compared to the (200) or (020) reflections, respectively, is about 0.5 whilst it is considerably more intense in the reference XRD pattern (cf. Figure 3.2). This indicates a preferred anisotropic growth along [200]/[020] in accordance with the 2D morphology observed in the SEM investigations (Figure 3.6 c).[18, 21] When the pH is finally raised to 13.0, the formation of Bi_2WO_3 stops altogether and monoclinic α-Bi_2O_3 (JCPDS No. 71-2274) is obtained as irregularly shaped microscale particles (Figure 3.6 d). These results demonstrate that the initial pH of the hydrothermal reaction exerts probably the strongest influence on both the phase and the morphology of the products obtained from the $Bi(NO_3)\cdot 5H_2O/K_2WO_4$ hydrothermal system and that the formation of hierarchical Bi_2WO_6 architectures mostly depends on highly acidic conditions.

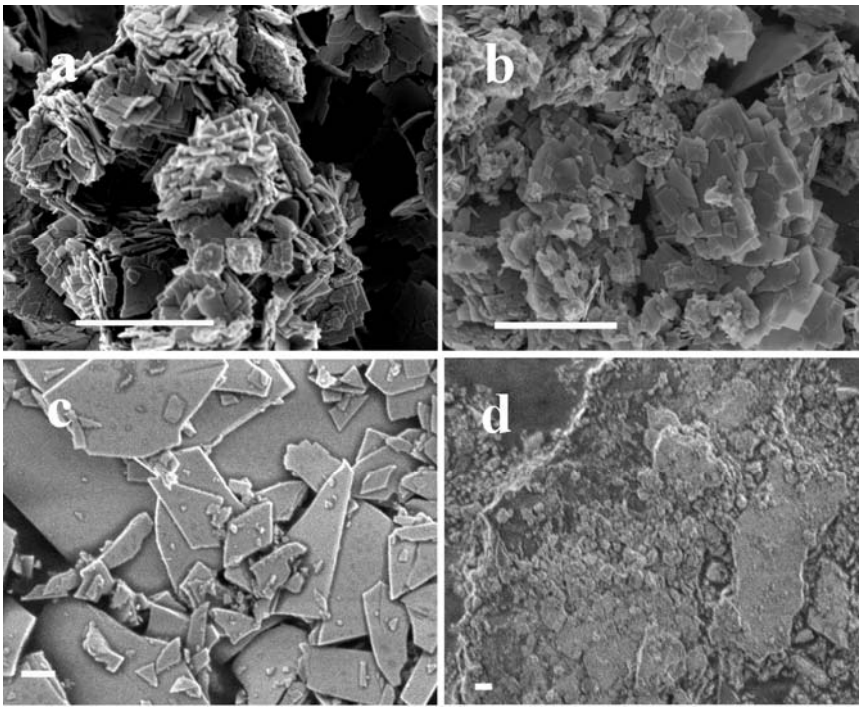

Figure 3.6. SEM images of Bi_2WO_6 samples obtained from different initial pH values: (a) pH 3.7; (b) pH 7.3; (c) pH 11.8; (d) pH 13.0 (scale bar = 1 μm).

Time-dependent formation: As outlined above, the formation mechanisms of hierarchically structured Bi_2WO_6 probably vary widely with the reaction conditions. In order to obtain

further insight into the growth of Bi_2WO_6 microsphere architectures, we have investigated their time-dependent formation with respect to structure and morphology in the range between 1 and 24 h of reaction time (cf. Figures 3.7 and 3.8). In the initial stage of the reaction (1 h), the sample consists mainly of nanoparticles with an average size around 20 nm and some platelet-shaped areas with internal nanostructuring (Figure 3.7 a-b). The products are still amorphous after the short hydrothermal treatment as indicated by the absence of reflections after 1 h in the XRD pattern (cf. Figure 3.8). After 3 h of reaction time, broad reflections of orthorhombic Bi_2WO_6 indicate the onset of the crystallization process. The intermediate morphologies formed after 5 h of treatment (Figure 3.7 c and d) can be described as microplates that are covered with nanoplatelets and a closer look at the cutting edges reveals that they probably also consist of them throughout. Furthermore, the first hierarchical structures are emerging from the microplate surfaces in a nest-like fashion as can be seen from SEM images taken at higher magnifications (Figure 3.7 d). Prolonged reaction times of 24 h finally bring forward the hierarchical Bi_2WO_6 microspheres in a quantitative fashion (cf. Figure 3.1 a). Generally, the size of the individual nanocrystallite building blocks increases with the reaction time as can be seen from the decrease of the full width at half maximum (FWHM) of the diffraction peaks after 3, 5, 10 and 24 h, respectively: The evaluation of the most intense (113) reflection according to the Scherrer equation indicates the corresponding crystallite sizes of 9, 10, 12 and 20 nm. Based on these observations, we propose the following formation mechanism for hierarchically structured Bi_2WO_6 (Figure 3.7, right): the microspheres probably result from the aggregation of individual nano-platelets starting from the particle centres rather than from an initial growth along the crystal planes (Figure 3.7 b). The smallest nano building blocks are formed quickly in the initial stages of the reaction (cf. Figure 3.7 a) and they subsequently aggregate into larger plates to minimize the surface area. The 2D features of the *Aurivillius*-type Bi_2WO_6 structure prevail in the hierarchical platelet morphologies that are observed during the earlier stages of the growth process (Figure 3.7 c). In the advanced phase of the reaction, the microspherical aggregates grow at the expense of the larger platelets through a second self-assembly process of individual nanoplatelets (Figure 3.7 d). Further investigations of the kinetics-morphology relations in the hydrothermal

formation of nanostructured Bi_2WO_6 as a model system for the study of hierarchical growth processes will be discussed in section 3.3.4.

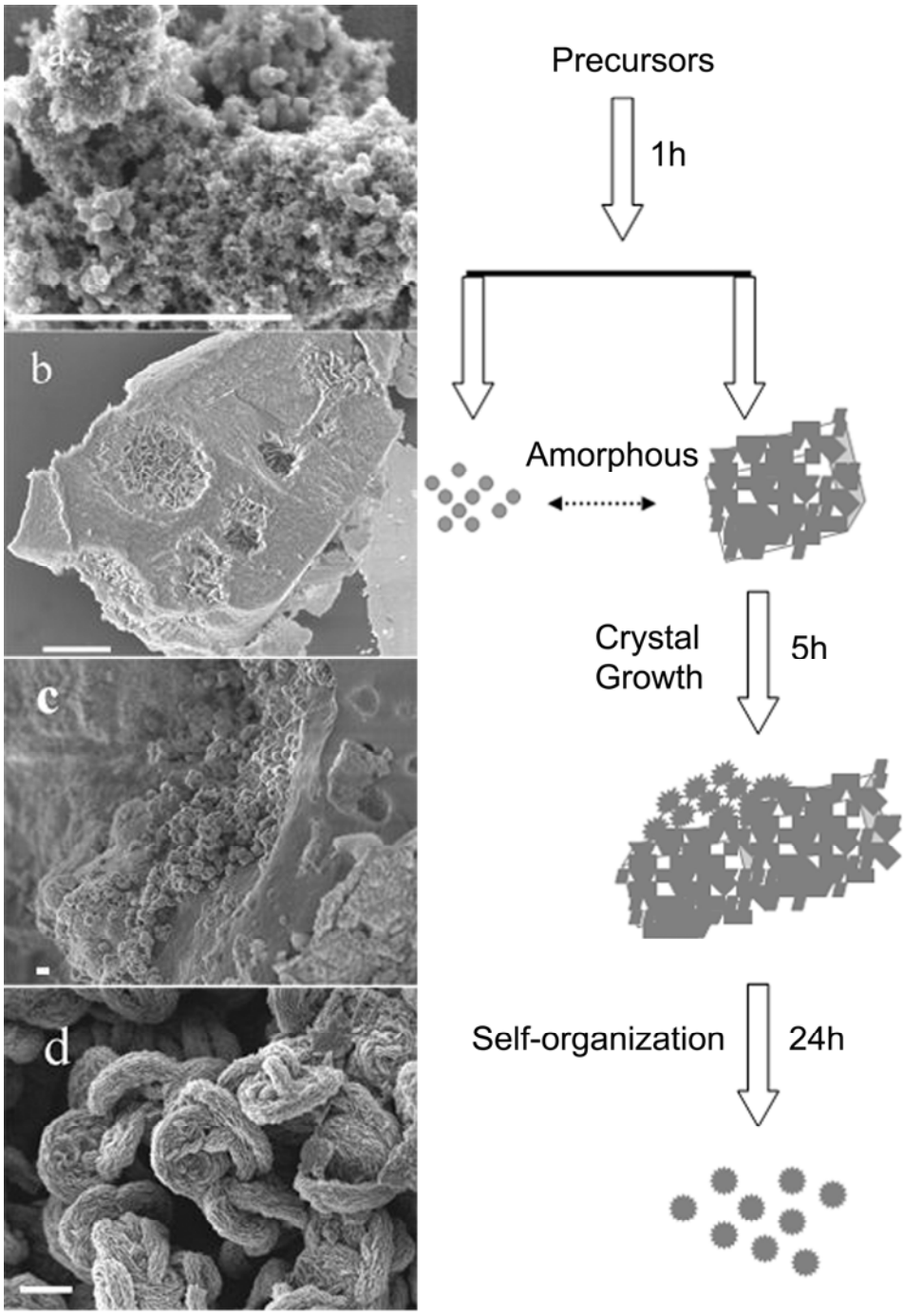

Figure 3.7. SEM images (left) of Bi_2WO_6 samples isolated after various reaction times: (a-b) 1 h; (c-d) 5 h (scale bar = 1 μm) and a possible mechanistic scenario for the formation of hierarchical Bi_2WO_6 microspheres (right).

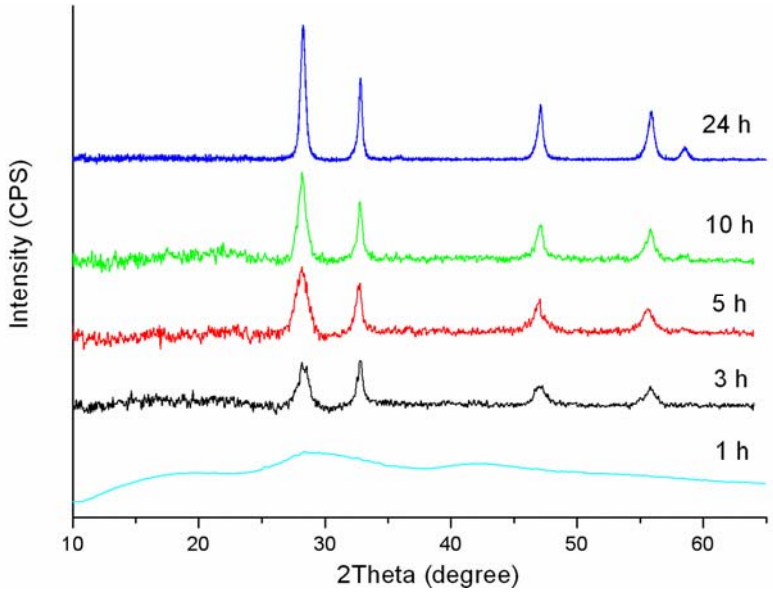

Figure 3.8. XRD patterns of Bi_2WO_6 samples isolated after different reaction times.

3.3.3 The influence of K_2SO_4 as an inorganic additive

In addition to 1D and 2D structural features as a driving force for the anisotropic growth of nanoparticles, the morphology of nanoparticles can also be steered through the use of appropriate capping agents as inhibitors or promoters for selective growth directions.[25, 26] For this purpose, inorganic ionic additives are attractive candidates, because they can be easily removed through simple washing after the reaction with no further organic contamination of the final product. Recently, K_2SO_4 has been discovered as a highly efficient morphology-directing agent for the formation of hexagonal WO_3 nanowires[25] and its role in the formation of $BiVO_4$ has been discussed in chapter 2. In order to apply this additive upon the hydrothermal formation of ternary Bi/W-oxides, we have investigated the influence of K_2SO_4 on the $Bi(NO_3)_3 \cdot 5H_2O/K_2WO_4$ system. Based on previous optimization experiments, a large excess of K_2SO_4 (6 mmol) was added to the hydrothermal reaction system and the phase and morphology of the resulting products were characterized for different pH values (cf. Figures 3.9 and 3.10). Quite unexpectedly, K_2SO_4 does not exert a productive effect on the hydrothermal system at lower pH values (around 2.5), because the obtained Bi_2WO_6 samples contain mixed morphologies (Figure 3.9 a) including fibers and irregular particles that are reflected in impurities in the XRD patterns (Figure 3.10). However, an increase of the pH to

4.9 brings forward pure orthorhombic Bi_2WO_6 with a multilayered hierarchical structure of densely packed 2D sheets, thereby widening the pH window of the reaction (Figure 3.9 b). When the pH is raised to 10.8, the formation of cubic $Bi_{3.84}W_{0.16}O_{6.24}$ (JCPDS 43-0447) sets in - however, the biphasic product still contains orthorhombic Bi_2WO_6 (Figure 3.10). Phase pure cubic $Bi_{3.84}W_{0.16}O_{6.24}$ is finally obtained at pH 11.8 (Figure 3.10). Interestingly, higher pH values (around 13.4) lead to the formation of pure metastable cubic γ-Bi_2O_3 (JCPDS 74-1375) with a characteristic microscale cubic morphology (Figure 3.9 d). This is a new hydrothermal route to this high-temperature modification of Bi_2O_3 under relatively mild conditions (160 °C). δ-Bi_2O_3 as another metastable Bi_2O_3 modification can be stabilized at lower temperatures through the incorporation of V.[27] Thus, the presence of W in our newly established access to cubic γ-Bi_2O_3 probably also exerts a stabilizing function. The presence of K_2SO_4 is furthermore essential, because we exclusively obtained α-Bi_2O_3 in the absence of the inorganic additive. All in all, the use of K_2SO_4 as an inorganic additive opens up three new preparative pathways to hierarchically structured orthorhombic Bi_2WO_6, cubic $Bi_{3.84}W_{0.16}O_{6.24}$ and γ-Bi_2O_3.

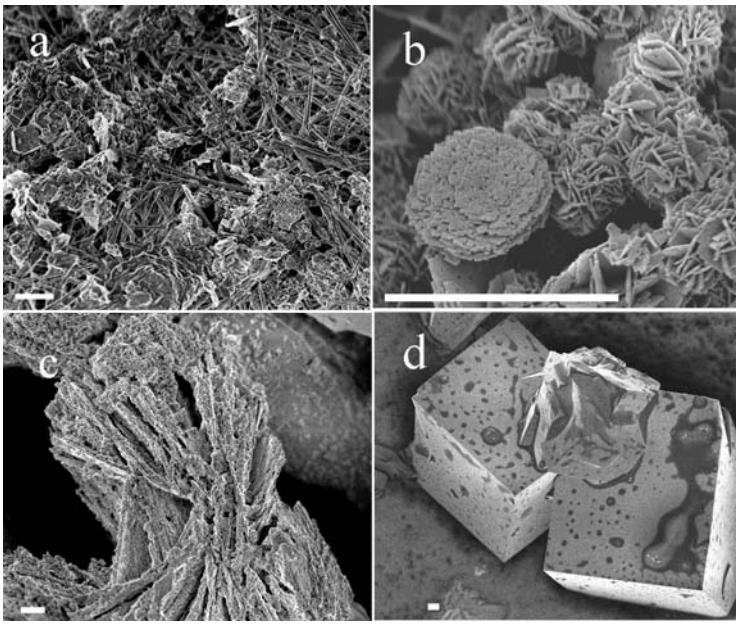

Figure 3.9. Representative SEM images of the products obtained from different pH values in the presence of K_2SO_4 as an inorganic additive: (a) pH 2.5; (b) 4.9; (c) 11.8; (d) 13.4 (scale bar = 2 μm).

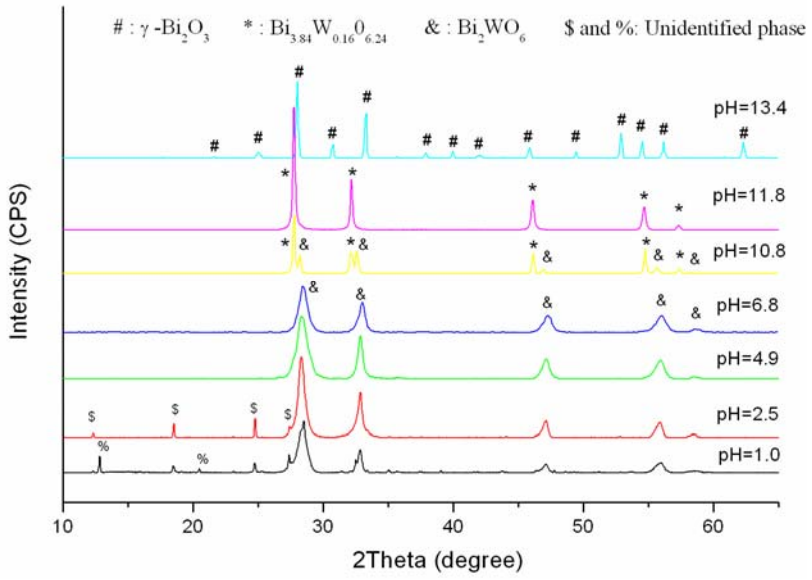

Figure 3.10. XRD patterns of the samples obtained at different pH values in the presence of K_2SO_4.

3.3.4 In situ EDXRD investigations

In situ EDXRD studies are well suited for the investigation of relationships between particle morphology and reaction kinetics. Hence, in situ EDXRD was used to study the hydrothermal crystallization kinetics of hierarchical Bi_2WO_6 nanostructures to derive more general rules for the fabrication of hierarchical nanostructures. A three-dimensional stack plot of the in situ EDXRD patterns recorded at 160 °C during the hydrothermal reaction is shown in Figure 3.11. After a short induction time of ca. 8 min. (cf. Table 3.1) during which no diffraction peaks are observed, several diffraction peaks corresponding to the reflections of orthorhombic Bi_2WO_6 phase appeared and the intensity of the diffraction peaks increased with the reaction time. The reaction is finished after approx. 70 min. and no crystallization intermediates could be detected in the course of the reaction. Furthermore, it is worth to mention that the induction time has been considerably reduced with respect to the conventional hydrothermal synthesis: this process in takes more than 1 h until the onset of the product formation in the absence of stirring (cf. Figure 3.8). This is probably due to a combination of stirring and different heating conditions.

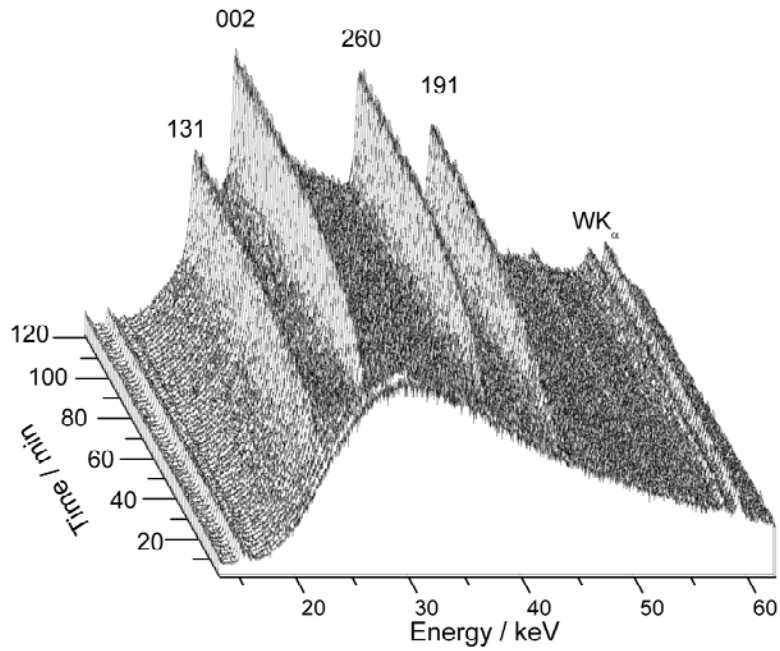

Fig. 3.11. Time-resolved EDXRD patterns measured during the hydrothermal crystallization of Bi_2WO_6 at 160 °C. The indices of the most intense lines of the product and the W K_α fluorescence lines are marked.

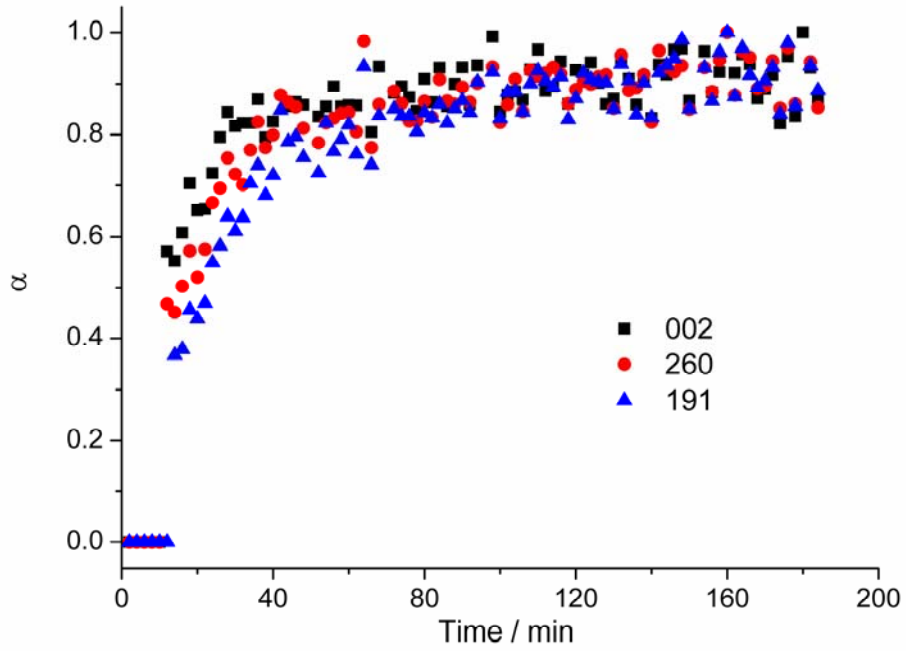

Figure 3.12. Extent of reaction α vs. time for the (002), (260) and (191) reflections of Bi_2WO_6 at 160 °C.

The extent of reaction α for the different main reflections ((002), (260) and (191)) of Bi_2WO_6 is plotted against the reaction time *t* in Figure 3.12. The sigmoidal curves are typical for a crystallization process including an initial induction period and a rapid crystallization, followed by the completion of crystal growth. Moreover, it is evident from Figure 3.12 that the crystal growth curves display the same basic shape, thereby confirming that no crystallographic growth direction is obviously favored. This is in line with previous reports on the isotropic growth process of the related *Aurivillius* type oxide Bi_2MoO_6.[28] Hence, the (260) reflections were selected for the following kinetic analysis.

The in situ EDXRD patterns monitoring the formation of Bi_2WO_6 at other reaction temperatures (150, 170 and 180 °C) are similar to the patterns recorded at 160 °C as shown in Figure 3.11. The product crystallizes directly from the amorphous precursor without the occurrence of any intermediate crystalline phases in the investigated temperature range (150 - 180 °C). Moreover, Figure 3.13 shows that a raise of the reaction temperature results in a remarkable reduction of both the induction time t_{ind} and the half-life time $t_{0.5}$ for the crystallization of the Bi_2WO_6 phase. For example, t_{ind} and $t_{0.5}$ decreased from 12 to 4 min. and from 28 to 12 min., respectively, when the temperature was raised from 150 to 180 °C (cf. Table 3.1). Nevertheless, the growth curves of Bi_2WO_6 exhibited little temperature-dependent variations, thereby indicating that the growth mechanism is independent of temperature in the given interval that is within the temperature windows of 120 - 180°C reported in section 3.3.2. The Sharp-Hancock plots of the kinetic data derived from the (260) reflection of Bi_2WO_6 are compared for different reaction temperatures in Figure 3.14. For the studied temperature range, linear graphs were obtained for $0.2 < \alpha < 0.85$, revealing a single reaction mechanism for the growth of Bi_2WO_6. The values of the Avrami exponent *m* were evaluated from the linear part of the curves for different temperatures and they are all close to 0.5 as shown in Table 3.1. This furthermore demonstrates that the reaction mechanism is not temperature-dependent. The low value for the exponent (~ 0.5) suggests that the crystallization mechanism of Bi_2WO_6 can be explained with a diffusion-controlled process under the given conditions.[30-33] For all other reaction mechanisms, the exponent *m* should be 1 or larger.[31] Until now, it has

been suggested in previous studies that diffusion-limited conditions are a prerequisite for the formation of 3D hierarchical Bi_2WO_6 nanostructures, but this hypothesis has never been backed with according data for this hydrothermal system.[24] Hence, our present in situ EDXRD results demonstrate that diffusion-controlled mechanisms may be a common denominator for the self-organization of nanosized building blocks into hierarchical structures among different hydrothermal systems, which are further demonstrated in chapter 8. The rate constant (k) values have not been added to Table 3.1 due to the following reasons: once the crystallization process of a diffusion-controlled reaction is started, the reaction rate is not significantly influenced by the nucleation rate any more, but it depends on the diffusion rates of the species in solution to the crystallization sites.[32, 33] Increasing the temperature should in principle increase the diffusion rates. On the other hand, the vigorous stirring during the reaction may exert a much higher influence on k than the investigated temperature range, thereby leading to opposite trends that are almost impossible to differentiate. In addition, the experimental errors of k are rather high and difficult to estimate precisely so that a disucssion of general trends is more appropriate.As mentioned in the experimental part, rapid stirring is important to conduct the present in situ experiments and it reduces the induction times for Bi_2WO_6 formation to several minutes in comparison with hour scale induction periods in the absence of stirring under conventional laboratory conditions. Obviously, the abovementioned rate-determining diffusion step can be significantly accelerated by an improved transport of the individual species to the nucleation sites through stirring. Therefore, the reaction constant k mainly depends on the stirring rate rather than on the inherent diffusion rate which also supported by preceding investigations.[32, 33]

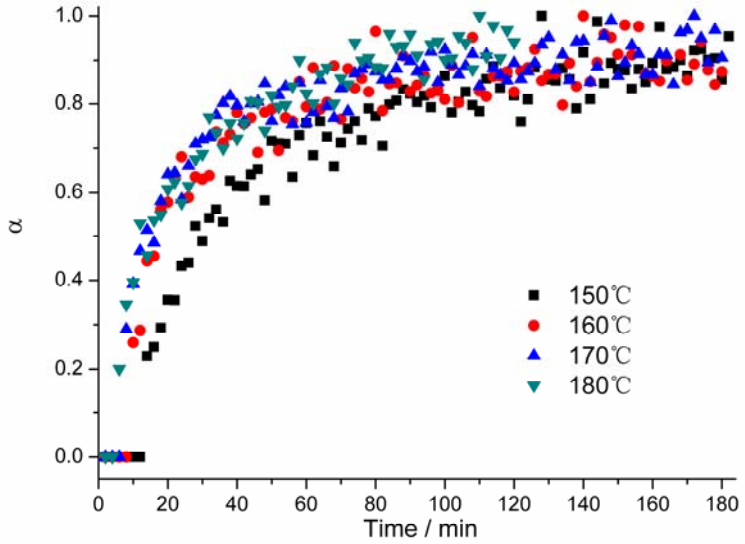

Figure 3.13. Extent of reaction α vs. time for the (260) reflection of Bi_2WO_6 recorded at different temperatures.

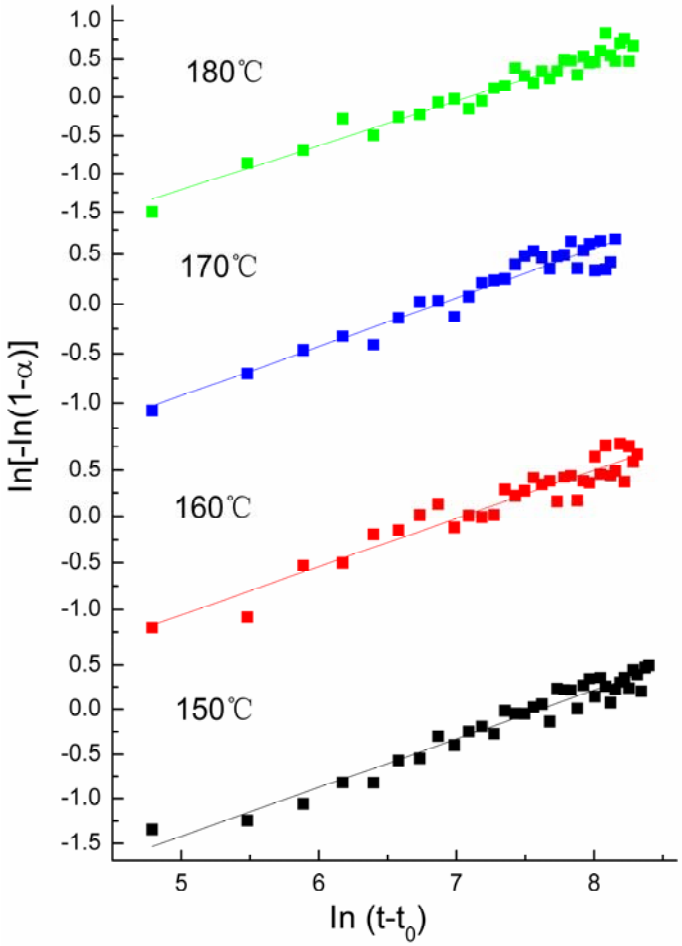

Figure 3.14. Sharp-Hancock plots for the data recorded at different temperatures over a data range of $0.2 < \alpha < 0.85$.

Table 3.1. Summary of the Avrami-Erofe'ev kinetic parameters for the crystallization of Bi_2WO_6 under different reaction conditions.

T/°C	pH	t_{ind} / min	$t_{0.5}$ / min	*m*
150	1.1	12	28	0.54 ± 0.02
160	1.1	8	16	0.52 ± 0.03
170	1.1	6	14	0.49 ± 0.03
180	1.1	4	12	0.57 ± 0.02
160	4.0	4	10	0.77 ± 0.06
160	4.6	4	7	*

*The reaction was too fast to generate sufficient data points for analysis

According to previous investigations, strongly acidic reaction conditions are an indispensable parameter for the formation of hierarchical Bi_2WO_6 microspheres,[22-24] because the 3D microspheres disintegrate into their individual nanoplate building blocks upon increasing pH values. A further pH raise to 10 even changes the phase of the obtained product (cf. Figure 3.5). Hence, it is very interesting and crucial to understand how the pH influences the reaction pathway and kinetics on the present hydrothermal system. The reaction temperature for the following in situ experiments was kept constant at 160 °C and the pH value of the precursor solution was adjusted through adding 8 M NaOH solution to the required values. Figure 3.16 displays the in situ EDXRD patterns for the formation of Bi_2WO_6 recorded at pH 4.0. The very fast crystallization kinetics and the very short half-life of crystallization $t_{0.5}$ (cf. Figure 3.15 and Table 3.1) illustrate that increasing the pH value of this hydrothermal system can significantly accelerate the Bi_2WO_6 formation process that most likely proceeds according to the following equation:[34]

$$2Bi^{3+} + WO_4^{2-} + 2H_2O \rightarrow Bi_2WO_6 \downarrow + 4H^+ \qquad (Eq.\ 3.1)$$

From the thermodynamic point of view, it is obvious that very low pH values, i.e. high H^+ concentrations, probably shift the equilibrium towards the precursors and thus restrain the formation of Bi_2WO_6.

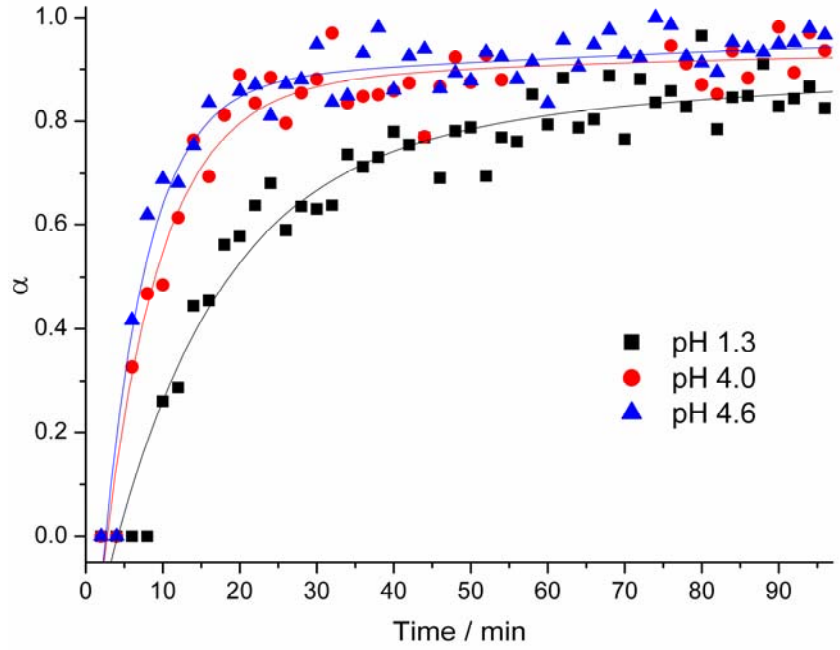

Figure 3.15. Extent of reaction α vs. time for the (260) reflection of Bi_2WO_6 recorded at different pH values.

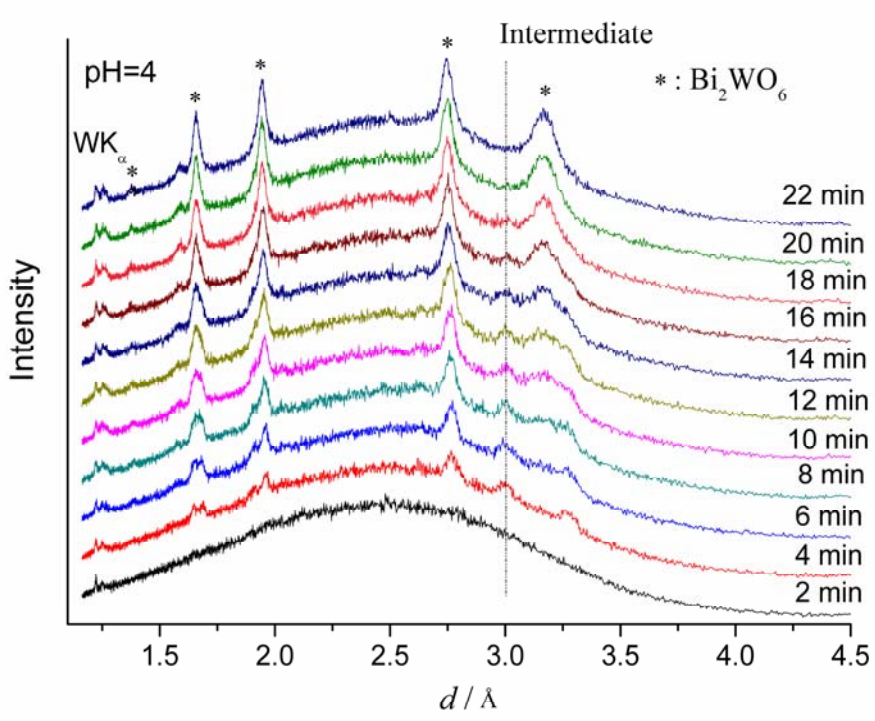

Figure 3.16. In situ EDXRD patterns for the formation of Bi_2WO_6 recorded at 160 °C for (a) pH 4.0 and (b) pH 4.6.

In addition, it is obvious from Figure 3.16 that an additional reflection at 3.0 Å occurred in the initial phase of the reaction after 4 min. and disapeared again after a run-time of around 22 min. Related phenomena can also be observed at pH 4.6. They probably point to the presence of a crystalline intermediate. The observation that this unknown intermediate phase could not be detected under strongly acidic conditions (pH 1.1, cf. Figure 3.11) underscores the significant effect of the pH on the course of the reaction. This is also evident from the kinetic analysis as summed up in Table 3.1. For the reaction at pH 4.6, the crystallization process is too fast to generate sufficient data for a detailed analysis, thereby demonstrating that increasing the pH value of this hydrothermal system can indeed accelerate the reaction kinetics. Moreover, when a pH value of 4.0 is reached, the Avrami exponent *m* increases to around 0.77: this suggests that the reaction mechanism is a function of the pH value of this hydrothermal system. Given that Avrami exponents around 1.0 were reported by *A. M. Beale* and *G. Sankar* for the hydrothermal formation of *Aurivillius* type Bi_2MoO_6 nanoplates,[28] the above mechanistic change probably causes the disintegration of hierarchical Bi_2WO_6 spheres into their plate-shaped building blocks at higher pH. These insights further support our hypothesis that diffusion-controlled processes (i.e. reaction exponents ~0.5) are essential for the fabrication of hierarchical nanostructures. Moreover, in chapter 8, we deomnstrate that the diffusion-limited conditions are also required for the formation of morphologically related hierarchical W/Mo-HTB oxides. This representative example demonstrates that adjusting the reaction kinetics on the basis of mechanistic insights is a powerful strategy to control the resulting morphology of hydrothermal products .

When the pH value was further increased to 11.0, the phase of the resulting product changed and cubic $Bi_{3.84}W_{0.16}O_{6.24}$ was obtained instead of orthorhombic Bi_2WO_6 as shown in Figure 3.17. Furthermore, no induction time was observed for the formation of $Bi_{3.84}W_{0.16}O_{6.24}$ so that this reaction is based on a rapid precipitation. The solubility of WO_4^{2-} is strongly pH-dependent:.[35] WO_4^{2-} has very high solubility in alkaline solution so that only limited amounts can contribute to the crystal growth process. Hence, the $Bi_{3.84}W_{0.16}O_{6.24}$ phase was obtained at pH 11.0. In section 3.3.2, we even reported the

formation of pure monoclinic Bi_2O_3 at pH 13.0.

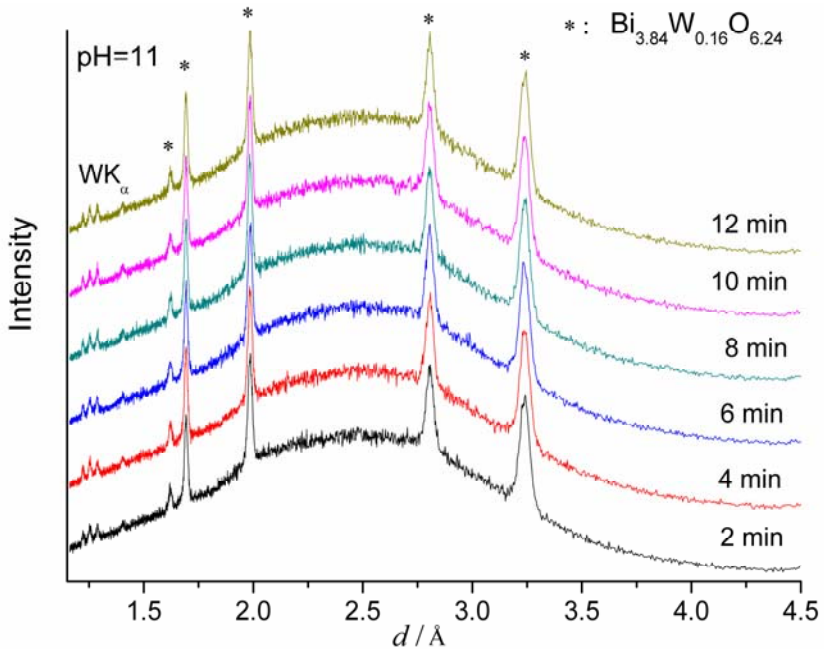

Figure 3.17. In situ EDXRD patterns for the formation of $Bi_{3.84}W_{0.16}O_{6.24}$ recorded at 160 °C and pH 11.0.

It is noteworthy that the morphology and phase of the products isolated after in situ experiments may be different from those obtained from the according laboratory experiments, e.g. due to different experimental setups and stirring conditions.[36] In order to prevent the discussion of relative artefacts, all solid products were collected after in situ EDXRD experiments and analyzed by ex situ XRD and SEM. Figure 3.18 shows the ex situ XRD patterns of the products synthesized at different pH values which agree well with the results obtained from in situ EDXRD patterns. The morphological evolution of the respective products is shown in Figure 3.19: hierarchical Bi_2WO_6 microspheres can be obtained at pH 1.1 (cf. Figure 3.19 a and b). At higher pH values (pH 4.6), the Bi_2WO_6 microspheres disintegrate into nanosheet building blocks (cf. Figure 3.19 c). When the pH value reaches 11.0, the orthorhombic Bi_2WO_6 product phase changes to cubic $Bi_{3.84}W_{0.16}O_{6.24}$. Moreover, the morphology is also significantly altered and regular particles with diameters below 100 nm are obtained as shown in Figure 3.19 d.

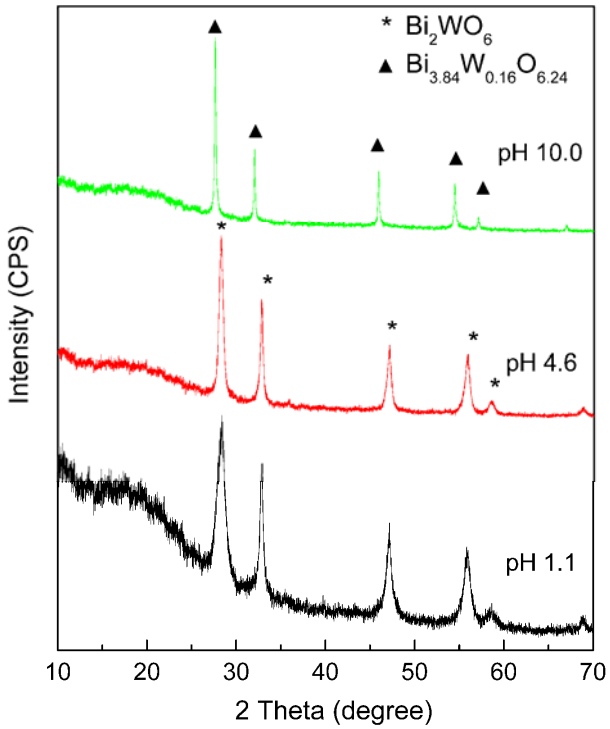

Figure 3.18. ex situ XRD patterns of the products synthesized at different pH values.

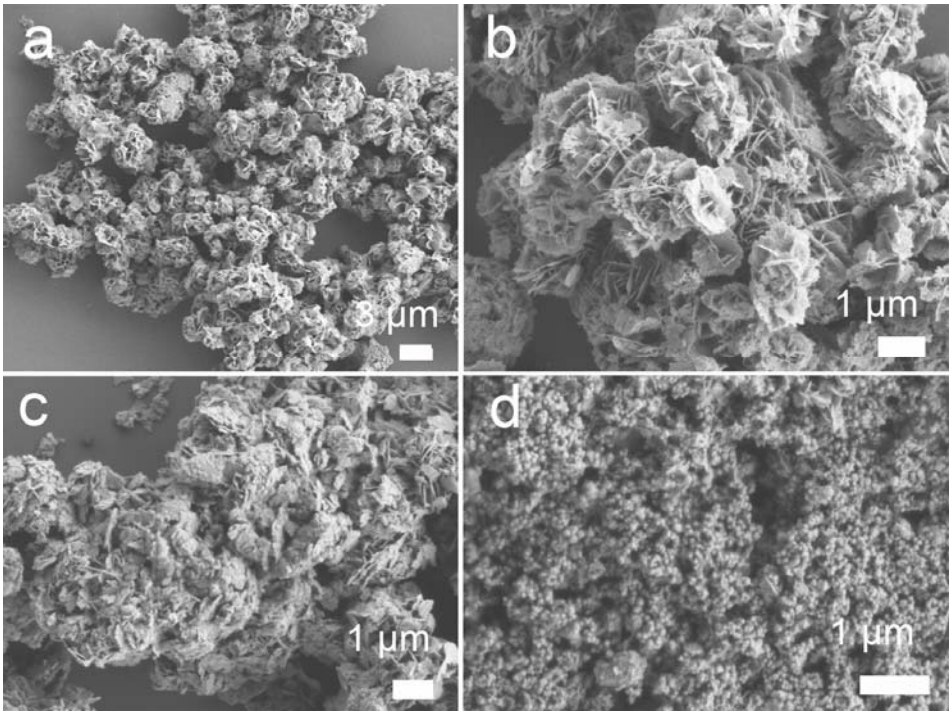

Figure 3.19. SEM images of the products synthesized at different pH values: (a) pH 1.1; (b) pH 1.1 with higher magnification; (c) pH 4.6; (d) pH 11. (The SEM image of the samples synthesized at pH 4 is similar to that obtained at pH 4.6; cf Fig. 3.19 c).

3.3.5 Optical properties and photocatalytic activity

The UV/Vis absorption spectra of the Bi_2WO_6 samples synthesized at different pH values in the absence of K_2SO_4 are summarized in Figure 3.20. The band gaps (E_g) of the Bi_2WO_6 samples obtained at pH 1.3, 3.7 and 7.3, were assigned as 3.04, 3.06 and 2.95 eV, respectively, according to the onset of the absorption edge and the obtained values are higher than the reported literature data (2.83 eV).[18] Furthermore, a red-shift of the absorption edge of the Bi_2WO_6 samples has been observed upon increasing the initial pH value of the hydrothermal system. Generally, the band gap energy of semiconductor nanoparticles increases with decreasing particle size. With increasing pH values, the emerging Bi_2WO_6 samples show less hierarchical nanostructuring and around pH 7.3, self-organization is completely absent (cf. Figure 3.6). Previous works have demonstrated that both particle size and hierarchical morphology of the sample considerably influence the band gap energies of nanoscale Bi_2WO_6 so that the overall value is a complex function of both factors.[20] Contrary to these preceding observations,[20] our samples display a blue shift with increasing internal nanostructuring. The band gap of 2.85 eV of the bismuth oxide sample obtained at pH 13.0 finally corresponds to the reported value for α-Bi_2O_3.[37] This is in line with the XRD patterns discussed above (cf. Figure 3.5).

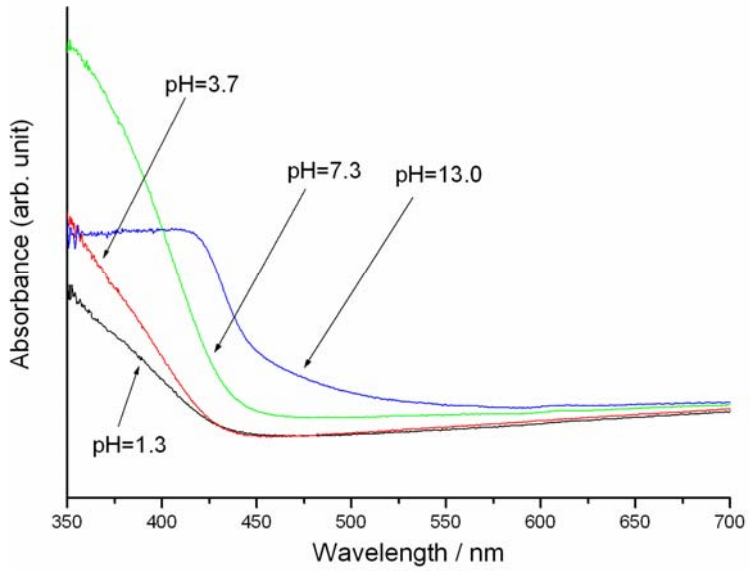

Figure 3.20. UV/Vis spectra of the products obtained at different pH values in the absence of K_2SO_4.

RhB is a widely used model dye to investigate the photocatalytic performance of inorganic materials, including Bi_2WO_6, in the decomposition of organic compounds. The strong absorption maximum of RhB at 554 nm was used to monitor its photocatalytic degradation while the reaction temperature was thermostated at 30 °C. The time-dependent evolution of the UV/Vis spectra during the photodegradation of RhB in the presence of hierarchical Bi_2WO_6 microspheres under visible light illumination (λ > 400 nm) is shown in Figure 3.21 and the expected rapid decrease of the RhB absorption at a wavelength of 554 nm is clearly observed. Figure 3.22 displays the photocatalytic efficiencies of Bi_2WO_6 microspheres compared to TiO_2 nanopowders (P-25) as a commercial standard under UV and visible light irradiation. c represents the concentration of RhB at the irradiation time t, whereas c_0 is the initial concentration at the absorption equilibrium on the photocatalysts prior to irradiation. Reference experiments show that the degradation of RhB is extremely low in the absence of a photocatalyst even under UV irradiation. The photodegradation efficiency of RhB is close to 100 % in the presence of commercial nanostructured anatase TiO_2 (P-25) under UV light irradiation after only 10 min. However, the efficiency of P-25 is quite low (about 29 %) under visible light irradiation even after 45 min due to the wide band gap (3.2 eV) of TiO_2.

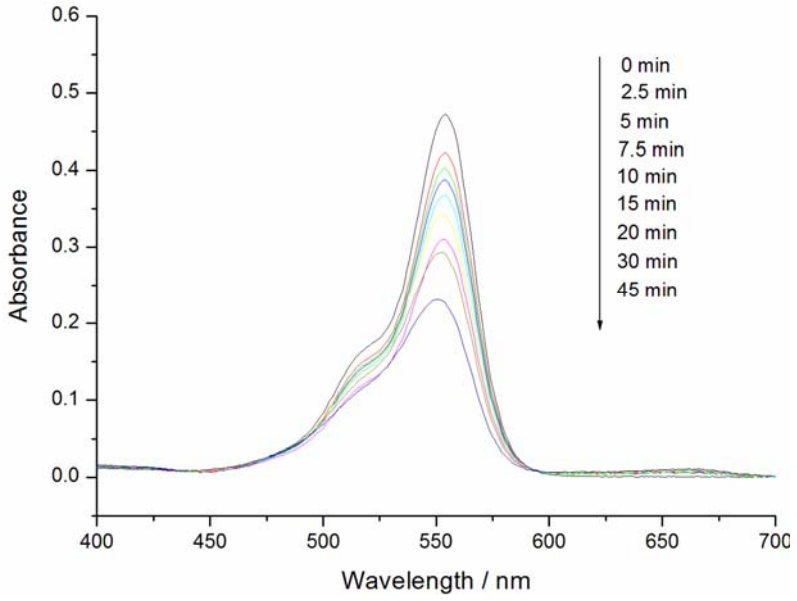

Figure 3.21. UV/Vis spectra of aqueous RhB solutions in the presence of hierarchical Bi_2WO_6 particles (catalyst: 50 mg, light source: Hg bulbs, max. intensity at 405 nm).

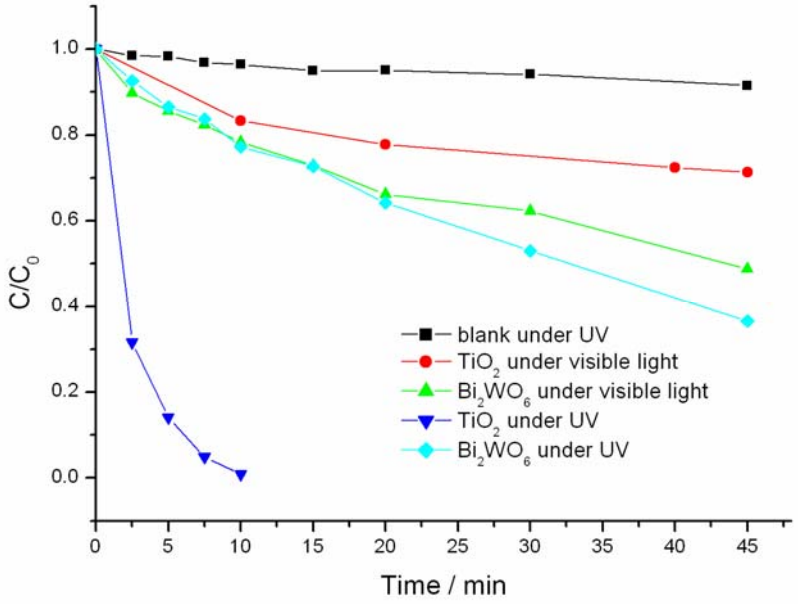

Figure 3.22. Degradation of RhB monitored at 554 nm as a function of the irradiation time (UV/Vis) in the presence of Bi_2WO_6 and TiO_2 standard (P-25).

3.4 Conclusion

In summary, we have established the most convenient one-step hydrothermal route to hierarchically nanostructured Bi_2WO_6 to date that is based on the direct reaction of $Bi(NO_3)_3{\cdot}5H_2O$ with K_2WO_4. As the development of straightforward and time/energy-saving procedures is essential for the technical production of nanomaterials, we have investigated the crucial parameter window for the formation of Bi_2WO_6 microsphere architectures: the reaction time (24 h) as well as the pH (optimal range of 1.3 – 2.5) turned out to exert the most significant influence on the phase and morphology of the hydrothermal products. Readily available inorganic additives are expected to play an important role as shape- and phase-controlling agents in these facile routes toward nanoparticles. We have demonstrated how our approach to Bi_2WO_6 can be morphologically altered through the use of K_2SO_4 as an additive. Starting from our pH dependent investigations, we furthermore discovered that the hydrothermal reaction of the precursor materials at elevated pH values in the presence of K_2SO_4 opens up new pathways to cubic $Bi_{3.84}W_{0.16}O_{6.24}$ and metastable cubic γ-Bi_2O_3.

Furthermore, we have directly monitored the hydrothermal crystallization of hierarchical Bi_2WO_6 nanostructures with in situ EDXRD methods. The crystallization data were modeled using Avrami-Erofe'ev theory and we found that the reaction under strongly acidic condition (pH 1.1) is diffusion controlled with Avrami exponents of ~ 0.5 in the investigated temperature range (150 - 180 °C). When the pH is raised to 4.0, the reaction kinetics were accelerated. Furthermore, the Avrami exponent *m* increases to approx. 0.77, thus indicating that the reaction mechanism of this hydrothermal system is pH-dependent. In line with the change of reaction mechanism, the hierarchical Bi_2WO_6 microspheres disintegrate into their individual nanosheet building blocks. Our results suggest that diffusion-controlled processes with exponents of ~ 0.5 are essential for the fabrication of hierarchical nanostructures. Finally,,cubic $Bi_{3.84}W_{0.16}O_{6.24}$ was obtained through a rapid precipitation at pH 11.0 instead of the orthorhombic Bi_2WO_6 phase due to the high solubility of WO_4^{2-} ions in alkaline solutions.

References

[1] D. B. Kuang, T. Brezesinski, B. Smarsly, *J. Am. Chem. Soc.* **2004**, *126*, 10534.

[2] D. H. M. Buchold, C. Feldmann, *Nano Lett.* **2007**, *7*, 3489.

[3] H. T. Shi, L. M. Qi, J. M. Ma, H. M. Cheng, *J. Am. Chem. Soc.* **2003**, *125*, 3450.

[4] F. F. Tao, M. Y. Guan, Y. M. Zhou, L. Zhang, Z. Xu, J. Chen, *Cryst. Growth Des.* **2008**, *8*, 2157.

[5] J. Ricote, L. Pardo, A. Castro, P. Millan, *J. Solid State Chem.* **2001**, *160*, 54.

[6] N. A. McDowell, K. S. Knight, P. Lightfoot, *Chem. Eur. J.* **2006**, *12*, 1493.

[7] Z. G. Yi, Y. X. Li, Z. Y. Wen, S. R. Wang, J. T. Zeng, Q. R. Yin, *Appl. Phys. Lett.* **2005**, *86*, 192906.

[8] M. Hamada, H. Tabata, T. Kawai, *Thin Solid Films* **1997**, *306*, 6.

[9] A. Kudo, S. Hijii, *Chem. Lett.* **1999**, *10*, 1103.

[10] J. W. Tang, Z. G. Zou, J. H. Ye, *Catal. Lett.* **2004**, *92*, 53.

[11] C. Zhang, Y. F. Zhu, *Chem. Mater.* **2005**, *17*, 3537.

[12] H. B. Fu, C. S. Pan, W. Q. Yao, Y. F. Zhu, *J. Phys. Chem. B* **2005**, *109*, 22432.

[13] H. B. Fu, L. W. Zhang, W. Q. Yao, Y. F. Zhu, *Appl. Catal. B* **2006**, *66*, 100.

[14] J. G. Yu, J. F. Xiong, B. Cheng, Y. Yu, J. B. Wang, *J. Solid State Chem.* **2005**, *178*, 1968.

[15] S. C. Zhang, C. Zhang, Y, Man, Y. F. Zhu, *J. Solid State Chem.* **2006**, *179*, 62.

[16] H. D. Xie, D. Z. Shen, X. Q. Wang, G. Q. Shen, *Mater. Chem. Phys.* **2007**, *103*, 334.

[17] M. Shang, W. Z. Wang, S. M. Sun, L. Zhou, L. Zhang, *J. Phys. Chem. C* **2008**, *112*, 10407.

[18] Y. Y. Li, J. P. Liu, X. T. Huang, G. Y. Li, *Cryst. Growth Des.* **2007**, *7*, 1350.

[19] J. Wu, F. Duan, Y. Zheng, Y. Xie, *J. Phys. Chem. C* **2007**, *111*, 12866.

[20] L. S. Zhang, W. Z. Wang, L. Zhou, H. L. Xu, *Small* **2007**, *3*, 1618.

[21] S. W. Liu, J. G. Yu, *J. Solid State Chem.* **2008**, *181*, 1048.

[22] L. S. Zhang, W. Z. Wag, Z. G. Chen, L. Zhou, H. L. Xu, W. Zhu, *J. Mater. Chem.* **2007**, *17*, 2526.

[23] F. Amano, K. Nogami, R. Abe, B. Ohtani, *Chem. Lett.* **2007**, *36*, 1314.

[24] F. Amano, K. Nogami, R. Abe, B. Ohtani, *J. Phys. Chem. C* **2008**, *112*, 9320.

[25] Z. J. Gu, Y. Ma, T. Y. Zhai, B. F. Gao, W. S. Yang, J. N. Yao, *Chem. Eur. J.* **2006**, *12*, 7717.

[26] Z. J. Gu, Y. Ma, W. S. Yang, G. J. Zhang, J. N. Yao, *Chem. Commun.* **2005**, 3597.

[27] X. Y. Chen, Z. J. Zhang, S. W. Lee, *J. Solid State Chem.* **2008**, *181*, 166.

[28] A. M. Beale, G. Sankar, *Chem. Mater.* **2003**, *15*, 146.

[29] Y. Zhou, K. Vuille, A. Heel, G. R. Patzke, *Z. Anorg. Allg. Chem.* **2009**, *635*, 1848.

[30] L. Engelke, M. Schaefer, M. Schur, W. Bensch, *Chem. Mater.* **2001**, *13*, 1383.

[31] S. F. Hulbert, *J. Br. Ceram. Soc.* **1969**, *6*, 11.

[32] R. J. Francis, S. O'Brien, A. M. Fogg, P. S. Halasyamani, D. O'Hare, T. Losieau, G. Férey, *J. Am. Chem. Soc.* **1999**, *121*, 1002.

[33] R. I. Walton, T. Loiseau, D. O'Hare, G. Férey, *Chem. Mater.* **1999**, *11*, 3201.

[34] D. Ma, S. Huang, W. Chen, S. Hu, F. Shi, K. Fan, *J. Phys. Chem. C* **2009**, *113*, 4369.

[35] S. Yao, J. Wei, B. Huang, S. Feng, X. Zhang, X. Qin, P. Wang, Z. Wang, Q. Zhang, X. Jing, J. Zhan, *J. Solid State Chem.* **2009**, *182*, 236.

[36] P. Norby, *Curr. Opin. Colloid In.* **2006**, *11*, 118.

[37] M. Chakrabarti, S. Dutta, S. Chattapadhyay, A. Sarkar, D. Santal, A. Chakrabarti, *Nanotechnology* **2004**, *15*, 1792.

4. Hydrothermal formation of hierarchical $Bi_2W_{0.75}Mo_{0.25}O_6$ nanostructures

4.1 Introduction

The development of new semiconductor photocatalysts shows that their activity is a complex function of a multitude of materials properties, including their band structure, crystal structure, crystallinity, particle size and surface area. Nevertheless, it is still extremely difficult to investigate the effect of a single factor on the photocatalytic activity while excluding other effects, because they are strongly correlated: changing one factor generally results in consequences for the remaining parameters. For example, annealing a given sample can improve the crystallinity, but on the other hand heat treatment can lead to a decrease of the surface area. Modifications of the hydrothermal reaction parameters can provide access to materials with different particle sizes and surface areas, but the morphologies and the exposed crystal planes of the materials, which play a key role in the catalytic activity, are changed as well. Therefore, it is highly challenging to correlate the overall photocatalytic activity to a selected parameter so that the optimization of photocatalysts remains a demanding task. An impressive example has recently been reported by *F. Amano* et al.[1] The photocatalytic activity of amorphous and crystalline Bi_2WO_6 materials with similar surface areas was compared and the results demonstrated that the activity of amorphous Bi_2WO_6 was negligible in comparison with crystalline Bi_2WO_6 due to the fast recombination of charge carriers. However, even in this study, the influence of the morphology can not be fully excluded, because the amorphous Bi_2WO_6 consists of nanoparticles, whilst crystalline Bi_2WO_6 grows as flakes composed of stacked rectangular platelets.

Generally, the *Aurivillius* type oxide Bi_2WO_6 is a very good model system to study these complex relationships. In chapter 3, we have investigated the optical properties and photocatalytic activities of hierarchical Bi_2WO_6 nanostructures. Although Bi_2WO_6 particles indeed exhibit activity under visible light irradiation, the band gap of Bi_2WO_6 nanostructures is 3.04 eV, which is still too wide for the visible light driven photocatalytic applications. One of the most elegant strategies to adjust the band structure and the resulting optical properties of the materials is to incorporate other elements in the structure to form solid solutions.[2-5]

Given that the coordination environments of W^{6+} and Mo^{6+} are closely related, a comparison of the optical properties and photocatalytic activities of Bi_2WO_6 and $Bi_2W_{1-x}Mo_xO_6$ solid solutions would be highly interesting. This calls for the synthesis of $Bi_2W_{1-x}Mo_xO_6$ materials with crystal structures, surface areas, particle sizes and morphologies that are similar to those of hierarchical Bi_2WO_6 nanostructures. In the course of a previous study, *A. Castro* et al. have reported on solid-state and mechanochemical activation methods to synthesize $Bi_2W_{1-x}Mo_xO_6$ solid solutions together with a structural study and the electrical characterization of $Bi_2W_{0.75}Mo_{0.25}O_6$.[6,7]

In the following, we present the first hydrothermal synthesis of $Bi_2W_{1-x}Mo_xO_6$ nanomaterials. The crystal structure of the obtained $Bi_2W_{1-x}Mo_xO_6$ was determined with Rietveld methods. Furthermore, the hydrothermal formation process of $Bi_2W_{1-x}Mo_xO_6$ was monitored with in situ XAS/EDXRD techniques. Finally, the optical properties and photocatalytic activities of Bi_2WO_6 and $Bi_2W_{1-x}Mo_xO_6$ are compared.

4.2 Experimental

4.2.1 Synthetic procedures

In a typical procedure, 97 mg (0.2 mmol) of $Bi(NO_3)_3 \cdot 5H_2O$, 25 mg (0.075 mmol) of K_2WO_4 and 5 mg (0.025 mmol) Na_2MoO_4 were placed into 10 mL of 20 vol.% acetic acid at room temperature and stirred magnetically for 20 min. to disperse all reagents homogeneously. The resulting precursor suspension was transferred into a Teflon-lined stainless steel autoclave with a capacity of 23 mL, maintained at 160 °C for 24 h, and subsequently cooled to room temperature. The precipitate was collected after filtration, washed with distilled water and dried in air.

4.2.2 Characterization

PXRD was conducted on a STOE STADI P diffractometer in transmission mode (flat sample holders, Ge monochromator, Cu $K_{\alpha 1}$ radiation) operated at 40 kV and 40 mA. Powder X-ray

data for structure refinement were collected between 5° and 110° (2θ) with a step size of 0.01° using the same diffractomater at room temperature. The structure was refined with Rietveld methods[8] using the program FULLPROF.[9] For SEM, performed on a Zeiss SUPRA 50VP microscope, samples were dispersed in ethanol and subsequently deposited on a silicon wafer. The specimen was investigated without conductive coating at rather low voltage (2 kV) to minimize charging effects. EDXS investigations were performed on the same microscope with an EDAX detector. TEM images were recorded on a field emission electron microscope (Tecnai F30, FEI, Supertwin lens), operated at 300 kV. BET surface area measurements were performed on a Quadrasorb SI in N_2-adsorption mode. The samples were degassed at 150 °C for 5 h in vacuum. The BET specific surface area was determined by a multipoint BET method using the adsorption data in the equilibrium relative pressure (P/P_0) range of 0.05-0.30. A desorption isotherm was used to determine the pore size distribution using the Barret-Joyner-Halenda (BJH) method.[10] Raman spectroscopy was performed on a Renishaw Ramascope 1000 with a green SpectraPhysics Argon laser with a wavelength of 524.5 nm and 50 mW capacity. Optical absorption spectra were recorded on a Cary 500 UV/Vis-NIR spectrophotometer.

4.2.3 In situ EDXRD measurements

In situ EDXRD experiments were performed at HASYLAB (Hamburg) bending magnet beamline F3, which provides an energy range from 13.31 to 62.54 keV with a maximum intensity at about 26 keV. The d-spacing range is given by $d = 6.199/(E \cdot \sin\theta)$. With a detector angle of approximately 4.9° the observable d-spacing range is 1.16 Å to 5.46 Å. The energy resolution $\Delta d/d$ is about 10^{-2} above 26 keV. The beam was collimated to 0.2 mm giving the best results. For the in situ experiments, autoclaves with glass liners of an internal diameter of 10 mm and a volume of 10 mL were used. A typical experiment was performed with 97 mg (0.2 mmol) $Bi(NO_3)_3 \cdot 5H_2O$, 25 mg (0.075 mmol) K_2WO_4, 5 mg (0.025 mmol) Na_2MoO_4 and 2 mL 20 vol.-% acetic acid as reactants. The in situ reactions were run at 160 °C. Data collection was started immediately after the introduction of the autoclave in the oven. The acquisition time for the in situ EDXRD data measured for the

given reactions was 120 s. After the in situ experiments, the solid products were collected by filtration, washed with distilled water and ethanol, and dried in air for further characterization. Note that due to sedimentation effects of the (Bi/W) containing products during the reaction, the in situ experiments have to be performed under rapid stirring.

4.2.4 In situ XAS measurements

In situ XAS experiments were performed at the superXAS beamline at the Swiss Light Source (SLS, Villigen, Switzerland). 30 mg $Bi(NO_3)_3 \cdot 5H_2O$, 6 mg Na_2MoO_4, and 6 mg K_2WO_4 were embedded between glass wool plugs to fix the solid phase and they were loaded together with 3mL 20 vol.-% acetic acid into a home-made spectroscopic cell as shown in Figure 1.3. The XAS scans around the Mo K edge were recorded between 19850 and 20240 eV under stationary conditions (liquid solution and solid phase) and were calibrated with a Mo reference foil. The following procedure was applied: Heating to 160 °C in 1.5 °C/min steps from RT to 50, 80, 120 and 160 °C. Pre-edge background substraction and normalization was carried out by fitting a linear polynomial to the pre-edge region and a cubic polynomial to the post-edge region of the absorption spectra using WinXAS 3.20.[11]

4.2.5 Photocatalytic activity experiments

Photocatalytic activities were evaluated through the degradation of methylene blue (MB) under visible light irradiation in a photoreactor equipped with 12 bulbs of blue light (Hg bulbs LCD M2-6S-01, max. intensity at 450 nm). The bulbs were arranged in a circular fashion around the reaction vessel that was thermostated at 30 °C with a circulating water pump. Prior to illumination, 50 mg of the photocatalyst powder were suspended in a MB solution (125 mL, 10^{-5} mol/L) through ultrasonication in the dark for 10 min. The MB degradation was determined by monitoring the decreasing intensity of the MB absorption maximum at 664 nm in a Varian Cary 50 Scan UV/Vis spectrometer.

4.3 Results and discussion

4.3.1 Formation of hierarchical $Bi_2W_{0.75}Mo_{0.25}O_6$ nanostructures

The hydrothermal treatment of $Bi(NO_3)_3 \cdot 5H_2O/K_2WO_4/Na_2MoO_4$ in acidic conditions at 160 °C for 24 h affords hierarchically nanostructured products with diameters of several micrometers consisting of nanosheet building blocks as shown in Figure 4.1. The products bear strong resemblance to the morphology of hierarchical Bi_2WO_6 microspheres (cf. Figure 3.1). EDXS analyses (cf. Figure 4.2) revealed that the products consist of Bi, W, Mo and O. The W/Mo molar ratio is around 3:1 and this corresponds to the initial molar ratio of the tungsten- and molybdenum-containing precursors.

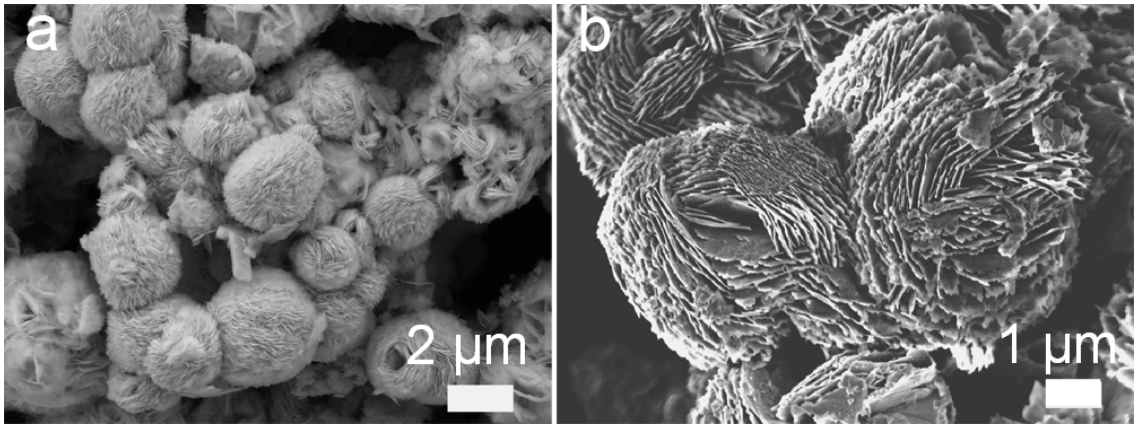

Figure 4.1. Representative SEM images of the products (a) recorded at lower magnification and (b) close-up view.

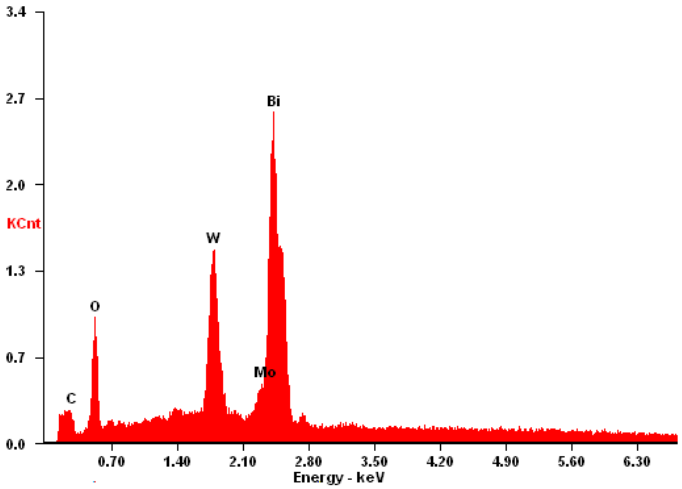

Figure 4.2. EDXS spectra of the hierarchically structured $Bi_2W_{0.75}Mo_{0.25}O_6$ microspheres.

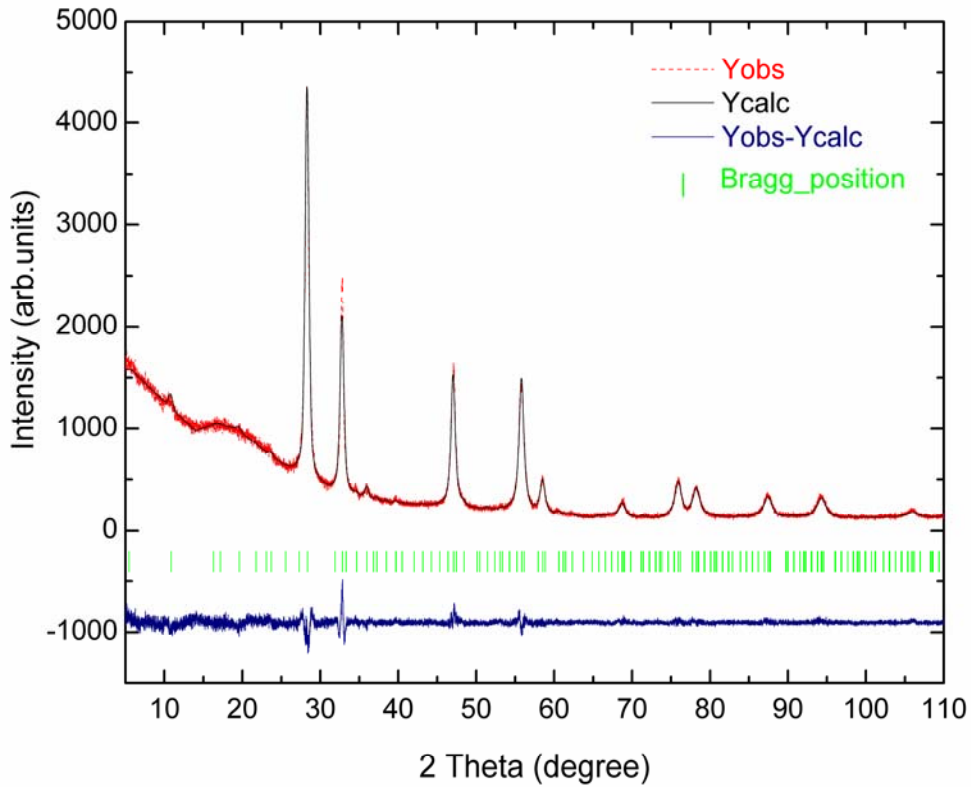

Figure 4.3. Rietveld refined powder XRD pattern of the products (dotted line: observed intensity data, solid line: calculated pattern, bottom line: difference between the observed and calculated intensities). The upper and lower vertical bars correspond to the Bragg positions of $Bi_2W_{0.75}Mo_{0.25}O_6$.[6]

The structure of the hydrothermal products was refined with Rietveld methods using the program Fullprof.[9] No regions were excluded in the refinement and a structural model for $Bi_2W_{0.75}Mo_{0.25}O_6$ (S.G. $Pca2_1$) was used.[6] Firstly, the scale factor and background parameters were refined, followed by the cell parameter, zero shift and FWHM parameters. A Thompson-Cox-Hastings (TCH) pseudo-Voigt peak shape function was used for peak fitting. No attempt was made to refine the W/Mo and O sites and the thermal displacement parameters so that they were left fixed. The good agreement of the experimental and Rietveld-refined powder XRD patterns (Figure 4.3) demonstrates that the nanostructured products can be identified as $Bi_2W_{0.75}Mo_{0.25}O_6$ (a = 5.458(1) Å, b = 16.377(2) Å, c = 5.461(1) Å, S. G. $Pca2_1$). The final atomic parameters, isotropic thermal displacement parameters and the reliability factors of the Rietveld refinement are shown in Table 4.1. The low R values further demonstrate the good agreement between experimental and calculated patterns. The structure

of the obtained hierarchical $Bi_2W_{0.75}Mo_{0.25}O_6$ particles can be described as an *Aurivillius* phase analogous to Bi_2WO_6 and Bi_2MoO_6, which is composed of $[(W/Mo)O_4]_n^{2-}$ sheets consisting of corner-sharing $(W/Mo)O_6$ octahedra alternating with $[Bi_2O_2]_n^{2+}$ slabs as shown in Figure 4.4. All in all, the obtained $Bi_2W_{0.75}Mo_{0.25}O_6$ materials basically display the *Aurivillius* structure of Bi_2WO_6 with 1/4 of the W positions in the Bi_2WO_6 structure substituted by Mo, which is also evident from the slightly changed unit cell parameters.

Table 4.1. Fractional atom coordinates and isotropic thermal displacement parameters ($Å^2$) of $Bi_2W_{0.75}Mo_{0.25}O_6$* (R_{wp} = 13.4 %, R_{exp} = 12.5 %, χ^2 = 1.15, R_F = 1.65 %, R_{Bragg} = 2.62 %).

Atom	**x**	**y**	**z**	***B***
Bi1	0.5232 (8)	0.420 (1)	0.965 (1)	0.27
Bi2	0.4900 (9)	0.078 (1)	0.975 (1)	0.27
W/Mo	0.009	0.249	0	0.05
O1	0.063	0.140	0.081	0.67
O2	0.260	0.999	0.270	0.31
O3	0.240	0.501	0.262	0.31
O4	0.704	0.232	0.257	0.45
O5	0.210	0.264	0.342	0.45
O6	0.554	0.359	0.571	0.67

* All atoms are located on the general 4a Wyckoff sites; the occupation factor for the mixed occupied W/Mo position is 0.75/0.25 (obtained from EDXS results).

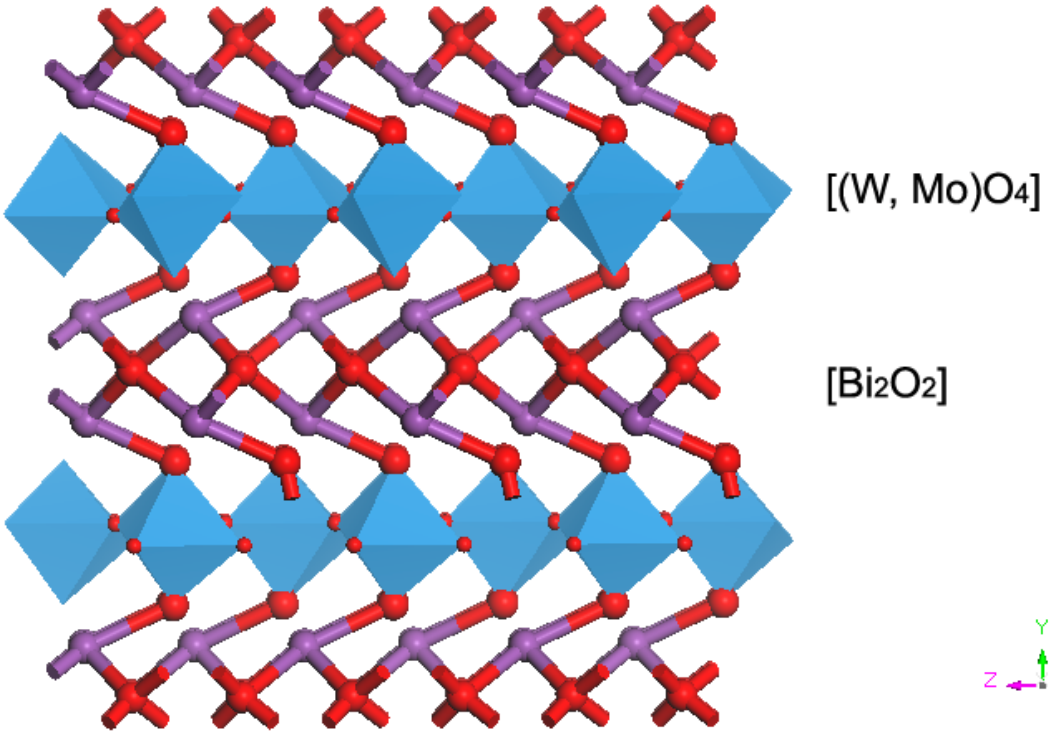

Figure 4.4. Crystal structure of $Bi_2W_{0.75}Mo_{0.25}O_6$ (Bi = violet, W/Mo = blue and O = red).

The Raman spectra of hierarchical Bi_2WO_6 and $Bi_2W_{0.75}Mo_{0.25}O_6$ nanostructures are compared in Figure 4.5. It has been reported that Bi_2WO_6 displays several peaks in the range of 600 - 1000 cm^{-1}, which can be assigned to the stretching vibrations of the W-O bonds.[12-15] The bands at 793 and 816 cm^{-1} are associated with antisymmetric and symmetric A_g modes of terminal W=O. The band at 720 cm^{-1} is interpreted as an antisymmetric bridging mode associated with the tungstate chain. The vibration at 306 cm^{-1} can be assigned to translational modes involving simultaneous motions of Bi^{3+} and WO_6^{6-}. Obviously, the substitution of W(VI) by Mo(VI) does not influence the crystal structure and the Raman spectra of $Bi_2W_{0.75}Mo_{0.25}O_6$ that are very close to the results for Bi_2WO_6, which is furthermore in line with the Rietveld refinement (cf. Figure 4.3). However, the W/Mo-O stretching vibrations for $Bi_2W_{0.75}Mo_{0.25}O_6$ are shifted to higher frequencies in comparison with those for Bi_2WO_6 at 793 and 816 cm^{-1}, indicating that the average W/Mo-O bond length in the $Bi_2W_{0.75}Mo_{0.25}O_6$ structure is slightly shorter than the W-O bond length in the isostructural Bi_2WO_6.[16] This is due to the different ionic radii of W^{6+} and Mo^{6+} ($r(W^{6+})$ = 0.060 Å and $r(Mo^{6+})$ = 0.059 Å for six-fold coordination).[17]

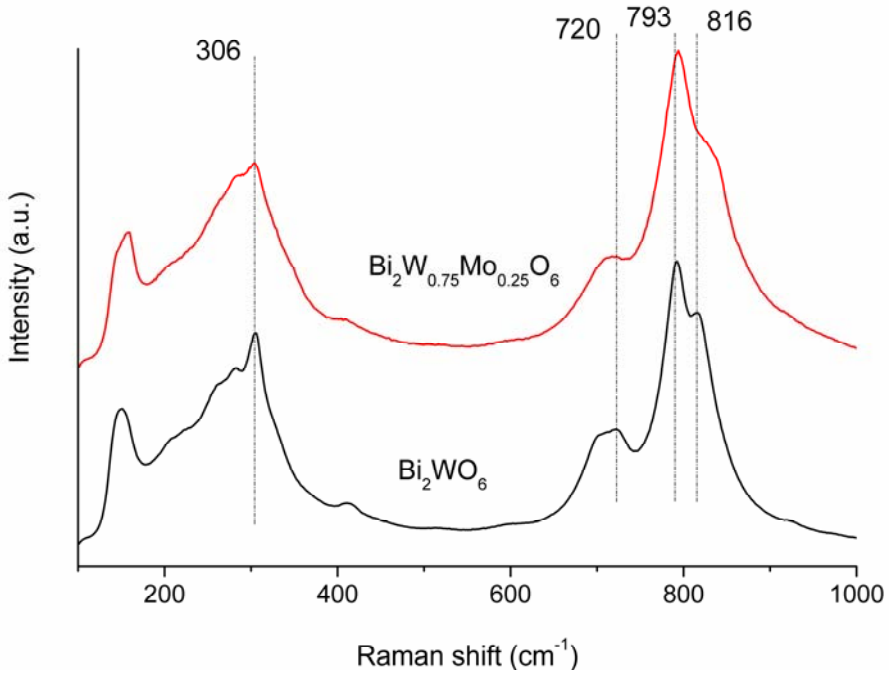

Figure 4.5. Raman spectra of Bi_2WO_6 and $Bi_2W_{0.75}Mo_{0.25}O_6$.

A more detailed insight into the microstructure of hierarchical $Bi_2W_{0.75}Mo_{0.25}O_6$ particles was obtained from TEM investigations. The individual plate-like building blocks can be clearly observed in the TEM images (cf. Figure 4.7 a). The corresponding SAED pattern is shown as an inset in Figure 4.7 a and the diffraction rings of the polycrystalline material can be indexed to orthorhombic $Bi_2W_{0.75}Mo_{0.25}O_6$ according to the unit cell obtained from Rietveld refinement (Figure 4.3). The HRTEM image of a plate-like particle (cf. Figure 4.7 b) exhibits clearly parallel crystal planes with interplanar distances of 0.316 and 0.274 nm, corresponding to the interplanar spacing of the (131), (002)/(060) planes of orthorhombic $Bi_2W_{0.75}Mo_{0.25}O_6$. This result also demonstrates the single crystalline character of the nanoplate building blocks. All in all, the TEM investigations confirm the aforementioned structure model obtained from Rietveld refinement (cf. Figure 4.4).

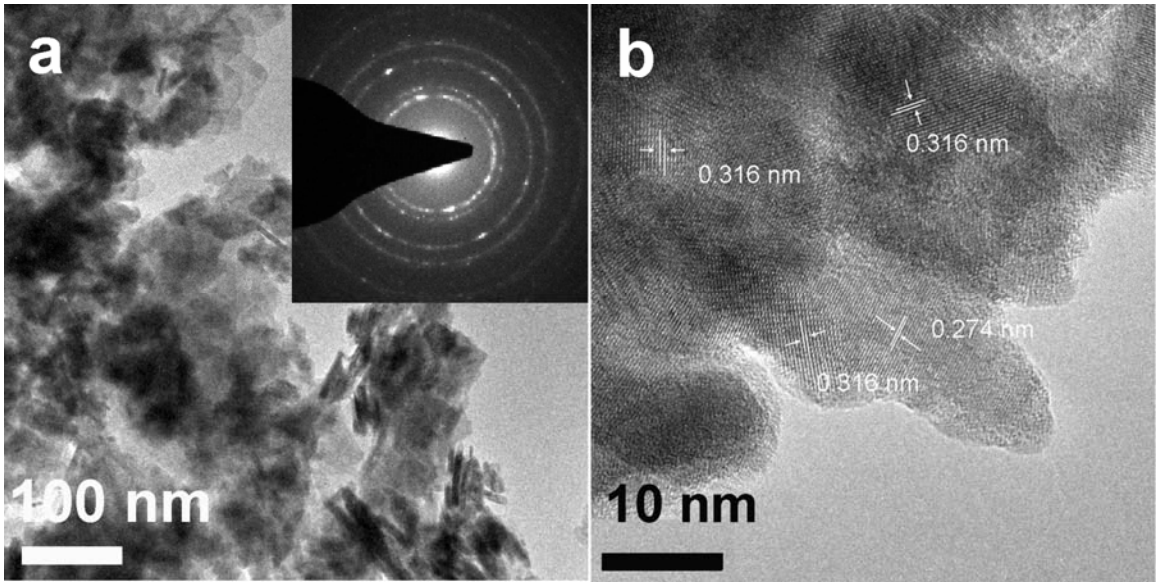

Figure 4.6. (a) Respesentative TEM of $Bi_2W_{0.75}Mo_{0.25}O_6$ (inset: corresponding SAED pattern); (b) HRTEM image of the $Bi_2W_{0.75}Mo_{0.25}O_6$ sample.

The nitrogen adsorption-desorption and internal pore size distribution isotherms of hierarchical Bi_2WO_6 and $Bi_2W_{0.75}Mo_{0.25}O_6$ nanostructures were further investigated and the results are shown in Figure 4.7. The BET surface areas of Bi_2WO_6 and $Bi_2W_{0.75}Mo_{0.25}O_6$ calculated from the linear part of the plots are 18.4 and 22.6 m^2/g, respectively. Moreover, it can be seen that both samples reveal a H3 type hysteresis loop which is frequently observed for aggregates of plate-like particles giving rise to slit-shaped pores.[10, 18] This is in line with the results from the SEM investigations as shown in Figure 4.1, because both hierarchical Bi_2WO_6 and $Bi_2W_{0.75}Mo_{0.25}O_6$ nanostructures are constructed from nanoplate building blocks. The corresponding pore size of the samples was determined with the Barret-Joyner-Halenda (BJH) method from desorption data. Both materials display a very narrow and similar pore size distribution as shown in the inset of Figure 4.6. The pore radius is around 2 nm which may correspond to the distance between neighboring nanoplate building blocks.[19]

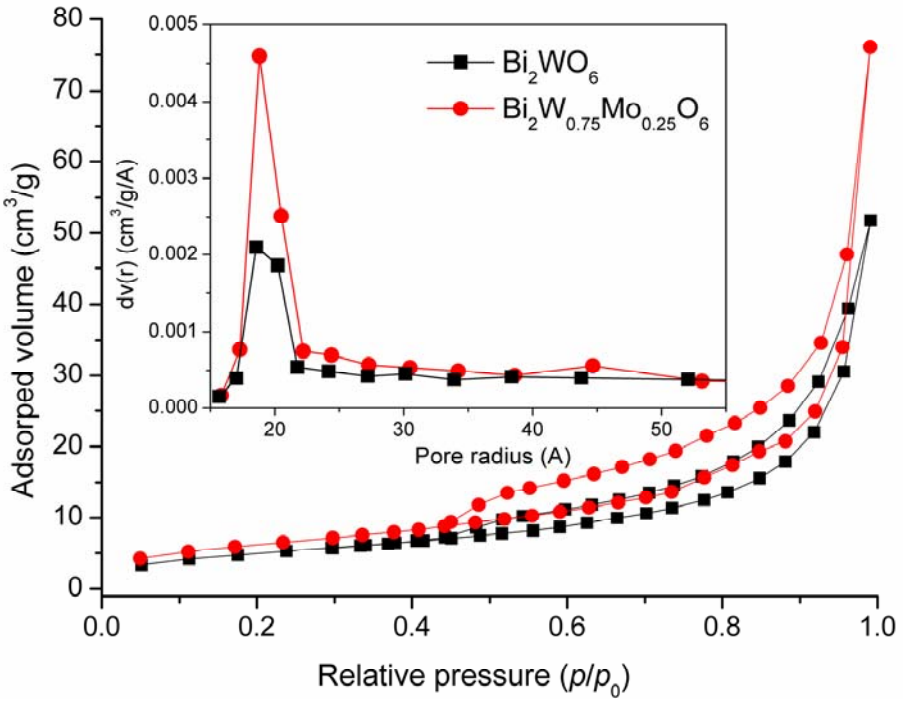

Figure 4.7. Nitrogen adsorption-desorption of Bi_2WO_6 and $Bi_2W_{0.75}Mo_{0.25}O_6$ (inset: pore-size distribution isotherm of Bi_2WO_6 and $Bi_2W_{0.75}Mo_{0.25}O_6$).

4.3.2 In situ XAS/EDXRD investigations

To understand the formation pathway of hierarchical $Bi_2W_{0.75}Mo_{0.25}O_6$ nanostructures, in situ XAS/EDXRD techniques were applied to monitor the hydrothermal process under real reaction conditions. XANES spectra at the Mo K edge were taken both at the middle of the cell (liquid part, Figure 4.8) and at the bottom of the cell (mainly solid part, Figure 4.9) during the reaction. It is observed that the Na_2MoO_4 precursor was already dissolved at 50 °C under acidic conditions. Furthermore, the concentration of Mo-containing species decreases with increasing temperature up to 80 °C, which points to the formation of solid products. Due to the strong absorption of Bi and W with respect to the X-ray source, high quality in situ XAS data for the solid part were extremely difficult to obtain. The in situ Mo K edge XAS during the hydrothermal reaction is shown in Figure 4.9 with respect to the Na_2MoO_4 precursor and for the $Bi_2W_{0.75}Mo_{0.25}O_6$ product. The results reveal that the coordination environment of Mo is completely different for the precursor and the hydrothermal product. The Mo K edge XAS

of Na_2MoO_4 exhibits very distinctive pre-edge features close to 19995 eV and a sharp absorption rise occurs at 20000 eV. This pre-edge feature is due to the forbidden transition from 1s to the 4d level, which can only be observed due to a mixing of d and p orbitals in the final state (e.g. in the case of tetrahedral symmetry). The strength of that feature depends on the amount of p character in the resulting state.[20,21] In comparison, the pre-edge intensity of the $Bi_2W_{0.75}Mo_{0.25}O_6$ product decreases sharply due to the transition from Mo in a tetrahedral environment to octahedrally coordinated Mo. Obviously, the addition of acetic acid and heating to higher temperatures promotes this conversion of tetrahedral to octahedral Mo coordination, which is in line with previous results.[22,23]

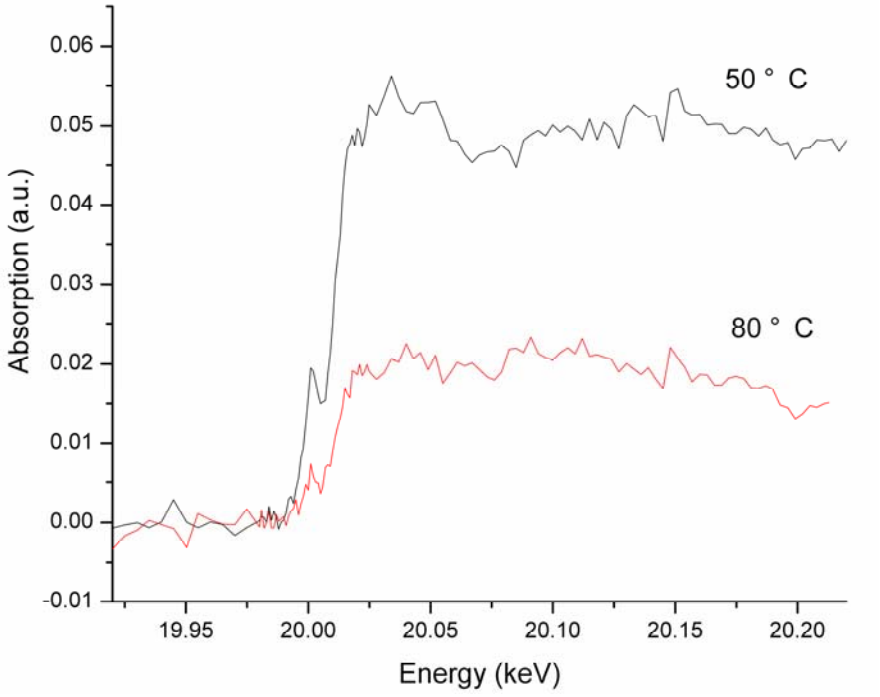

Figure 4.8. Mo K edge XAS during the hydrothermal conversion of $Bi(NO_3)_3{\cdot}5H_2O/K_2WO_4/Na_2MoO_4$ to $Bi_2W_{0.75}Mo_{0.25}O_6$ (liquid phase).

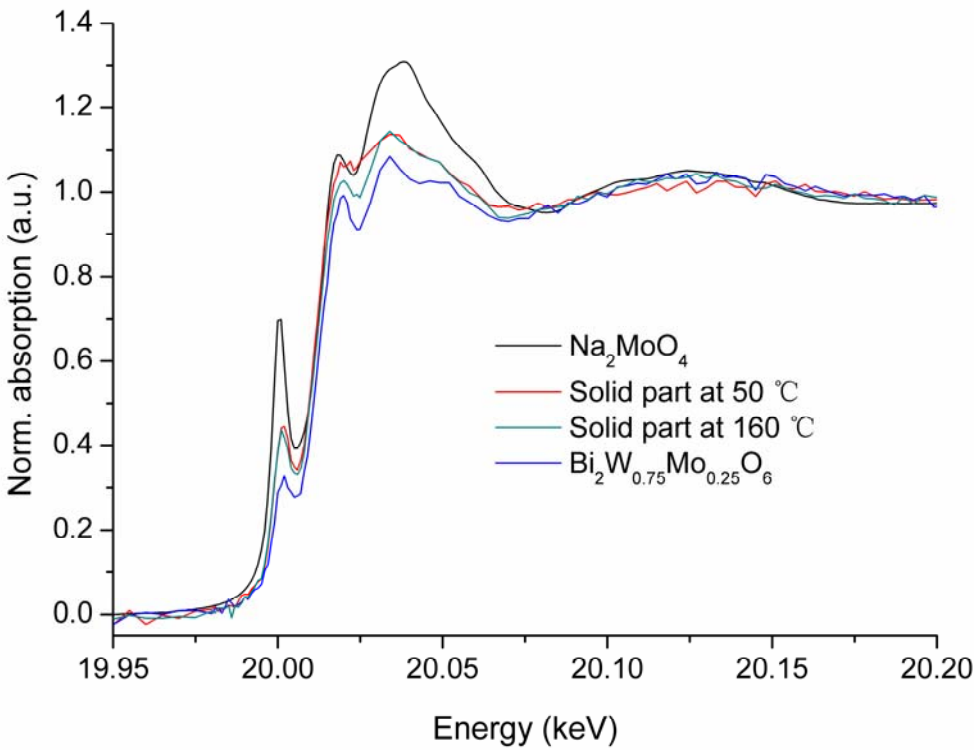

Figure 4.9. Mo K edge XAS during the hydrothermal reaction of $Bi(NO_3)_3{\cdot}5H_2O/K_2WO_4/Na_2MoO_4$ to $Bi_2W_{0.75}Mo_{0.25}O_6$ (solid phase) and Mo K edge XAS of the Na_2MoO_4 precursor and the $Bi_2W_{0.75}Mo_{0.25}O_6$ product as references.

In situ EDXRD techniques were further employed to investigate the hydrothermal crystallization of hierarchical $Bi_2W_{0.75}Mo_{0.25}O_6$ microspheres. A typical result of the time dependent evolution of the diffraction patterns is shown in Figure 4.10. The W and Mo resonances can be detected immediately from the beginning of the reaction. After a very short induction time, several diffraction peaks corresponding to the reflections of orthorhombic $Bi_2W_{0.75}Mo_{0.25}O_6$ appeared and the intensity of the diffraction peaks increased with the reaction time. No crystalline intermediates were observed in the course of this hydrothermal reaction. Figure 4.11 shows the extent of reaction α determined from the most intense reflections ((002), (260) and (191)) of $Bi_2W_{0.75}Mo_{0.25}O_6$ vs. the reaction time. All crystal growth curves basically have a similar shape in common so that no crystallographic growth direction is obviously favored. This is in line with our in situ study of the hydrothermal crystallization of Bi_2WO_6 (cf. chapter 3). Hence, further kinetic analysis was performed on the basis of the (260) reflection.

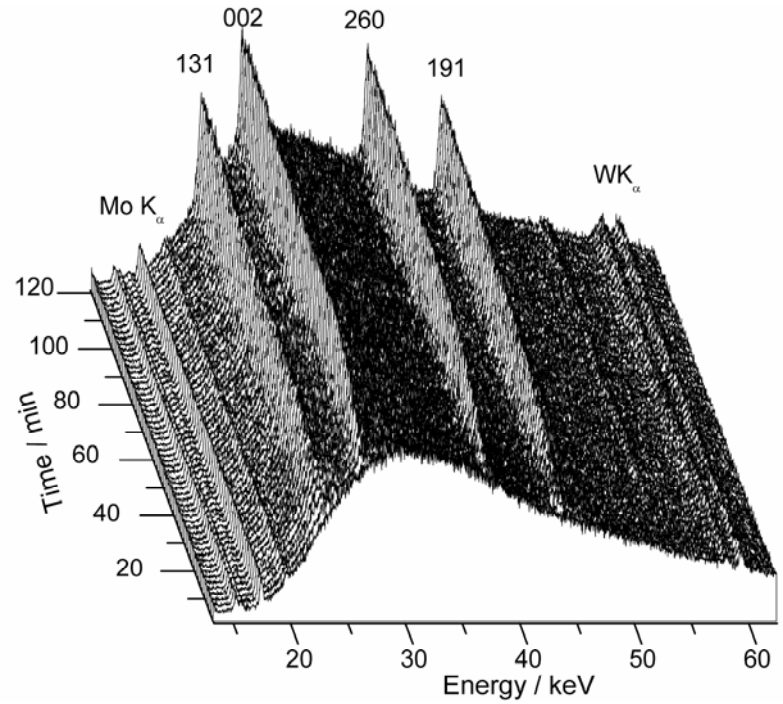

Figure 4.10. Time-resolved EDXRD patterns recorded during the hydrothermal crystallization of $Bi_2W_{0.75}Mo_{0.25}O_6$ at 160 °C. The indices of intense lines of the product phase as well as the Mo K_α and W K_α fluorescence lines are marked.

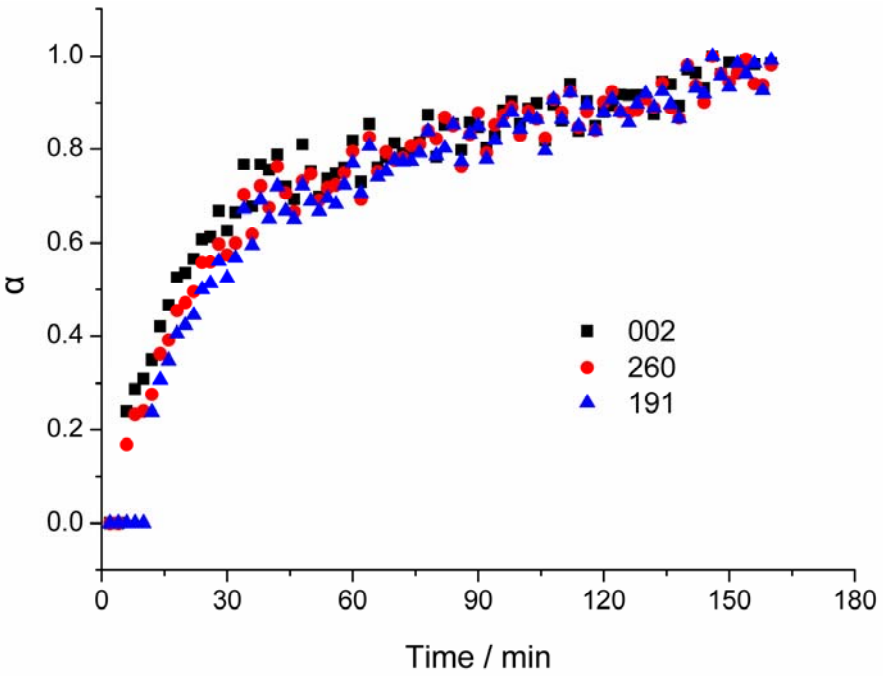

Figure 4.11. Extent of reaction α vs. time for the (002), (260) and (191) reflections of $Bi_2W_{0.75}Mo_{0.25}O_6$ at 160 °C.

Although Bi_2WO_6 and Bi_2MoO_6 have the same *Aurivillius* structure in common, it is extremely difficult to obtain hierarchical Bi_2MoO_6 nanostructures. Bi_2MoO_6 nanoplates, however, are well-known and easily accessed.[24-27] Given that the binary materials exhibit such fundamental morphological differences, it is highly interesting to compare the hydrothermal reaction kinetics of Bi_2WO_6, $Bi_2W_{0.75}Mo_{0.25}O_6$, and Bi_2MoO_6. The growth curves for the hydrothermal formation of Bi_2MoO_6 nanoplates, hierarchically structured Bi_2WO_6 and $Bi_2W_{0.75}Mo_{0.25}O_6$ nanostructures are compared in Figure 4.12. The formation of Bi_2MoO_6 nanoplates exhibits very fast reaction kinetics and the induction time t_{ind} and half-life times $t_{0.5}$ are only 2 and 4 min., respectively. Surprisingly, whereas t_{ind} of $Bi_2W_{0.75}Mo_{0.25}O_6$ is shorter, $t_{0.5}$ is longer in comparison with the formation of Bi_2WO_6 (cf. Figure 4.11 and Table 4.2). The fast formation kinetics of Bi_2MoO_6 may be the reason why the self-assembly of nanoplates into hierarchical nanostructures has not been observed. Similar results have been reported for the combination of the MoO_3 and tungsten bronze-based hydrothermal systems:[28] whereas the formation of MoO_3 fibers proceeds via a very fast reaction within several minutes in a quick dissolution-precipitation sequence, the nucleation-controlled growth of M_xWO_3 (M = Li to Cs) takes between 2 h and 5 h to completion, depending on the cation involved. Generally, the substitution of W with Mo speeds up the kinetics of these hydrothermal systems.

A more detailed analysis of the kinetic data can be performed on the basis of Sharp-Hancock plots as shown in Figure 4.13: the kinetic data were derived from monitoring the (260) reflections of Bi_2WO_6 and $Bi_2W_{0.75}Mo_{0.25}O_6$, respectively. The velocity of the hydrothermal formation of Bi_2MoO_6 is too fast to afford sufficient data for further kinetic evaluations which is analogous to the rapid hydrothermal formation of MoO_3 rods.[29] It is obvious from Figure 4.13 that both graphs are linear for $0.2 < \alpha < 0.85$ and thus point to a single reaction mechanism for the growth of Bi_2WO_6 and $Bi_2W_{0.75}Mo_{0.25}O_6$, respectively. As we discussed in chapter 3, hierarchical Bi_2WO_6 nanostructures are formed via a diffusion-controlled reaction mechanism with an Avrami exponent *m* close to 0.5, because *m* should be 1 or larger for all other reaction mechanisms.[30, 31] The Avrami exponent *m* for the formation of $Bi_2W_{0.75}Mo_{0.25}O_6$ increases to 0.65. Given that *m* values around 1.0 were reported for the

hydrothermal formation of Bi_2MoO_6 nanoplates,[21] the formation of $Bi_2W_{0.75}Mo_{0.25}O_6$ exhibits an intermediate reaction mechanism. Figure 4.14 demonstrates that $Bi_2W_{0.75}Mo_{0.25}O_6$ samples isolated after the brief in situ EDXRD investigation times already bear considerable resemblance to the fully developed materials after 24 h of hydrothermal treatment (cf. Figure 4.1). We have demonstrated in chapter 3 that diffusion-controlled processes might be essential for the formation of hierarchical nanostructures. An increase of the Avrami exponent *m* from 0.5 to 1 causes the disintegration of Bi_2WO_6 spheres into their platelet-shaped building blocks. In the present study, the Avrami exponent for the formation of $Bi_2W_{0.75}Mo_{0.25}O_6$ is around 0.65 and this is far below 1.0, so that the formation of hierarchical nanostructures is still supported. On the other hand, one should keep in mind that the hydrothermal reaction mechanism in its entire complexity can not be fully explained on the basis of reaction kinetics alone. All in all, the comparison of the reaction kinetics of the different oxide systems demonstrates that the fast reaction kinetics of Bi_2MoO_6 could be clearly set apart from those of Bi_2WO_6 and $Bi_2W_{0.75}Mo_{0.25}O_6$ and this is well in line with the different morphological characteristics of bismuth molybdate.

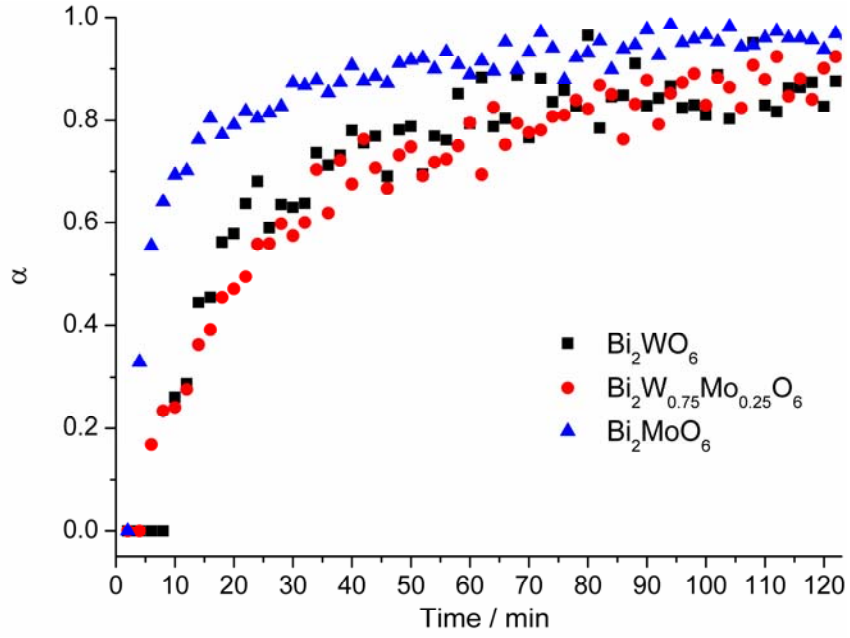

Figure 4.12. Extent of reaction α vs. time for the growth of Bi_2MoO_6, Bi_2WO_6 and $Bi_2W_{0.75}Mo_{0.25}O_6$ at 160 °C.

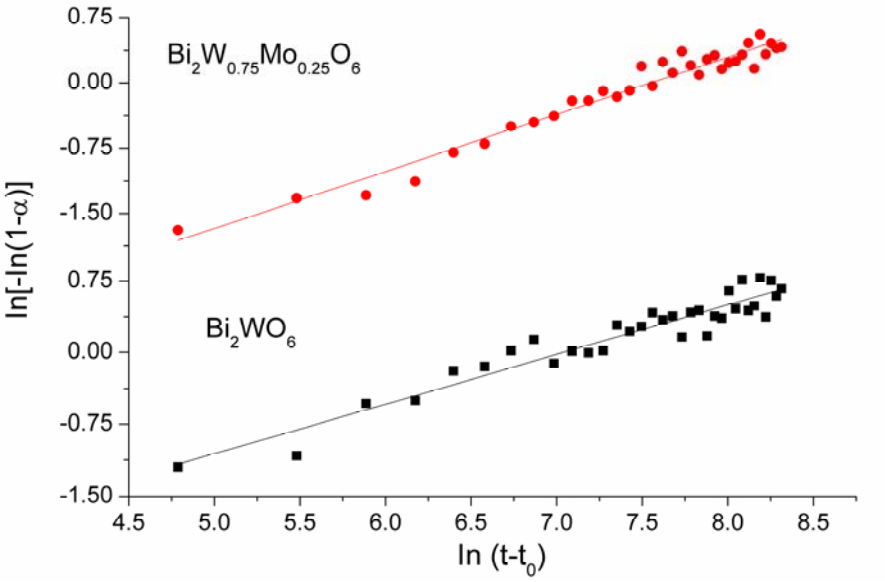

Figure 4.13. Sharp-Hancock plots derived from the kinetic data of Bi_2WO_6 and $Bi_2W_{0.75}Mo_{0.25}O_6$ recorded at 160 °C over a data range of $0.2 < \alpha < 0.85$.

Table 4.2. Survey of kinetic data for different oxide systems.

Sample	t_{ind} / min	$t_{0.5}$ / min	*m*
Bi_2MoO_6	2	4	*
Bi_2WO_6	8	16	0.52 ± 0.03
$Bi_2W_{0.75}Mo_{0.25}O_6$	4	22	0.65 ± 0.02

* The reaction was too fast to generate sufficient data points for analysis

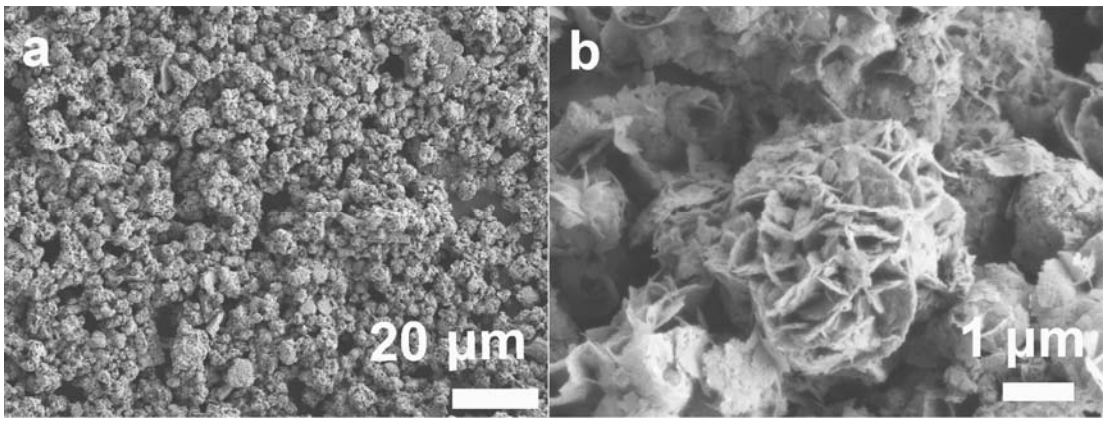

Figure 4.14. Representative SEM images of the products after in situ EDXRD experiments (a) survey at low magnification, (b) close-up view of an individual particle.

4.3.3 Optical properties and photocatalytic activity

The UV/vis spectra of Bi_2WO_6 and $Bi_2W_{0.75}Mo_{0.25}O_6$ are compared in Figure 4.15. The band gaps of nanostructured Bi_2WO_6 and $Bi_2W_{0.75}Mo_{0.25}O_6$ were determined as 3.04 eV and 2.87 eV, respectively. This is in line with the different color of the samples: Bi_2WO_6 is light green and $Bi_2W_{0.75}Mo_{0.25}O_6$ is yellow. As the morphology and BET surface area of the Bi_2WO_6 and $Bi_2W_{0.75}Mo_{0.25}O_6$ samples are very similar, it is reasonable to assign the different band gaps to the differences in the electronic structures.

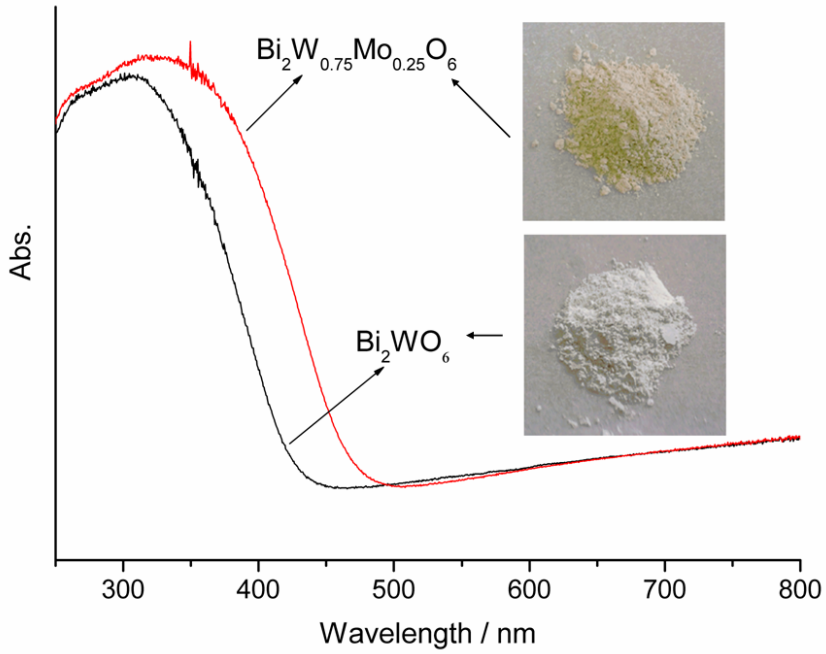

Figure 4.15. UV/vis spectra of nanostructured Bi_2WO_6 and $Bi_2W_{0.75}Mo_{0.25}O_6$.

To understand the effect of Mo in the crystal structure on the optical properties, the band structure and density of states (DOS) of Bi_2WO_6 and $Bi_2W_{0.75}Mo_{0.25}O_6$ were calculated based on density functional theory (DFT) methods using the VASP code.[32, 33] $Bi_2W_{0.75}Mo_{0.25}O_6$ was modeled by substituting one W atom in a supercell containing 36 atoms with one Mo atom as shown in Figure 4.16. The influence of the Mo atom position in the structure on the total energy of the system was studied by replacing different W atoms. The results revealed that the total energy remains more or less unchanged irrespective of the

particular replacement of W with Mo. The crystal geometries of both Bi_2WO_6 and $Bi_2W_{0.75}Mo_{0.25}O_6$ were fully optimized to an energy minimum. Table 4.3 shows the calculated and experimental lattice parameters of Bi_2WO_6 and $Bi_2W_{0.75}Mo_{0.25}O_6$. The calculated results are in line with the results from Rietveld refinements (cf. Figure 4.3): after incorporating Mo in the structure, the *a*- and *c*-axes increased only slightly, whereas the *b*-axis significantly decreased. Furthermore, the optimized lattice parameters were in close agreement with the experimental values.

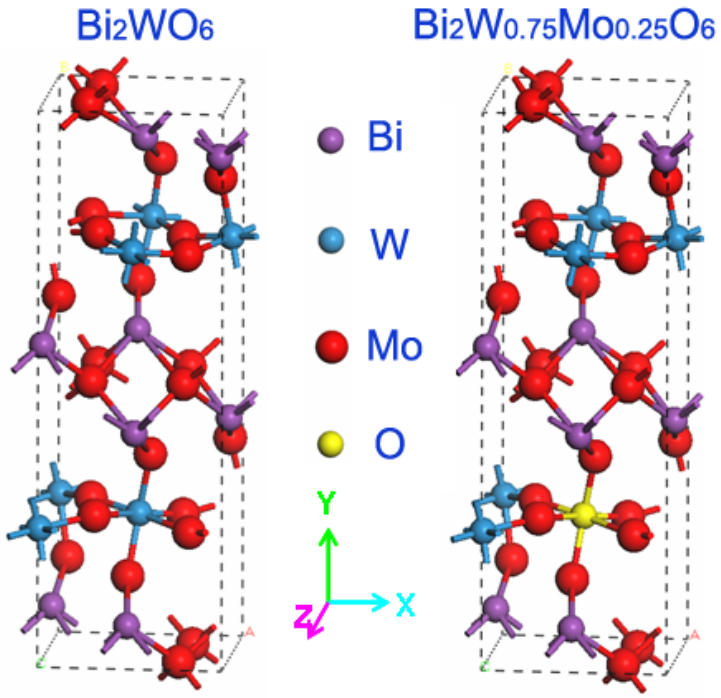

Figure 4.16. Structural models of Bi_2WO_6 and $Bi_2W_{0.75}Mo_{0.25}O_6$ used for DFT calculations.

Table 4.3. Calculated and experimental lattice parameters of Bi_2WO_6 and $Bi_2W_{0.75}Mo_{0.25}O_6$.

Lattice parameters	***a* / Å**	***b* / Å**	***c* / Å**
Bi_2WO_6 (experimental)[34]	5.4373(2)	16.4302(5)	5.4584(2)
$Bi_2W_{0.75}Mo_{0.25}O_6$ (experimental)	5.458(1)	16.377 (2)	5.461(1)
Bi_2WO_6 (calculated)	5.4384	16.4131	5.4243
$Bi_2W_{0.75}Mo_{0.25}O_6$ (calculated)	5.4464	16.3705	5.4317

The calculated band structure of Bi_2WO_6 and $Bi_2W_{0.75}Mo_{0.25}O_6$ (cf. Figure 4.17) show a

minimum band gap located at the *Γ*-point, which indicates that both Bi_2WO_6 and $Bi_2W_{0.75}Mo_{0.25}O_6$ are direct band gap materials. The band gaps from DFT calculations were 1.85 eV and 1.71 eV for Bi_2WO_6 and $Bi_2W_{0.75}Mo_{0.25}O_6$, respectively, thereby lower than the experimental values of 3.04 eV and 2.87 eV. However, electronic structures calculated with DFT methods frequently afford bad gap values that are too low in comparison with the experimental results.[35-37] Nevertheless, both the experimental and calculated trends demonstrate that $Bi_2W_{0.75}Mo_{0.25}O_6$ exhibits a smaller band gap than Bi_2WO_6. To investigate the origin of the electronic structure modification of $Bi_2W_{0.75}Mo_{0.25}O_6$, the DOS plots of both materials are compared in Figure 4.18. The top of the valence band mainly consists of O 2p orbitals that remain unchanged for both Bi_2WO_6 and $Bi_2W_{0.75}Mo_{0.25}O_6$, while the respective bottoms of the conduction band are different. The conduction band of Bi_2WO_6 is mainly derived from W 5d orbitals, whereas the conduction band of $Bi_2W_{0.75}Mo_{0.25}O_6$ is composed of hybrid orbitals of Mo 4d and W 5d so that it is wider. Therefore, the band gap of $Bi_2W_{0.75}Mo_{0.25}O_6$ is reduced by 0.14 eV with respect to Bi_2WO_6. Our results clearly revealed that the the electronic structure of Bi_2WO_6 can be modified through the formation of $Bi_2W_{0.75}Mo_{0.25}O_6$ solid solutions as an useful strategy to enhance the visible light absorption performance.

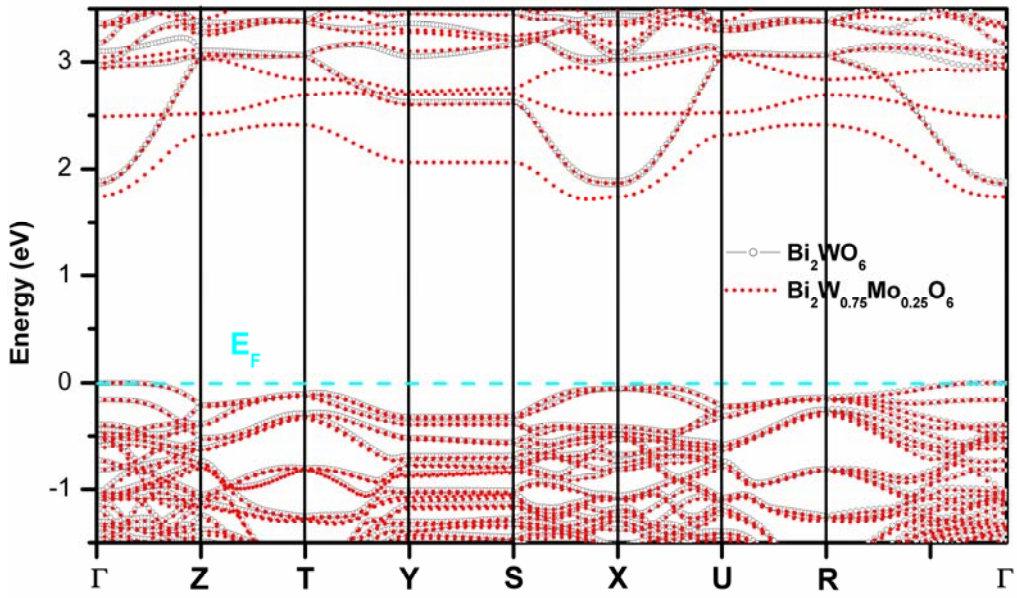

Figure 4.17. Comparison of the calculated band structure (DFT methods) for Bi_2WO_6 and $Bi_2W_{0.75}Mo_{0.25}O_6$.

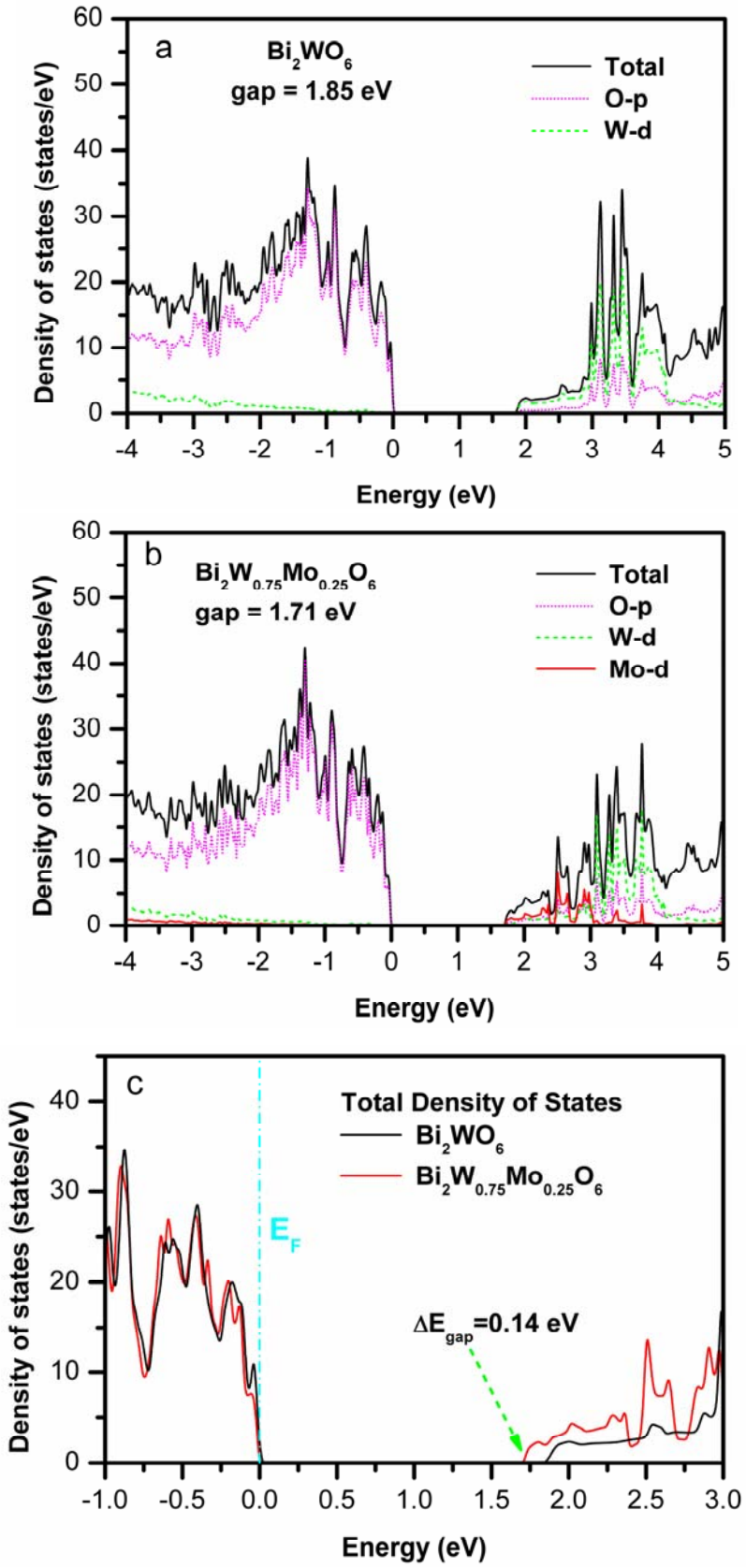

Figure 4.18. DOS of (a) Bi_2WO_6 and (b) $Bi_2W_{0.75}Mo_{0.25}O_6$, (c) DOS comparison for Bi_2WO_6 and $Bi_2W_{0.75}Mo_{0.25}O_6$.

The photocatalytic degradation of MB was compared for hierarchical Bi_2WO_6 and $Bi_2W_{0.75}Mo_{0.25}O_6$ nanostructures through monitoring the intensity of the characteristic MB absorption peak at 664 nm as shown in Figure 4.19. The photolysis of MB under visible light irradiation in the absence of a catalyst is negligible. In the presence of Bi_2WO_6 particles, the degradation of MB is only around 9 % over a period of 45 min. Interestingly, $Bi_2W_{0.75}Mo_{0.25}O_6$ exhibited a threefold higher photocatalytic activity under visible light irradiation in comparison with Bi_2WO_6. The enhanced photocatalytic activity of $Bi_2W_{0.75}Mo_{0.25}O_6$ can be attributed to the narrow band gap that facilitates visible light absorption. Given that the structure, morphology, BET surface size and pore size distribution of Bi_2WO_6 and $Bi_2W_{0.75}Mo_{0.25}O_6$ are quite similar, we can correlate this increase in the photocatalytic activity to the differences of electronic structures.

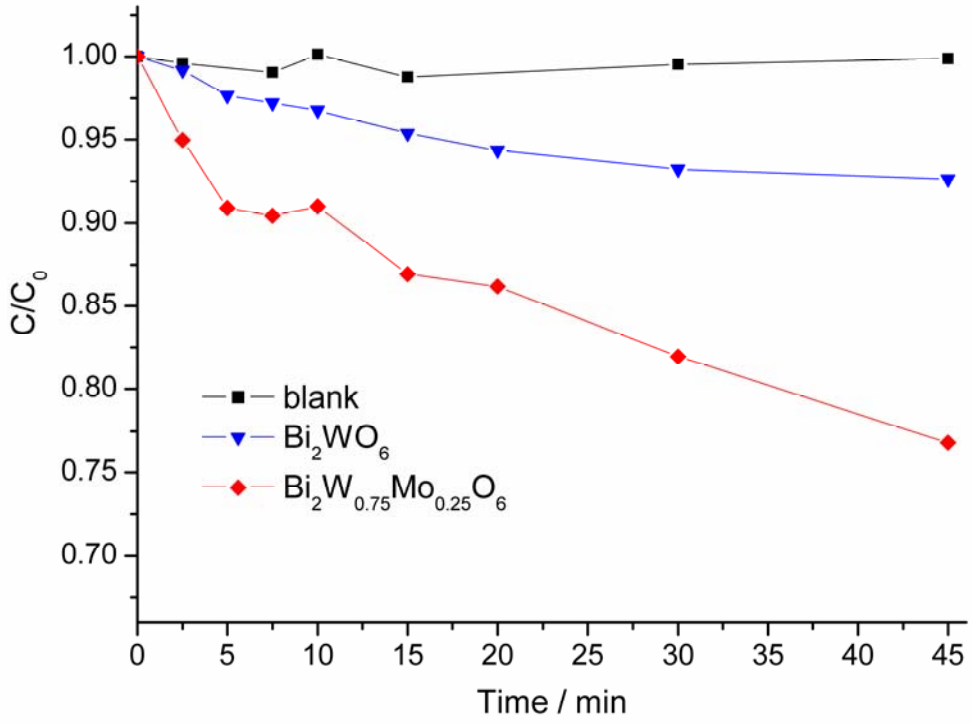

Figure 4.19. Degradation of MB in the absence and presence of different photocatalysts under visible light irradiation (catalyst: 50 mg; lamp: Hg bulbs, max. intensity at 450 nm).

4.4 Conclusions

We have established a new hydrothermal protocol for the synthesis of hierarchical $Bi_2W_{0.75}Mo_{0.25}O_6$ nanostructures. The Rietveld refinement results demonstrated that the substitution of tungsten by molybdenum in Bi_2WO_6 leads to $Bi_2W_{0.75}Mo_{0.25}O_6$ solid solutions that maintain the structural framework of the *Aurivillius* type. Furthermore, the morphology, BET surface area and particle size distribution of hierarchical $Bi_2W_{0.75}Mo_{0.25}O_6$ architectures are quite similar to Bi_2WO_6. This permits the correlation of the photocatalytic activity with the changes in the electronic structure. The band gap of $Bi_2W_{0.75}Mo_{0.25}O_6$ particles is 2.87 eV, which is smaller than that of Bi_2WO_6 (3.04 eV). Therefore, the formation of $Bi_2W_{0.75}Mo_{0.25}O_6$ solid solutions enhances the visible light absorption properties through modifications of the electronic structure. This results in a three-fold higher photocatalytic activity of $Bi_2W_{0.75}Mo_{0.25}O_6$ in comparison to Bi_2WO_6. Moreover, the hydrothermal crystallization mechanism of hierarchical $Bi_2W_{0.75}Mo_{0.25}O_6$ nanostructures was studied with combined in situ XAS/EDXRD methods. The addition of molybdenum containing precursors to the Bi-based hydrothermal systems significantly accelerates the reaction kinetics so that no hierarchical nanostructures of Bi_2MoO_6 are formed in the absence of tungsten. The Avrami exponent for the formation of $Bi_2W_{0.75}Mo_{0.25}O_6$ is thus increased to 0.65, which is slightly higher than that for the analogous reaction with Bi_2WO_6 (~ 0.5), but the overall diffusion controlled reaction mechanism remains basically the same.

References

[1] F. Amano, A. Yamakata, K. Nogami, M. Osawa, B. Ohtani, *J. Am. Chem. Soc.* **2008**, *130*, 17650.

[2] W. Yao, J. Ye, *Chem. Phys. Lett.* **2008**, *450*, 370.

[3] H. Liu, J. Yuan, W. Shangguan, Y. Teraoka, *J. Phys. Chem. C* **2008**, *112*, 8521.

[4] Z. Zou, J. Ye, K. Sayama, H. Arakawa, *Nature* **2001**, *414*, 625.

[5] M. Tian, W. Shangguan, J. Yang, L. Jiang, M. Chen, J. Shi, Z. Ouyang, S. Wang, *Appl. Catal. A* **2006**, *309*, 76.

[6] A. Castro, P. Begue, B. Jimenez, J. Ricote, R. Jimenez, J. Galy, *Chem. Mater.* **2003**, *15*, 3395.

[7] R. Jimenez, A. Castro, B. Jimenez, *Appl. Phys. Lett.* **2003**, *83*, 3350.

[8] H. M. Rietveld, *J. Appl. Crystallogr.* **1969**, *2*, 65.

[9] J. Rodriguez-Carvajal, *Physica B* **1993**, *192*, 55.

[10] K. S. W. Sing, D. H. Everett, R. A. W. Haul, L. Moscou, R. A. Pierotti, J. Rouquerol, T. Siemieniewska, *Pure Appl. Chem.* **1985**, *57*, 603.

[11] T. Ressler, *J. Synchrotron Radiat.* **1998**, *5*, 118.

[12] Y. Li, J. Liu, X. Huang, J. Yu, *Dalton Trans.* **2010**, *39*, 3420.

[13] L. Zhang, Y. Wang, H. Cheng, W. Yao, Y. Zhu, *Adv. Mater.* **2009**, *21*, 1286.

[14] R. Shi, G. Huang, J. Lin, Y. Zhu, *J. Phys. Chem. C* **2009**, *113*, 19633.

[15] M. Crane, R. Frost, P. Williams, T. Kloprogge, *J. Raman Spectrosc.* **2002**, *33*, 62.

[16] J. Yu, A. Kudo, *Adv. Funct. Mater.* **2006**, *16*, 2163.

[17] R. D. Shannon, *Acta Cryst. A* **1976**, *32*, 751.

[18] J. Yu, H. Yu, B. Cheng, C. Trapalis, *J. Mol. Catal. A* **2006**, *249*, 135.

[19] Y. Li, J. Liu, X. Huang, G. Li, *Cryst. Growth Des.* **2007**, *7*, 1350.

[20] A. M. Beale, G. Sankar, *Nucl. Instrum. Methods Phys. Res. B* **2003**, *199*, 504.

[21] A. M. Beale, G. Sankar, *Chem. Mater.* **2003**, *15*, 146.

[22] C. Kongmark, V. Martis, A. Rubbens, C. Pirovano, A. Löfberg, G. Sankar, E. Bordes-Richard, R. Vannier, W. v. Beek, *Chem. Commun.* **2009**, 4850.

[23] C. Kongmark, V. Martis, C. Pirovano, A. Löfberg, W. v. Beek, G. Sankar, A. Rubbens, S. Cristol, R.-N. Vannier, E. Bordes-Richard, *Catal. Today* **2010**, doi:10.1016/ j.cattod.2010.02.071.

[24] L. Xie, J. Ma, G. Xu, *Mater. Chem. Phys.* **2008**, *110*, 197.

[25] X. Zhao, T. Xu, W. Yao, Y. Zhu, *Appl. Surf. Sci.* **2009**, *255*, 8036.

[26] H. Xie, D. Shen, X. Wang, G. Shen, *Mater. Chem. Phys.* **2008**, *110*, 332.

[27] Y. Zheng, F. Duan, J. Wu, L. Liu, M. Chen, Y. Xie, *J. Mol. Catal. A* **2009**, *303*, 9.

[28] R. Kiebach, N. Pienack, W. Bensch, J.-D. Grunwaldt, A. Michailovski, A. Baiker, T. Fox, Y. Zhou, G. R. Patzke, *Chem. Mater.* **2008**, *20*, 3022.

[29] A. Michailovski, J.-D. Grunwaldt, A. Baiker, R. Kiebach, W. Bensch, G. R. Patzke, *Angew. Chem. Int. Ed.* **2005**, *44*, 5643.

[30] S. F. Hulbert, *J. Br. Ceram. Soc.* **1969**, *6*, 11.

[31] R. J. Francis, S. O'Brien, A. M. Fogg, P. S. Halasyamani, D. O'Hare, T. Losieau, G. Férey, *J. Am. Chem. Soc.* **1999**, *121*, 1002.

[32] G. Kresse, J. Furthmüller, *Comput. Mater. Sci.* **1996,** *6*, 15.

[33] G. Kresse, J. Furthmüller, *Phys. Rev. B* **1996**, *54*, 11169.

[34] K. S. Knight, *Mineral. Mag.* **1992**, *56*, 399.

[35] R. Shi, G. Huang, J. Lin, Y. Zhu, *J. Phys. Chem. C* **2009**, *113*, 19633.

[36] M. Long, W. Cai, H. Kisch, *Chem. Phys. Lett.* **2008**, *461*, 102.

[37] Y. Shimodaira, H. Kato, H. Kobayashi, A. Kudo, *J. Phys. Chem. B* **2006**, *110*, 17790.

5. Photocatalytically active bismuth oxide composites through coating approaches

5.1 Introduction

Up to now, TiO_2 nanoparticles are still among the most powerful photocatalytic materials currently on the market (e.g. P25 standard), but they suffer from two main practical drawbacks: in the fist place, the band gap of 3.2 eV limits the light absorption features of TiO_2 to the UV region. Secondly, the small size of the catalytic TiO_2 nanoparticles renders them extremely difficult to remove and recollect through filtration after the photocatalytic process has been finished. Recently, coupling TiO_2 with other metal oxides has attracted considerable attention as an elegant approach for improving the photocatalytic properties of TiO_2.[1-3] For this purpose, hierarchical Bi_2WO_6 microspheres are an ideal substrate to support TiO_2 nanoparticles, because hierarchical Bi_2WO_6 nanostructures can not only provide high surface areas to deposit nanoparticles but they also offer absorption features in the visible light region (cf. Figures 3.1 and 3.20). Bi-based oxides can be coupled with TiO_2 to construct heterojunction interfaces between the semiconductors with matching band potentials. This can extend the lifetime of the photon-induced electron-hole pairs.[4] Furthermore, anatase TiO_2 with a less dense structure than rutile displays convenient features for hole transport processes, whilst n-type semiconductors are suitable for electron transport – this opens up interesting combinations for heterojunction systems.[5] *Y. Bessekhouad* et al., for example, have prepared n-type Bi_2O_3/TiO_2 heterojunctions with enhanced visible light driven photocatalytic activity by directly mixing two semiconductors.[6] Nevertheless, this method only afforded a random mixture of Bi_2O_3 and TiO_2. The preparation of genuinely heterostructured materials is still a considerable challenge due to the structural complexity and difficulties in coordinating the crystal growth of two different materials.

After the synthesis and photocatalytic activity of hierarchically structured Bi_2WO_6 has been discussed in the previous chapters, we report in the following on two novel and simple processes for the coating of hierarchical Bi_2WO_6 microspheres with anatase TiO_2 nanoparticles. The obtained hierarchically structured Bi_2WO_6/TiO_2 nanocomposites exhibit significantly improved visible-light-driven photocatalytic activity in comparison with isolated

Bi_2WO_6 microspheres and TiO_2 nanoparticles. Furthermore, our current route offers general synthetic options: the oxide substrates can be varied to access other heterostructured materials, such as $BiVO_4/TiO_2$ or Bi_2MoO_6/TiO_2.

5.2 Experimental

5.2.1 Two-step coating method

For the coating of hierarchical Bi_2WO_6 particles with anatase TiO_2 nanopartices, 62 mg TiF_4 and 50 mg as-synthesized Bi_2WO_6 powder (cf. chapter 3) were added to 50 mL H_2O in a 100 mL glass beaker. The glass beaker was then sealed with a glass cover and the suspension was stirred magnetically at 60 °C for 7 h (step 1). The products were washed, collected and dried in air. The resulting powders were calcined in air at different temperatures for 7 h (step 2).

5.2.2 One-step hydrothermal coating approach

For the one-step hydrothermal coating procedure, 25 mg as-synthesized Bi_2WO_6 microspheres and 31 mg TiF_4 with 10 mL H_2O were put into a Teflon-lined stainless steel autoclave, maintained at 90 °C for 24 h, and subsequently cooled to room temperature. The precipitate was washed with distilled water and dried in air.

5.2.3 Analytical characterization

PXRD was conducted on a STOE STADI P diffractometer in transmission mode (flat sample holders, Ge monochromator, Cu $K_{\alpha 1}$ radiation) operated at 40 kV and 40 mA. Powder X-ray data for structure refinement were collected between 5° and 105° (2θ) with a step size of 0.01° using the same diffractomator at room temperature. The structure was refined with Rietveld methods[7] with the program FULLPROF[8] using the corresponding bulk crystal structures as starting points for refinement. For SEM, performed on a Zeiss SUPRA 50VP microscope, samples were dispersed in ethanol and subsequently deposited on a silicon wafer. The specimen was investigated without conductive coating at rather low voltage (2 kV) to

minimize charging effects. TEM images were recorded on a field emission electron microscope (Tecnai F30, FEI, Supertwin lens), operated at 300 kV. The BET surface area measurements were performed on a Quadrasorb SI in N_2-adsorption mode. The samples were degassed at 150 °C for 5 h in vacuum. Raman spectroscopy was performed on a Renishaw Ramascope 1000 with a green SpectraPhysics Argon laser with a wavelength of 524.5 nm and 50 mW capacity. Optical absorption spectra were recorded on a Cary 500 UV/Vis-NIR spectrophotometer.

5.2.4 Photocatalytic activity evaluation

Photocatalytic activities were evaluated through the degradation of MB under visible-light irradiation in a photoreactor equipped with 12 bulbs of blue light (Hg bulbs LCD M2-6S-01, max. intensity at 450 nm). The bulbs were arranged in a circular fashion around the reaction vessel that was thermostated at 30 °C with a circulating water pump. Prior to illumination, 50 mg of the photocatalyst powder were suspended in a MB solution (125 mL, 10^{-5} mol/L) through ultrasonication in the dark for 10 min. The MB degradation was determined by recording the different intensities of the MB absorption maximum at 664 nm in a Varian Cary 50 Scan UV/Vis spectrometer.

5.3 Results and discussion

5.3.1 Coating of hierarchical Bi_2WO_6 nanostructures with TiO_2 nanoparticles

We have developed a TiO_2 coating process for hierarchical Bi_2WO_6 microspheres that is based on the impregnation of Bi_2WO_6 particles in TiF_4 solutions, followed by thermal treatment (Figure 5.1). The XRD pattern after the room-temperature solution treatment (Figure 5.2 b) does not show any reflections of TiO_2 whatsoever. We have optimized the calcination post-treatment so that anatase TiO_2 nanoparticles (20 – 40 nm in diameter) with a homogeneous morphology are formed on top of the Bi_2WO_6 substrate after 5 h of annealing at 500 °C (Figure 5.1 and 5.2).

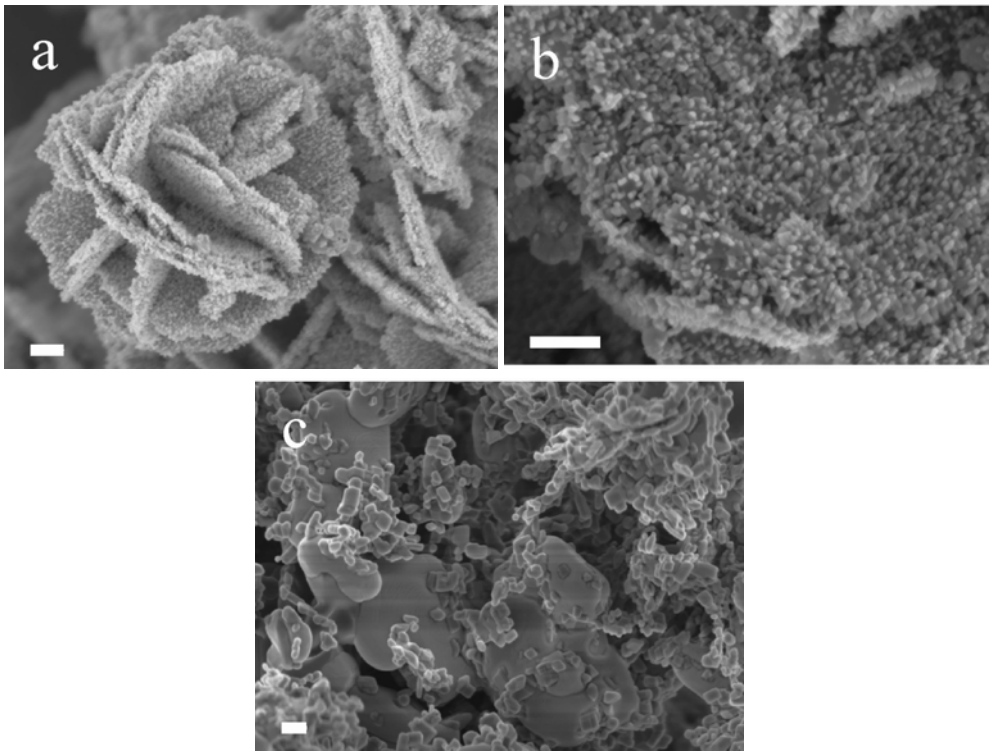

Figure 5.1. Bi_2WO_6 after coating with 62 mg TiF_4, followed by calcination at 500 °C (a, b) and 800 °C (c; scale bar = 200 nm).

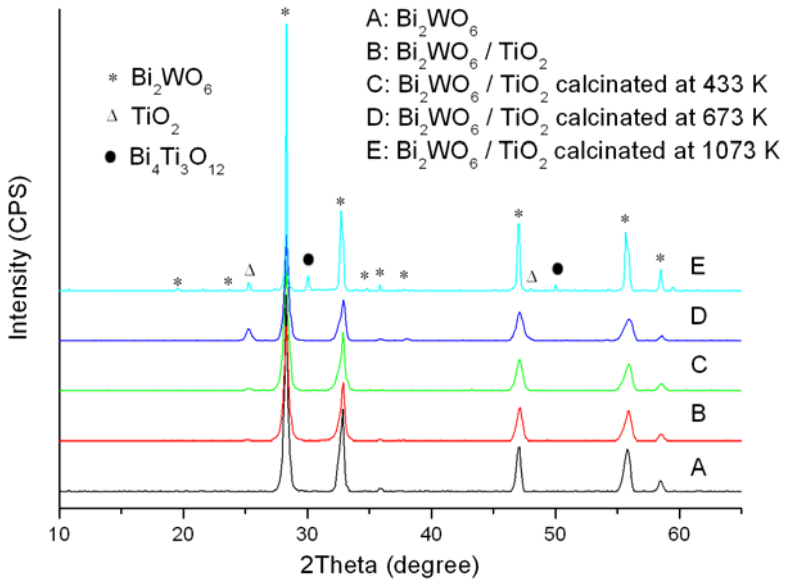

Figure 5.2. XRD patterns of hierarchical Bi_2WO_6 microspheres coated with TiF_4, followed by calcination at different temperatures.

Furthermore, EDXS results of these composites after heat treatment at 500 °C clearly demonstrated that their main components are Bi, W, Ti and O as shown in Figure 5.3. At

calcination temperatures above 800 °C, the substrate morphology gives in and $Bi_4Ti_3O_{12}$ is formed as a side product (cf. Figure 5.1 and 5.2). The hierarchical morphology of the Bi_2WO_6 spheres can withstand thermal processing up to 500 °C. Moreover, their BET surface increases from 17 (+/-1) m^2/g to 24 (+/-1) m^2/g

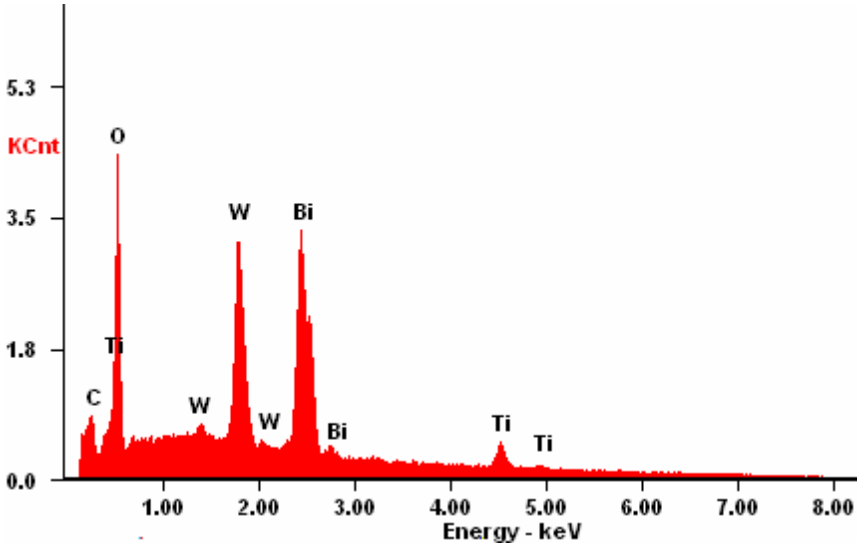

Figure 5.3. EDXS spectra of Bi_2WO_6 microspheres coated with TiO_2 nanoparticles.

5.3.2 Hydrothermal coating approach for Bi_2WO_6/TiO_2 hierarchical heterostructures

Preparation and morphology: In section 5.3.1, we have introduced a multi-step synthesis of Bi_2WO_6/TiO_2 composites. However, this complex reaction sequence and the required thermal post-treatment are rather time- and energy consuming so that more elegant and low temperature TiO_2-coating approaches are required that can furthermore be applied upon a wide range of target oxides. Compared to other methods, hydrothermal syntheses are an attractive approach for the synthesis of heterostructured materials due to their manifold advantages: they are environmentally friendly, technically convenient, flexible, up-to-date and they offer low-cost production options. Hydrothermal syntheses often involve the dissolution of the starting compounds so that the products might not bear any structural resemblance to the precursor.[9] On the other hand, if one of the precursor materials remains structurally stable under hydrothermal conditions, it can thus provide active sites for the nucleation and growth of a second coating phase.[10] Therefore, we

developed a flexible hydrothermal route to Bi_2WO_6/TiO_2 composites, taking advantage of the fact that the hierarchical Bi_2WO_6 particles are quite stable and maintain their structure and morphology under hydrothermal treatment at 160 °C for 24 h. Figure 5.4 a shows a typical SEM image of Bi_2WO_6 displaying a hierarchical morphology constructed from nanosheets: the individual nanoparticles of 10 – 40 nm in size are arranged into sheets that furthermore form spherical aggregates with an average size around 3 μm. It is obvious that the surfaces of the Bi_2WO_6 microspheres are relatively smooth and free of secondary nanostructures. After hydrothermal treatment of Bi_2WO_6 particles in TiF_4 solution at 90 °C for 24 h, the Bi_2WO_6 microspheres still display their hierarchical morphology. Moreover, the secondary nanoparticles are now uniformly distributed across the surface of Bi_2WO_6 microspheres without aggregation (cf. Figure 5.4 b). EDXS analyses of this sample demonstrate that Bi, W, Ti and O are the main components, thereby suggesting that the secondary nanoparticles consist of TiO_2.

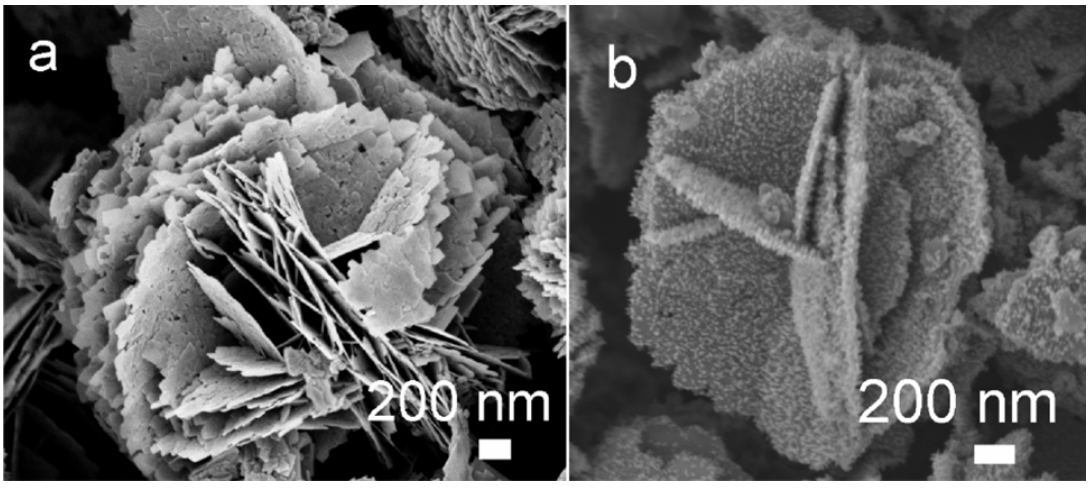

Figure 5.4. SEM images of (a) pristine Bi_2WO_6 microspheres and (b) the TiO_2-coated sample.

The good agreement of the experimental and Rietveld-refined powder XRD patterns (Figure 5.5) demonstrates the presence of orthorhombic Bi_2WO_6 and anatase TiO_2. Note that the Bi_2WO_6 phase exhibits strong preferred orientation along the (060) and/or (002) planes due to the two dimensional features of the *Aurivillius*-type Bi_2WO_6 structure

constructed from alternating perovskite-like slabs of corner-sharing WO_6 octahedra and $[Bi_2O_2]^{2+}$ layers.[11] The weight ratio (absorption effects are not taken into account) between Bi_2WO_6 and anatase TiO_2 was approx. 4:1. The lattice constants of the two phases and the reliability factors of the Rietveld refinement are summarized in Table 5.1.

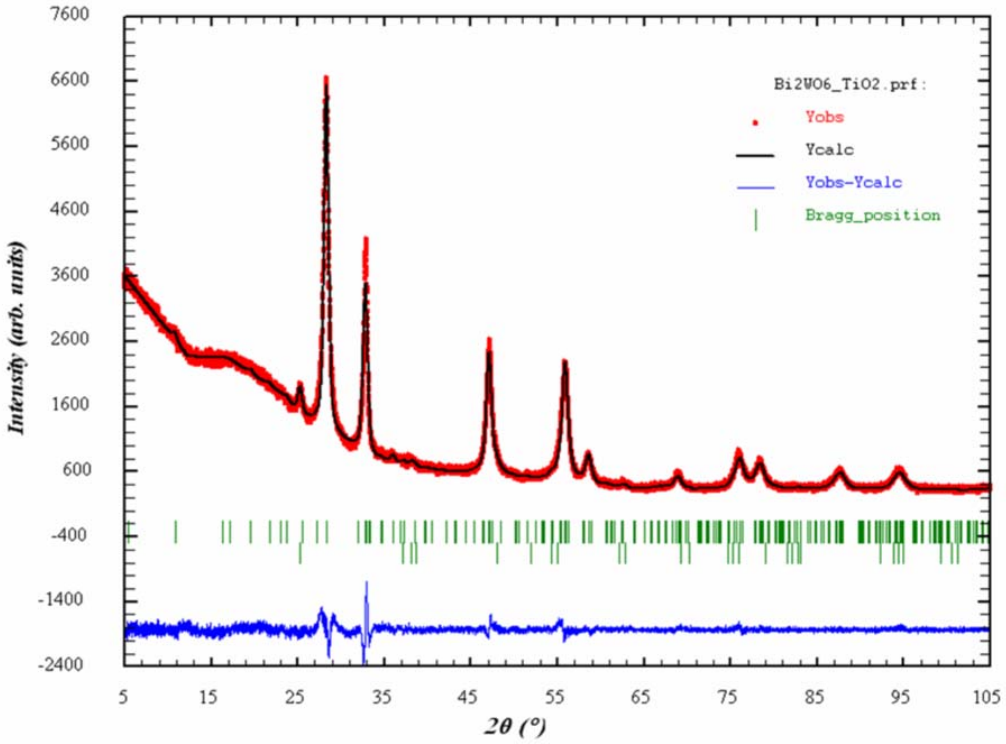

Figure 5.5. Rietveld refined powder XRD of the products (dotted line: observed intensity data, solid line: calculated pattern, bottom line: difference between the observed and calculated intensities). The upper and lower vertical bars correspond to the Bragg positions of Bi_2WO_6 (ICSD No.67647) and anatase TiO_2 (ICSD No.154601), respectively.

Table 5.1. Unit-cell parameters, weight fractions and reliability factors of the Rietveld refinement of the coated samples.*

Phase 1: Bi_2WO_6	**Phase 2: TiO_2**
Weight fraction: 80.1(7) %	Weight fraction: 19.9(5) %
Space group: $Pca2_1$	Space group: $I4_1/amd$
a = 5.444(1) Å	a = 3.7906(5) Å
b = 16.337(3) Å	b = 3.7906(5) Å
c = 5.4603(8) Å	c = 9.438(2) Å
R_{Bragg} 2.68%	R_{Bragg} 12.60%
R_F 1.77%	R_F 4.45%

*Rietveld R-factors (R_{wp}: 4.42 %, R_{exp}: 3.15 %, χ^2: 1.97)

Bi_2WO_6/TiO_2 heterojunctions: On the basis of these results, the coated samples can be described as hierarchical nanocomposites of Bi_2WO_6 and TiO_2. A more detailed insight into the microstructure of these nanocomposites was obtained by TEM investigations. TEM images of the coated samples (Figure 5.6 a) show that the TiO_2 nanoparticles are attached to the surface of Bi_2WO_6 particles which is in agreement with the SEM results. A representative SAED pattern of the composite is shown as an inset in Figure 5.6 a and the diffraction rings of the polycrystalline material can be indexed to a mixture of orthorhombic Bi_2WO_6 and anatase TiO_2. HRTEM provides direct evidence for the formation of a Bi_2WO_6/TiO_2 heterojunction (Figure 5.6 b).

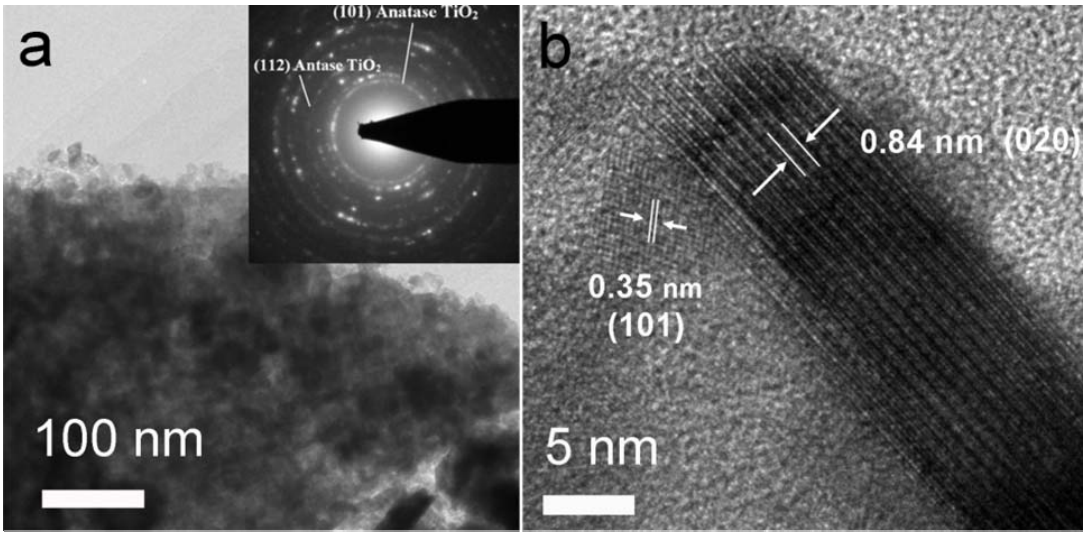

Figure 5.6. (a) Representative TEM image of the coated sample prepared at 90 °C (inset: corresponding SAED pattern); (b) HRTEM image of hierarchical Bi_2WO_6/TiO_2 heterostructures.

The HRTEM image of the coated sample displays anisotropic crystals that appear with dark contrast. They comprise a layer structure with an interlayer distance of ca. 0.84 nm that corresponds to the d-value of (020) of Bi_2WO_6. Crystalline particles with brighter appearance are attached to this Bi_2WO_6 crystal. The fringe observed corresponds to the interplanar distance of 0.35 nm which agrees well with the lattice spacing of the (101) plane of anatase TiO_2, thereby demonstrating the simultaneous presence of crystalline Bi_2WO_6 and TiO_2 in the region of the junction. HRTEM investigations furthermore indicated that Bi_2WO_6

displays a preferred orientation along the (020) plane which is in line with the Rietveld refinements (cf. Figure 5.5). All in all, the HRTEM results demonstrate that heterostructures are readily formed between Bi_2WO_6 nanosheets and TiO_2 nanoparticles: this may improve the charge separation efficiency and enhance the photocatalytic activity of the oxide composite.[12-14]

5.3.3 Parameter studies on the formation of hierarchical Bi_2WO_6/TiO_2 composites

In order to optimize the fabrication and to understand the formation process of the hierarchical Bi_2WO_6/TiO_2 composites, we investigated the influence of the hydrothermal parameters, especially reaction temperature and time, on the coating process. Figure 5.7 shows SEM images of samples that were coated at different temperatures. Even after hydrothermal treatment of Bi_2WO_6 microspheres in TiF_4 solution at temperatures as low as 60 °C for 24 h, secondary nanoparticles are already observed on the surface of the Bi_2WO_6 particles.

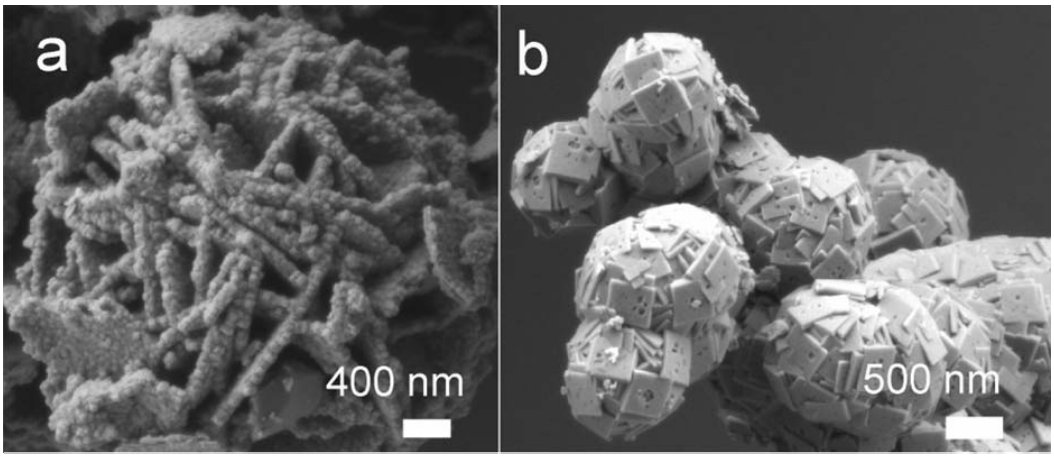

Figure 5.7. Representative SEM images of Bi_2WO_6/TiO_2 samples coated (a) at 160 °C for 24 h; (b) at 200 °C for 24 h (the SEM images of the samples coated at 60 °C and 120 °C are similar to those coated at 90 °C, cf. Figure 6.4 b).

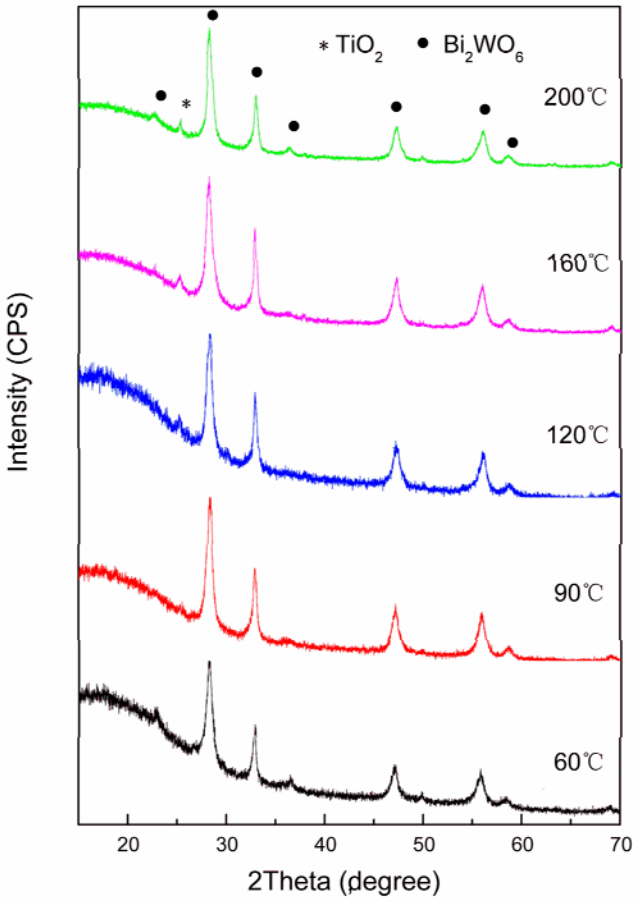

Figure 5.8. XRD patterns of Bi_2WO_6/TiO_2 samples coated at different temperatures.

The corresponding XRD patterns (Figure 5.8) demonstrate that no diffraction peaks of TiO_2 are present beside the diffraction peaks of Bi_2WO_6, indicating that amorphous TiO_2 nanoparticles are deposited on the Bi_2WO_6 substrate at lower temperatures. Generally, TiO_2 particles obtained from controlled low temperature hydrolysis processes are also of low crystallinity. When the reaction temperature was raised to 90 °C, the diffraction peaks of anatase TiO_2 appeared in the XRD pattern (cf. Figure 5.5), thus pointing to the onset of anatase TiO_2 nanocrystal formation (Figure 5.6 b). The structure and morphology of the samples coated at 120 °C are closely related to those obtained at 90 °C. However, a further raise of the reaction temperature to 160 °C led to a significant increase of the TiO_2 particle size (Figure 5.7 a). Finally, coating experiments at 200 °C led to a collapse of the flower-like hierarchical morphology and spheres consisting of densely packed plates are observed instead (Figure 5.7 b). Despite the changes in morphology, the XRD patterns of the samples coated at

160 and 200 °C showed their main components to be still Bi_2WO_6 and crystalline anatase TiO_2 (Figure 5.8). The BET surface area of the Bi_2WO_6 microspheres is compared to the samples coated at different temperatures in Figure 5.9. After the coating process, the BET surface area is significantly increased due to the formation of TiO_2 nanoparticles on the surface of the Bi_2WO_6 microspheres. The only exception from this trend is the sample coated at 200 °C, because the higher reaction temperature led to the formation of a dense outer surface (Figure 5.7 b). In line with these temperature-dependent morphological changes, the BET surface area of the coated samples decreased from 34.8 m^2/g (coated at 60 °C) to 8.4 m^2/g (coated at 200 °C). Although the samples coated at 60 °C display the highest BET surface area, the TiO_2 particles on the surface are amorphous as mentioned above (Figure 5.8). Therefore, the optimized temperature window for the formation of hierarchical Bi_2WO_6/TiO_2 composites is between 90 and 120 °C.

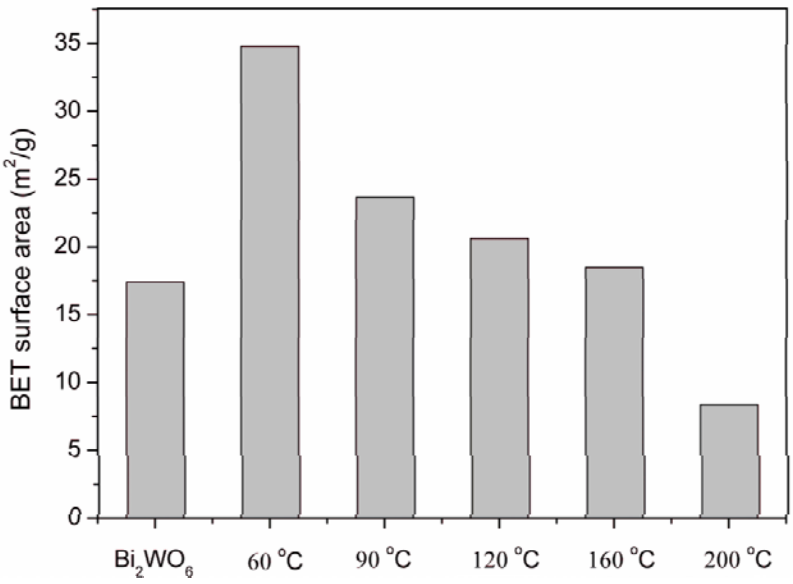

Figure 5.9. BET surface areas of Bi_2WO_6 microspheres and the Bi_2WO_6/TiO_2 samples coated at different temperatures.

In order to obtain further insight into the growth process of TiO_2 nanoparticles on Bi_2WO_6 surfaces, their time-dependent formation was investigated with respect to structure and morphology in the interval of 1 – 24 h. The coating temperature was kept constant at 90 °C. The growth process of TiO_2 particles was monitored through Raman spectroscopy (cf.

Figure 5.10), because the XRD patterns of the coated samples are dominated by the Bi_2WO_6 phase and even after prolonged coating times of 24 h, only a weak reflection of the TiO_2 nanoparticles was observed (cf. Figure 5.5).

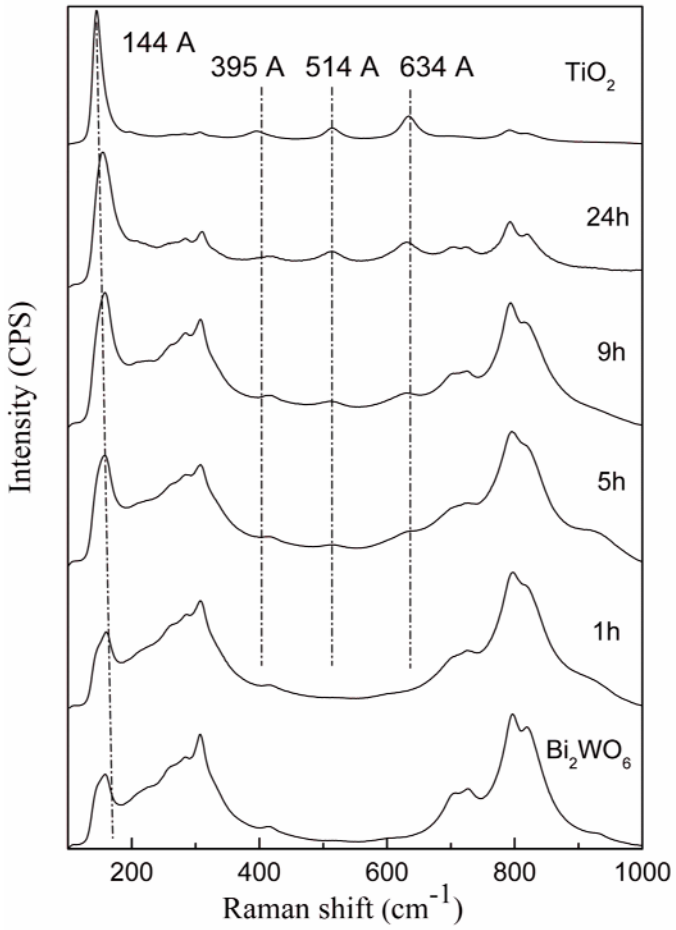

Figure 5.10. Raman spectra of Bi_2WO_6/TiO_2 samples coated at 90 °C for different reaction times, compared to pristine Bi_2WO_6 microspheres and TiO_2 particles (A: anatase).

The Raman modes at 144, 395, 514 and 634 cm^{-1} can be assigned as E_g, B_{1g}, A_{1g} (or B_{1g}), and E_g modes of anatase TiO_2 phase.[15] In the initial phase of the reaction (1 h), Raman modes of crystalline anatase TiO_2 are not observed. The corresponding SEM images (Figure 5.11 a) show that the surface of Bi_2WO_6 microspheres remains smooth and no crystalline anatase TiO_2 particles are formed at this stage. After 5 h of reaction time, highly dispersed nanoparticles with diameters around 10-30 nm are observed on the surface of the Bi_2WO_6 microspheres (cf. Figure 5.11 b) and the corresponding Raman spectra point to the formation

of crystalline anatase TiO_2. The intensity of the corresponding Raman modes increases upon further prolonged reaction times (cf. Figure 5.10), indicating that the deposition of the anatase phase on the surface of Bi_2WO_6 continued (cf. corresponding SEM images in Figure 5.11 c). The crystallinity of anatase TiO_2 further benefits from longer reaction times. It is worth to mention that the TiO_2 nanoparticles assemble into large agglomerates in the absence of Bi_2WO_6 particles. Therefore, the morphology and size of the secondary oxide phase TiO_2 is strongly affected by the presence of the Bi_2WO_6 substrate as shown in the reference experiment (Figure 5.11 d).

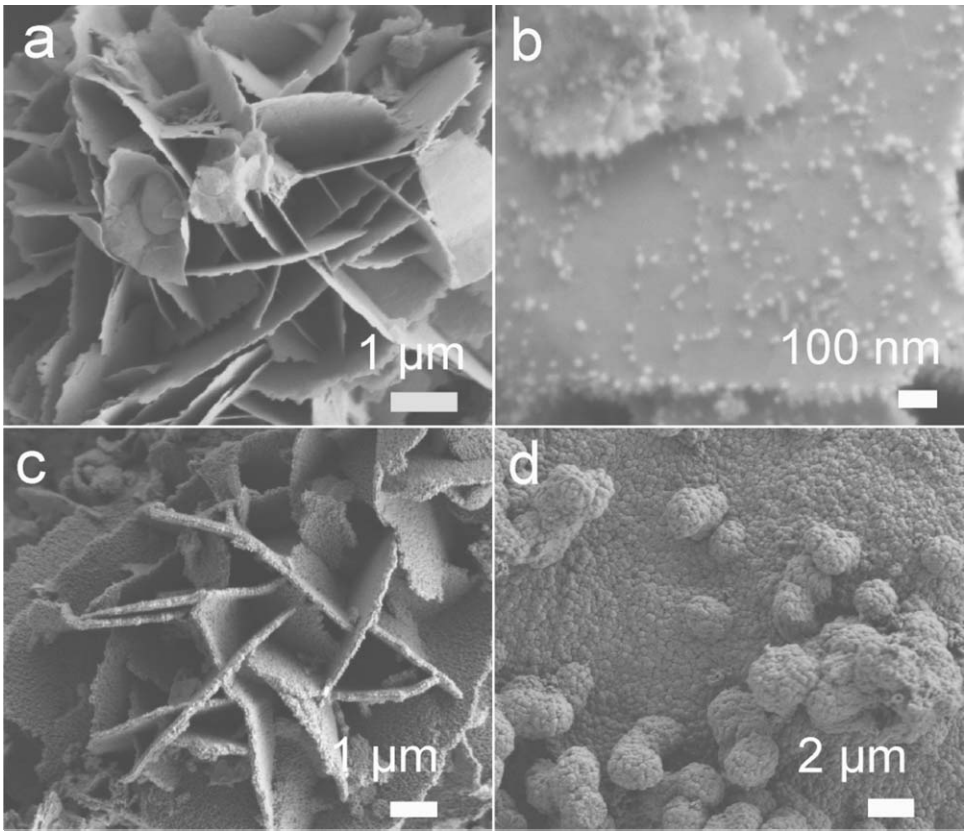

Figure 5.11. SEM images of the samples coated at 90 °C for different times: (a) 1 h; (b) 5 h; (c) 9 h. A representative SEM image of the samples coated for 24 h is shown in Figure 5.4 b. (d) SEM image of TiO_2 particles formed in the absence of the Bi_2WO_6 precursor.

Based on these observations, we summarize the following key steps in the formation process of TiO_2 nanoparticles on the surface of Bi_2WO_6: Firstly, the defect sites on the surface of Bi_2WO_6 were regarded as heterogeneous nucleation sites for the anatase TiO_2 phase due to a

lower free energy compared to homogeneous nucleation (cf. Figure 5.6 b). Furthermore, TiO_2 was formed through the following hydrolysis reaction:[16]

$$TiF_4 + 2\ H_2O \rightarrow TiO_2 + 4\ HF \qquad (Eq.\ 5.1)$$

As HF emerges as a side product, the precursor materials have to be stable under strongly acidic conditions. In addition, the crystallinity of the freshly nucleated anatase TiO_2 nanoparticles can be improved within a specific parameter window through prolonged reaction times or elevated reaction temperatures up to 160 °C (Figures 5.8 and 5.10).

5.3.4 Optical properties and photocatalytic activity

The room temperature UV/Vis spectra of TiO_2 nanoparticles, Bi_2WO_6 microspheres, and hierarchical Bi_2WO_6/TiO_2 particles are compared in Figure 5.12. The band gaps (E_g) of these three samples are estimated to be about 3.20, 3.03 and 3.01 eV, respectively, from the first derivative of the absorption edge, which indicates that the Bi_2WO_6/TiO_2 composites absorb in the visible light range. The photocatalytic degradation process of MB was monitored through the intensty of the characteristic absorption peak at 664 nm against TiO_2 nanoparticles (P25, Degussa, 80 % anatase phase) as a reference (cf. Figure 5.13). The photolysis of MB under visible light irradiation in the absence of a catalyst is negligible and the energy distribution of the blue light bulb excludes the self-photosensitized effects of MB. Although Bi_2WO_6 particles exhibited high visible-light-driven photocatalytic activity for the decomposition of RhB under visible light irridation, the according degradation of MB is quite low, as has been reported by other groups.[17, 18] In our current work, the decrease of MB concentration in the presence of Bi_2WO_6 microspheres is as low as 9 % over a period of 45 min. which is even lower than the values observed in the presence of TiO_2 nanoparticles (19 %) under visible light irradiation. The MB degradation in the presence of hierarchical Bi_2WO_6/TiO_2 heterostructures is much higher (3 times) than the values obtained for Bi_2WO_6 microspheres after irradiating for 45 min. It is very important to compare the relative potential levels of the individual band edges to understand the influence of TiO_2 on the phoctocatalytic activity of Bi_2WO_6/TiO_2 composites.

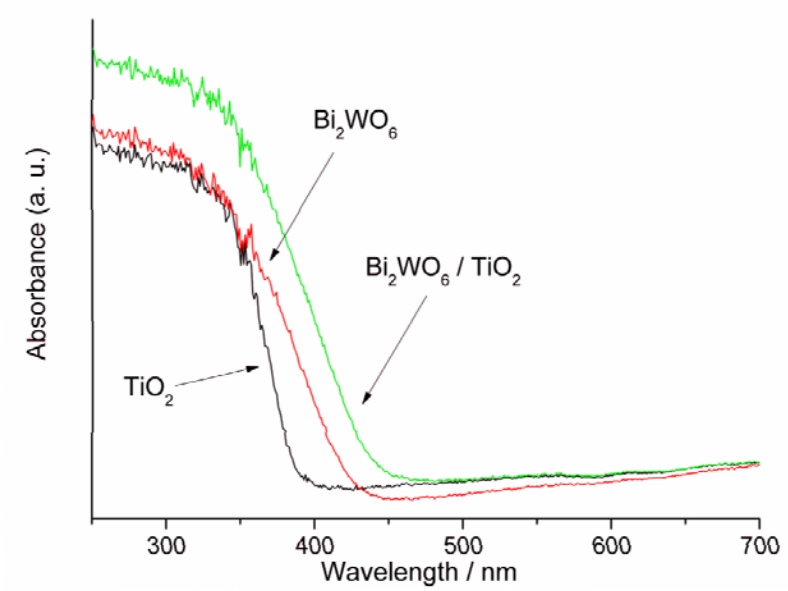

Figure 5.12. UV/Vis spectra of TiO_2 nanoparticles, Bi_2WO_6 microspheres, and hierarchical Bi_2WO_6/TiO_2 heterostructures.

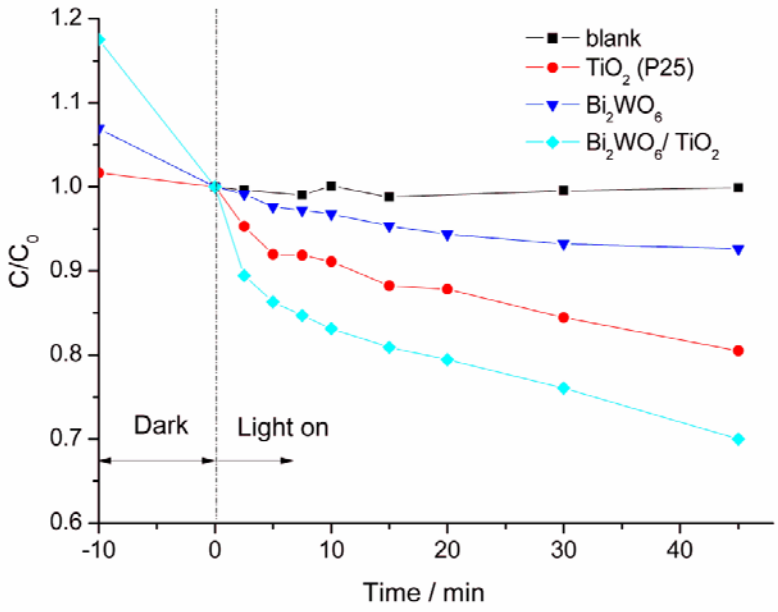

Figure 5.13. Degradation of MB in the presence of different photocatalysts under visible light irradiation (catalyst: 50 mg; lamp: Hg bulbs, max. intensity at 450 nm).

The conduction band edge of a metal oxide at the point of zero charge can be calculated according to the following empirical equation:[19]

$$E^0_{CB} = E_0 - \chi + 1/2E_g \qquad (Eq.\ 5.2)$$

Here χ is the absolute electronegativity of the semiconductor, E_g is the band gap of the semiconductors and E_0 (+ 4.5 eV) is the energy of a free electron on the H_2 redox scale. The calculated band edge positions of Bi_2WO_6 and TiO_2 are shown in Table 5.2. The CB edge potential of TiO_2 (-0.41 eV) is more negative than that of Bi_2WO_6 (0.35 eV), hence photoinduced electrons on the TiO_2 particle surface can easily be transferred to Bi_2WO_6. On the other hand, photoinduced holes on the Bi_2WO_6 surface migrate to TiO_2 due to the different VB edge potentials. It is clear that the separation of electron-holes pairs is quite effective as shown in Figure 5.14. Therefore, the enhanced photocatalytic activity of the Bi_2WO_6/TiO_2 composites can be attributed to several factors: (1) the Bi_2WO_6/TiO_2 hierarchical particles can absorb the highest amount of MB molecules in the dark prior to irradiation (cf. Figure 5.13); (2) the Bi_2WO_6/TiO_2 heterojunction (cf. Figure 5.6 b) promotes charge separation and results in more electrons accumulating in the Bi_2WO_6 and more holes in the TiO_2 part which display a strong oxidation potential and can thus degrade the MB adsorbed on the surface as shown in Figure 5.14. Furthermore, the particle size is a crucial factor for the practical application of photocatalysts. In this context, nanoparticles can be extremely difficult to separate from solutions after the photocatalytic reaction. The fixation of TiO_2 nanoparticles on the Bi_2WO_6 microsphere carriers, however, is an efficient way to separate and to recycle the photocatalyst. The hierarchical Bi_2WO_6/TiO_2 particles can be sedimented from aqueous suspensions in less than 1 h. SEM investigations of the recycled photocatalysts showed that they did not undergo morphological changes during the reaction. Further detailed investigations of the precise composition of the heterojunction region after the reaction, however, would be highly demanding in terms of HRTEM techniques and local elemental analysis so that they are beyond the scope of the present study.

Table 5.2 Calculated band-edge positions of TiO_2 and Bi_2WO_6 at the point of zero charge.

Semiconductor oxide	**Estimated energy band gap *E*g (eV)**	**Calculated conduction band edge (eV)**	**Calculated valence band edge (eV)**
TiO_2	3.20	-0.41	2.79
Bi_2WO_6	3.03	0.35	3.38

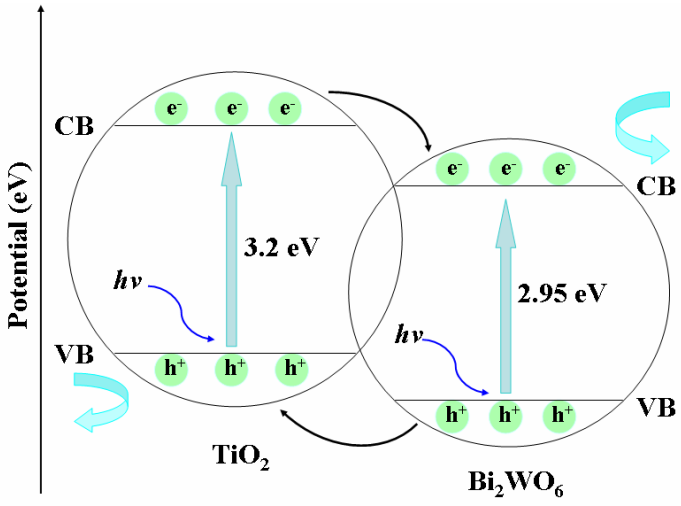

Figure 5.14. Schematic diagram for energy band matching and electron-hole separations.

5.3.5 Synthesis of hierarchical $BiVO_4/TiO_2$ and Bi_2MoO_6/TiO_2 composites

Based on our understanding of the abovementioned TiO_2 coating process, we propose that this route can be applied for the coating of other technically relevant bismuth oxides which are stable under strongly acidic hydrothermal conditions. Two examples of related bismuth oxides with special anisotropic features have been selected to investigate their morphological and phase stability during the synthetic procedure. In the first step, $BiVO_4$ microtubes and Bi_2MoO_6 nanosheets were synthesized through hydrothermal reactions (cf. Figures 5.15 a and c).[20] Subsequently, the synthesized $BiVO_4$ microtubes or Bi_2MoO_6 nanosheets and TiF_4 were put with water into an autoclave that was operated at 90 °C for 24 h. The morphology of the coated products is shown in Figures 5.15 b and d. The precursor materials remain intact under the reaction conditions, and they are successfully coated with secondary TiO_2 nanoparticles. Interestingly, both the interior and the outer surface of the $BiVO_4$ microtubes are fully covered with TiO_2 nanoparticles. This result clearly demonstrates that the present one-step route is suitable for the treatment of more complicated oxide morphogies that might not withstand a multi-step coating process with thermal post-treatment involved. Thus, our current approach is a flexible option for the coating of photocatalytically active oxides which

opens up new preparative pathways to heterostructured materials with high application potential.

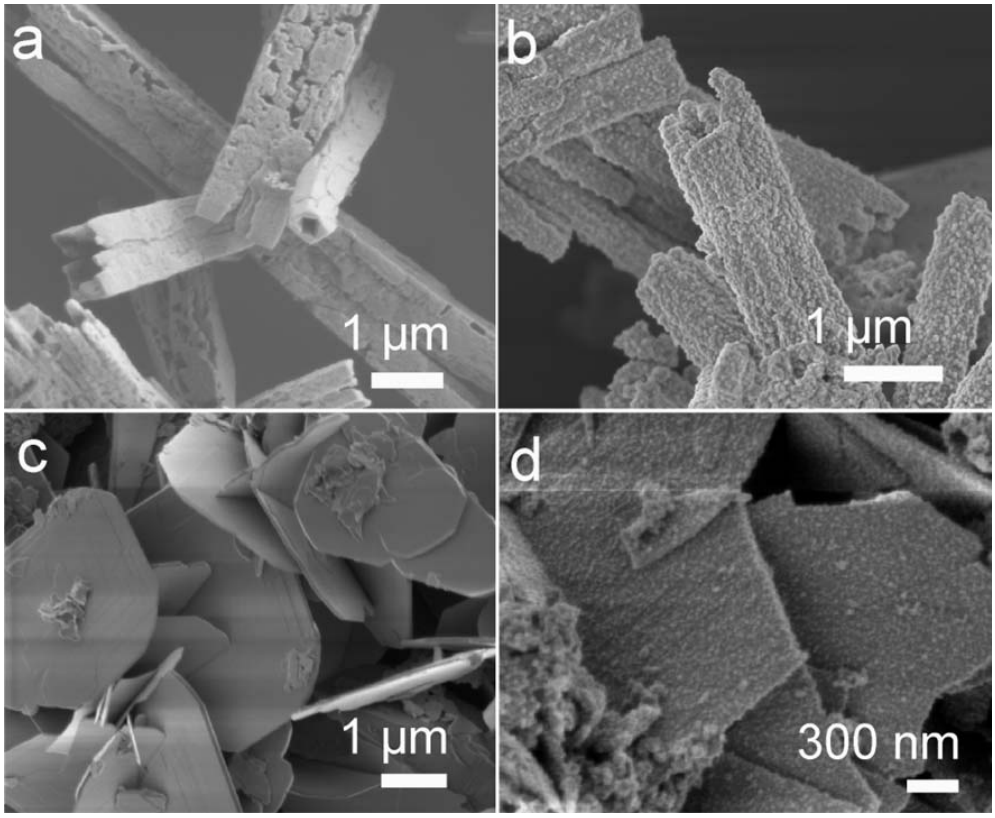

Figure 5.15. SEM images of $BiVO_4$ microtubes (a) before coating; (b) after coating with TiO_2; (c) Bi_2MoO_6 nanosheets before coating; (d) after coating with TiO_2.

5.4 Conclusion

In this chapter, we have successfully developed flexible coating approaches to Bi_2WO_6/TiO_2 hierarchical heterostructures through a low temperature and template-free hydrothermal method. The hierarchical Bi_2WO_6/TiO_2 composites exhibited higher visible-light-driven photocatalytic activity than isolated TiO_2 nanoparticles and Bi_2WO_6 microspheres which is attributed to their higher adsorption affinity towards MB molecules and to their enhanced charge separation efficiency. Furthermore, our current route can be applied upon the synthesis of other heterostructured materials with high application potential in photocatalysis and solar cells, such as $BiVO_4/TiO_2$ and Bi_2MoO_6/TiO_2.

References

[1] G. Li, D. Zhang, J. C. Yu, *Phys. Chem. Chem. Phys.* **2009**, *11*, 3775.

[2] V. Puddu, R. Mokaya, G. L. Puma, *Chem. Commun.* **2007**, 4749.

[3] J. H. Park, O O. Park, S. Kim, *Appl. Phys. Lett.* **2006**, *89*, 163106.

[4] Z. Bian, J. Zhu, S. Wang, Y. Cao, X. Qian, H. Li, *J. Phys. Chem. C* **2008**, *112*, 6258.

[5] X. Lin, J. Xing, W. Wang, Z. Shan, F. Xu, F. Huang, *J. Phys. Chem. C* **2007**, *111*, 18288.

[6] Y. Bessekhouad, D. Robert, J. V. Weber, *Catal. Today* **2005**, *101*, 315.

[7] H. M. Rietveld, *J. Appl. Crystallogr.* **1969**, *2*, 65.

[8] J. Rodriguez-Carvajal, *Phys. B* **1993**, *192*, 55.

[9] Y. Zhou, N. Pienack, W. Bensch, G. R. Patzke, *Small* **2009**, *5*, 1978.

[10] L. Shi, Y. Xu, H. Suikong, Y. Liu, S. Wang, L. Peng, K. Wong, Q. Li, *Nano. Lett.* **2007**, *7*, 3559.

[11] J. Ricote, L. Pardo, A. Castro, P. Millan, *J. Solid State Chem.* **2001**, *160*, 54.

[12] J. Zhang, Q. Xu, Z. Feng, M. Li, C. Li, *Angew. Chem. Int. Ed.* **2008**, *47*, 1766.

[13] H. Y. Yang, S. F. Yu, S. P. Lau, X. Zhang, D. D. Sun, G. Jun, *Small* **2009**, *5*, 2260.

[14] M. Shang, W. Wang, L. Zhang, S. Sun, L. Wang, L. Zhou, *J. Phys. Chem. C* **2009**, *113*, 14727.

[15] K. Zhu, M. Zhang, Q. Chen, Z. Yin, *Phys. Lett. A* **2005**, *340*, 220.

[16] H. G. Yang, H. C. Zeng, *Chem. Mater.* **2003**, *15*, 3113.

[17] H. Xie, D. Shen, X. Wang, G. Shen, *Mater. Chem. Phys.* **2007**, *103*, 334.

[18] Q. Xiao, J. Zhang, C. Xiao, X. Tan, *Catal. Commun.* **2008**, *9*, 1247.

[19] F. E. Osterloh, *Chem. Mater.* **2008**, *20*, 35.

[20] L.Zhou, W. Wang, L. Zhang, H. Xu, W. Zhu, *J. Phys. Chem. C* **2007**, *111*, 13659.

Part II

Humidity and Gas Sensors

6. Novel humidity sensors based on Bi_2MO_6 (M = W, Mo) films

6.1 Introduction

Humidity sensors are very important for key applications in environmental monitoring, industrial process control and in our daily life.[1-3] One of the most versatile sensing substances is the solid electrolyte LiCl that displays an outstanding sensitivity towards humidity variations. However, the solubility of LiCl upon exposure to high humidity levels renders its use in solid state devices impossible.[4] This problem can easily be solved through the use of metal oxide semiconductors that combine a high chemical and thermal stability with humidity resistance. Therefore, oxide materials have recently attracted considerable attention in sensor development and various oxides have been investigated with respect to humidity sensing, such as TiO_2,[5] ZnO,[6] SnO_2,[7] WO_3,[8] and $BaZrO_3$.[9] However, even these oxide materials are still prone to etching by corrosive atmospheres and to surface contamination by organic hydrophilic layers.[10] This calls for new materials with quick response/recovery to fabricate highly sensitive and stable humidity sensors. Given that oxides offer an almost endless spectrum of structural motifs and properties that can be tuned through substitution reactions and nanomaterials formation, there is plenty of room for further investigations to enhance their humidity sensing features.

Among the manifold ternary oxide structures, the layered *Aurivillius* type is an exceptionally flexible motif and Bi_2MO_6 (M = W or Mo) are its most elementary representatives: they are constructed from alternating $[Bi_2O_2]^{2+}$ slabs and layers of corner-sharing $(W/Mo)O_6$ octahedra as shown in Figure 6.2.[11] Generally, Bi_2MO_6 materials have attracted special attention due to their important physical and chemical properties, such as ferroelectricity,[12] oxide anion conductivity,[13] and nonlinear dielectric susceptibility.[14] Bi_2MO_6 oxides excel through their photocatalytic properties, namely the photocatalytic O_2 evolution from $AgNO_3$ solution[15] and the degradation of organic compounds under visible light irradiation.[16] This has triggered an immense research interest in the synthesis of nanostructured Bi_2MO_6 oxides and in the investigation of the corresponding relations between photocatalytic activity and morphology.[17-19] Our studies on the flexible hydrothermal synthesis of hierarchical Bi_2WO_6

microspheres and Bi_2MoO_6 nanoplates[20, 21] have demonstrated that such oxide materials with special morphological features are quite promising for photocatalytic applications (for a detailed discussion of these results cf. chapters 3 - 5). Furthermore, the high thermal stability of the *Aurivillius* type Bi_2MO_6 oxides in combination with their corrosion resistance in acidic media[21] is a further incentive to explore their application in other fields of materials science. In the following, we report on a new type of humidity sensors based on *Aurivillius* type Bi_2MO_6 (M = W, Mo) films for the first time and we investigate their humidity dependent impedance and capacitance characteristics. These new oxide-based sensors are promising for humidity sensing due to their high sensitivity, quick response/recovery time and good reproducibility features.

6.2 Experimental

6.2.1 Preparative methods

Hierarchical Bi_2WO_6 microspheres were prepared via a hydrothermal method according to the experimental conditions in section 3.2.1. In a typical procedure, 97 mg (0.2 mmol) of $Bi(NO_3)_3 \cdot 5H_2O$ and 33 mg (0.1 mmol) K_2WO_4 were placed into 10 mL of 20 vol.% acetic acid at room temperature and stirred magnetically for 20 min. to disperse all reagents homogeneously. The resulting precursor suspension was transferred into a Teflon-lined stainless steel autoclave with a capacity of 23 mL, maintained at 160 °C for 24 h, and subsequently cooled to room temperature. The precipitate was collected after filtration, washed with distilled water and dried in air. The Bi_2MoO_6 particles can be synthesized by simply replacing K_2WO_4 with 21 mg (0.1 mmol) Na_2MoO_4 in the above procedure.

6.2.2 Analytical characterization

XRD analysis was conducted on a STOE STADI P diffractometer in transmission mode (flat sample holders, Ge monochromator, and Cu $K_{\alpha 1}$ radiation) operated at 40 kV and 40 mA. The diffraction data were refined with Pawley methods using the ReflexPlus Package of Materials

Studio (Accelrys Inc.).[22] For SEM, performed on a Zeiss SUPRA 50VP microscope, samples were dispersed in ethanol and subsequently deposited on a silicon wafer. The specimens were investigated without conductive coating at rather low voltage (2 kV) to minimize charging effects. The BET surface area measurements were performed on a Quadrasorb SI in N_2-adsorption mode. The samples were degassed at 150 °C for 5 h under vacuum.

6.2.3 Humidity sensor fabrication and measurement

For the fabrication of humidity sensors, 0.2 mL terpineol mixed with 5 wt% ethylcellulose and 0.04 mL acetylacetone was added to 200 mg as-synthesized Bi_2MO_6 powders to obtain a paste. After grinding, the paste was coated onto a quartz slide covered with Au electrodes according to the 'Doctor Blade' method.[23] The spacing between the neighboring Au electrodes was 200 μm. The film was gradually heated in air at 150 °C for 10 min. to evaporate the solvent, then for 10 min at 350 °C to melt the acetylacetone and finally for further 30 min at 500 °C to thoroughly decompose the organic addictives, followed by cooling to room temperature. Consequently, a film with a thickness of about 10 μm was formed across the Au electrodes. Figure 6.1 shows the home-made set up for the humidity sensing measurements. The characteristic curves of humidity sensitivity were measured with a TH2617 LCR analyzer (Changzhou, China) with an applied voltage of AC 1 V and for frequencies varying from 100 Hz to 100 kHz. The complex impedance module and complex angle (Nyquist diagram) of the sensors were measured on a PAR 2273 electrochemical station. The controlled humidity environments for all measurements were achieved by using saturated aqueous solutions of different salts (LiCl, $MgCl_2$, $Mg(NO_3)_2$, KCl and KNO_3) in a sealed glass vessel with corresponding relative humidity (RH) values of 11 %, 33 %, 54 %, 75 %, 85 % and 95 %, respectively. All sensors were placed into the chamber with RH of 95 % for 10 h of aging prior to the humidity sensing measurements and the measurements were carried out at ~25 ^oC.

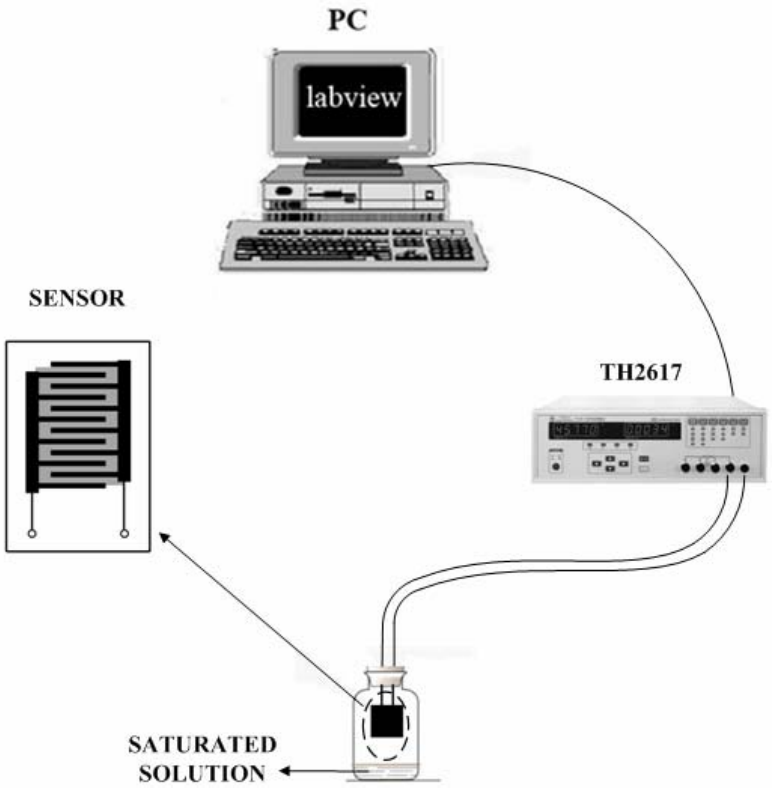

Figure 6.1. Schematic representation of the humidity sensor and of the measurement setup.

6.3 Results and discussion

6.3.1 Structure and morphology of Bi_2MO_6 films

In line with the experimental results reported in chapter 3 and 5, the as-synthesized products were indexed to phase pure orthorhombic Bi_2WO_6 and γ-Bi_2MoO_6, respectively. The obtained hierarchical Bi_2WO_6 microspheres are constructed of nanosheets (ca. 30 nm thick) and their BET surface area was determined as 18.4 m^2/g. As the Bi_2MoO_6 samples consist of larger plates (sizes around several μm, less than 100 nm thick), their surface area of 8.6 m^2/g is lower. However, both starting materials might undergo phase and morphological changes during the sensor fabrication process at high temperatures so that the resulting films were re-investigated accordingly. The XRD patterns of the fabricated films are shown in Figure 6.2. The unit cells obtained by Pawley refinement of both oxide materials constituting the films agree well with the ICSD data of Bi_2WO_6 (PDF 39-0256) and γ-Bi_2MoO_6 (PDF 84-0787), respectively (Bi_2WO_6: a = 5.4442(5) Å, b = 16.4285(8) Å and c = 5.4564(3) Å; Bi_2MoO_6:

a = 5.47948(7) Å, *b* = 16.2112(2) Å and *c* = 5.50105(7) Å). The results are in line with the above-mentioned high thermal stability of the *Aurivillius* structure type so that both the Bi_2WO_6 and Bi_2MoO_6 films remain unchanged after treatment at 500 °C (cf. Figure 6.2). Furthermore, the evaluation of the most intense (131) reflection of both the Bi_2WO_6 and Bi_2MoO_6 materials according to the Scherrer equation points to crystallite sizes of 21 nm and > 100 nm, respectively. Typical SEM images of the films are shown in Figure 6.3. The Bi_2WO_6 films exhibit hierarchical nanostructures, whereas the Bi_2MoO_6 films consist of plate-like particles with larger individual size (cf. above).

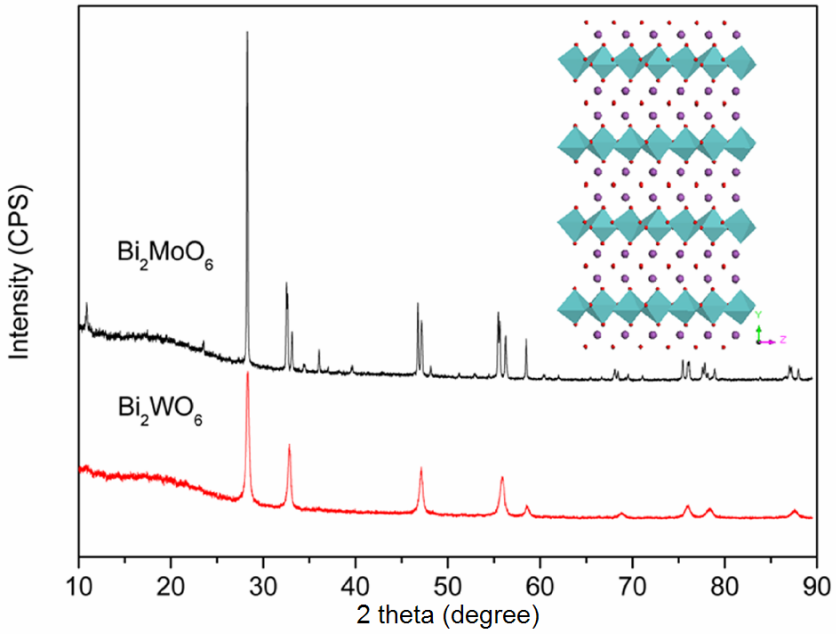

Figure 6.2. XRD patterns of Bi_2WO_6 and Bi_2MoO_6 films together with the *Aurivillius* structure motif (inset).

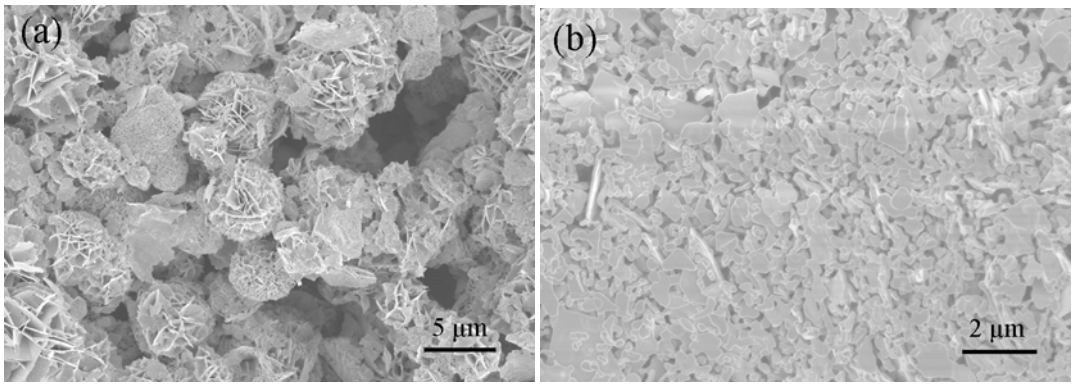

Figure 6.3. Representative SEM images of (a) Bi_2WO_6 films and (b) Bi_2MoO_6 films after thermal treatment.

6.3.2 Humidity-dependent impedance response

Generally, the characteristics of humidity sensors are strongly related to the applied frequency. In order to optimize the working parameters for the present setup, the humidity-dependent impedance of both sensors is shown in Figures 6.4 a-b for different signal frequencies (100 Hz, 1 kHz, 10 kHz, 40 kHz and 100 kHz) at room temperature. The impedances of the two sensor types decreased sharply with increasing humidity as a general trend, but the signal frequencies can also modulate the humidity-dependent impedance response. A more detailed evaluation shows that the logarithmic impedances are independent of frequency in the intermediate range of RH (i.e. from 30-75 % for Bi_2WO_6 and 50-90 % for Bi_2MoO_6, respectively), whereas in the low RH range (i.e. from 10-30 % for Bi_2WO_6 and 10-50 % for Bi_2MoO_6), the slope of the humidity vs. impedance curve decreases with the increase of the signal frequency. In particular, the impedance remains almost constant for low RH with 100 kHz signals for both sensors. This can be explained through a delayed polarization of the adsorbed water molecules at high frequencies.[7] All in all, it can be observed that the sensors exhibit linear humidity-dependent impedance response in the widest RH range at a signal frequency of 1 kHz (cf. Figure 6.4 a-b). Thus, the operational AC voltage and frequency were kept constant at 1 V and 1 kHz, respectively, for all following experiments. The corresponding impedance vs. RH plots compared for both sensors are shown in Figure 6.4 c. The sensitivities of the Bi_2WO_6 and Bi_2MoO_6-based sensors are quite similar over a wide impedance range of five orders of magnitude (10^9 to 10^4 Ω) with the RH varying from 11 to 95 %. The sensitivity (defined as $R_{11\%}/R_{95\%}$) of the Bi_2WO_6 sensor ($1.2E^5$) is higher than that of the Bi_2MoO_6 sensor ($7.7E^4$). The adsorption (solid line) and desorption (dashed line) characteristics of the humidity hysteresis are compared for both sensors as shown in Figure 6.5. The Bi_2WO_6 sensor exhibits a narrow hysteresis loop with only slight deviations around 55 % RH, whereas the impedance of the Bi_2MoO_6 deviates over a wider range from 33 % RH to 75 % RH.

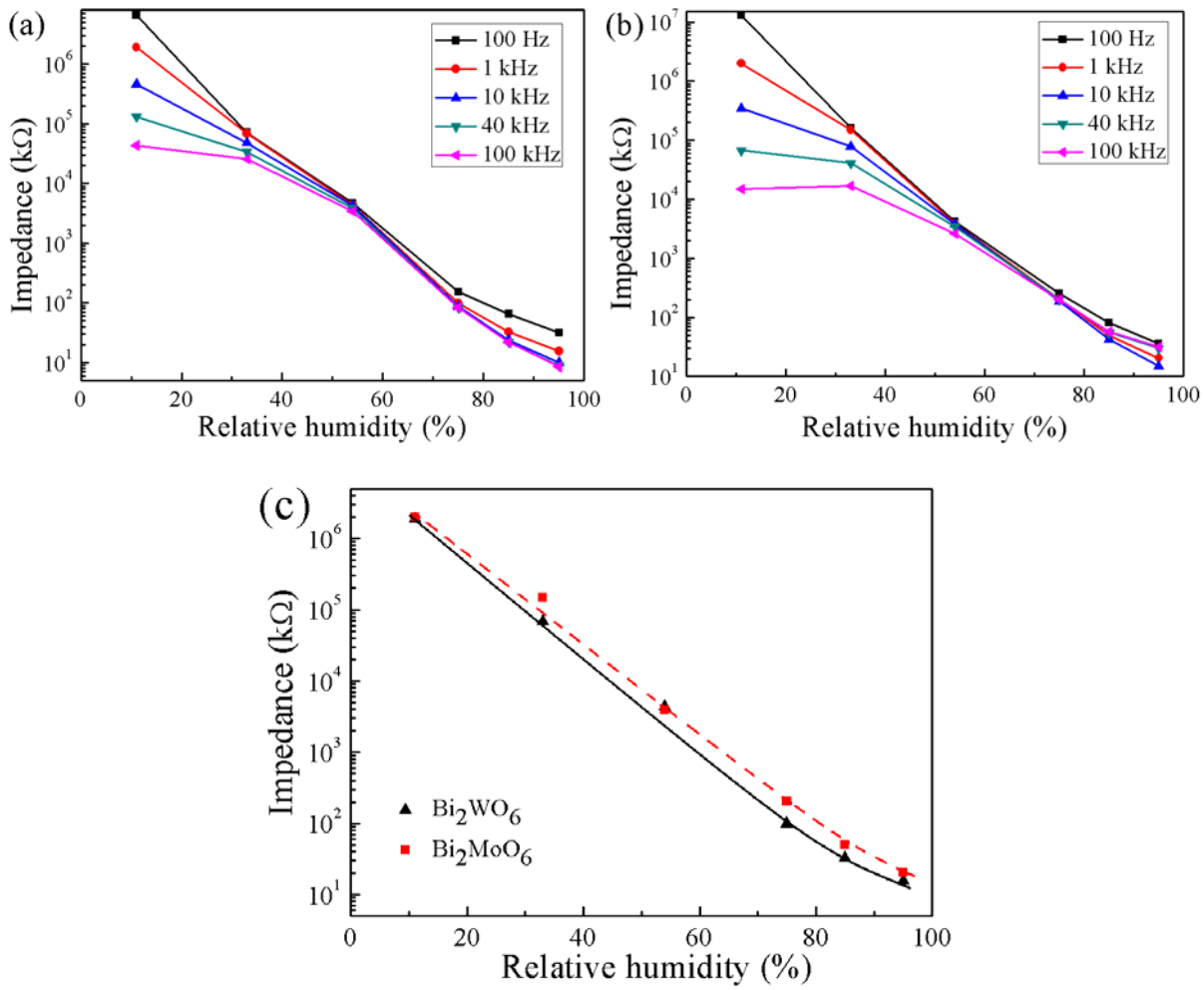

Figure 6.4. Impedance of (a) Bi_2WO_6, and (b) Bi_2MoO_6 sensors at different frequencies, (c) impedance vs. RH plots for both sensors (frequency = 1 kHz).

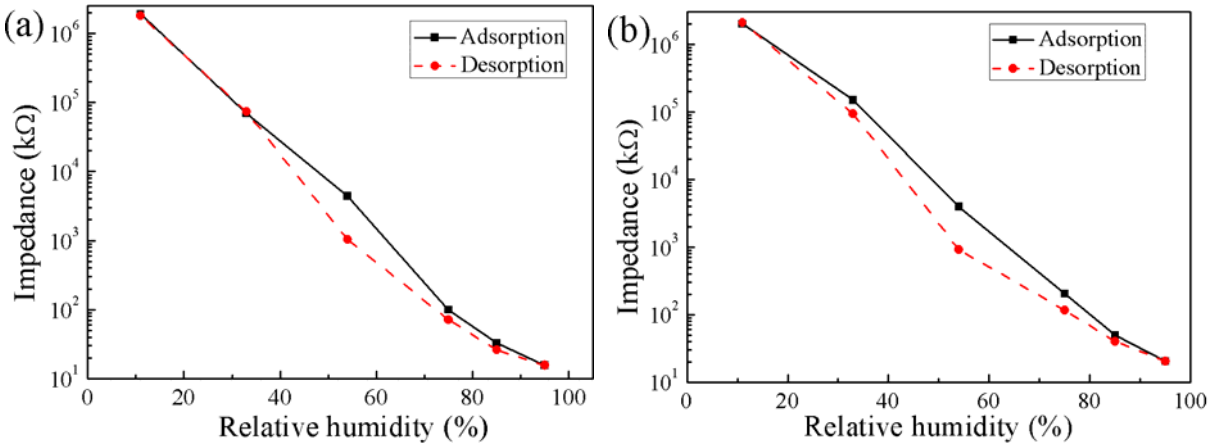

Figure 6.5. Hysteresis characteristics of (a) Bi_2WO_6, and (b) Bi_2MoO_6 humidity sensors. The AC voltage and the frequency are 1 V and 1 kHz, respectively.

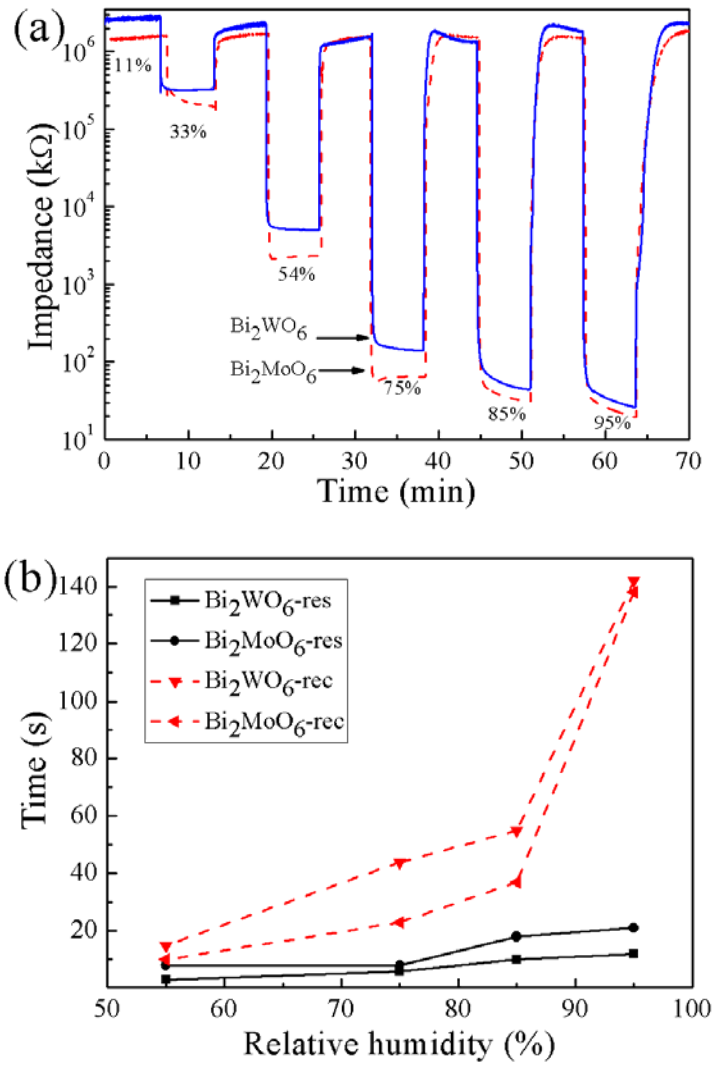

Figure 6.6. (a) Characteristic response and recovery curves for selected RH values; (b) comparison of actual response and recovery times vs. RH for both sensor types.

It is well known that response and recovery behavior is an important characteristic for evaluating the performance of humidity sensors. Figure 6.6 displays the sensing response and recovery behavior of both sensors. The response and recovery times are defined as the interval required to achieve 90 % of the total impedance change in the adsorption and desorption processes, respectively. The response/recovery cycles are compared in Figure 6.6 a for selected humidity values between 11 % and 95 % RH. Generally, the response and recovery time of both sensors increase with increasing RH and the actual values are plotted in Figure 6.6 b: the response and recovery times for both sensors are relatively short for RH below 85 %. Nevertheless, the recovery time over the entire RH range under investigation is longer

than the response time for both sensors (Figure 6.6 b). The difference between the recovery and the response time finally increases to one order of magnitude at 95 % RH. The sudden change of the recovery plots indicates the presence of two different sensing mechanisms for low RH and high RH values, respectively, which will be discussed in the following (cf. section 6.3.4).

In addition, the Bi_2WO_6 sensor exhibits a faster response but a slower recovery time in comparison with its Bi_2MoO_6 analogue. The differences in recovery times are most pronounced in the RH range between 75 % and 85 %, whereas both sensors display almost equal performance in the highest RH (> 95%) as well as in the lower RH range (< 55%). Furthermore, it is noteworthy that the sensing characteristics of both Bi_2WO_6 and Bi_2MoO_6 sensors display very good reproducibility (for details cf. Figure 6.7).

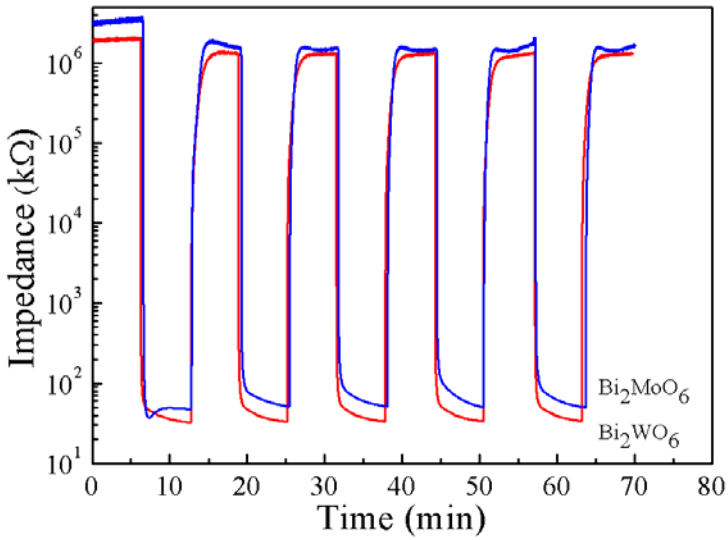

Figure 6.7. Reproducible impedance response of the sensors over a RH range from 11 % to 85 % for 5 cycles.

6.3.3 Humidity-dependent capacitance study

In addition to impedance measurements, capacitance is another physical quantity that is suitable for monitoring RH variations. Therefore, the humidity-dependent capacitance of the sensors has been studied at various frequencies ranging from 100 Hz to 100 kHz as shown in Figure 6.8. Unlike the impedance response, the capacitance of a given sensor depends on the

permittivity of the materials involved. The permittivity of the sensor film increases after water adsorption so that the capacitance increases accordingly. On the other hand, the capacitance vs. RH plots are less linear for the Bi_2MO_6 (M = W, Mo) sensors than the respective impedance signals (cf. Figure 6.4) and the capacitance remains almost constant for low RH. The capacitance furthermore displays a more pronounced dependence on the signal frequencies that can be described as follows: (1) The sensitivity of both sensors considerably increases with decreasing frequencies, (2) the capacitance vs. RH plots can be clearly divided into two different regions of linear response at low and high RH. This is another indication that two different sensing mechanisms are occurring at low RH and high RH, respectively. When the frequency is decreased, the "turning point" between these two regions is shifted towards the low RH region, i.e. the linear range in the RH region is enlarged. In the case of Bi_2WO_6, for example, the humidity sensitivity (defined as $C_{95\%}/C_{11\%}$) increases from 6.9 to 11510 with a frequency decrease from 100 kHz to 100 Hz so that the linear range can be extended from 75 % ~ 95 % RH to 33 % ~ 95 % RH. For a comparison with the impedance signal, the operational frequency was kept to 1 kHz in the following and the logarithmic capacitances of both sensors are plotted vs. RH in Figure 6.8 c. The sensing performance of Bi_2WO_6 materials is superior to Bi_2MoO_6 at high RH levels. Nevertheless, both materials display a practically identical performance for 54 % RH and below.

The capacitance response and recovery cycles from 11 % RH to 95 % RH are displayed for selected steps in Figure 6.9 a. The response and recovery times (defined as the time to achieve 90 % of the total capacitance change in the process of adsorption and desorption, respectively) increases for both sensors with increasing RH and the recorded values are shown in Figure 6.9 b. Note that the trend differs from the impedance measurement results as the capacitance recovery time is smaller than the response time. This may be due to the thickness of the films and this parameter is discussed in the following part. Bi_2WO_6 and Bi_2MoO_6 films display almost identical response/recovery times and only at rather high RH (> 80 %) a notable difference in response times is observed. Moreover, the reproducibility of the capacitance signals is superior to the impedance, because the absolute peak values remain almost unchanged (cf. Figure 6.10).

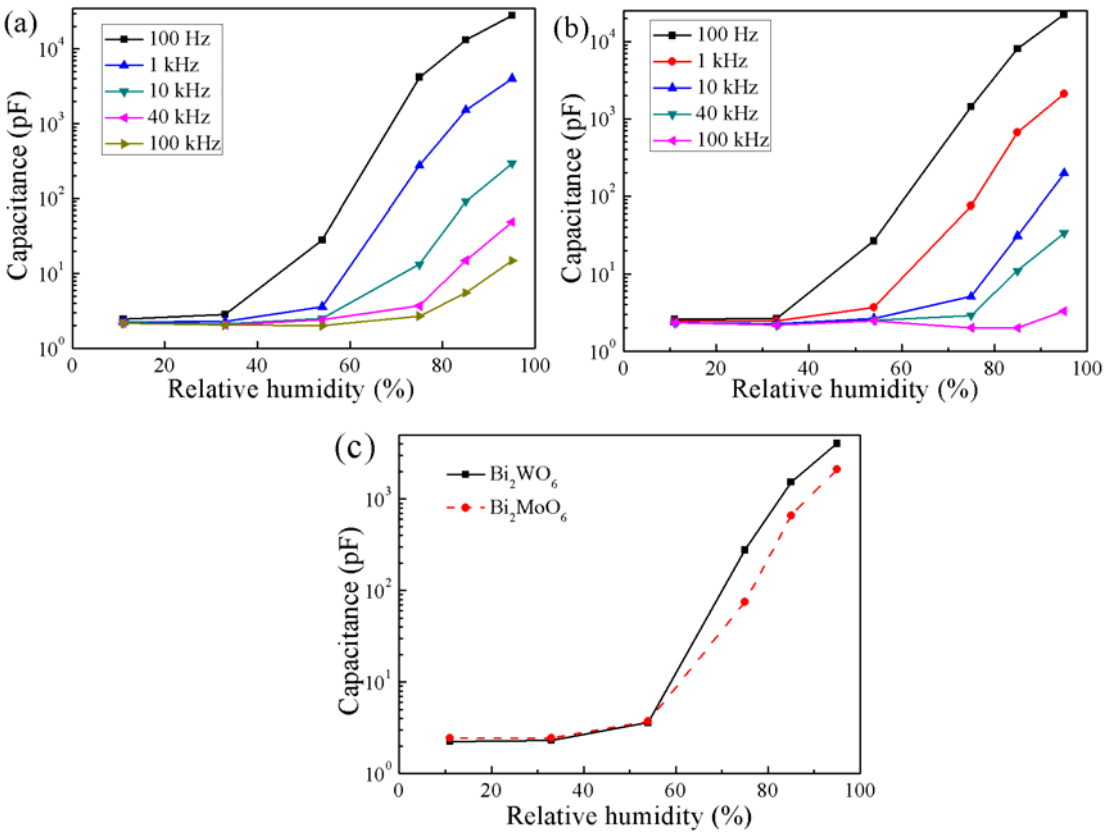

Figure 6.8. Capacitances of (a) Bi_2WO_6, and (b) Bi_2MoO_6 sensors at different frequencies, (c) impedance vs. RH relationships of both sensors (frequency = 1 kHz).

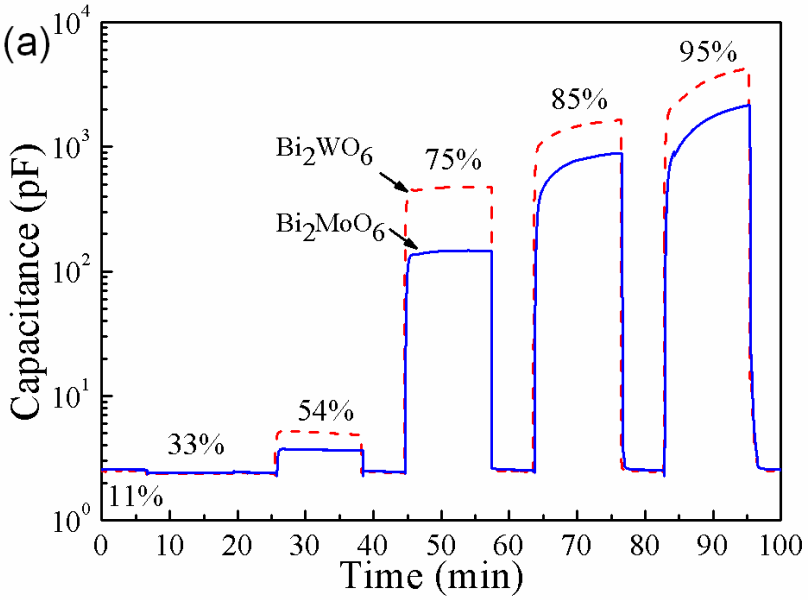

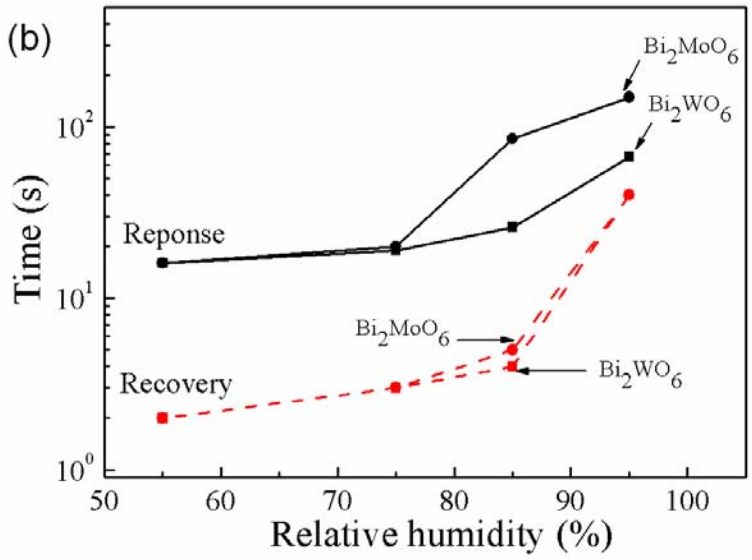

Figure 6.9. (a) Characteristic capacitive response and recovery curves recorded at various humidities, (b) measured response and recovery times vs. RH for both sensor types.

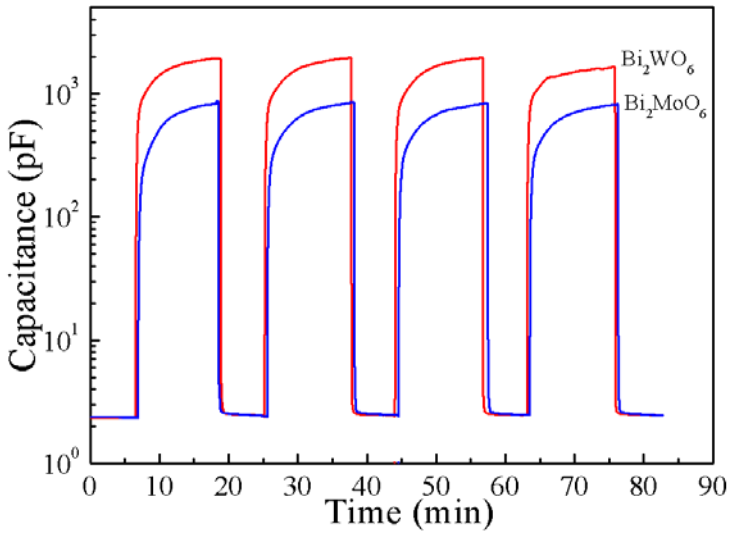

Figure 6.10. Reproducible capacitance response of the sensors over a RH range from 11 % to 85 % for 4 cycles.

6.3.4 Humidity sensing mechanisms

According to previous studies, the humidity sensing process of semiconductor-based sensors includes the following two stages:[25, 26] (1) in the low humidity range, a "non-Debye" behavior is observed and the surface coverage with H_2O molecules is incomplete. Hence, the protons dissociated from adsorbed water molecules can only migrate by hopping from site to

site across the surface. (2) an "ion-transport" process takes place in the high RH range: in this scenario, the materials surface is covered with one or several water layers so that the transfer of H^+ or H_3O^+ is accelerated, thereby leading to a sharp impedance decrease. These two processes can be easily distinguished in the impedance vs. RH plots at different frequencies shown in Figure 6.4 a-b. In the "non-Debye" region, the impedance vs. RH relationship can be easily modulated by signal frequencies, and in the "ion-transport" region, the impedance is independent of the signal frequencies. Moreover, it can be derived that the transition between the two mechanisms occurs at a lower RH threshold for the Bi_2WO_6-based sensor than for the Bi_2MoO_6-based sensor. Analogous phenomena can also be observed via complex plane impedance analysis (cf. Figure 6.11). The complex impedance measurements can be used to differentiate between conduction processes through equivalent circuit models and to analyze the mechanism of the sensing materials.[27] ReZ and ImZ are the real part and imaginary part of the complex impedance, respectively. The shape of the complex impedance plots changes with increasing RH from half semicircles over semicircles to semicircles with straight lines in the low frequency range and finally to straight lines, which demonstrates the occurrence of different sensing mechanisms. A semicircle plot represents a "non-Debye" behavior, which can be modeled with an equivalent circuit of parallel resistor and capacitor as shown in Figure 6.12 a. Here, R_f represents the intrinsic resistance of material, and C_f is the capacitance of the film. In addition, a semicircular plot connected with a line points to an "ion-transport" process, which can be modeled with the equivalent circuit shown in Figure 6.12 b (Z_i is the Warburg impedance at the electrode/sensing film interface, which is due to the diffusion of the electroactive species at the electrode). Moreover, it is observed that the transition between both mechanisms occurs at different RH threshold levels for the two sensor types: 75 % RH for the Bi_2WO_6-based sensor compared to the onset of the ion-transport process at 85 % RH for the Bi_2MoO_6-based sensor. This may indicate different hydrophilic surface properties, which can be further discussed with respect to the following factors: (a) the surface states of the material and (b) the nanoscale morphology. The chemisorption process is probably mediated through the formation of adsorption sites generated via the dissociation of hydrophilic Bi-O, W-O or Mo-O bonds on the surface. Thus, the different degrees of

hydrophilicity of the W-O and Mo-O bonds resulting from the different electronegativity values (2.16 and 2.36) could be a factor that contributes to the different hydrophilic surface properties. Next, the influence of the morphological differences of the given materials needs to be taken into account: the larger surface-volume ratio of the nanostructured Bi_2WO_6 films (Figure 6.3) might give rise to more potential adsorption sites to cover the surface with a layer of water molecules, thereby improving the sensitivity. In addition, the large surface-volume ratio of Bi_2WO_6 enhances the surface energy so that the response time is reduced due to accelerated chemisorption of water molecules. The opposite effect applies for Bi_2MoO_6: the insufficient adsorption of water on the surface facilitates the desorption process and this speeds up the recovery process of the Bi_2MoO_6-based sensors (cf. Figures 6.6 b). However, we note that it is difficult to separate the individual effects of electronegativity difference or different microstructures on the observed differences in the humidity sensing properties of Bi_2WO_6 and Bi_2MoO_6 sensors: this would require the synthesis of both oxides with the same microscale morphology, which is still a considerable challenge.[28] Moreover, two types of charge carriers are present on the surface of both sensors:[29] (1) protons are transferred among hydronium ions ($H_2O + H^+ = H_3O^+$) in the very first chemisorbed monolayer of water; and (2) protons furthermore exist in the following physisorbed multilayer of water. At high humidity levels, the latter are the majority species that dominates the conductivity mechanism of the sensors. As a result, the influences of the different surface states on the sensing properties are equalized so that the response and recovery times of both sensors become similar at 95 % RH as shown in Figures 6.6 b and 6.9 b.

Furthermore, the above-mentioned differences in recovery time and response time between impedance measurements and capacitance measurements can be explained as follows: the films used in our experiments with a thickness around 10 μm can be regarded as a parallel connection of surface and inner layer. During the impedance measurements, the surface layer quickly absorbs water molecules and turns into a state of low resistance resulting in the swift response. On the other hand, the rather difficult desorption process in the inner layer slows down the recovery considerably. In the course of the capacitance measurements, the two capacities in parallel connection are equally functionalized as a series of connected resistances

in which the slow absorption in the deep layer dominates the response time and the fast desorption in the surface layer dominates the recovery time. This results in longer recovery times for the impedance measurements and faster recoveries observed during the capacitance measurements compared with the respective response times.

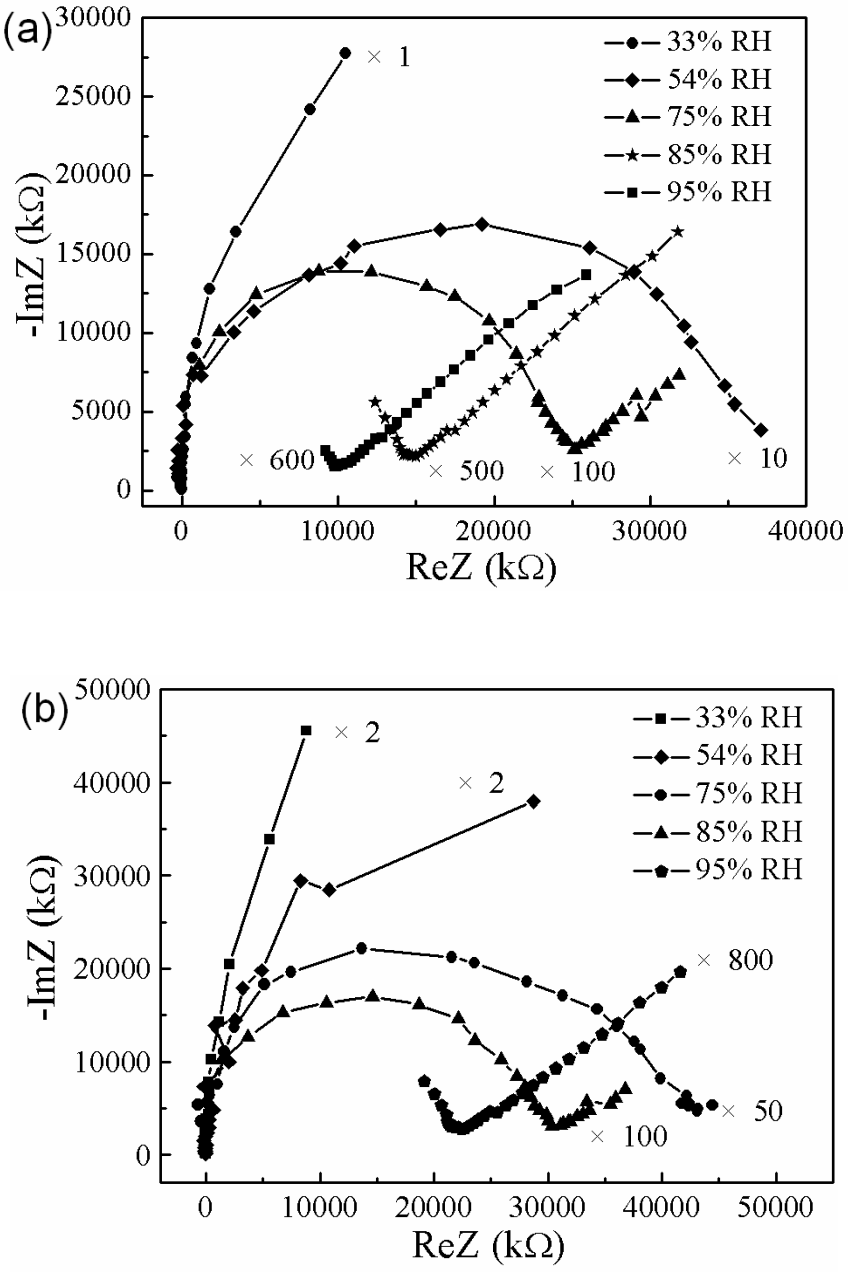

Figure 6.11. Complex impedance plots of (a) Bi_2WO_6 sensors and (b) Bi_2MoO_6 sensors.

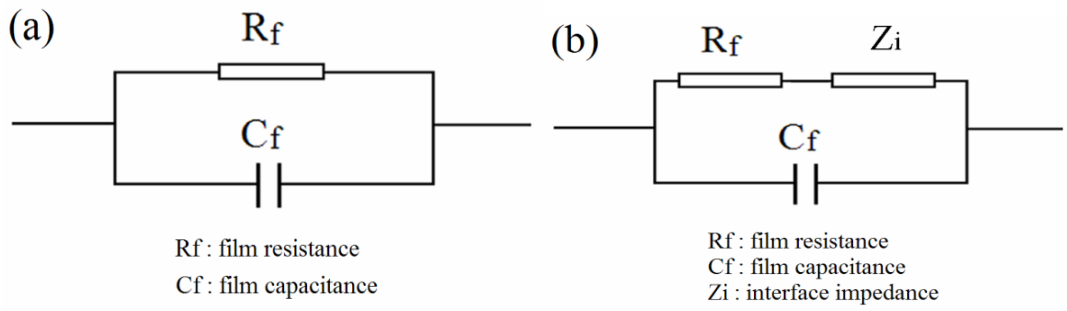

Figure 6.12. Equivalent circuits representing the above impedance plots.

Moreover, we also reported on a synthetic approach to cubic $Bi_{3.84}W_{0.16}O_{6.24}$ in chapter 3 in addition to the *Aurivillius* type Bi_2WO_6. The structural features of $Bi_{3.84}W_{0.16}O_{6.24}$ are completely different from the layered *Aurivillius* oxides. To investigate the influence of crystal structure on the humidity sensing properties of bismuth tungstates, we have furthermore fabricated a humidity sensor based on $Bi_{3.84}W_{0.16}O_{6.24}$ according to the above-mentioned method (cf. section 6.2.3). Figure 6.13 shows the humidity dependent impedance of $Bi_{3.84}W_{0.16}O_{6.24}$ sensor recorded at different frequencies. As observed before, the humidity dependent impedance response of humidity sensor is strongly related to the frequency. For the sake of comparison with the Bi_2WO_6 sensor, the operational AC voltage and frequency were kept constant at 1 V and 1 kHz, respectively, and the corresponding impedance vs. RH plots for $Bi_{3.84}W_{0.16}O_{6.24}$ and Bi_2WO_6 sensors are shown in Figure 6.14 b. The sensitivity (defined as $R_{11\%}/R_{95\%}$) of $Bi_{3.84}W_{0.16}O_{6.24}$ sensor is only $2.1E^2$, which is much lower than that of Bi_2WO_6 sensor ($1.2E^5$). Our results clearly demonstrate that the crystal structure of the selected bismuth tungstate exerts a significant influence on the humidity sensing properties and *Aurivillius* type oxides exhibit much higher sensitivity than cubic bismuth tungstate.

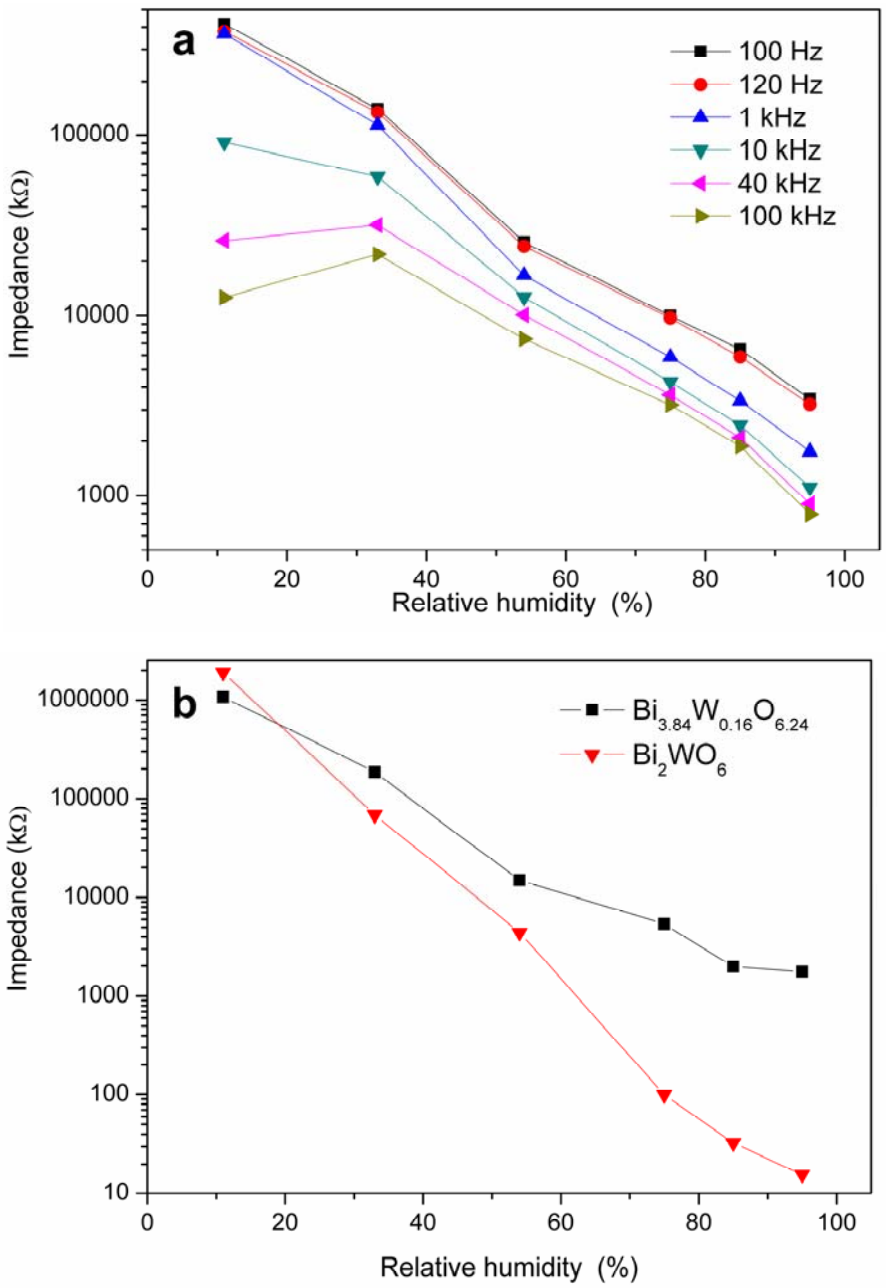

Figure 6.13. (a) Impedance of $Bi_{3.84}W_{0.16}O_{6.24}$ sensors measured at different frequencies and (b) impedance vs. RH plots for $Bi_{3.84}W_{0.16}O_{6.24}$ and Bi_2WO_6 sensors.

6.4 Conclusion

In summary, *Aurivillius* type Bi_2MO_6 oxide films (M = W, Mo) have been fabricated for humidity sensing applications. The humidity tests indicate high sensitivities with impedance changes of 5 orders of magnitude for RH values increasing from 11 to 95 %. Both materials display rapid response and recovery times as well as good reproducibility. The investigation

of the capacitive humidity sensing properties revealed a non-linear capacitance vs. RH relationship indicating the presence of two different "non-Debye" and "ion transport" sensing mechanisms that have been further proved through complex impedance measurements. In comparison with the Bi_2MoO_6-based sensor, Bi_2WO_6 exhibits a higher sensitivity and quicker response, but a slower recovery process as a sensor material. This can be explained in terms of the different surface-to-volume ratios and electronegativity differences between these two materials. The results indicate that *Aurivillius* type oxides have a promising application potential for the fabrication of effective, stable, and low-cost humidity sensors.

References

[1] W. S. Wang, A. V. Virkar, *Sens. Actuators B* **2004**, *98*, 282.

[2] K. M. Willett, N. P. Gillett, P. D. Jones, P. W. Thorne, *Nature* **2007**, *446*, 710.

[3] E. J. Park, J. Kang, J. Park, S. Mun, *Sens. Actuators B* **2001**, *76*, 322.

[4] E. Traversa, *Sens. Actuators B* **1995**, *23*, 136.

[5] A. H. Sun, L. Huang, Y. Li, *Sens. Actuators B* **2009**, *139*, 543.

[6] N. Zhang, K. Yu, Z. Q. Zhu, D. S. Jiang, *Sens. Actuators A* **2008**, *143*, 245.

[7] X. F. Song, Q. Qi, T, Zhang, C. Wang, *Sens. Actuators B* **2009**, *138*, 368.

[8] Y. F. Dong, L. Y. Li, W. F. Jiang, H. Y. Wang, X. J. Li, *Physica E* **2009**, *41*, 711.

[9] X. X. Chen, L. Rieth, M. S. Miller, F. Solzbacher, *Sens. Actuators B* **2009**, *137*, 578.

[10] Q. Qi, T. Zhang, Q. J. Yu, R. Wang, Y. Zheng, L. Liu, H. B. Yang, *Sens. Actuators B* **2008**, *133*, 638.

[11] J. Ricote, L. Pardo, A. Castro, P. Millan, *J. Solid State Chem.* **2001**, *160*, 54.

[12] N. A. McDowell, K. S. Knight, P. Lightfoot, *Chem. Eur. J.* **2006**, *12*, 1493.

[13] Z. G. Yi, Y. X. Li, Z. Y. Wen, S. R. Wang, J. T. Zeng, Q. R. Yin, *Appl. Phys. Lett.* **2005**, *86*, 192906.

[14] M. Hamada, H. Tabata, T. Kawai, *Thin Solid Films* **1997**, *306*, 6.

[15] A. Kudo, S. Hijii, *Chem. Lett*. **1999**, *10*, 1103.

[16] J. W. Tang, Z. G. Zou, J. H. Ye, *Catal. Lett.* **2004**, *92*, 53.

[17] L. S. Zhang, W. Z. Wang, L. Zhou, H. L. Xu, *Small* **2007**, *3*, 1618.

[18] J. Q. Yu, A. Kudo, *Chem. Lett.* **2005**, *34*, 1528.

[19] C. Zhang, Y. F. Zhu, *Chem. Mater.* **2005**, *17*, 3537.

[20] Y. Zhou, F. Krumeich, A. Heel, G. R. Patzke, *Dalton Trans.* **2010**, *39*, 6043.

[21] Y. Zhou, K. Vuille, A. Heel, G. R. Patzke, *Z. Anorg. Allg. Chem.* **2009**, *635*, 1848.

[22] Part of the Accelrys Materials Studio software package, Accelrys Software Inc. 2001-2009.

[23] Z. Li, H. Zhang, W. Zheng, W. Wang, H. Huang, C. Wang, A. G. MacDiarmid, Y. Wei, *J. Am. Chem. Soc.* **2008**, *130*, 5036.

[24] Y. Li, M. J. Yang, Y. She, *Talanta* **2004**, *62*, 707.

[25] E. Traversa, A. Bearzotti, M. Miyayama, H. Yanagida, *Sens. Actuators B* **1995**, *25*, 714.

[26] C. D. Feng, S. L. Sun, H. Wang, C. U. Segre, J. R. Stetter, *Sens. Actuators B* **1997**, *40*, 217.

[27] Y. C. Yeh, Y. Y. Tseng, *J. Mater. Sci.* **1989**, *24*, 2739.

[28] F. Amano, A. Yamakata, K. Nogami, M. Osawa, B. Ohtani, *J. Am. Chem. Soc.* **2008**, *130*, 17650

[29] M. Zhang, C. Hu, H. Liu, Y. Xiong, Z. Zhang, *Sens. Actuators B* **2009**, *136*, 128.

7. Novel $Bi_6S_2O_{15}$ nanowires: Structural, in situ and humidity sensing studies

7.1 Introduction

Recently, 1D nanostructures such as wires, rods and tubes have attracted increasing research attention due to their unique applications in mesoscopic physics, chemical sensors and for the fabrication of nanoscale devices.[1-4] Generally, 1D nanostructures are excellent model systems to investigate the dependence of electrical and thermal transport or mechanical properties on dimensionality and size reduction. Furthermore, they play an important role as both interconnecting and functional units in the fabrication of electronic, optoelectronic and electrochemical devices with nanoscale dimensions.[5] These days, the synthesis, properties and related potential applications of binary oxide nanowires such as ZnO, TiO_2 and SnO_2 are in the focus of intense research activities. These and other binary oxides are furthermore quite promising building blocks for the development of renewable energy sources, as well as for environmental remediation and monitoring.[6-8] On the other hand, ternary oxides with their manifold structure motifs provide significantly more options to adjust the structure of the respective materials according to their specific target applications. Nevertheless, the reported number of ternary oxide nanowires still remains quite limited due to the synthetic challenge of organizing two or more cations into an 1D morphology with a desired structure.[9] Moreover, the structural flexibility of ternary oxides renders the structure determination of newly emerging ternary oxide nanomaterials a demanding yet indispensable task that is essential to influence their morphology and the resulting physiochemical properties.[10]

Among the large family of oxide materials that can be accessed with hydrothermal strategies, bismuth-containing compounds keep attracting considerable interest due to their manifold structural motifs that give rise to oxide types with tremendous technological potential.[11] Whereas many bismuth oxide-based materials were developed through substitution reactions in the cationic sublattice,[12] the effect of anionic substitutions on the structural chemistry and properties of bismuth oxides is an alternative strategy that merits further exploration.[13] Bismuth oxide sulfates, for example, are a particularly interesting starting point for these

studies: until now, their only representatives are defect fluorite type-related compounds with remarkable ionic conductivities.[14]

In the following, we investigate the hydrothermal formation of a new type of bismuth oxysulfate nanowires, $Bi_6S_2O_{15}$, from a multi-disciplinary point of view. Firstly, we discuss the hydrothermal synthesis of the newly discovered material and its structure determination with the help of various electron microscopy techniques. Next, we compare the efficiency of different in- and ex situ approaches for tracking the formation steps of the $Bi_6S_2O_{15}$ nanowires with special emphasis on in situ XAS techniques. This is followed by an investigation of the electric properties of individual $Bi_6S_2O_{15}$ nanowires. To illustrate the application potential of the $Bi_6S_2O_{15}$ nanowires, we have furthermore characterized their humidity sensing properties.

7.2 Experimental

7.2.1 Synthesis

In a typical synthesis, 47 mg (0.1 mmol) of Bi_2O_3 powder (Aldrich, 99.999 %) and 1044 mg (6 mmol) K_2SO_4 (Aldrich, 99.0 %) were placed in 10 mL of distilled water at room temperature and stirred magnetically for 30 min. The final solution was transferred into a Teflon-lined stainless steel autoclave with a capacity of 23 mL, maintained at 160 °C for 72 h, and subsequently cooled to room temperature. The precipitate was collected after filtration, washed with distilled water and ethanol, and dried in air. For the quenching experiments, Bi_2O_3 powder (24 mg, 0.05 mmol), K_2SO_4 (350 mg, 2 mmol), and water (2.5 mL) were added to a glass ampoule (6 mL) which was sealed under atmospheric pressure. The ampoules were heated for 5, 10, 15, 20, 30, 60, or 120 min at 160 °C and subsequently quenched in a NaCl/ice mixture. After the reaction mixture was cooled down, the resulting light-yellow solid products were filtered, washed with distilled water and ethanol to remove adherent residues of K_2SO_4 from the final products and dried in air.

7.2.2 Characterization

PXRD was performed on a STOE STADI P diffractometer in transmission mode (flat sample holders, Ge monochromator and Cu $K_{\alpha 1}$ radiation) equipped with a position sensitive detector. X-ray data for structure refinement were collected between 3° and 110° (2θ) with a step size of 0.01° at room temperature. The structure was refined with Rietveld methods using the ReflexPlus Package of Materials Studio (Accelrys Inc.).[15] No regions were excluded in the refinement. For SEM, performed on a LEO 1530 (FEG) microscope, samples were dispersed in ethanol and subsequently deposited on a silicon wafer. The specimens were investigated without conductive coating at rather low voltage (2 kV) to minimize charging effects. For (scanning) transmission electron microscopy ((S)TEM), the material was deposited on a perforated carbon foil supported on a copper grid. TEM and electron diffraction investigations were performed on a FEI CM30ST (LaB_6 cathode), STEM on a FEI Tecnai F30 microscope (FEG); both instruments were operated at 300 kV. Suitable wires were oriented in diffraction mode along low index directions using a double tilt holder. The camera length of the CM30 was calibrated using a polycrystalline Au sample. In the STEM mode, the electron beam was placed in a selected area, and an elemental analysis by energy-dispersive X-ray spectroscopy (EDXS, EDAX detector) was performed there. Simulations of HRTEM images were calculated using a multi-slice algorithm and of electron diffraction patterns by a kinematical approximation (EMS package).[16] BET surface area measurements were performed on a Coulter SA 3100 in N_2-adsorption mode. The substance was put into an exactly scaled glass vessel and was then dried at 180 °C for 2-3 h under N_2 before the measurement. The infrared (IR) spectra were recorded in KBr on a spectrum BX FT-IR-System spectrometer of PerkinElmer Instruments. Raman spectroscopy was performed on a Renishaw Ramascope 1000 with a green SpectraPhysics Argon laser with a wavelength of 524.5 nm and 50 mW capacity.

7.2.3 In situ EDXRD measurements

In situ EDXRD experiments were performed at HASYLAB (Hamburg) bending magnet

beamline F3, which provides an energy range from 13.7 to 72.8 keV with a maximum at about 20 keV. The diffracted beam is monitored by a nitrogen cooled solid state germanium detector. The detector angle was chosen so that all important Bragg reflections can be detected. The *d*-spacing range is given by $E = 6.199/(d \cdot \sin\theta)$. With a detector angle of approximately 2.36° the observable d-spacing range is 2.1 Å to 11.0 Å. The energy resolution $\Delta d/d$ is about 10^{-2} above 26 keV. The beam was collimated to 0.1 mm giving the best results. For the in situ investigations, autoclaves with glass liners with an internal diameter of 10 mm and a volume of 10 mL were used. A typical experiment was performed starting from 96 mg Bi_2O_3, 350 mg K_2SO_4 and 1.5 mL distilled water, followed by heating to 160 °C. Data collection was started immediately after the introduction of the autoclave into the experimental setting.

7.2.4 In situ QEXAFS experiments

QEXAFS[17] spectra were recorded at the superXAS beamline at the Swiss Light Source (SLS, Villigen, Switzerland) using an continuously scanning monochromator. The ring current was approximately 400 mA and operated in top-up mode. The polychromatic radiation from a superbend magnet, with a magnetic field of 2.9 T and critical energy of 11.9 keV, was focused by mirrors and then monochromatized using a channel cut Si (111) double crystal and an excenter disc of 0.30° in the QEXAFS monochromator. The beam was focused with another mirror on the sample with a spot-size of approximately 100 μm × 100 μm and a flux of about 10^{12} photons/s. The spectra were measured with a setup of three ionization chambers filled with air, two of them placed in front of and behind the sample, while a third one was used to measure a platinum foil as reference in parallel. The signal of the chambers was acquired in synchronization with the angle of the crystal in the QEXAFS monochromator to get an accurate energy scale. The crystal was oscillating with 1 Hz resulting in a maximum time resolution of 0.5 seconds per spectrum. 47 mg Bi_2O_3 and 300 mg K_2SO_4 were embedded between glass wool plugs to fix the solid phase and loaded together with 3 mL water into a home-made spectroscopic cell.[18] Pre-edge background subtraction and

normalization was carried out by fitting a liner polynomial to the pre-edge region and a cubic polynomial to the post-edge region of the absorption spectra by WinXAS 3.10.[19]

7.2.5 Fabrication of individual nanowire transistors

In order to investigate the transport properties of the nanowires, a field effect transistor (FET) based on individual nanowires was fabricated on a Si/SiO_2 (300 nm) substrate through focused ion beam (FIB) fabrication. The detailed experiment process is described as following: a 10 nm layer of Ni and a 100 nm layer of Au were evaporated onto a silicon chip capped with a 300 nm layer of SiO_2. Next, an array of square Ni/Au patterns was fabricated by photolithography method. The size of the square is 100 × 100 μm, and the distance between adjacent patterns is 3 ~ 5 μm, which resulted in (ohmic) source and drain electrodes. The as-grown nanowires were separated by ultrasonication in alcohol for a few minutes. Thus a nanowire suspension was formed and the concentration of nanowires depends on the quantity of nanowires and the amount of alcohol. The nanowire suspension was dropped onto the as-obtained chip so that the nanowires were deposited with certain density after the evaporation of the solvent. Nanowires with two endings contacting a pair of adjacent electrode squares were located by optical microscopy or SEM. The fabricated device was then ready for electrical measurements after electrode bonding.

7.2.6 Sensor fabrication and measurements

The $Bi_6S_2O_{15}$ nanowires were separated by ultrasonication in alcohol for a few minutes. A nanowire suspension was then dropped onto the as-obtained interdigital gold electrodes with a distance of 30 μm fabricated on a Si/SiO_2 (300 nm) substrate by photolithography. The characteristic humidity sensing curves were measured with a TH2617 LCR analyzer (Changzhou, China) with an applied voltage of 1 V and different frequencies. Controlled humidity environments for measurements were achieved by using saturated aqueous solutions of different salts (LiCl, $MgCl_2$, $Mg(NO_3)_2$, KCl and KNO_3) in a sealed glass vessel with

corresponding RH values of 11 %, 33 %, 54 %, 75 %, 85 % and 95 %, respectively. All sensors were placed into the chamber with RH of 95 % for 10 hour aging prior to humidity sensing measurements that were all carried out at ~25 ^{o}C.

7.3 Results and discussion

7.3.1 Conversion of bulk Bi_2O_3 into nanowires

The starting material, bulk α-Bi_2O_3, displays no nanoscale or anisotropic features at all (cf. Figure 7.1 a). Interestingly, after hydrothermal treatment in the presence of K_2SO_4 and water, the commercial Bi_2O_3 particles are transformed into high aspect ratio nanowires with diameters in the range of 100-300 nm and lengths exceeding several tens of micrometers (Figure 7.1 b).

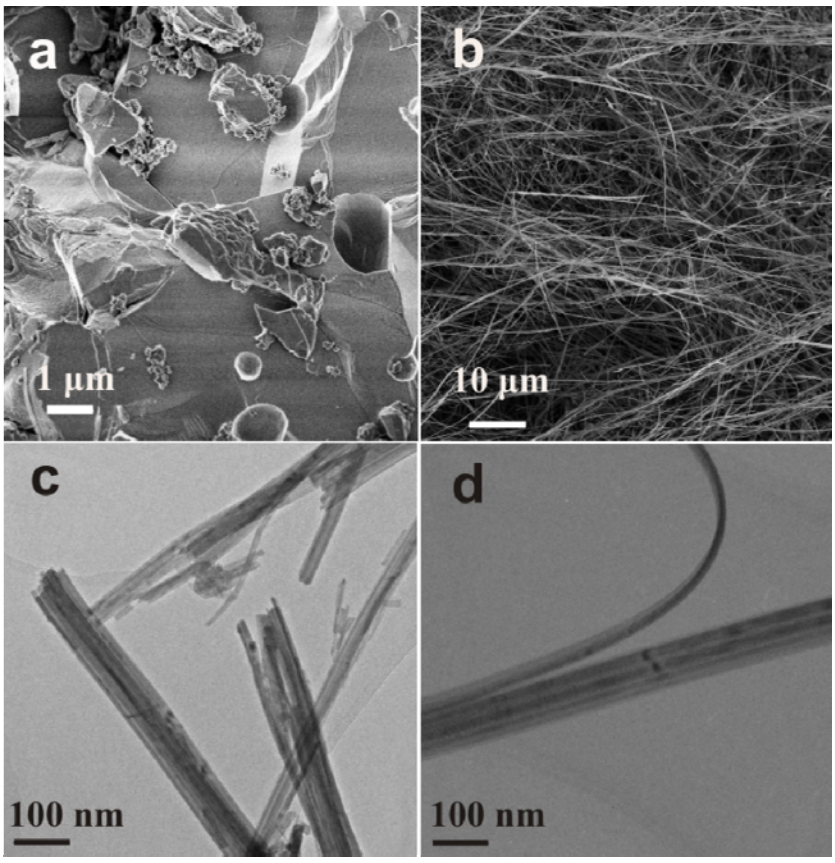

Figure 7.1. Representative SEM images of (a) Bi_2O_3 precursor and (b) nanowire products; (c) and (d) representative TEM images of the nanowire products.

TEM images (Figure 7.1 c) reveal that the nanowires in fact are bundles of smaller fibers that are nearly arranged in parallel. These smaller fibers are 10-50 nm thick. Selected single fibers were separated from the bundle and tilted (bent fiber in Figure 7.1 d). The small width in conjunction with a dark contrast in the TEM image indicates a high thickness in viewing direction and thus points to a tape-like morphology.

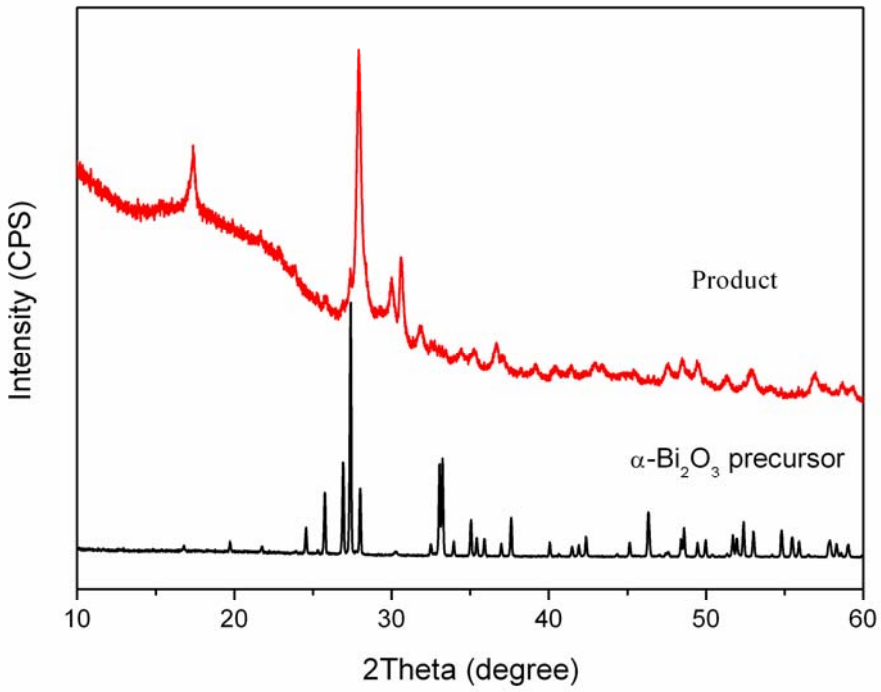

Figure 7.2. XRD patterns of the α-Bi_2O_3 precursor and the nanowire products after hydrothermal treatment in the presence of K_2SO_4.

The diffraction peaks of the starting material can be indexed to monoclinic α-Bi_2O_3 (cf. JCPDS No. 71-0465). A broadening of the peaks in the XRD pattern of the product clearly indicates a small crystal size (cf. Figure 7.2). The N_2 BET surface area of the nanowires is 10 m^2/g. This confirms the increase in surface and nanostructuring during the reaction, because the BET surface area of the starting material is significantly lower (0.2 m^2/g). However, the XRD patterns of the product can not be indexed on the basis of any known Bi_2O_3 polymorph. EDXS analyses of the nanowires demonstrated that they display a homogeneous composition with Bi and O as the main components (Figure 7.3). A careful evaluation of the strongest Bi peak caused by ionization of the M shell at about 2.5 keV revealed a small but significant

shoulder that can be attributed to the K_α peak of S at 2.31 keV (inset in Figure 7.3). The presence of sulfur as SO_4^{2-} in the products was confirmed through IR spectroscopy that displayed the triply asymmetric stretching mode ν_3 (F_2) of SO_4^{2-} at 1106 and 1024 cm^{-1} and the non-degenerate stretching mode ν_1 (A_1) of SO_4^{2-} as one band at 960 cm^{-1} (cf. Figure 7.4).[20] However, the XRD patterns of the nanowire products did not correspond to any of the known bismuth oxide sulfate phases and all primary efforts to index this unknown phase failed due to the broad diffraction peaks and poor crystallinity

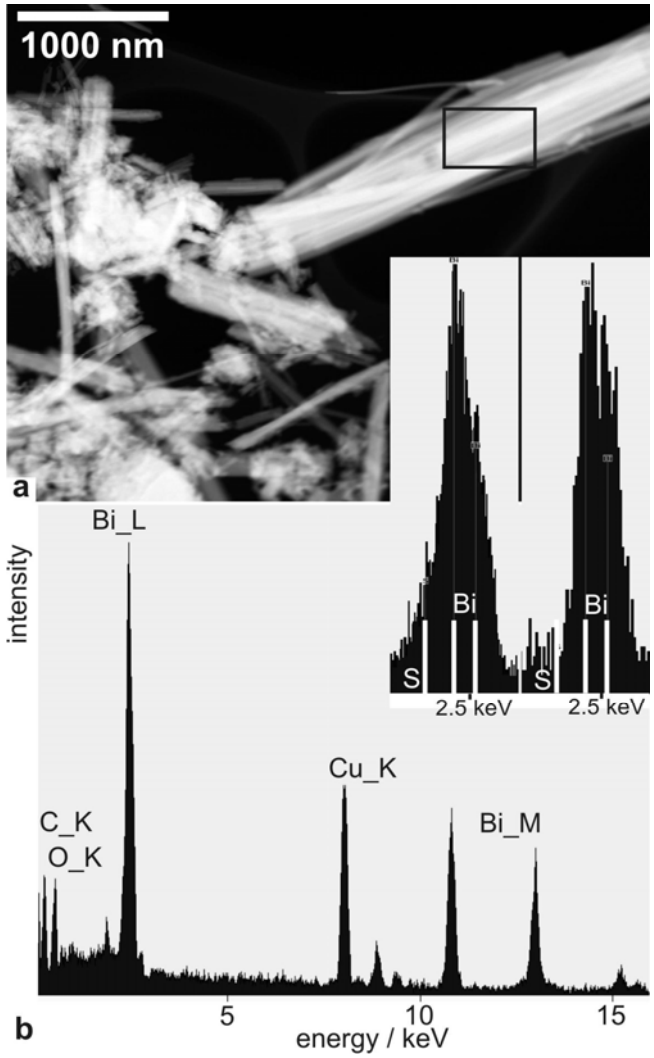

Figure 7.3. (a) STEM image of nanowires and (b) EDXS analysis of the area marked in (a). The Cu peak is due to the supporting Cu grid, the C peak to the C foil and contamination. The inset shows sections of the EDX spectra of the nanowires (left) and of a S-free Bi compound (right) for comparison. Simulation and quantification of the spectra clearly indicate the presence of S in the nanowires with a Bi:S ratio of ca. 2-3 : 1.

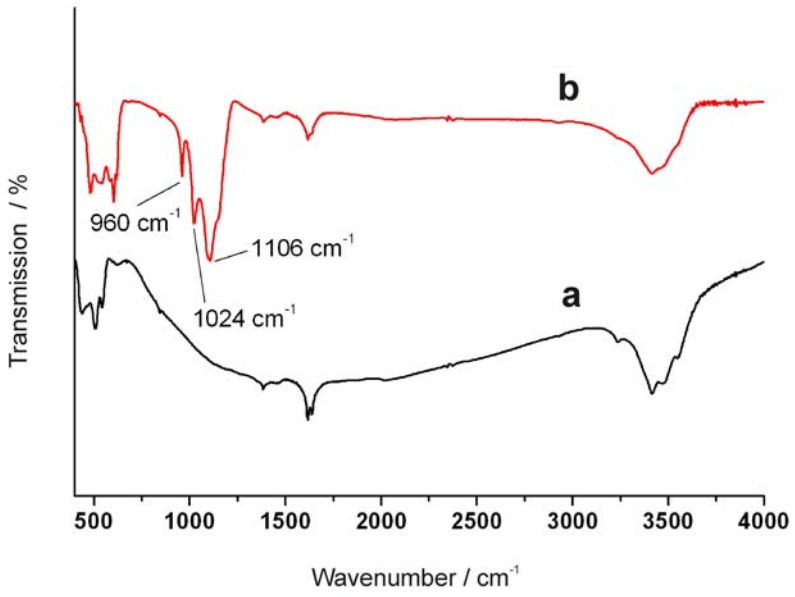

Figure 7.4. IR spectra of (a) the α-Bi_2O_3 precursor and (b) the nanowire products obtained in the presence of K_2SO_4.

7.3.2 Structure determination of the bismuth oxysulfate nanowires

Raman spectroscopy as a complementary spectroscopic technique to IR further permitted the assignment of different sulfate components and structural motifs and the results are shown in Figure 7.5. The Raman bands of the fundamental vibrational modes of the sulfate ion are reported to appear at 450, 614, 981, and 1105 cm^{-1}, respectively.[21] Furthermore, it is well known that Raman lines originating from degenerate vibrational modes can be splitted into multiple lines due to the lowering of molecular symmetry in a crystal lattice. The triply degenerate v_2 (E) bending mode and v_4 (T_2) vibrational modes of the sulfate ion (observed at 450 and 614 cm^{-1}) are observed as a triplet at 428, 444 and 480 cm^{-1}, and three corresponding Raman-active vibrations at 582, 609 and 629 cm^{-1}, respectively. The doublet peaks appearing at 1023 and 1088 cm^{-1} are likely to originate from the doubly degenerate v_3 (T_2) vibrational mode of the sulfate ion that is located at 1105 cm^{-1}. The three sharp Raman bands observed at 154, 188 and 316 cm^{-1} can be assigned to three unique Bi-O stretching modes.[22] Recently, empirical relations have been established between the metal-oxygen Raman stretching

frequencies and metal-oxygen bond lengths and they can be quantified with a simple exponential expression:[23]

$$\nu = A\exp(BR) \qquad (Eq.\ 7.1)$$

where A and B are fitting parameters, ν is the Raman stretching frequency in wavenumbers, and R is the metal-oxygen bond length in Å. This method has already been used to determine the Bi-O bond lengths and oxygen coordinations of BiO_x polyhedra from the according Raman spectra.[23] In line with this approach, A and B can be assigned as 92760 and -2.511, respectively. Therefore, the Raman stretching frequencies at 154, 188 and 316 cm^{-1} correspond to Bi-O bond lengths of 2.55(3), 2.48(3) and 2.26(3) Å, the latter two being in line with the obtained structural model of the product (cf. Table 7.1). Based on the combined results of IR and Raman spectroscopy, it is expected that the structure of bismuth oxysulfate contains BiO_x polyhedra and SO_4^{2-} tetrahedra as key elements.

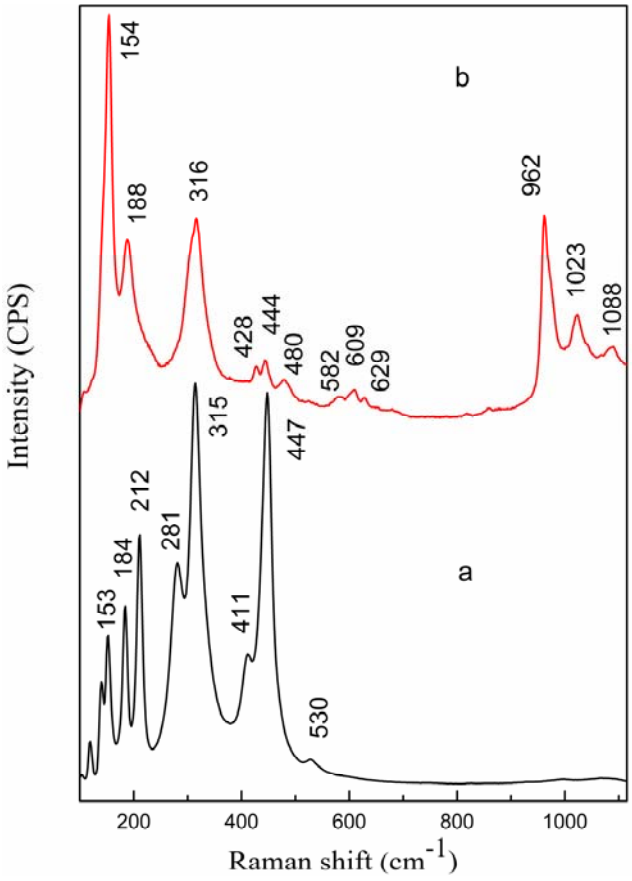

Figure 7.5. Raman spectra of (a) the α-Bi_2O_3 precursor and (b) the nanowire products.

Electron diffraction patterns of isolated nanowires demonstrate that they are single crystalline. SAED patterns were recorded from several nanowires along different directions to determine the unit cell parameters and to assign possible space groups (Figures 7.6 and 7.7). The shortest distances observed there correspond to real-space values of approximately 10.2 and 9.8 Å, respectively. Besides primitive spot arrays, certain SAED patterns show extinctions that point to the centering of one crystal face of the unit cell (Figures 7.6 c and 7.7 a, c - d). Owing to this centering, the 9.8 Å distance is half of a probable lattice parameter. The frequent observation of *d* values of ca. 5.8 Å and its half, i.e. 2.9 Å, reveal a structural relationship to the cubic fluorite type (e.g., a = 5.66 Å for δ-Bi_2O_3).[24] This distance appears to be another lattice parameter and furthermore corresponds to the needle axis (see below). If the nanowire of Figure 7.6 a is slightly tilted from the zone axis, the first order Laue zone (FOLZ) is observable (Figure 7.6 b). In the FOLZ, reflections appear that indicate a doubling of the distance of 2.9 Å. This additional reflection condition points to the presence of a glide plane besides the face centering. The SAED pattern reproduced in Figure 7.6 a is the most frequently observed one, indicating a preferred orientation of the nanowires. Obviously, this orientation corresponds to the plane of the tape-like fibers that preferentially lie flat on the carbon support of the TEM grid (Figure 7.1 d). A typical problem for the characterization of such anisotropic structures is the impossibility to observe the plane perpendicular to the needle axis. Therefore, series of electron diffraction patterns were recorded here by tilting single crystalline nanowires in different orientations for a more comprehensive exploration of reciprocal space. A series of SAED patterns obtained by rotating around the axis with 9.8 Å is shown in Figure 7.7. Considering the distances perpendicular to this axis and the tilt angle measured from the goniometer of the microscope, the reciprocal plane perpendicular to the rotation axis was reconstructed (Figure 7.7 e). A shortest distance of ca. 6.2 Å occurs between the observed reflections. Due to the presence of extinct reflections – one of them indicated by the arrow in Figure 7.7 e – this distance has to be doubled.

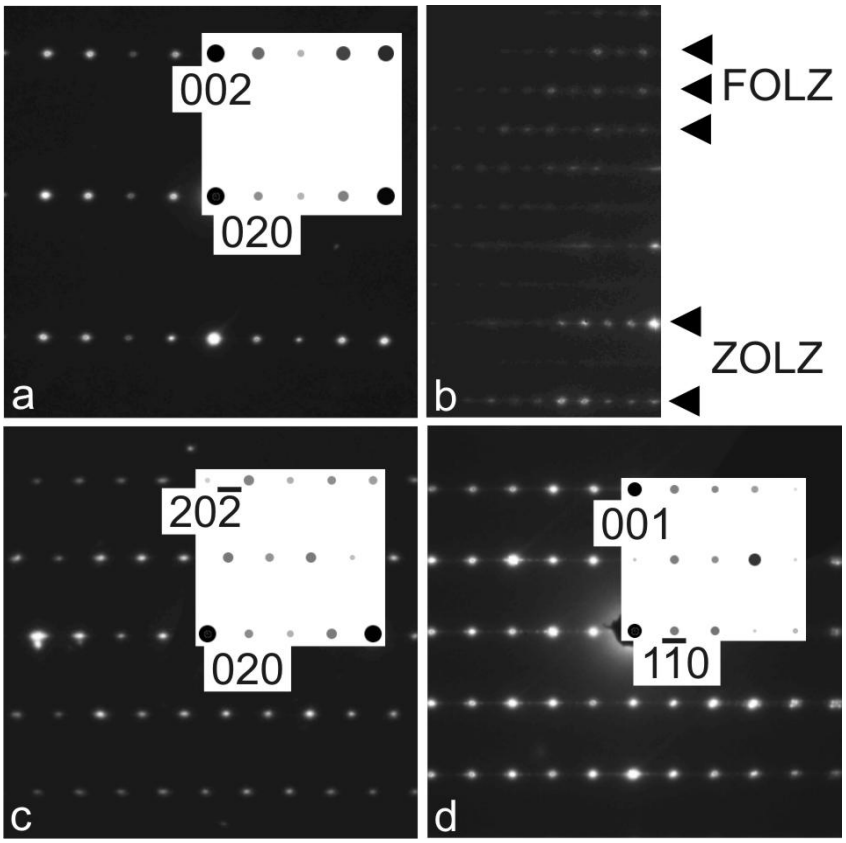

Figure 7.6. Typical SAED patterns of single nanowires oriented along [100] (a), [101] (c) and [110] (d). Some indices *hkl* are given below the corresponding reflection. The nanowire in (b) is slightly tilted out of the zone axis [100] so that the first order Laue zone (FOLZ) appears ((b) is reproduced with a different magnification). The insets show simulated ED patterns with inverted contrast.

The electron diffraction patterns can be indexed on the basis of an orthorhombic unit cell with the following approximate lattice parameters: $a \approx 12.0$; $b \approx 19.8$; $c \approx 5.8$ Å. Remarkably, the longest distance appearing in the SAED pattern, namely 10.2 Å, is not an axis of the unit cell but represents the *d* value of the 110 plane. The observed reflection conditions are: $h + k = 2n$ for *hkl* and $k,l = 2n$ for 0*kl*. Thus, the symmetry present in the observed SAED patterns is consistent with all space groups having the partial symbol *Cc*_ _.[25] With these cell parameters, indices could be assigned to all reflections present in the SAED patterns (Figure 7.6). Sections of simulated SAED patterns calculated with the structural data obtained from XRD powder diffraction (Table 7.1) are shown as insets in Figures 7.6 and 7.7. The sites of

the reflections in simulated and experimental patterns agree with each other confirming the metric and symmetry of the proposed unit cell.

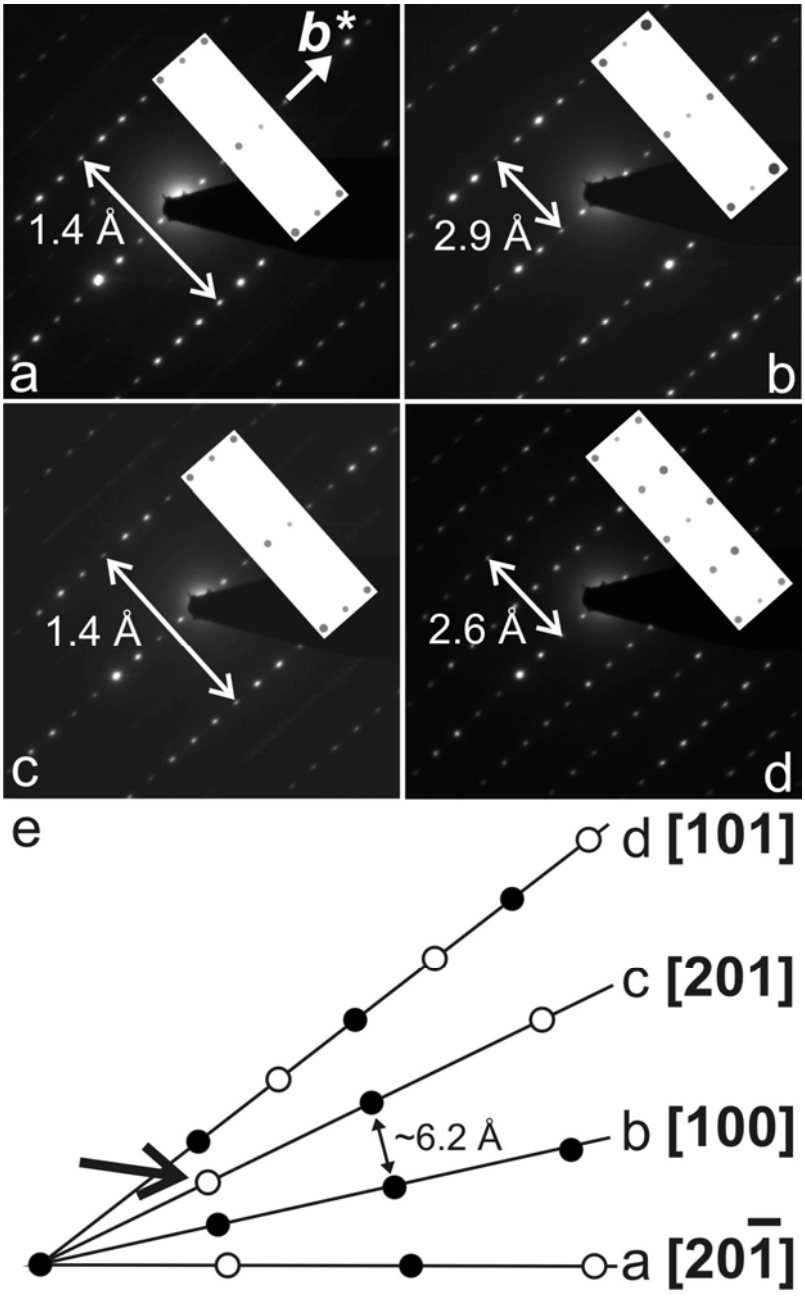

Figure 7.7. (a)-(d) SAED patterns of a tilt series with the rotation axis being the *a** axis. (e) Model of the plane *b***c**. Filled circles represent observed reflections and empty ones extinct reflections in the directions perpendicular to *c**. The large arrow indicates an extinction that can only be assigned after doubling the lattice parameter (see text). Some distances between reflections are given as real space values. (The *d*-values were measured with an accuracy of ca. ± 0.1 Å, the tilting angles were determined from the goniometer of the TEM with an accuracy of ca. ± 1 degree.)

The unit cell parameters and symmetry obtained from the evaluation of ED patterns and the structural information from IR and Raman spectroscopy indicate a resemblance to the bismuth chromate phase $Bi_6Cr_2O_{15}$.[26]

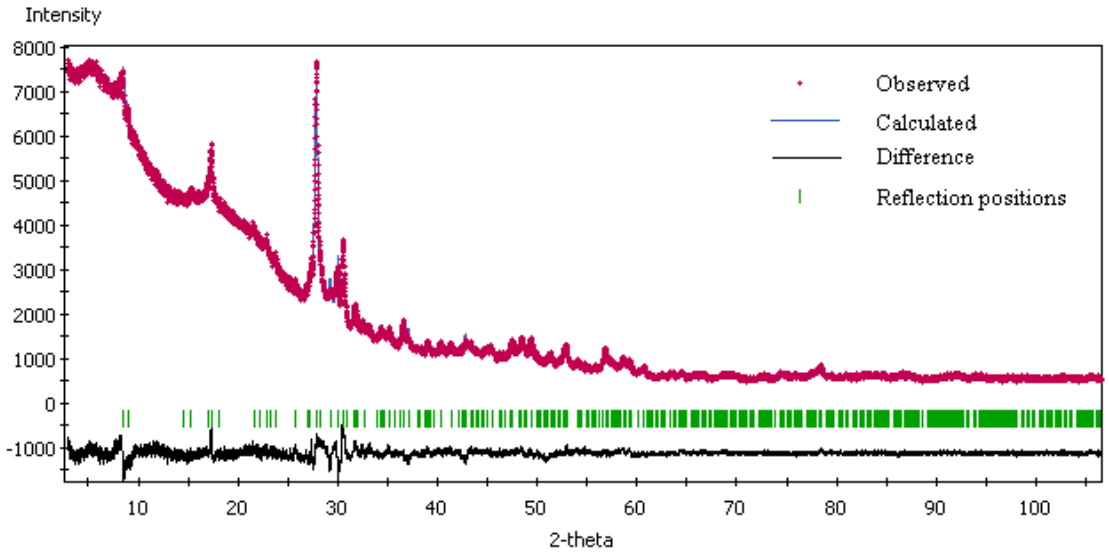

Figure 7.8. Rietveld refined powder X-ray diffraction pattern of the nanowire product (dotted line: observed intensity data, solid line: calculated pattern, bottom line: difference between the observed and calculated intensities, vertical ticks: Bragg positions; R_{wp} = 3.75 % and R_p 2.63 %).

This ternary oxide is constructed from $(Bi_{12}O_{14})_n^{8n+}$ columns and CrO_4^{2-} tetrahedra (a = 12.30184(5), b = 19.87492(7), c = 5.88162(2) Å, S.G. *Ccc2*).[26] Therefore, $Bi_6Cr_2O_{15}$ was used as a starting model for the structure refinement of the apparently isostructural nanowires. The Rietveld refinement as shown in Figure 7.8 resulted in R_{wp} of 3.75 % and R_p of 2.63 %, because only the bismuth sites were refined. Compared to the heavy Bi atoms, the scattering contribution of oxygen and sulfur atoms to the overall powder XRD patterns is small so that the lighter atoms cannot be easily distinguished from the Bi centers due to the limited data quality obtained from the highly anisotropic nanowires. Therefore, no attempt was made to refine the oxygen and sulfur sites, and they were left fixed on the same positions as in $Bi_6Cr_2O_{15}$. The final atomic parameters for the nanowire structure are given in Table 7.1. These refinement results demonstrate that the nanowires represent a new bismuth oxysulfate type, $Bi_6S_2O_{15}$ (a = 12.206(1), b = 19.611(2), c = 5.8388(7) Å; S.G. *Ccc*2). The crystal

structure of $Bi_6S_2O_{15}$ is closely related to $Bi_6Cr_2O_{15}$ and can thus be described as $(Bi_{12}O_{14})_n^{8n+}$ columns extending along the *c* axis. The columns are separated by SO_4^{2-} tetrahedra with each column surrounded by eight SO_4^{2-} tetrahedra (cf. Figure 7.9 a). Similar structure motifs appear also among the Bi-Mo oxides.[27]

Table 7.1. Atomic parameters for $Bi_6S_2O_{15}$ (a = 12.206(1), b = 19.611(2), c = 5.8388(7) Å, S.G. *Ccc*2 (No. 37)). The Bi positions were obtained from Rietveld refinement while the given positions of O are the same as in $Bi_6Cr_2O_{15}$ with that of S corresponding to the Cr site (R_{wp} = 3.75 % and R_p 2.63 %).

Atom	Site	x	y	z
Bi1	8*d*	0.1003 (5)	0.0639 (3)	0.273 (4)
Bi2	8*d*	0.1066 (5)	0.2037 (2)	0.858 (4)
Bi3	8*d*	0.3307 (3)	0.0668 (3)	0.871 (4)
S	8*d*	0.3667	0.1642	0.3499
O1	8*d*	0.2534	0.0007	0.094
O2	8*d*	0.0860	0.1561	0.1037
O3	8*d*	0.8435	0.0962	0.3829
O4	4*α*	0.0000	0.0000	0.0579
O5	8*d*	0.3097	0.1758	0.1030
O6	8*d*	0.2725	0.1599	0.5563
O7	8*d*	0.4292	0.091	0.3447
O8	8*d*	0.4516	0.2241	0.4149

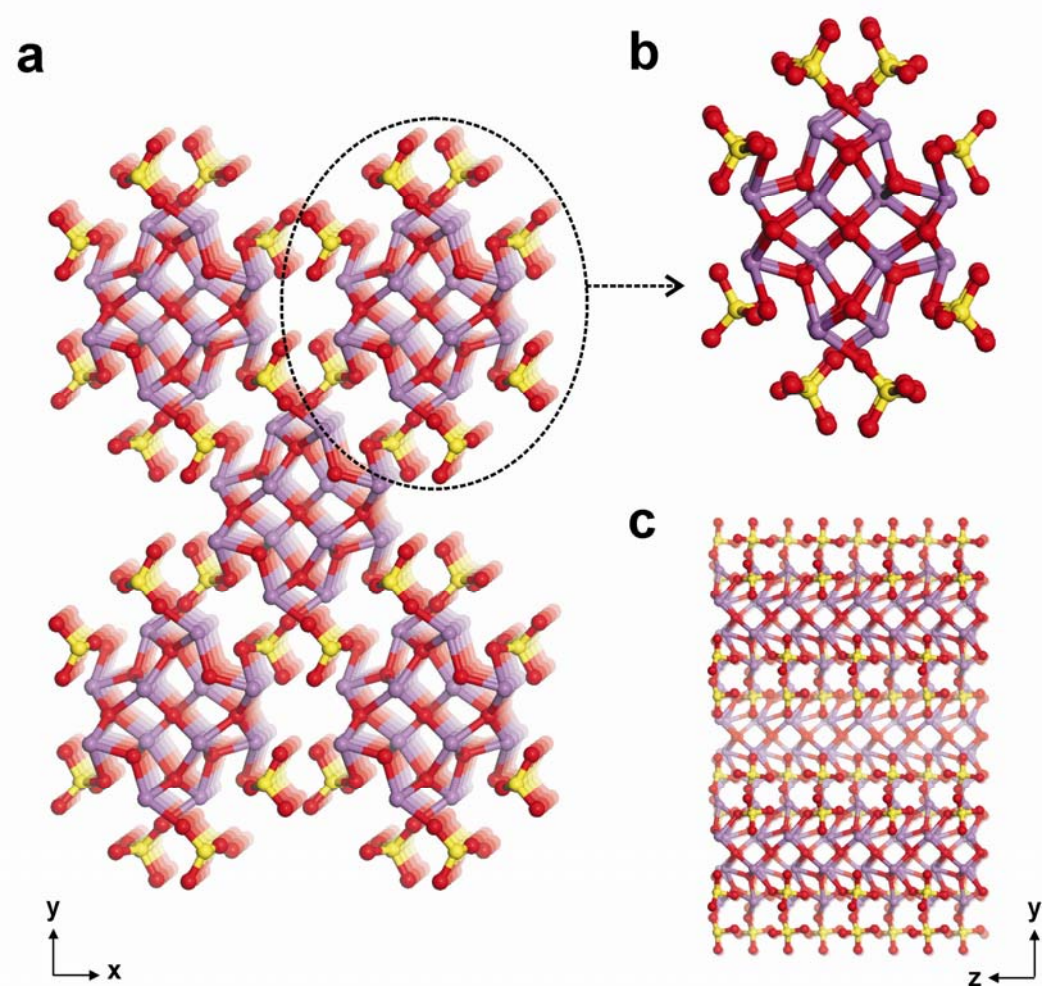

Figure 7.9. (a) Crystal structure of $Bi_6S_2O_{15}$; (b) $(Bi_{12}O_{14})_n^{8n+}$ columns surrounded by SO_4^{2-} tetrahedra; (c) structural view along the *b* axis. Oxygen atoms are omitted for clarity (Bi = violet, O = red, S = yellow).

To further prove the validity of the structure of $Bi_6S_2O_{15}$, HRTEM images (Figure 7.10) of the nanowires were recorded close to Scherzer defocus so that the centers of high scattering potential, i.e. the Bi atoms, appear with dark contrast. All images show a perfect crystal structure. As already observed by electron diffraction, the needle axis is always parallel to the crystallographic *c* axis. The HRTEM investigation is impeded by an electron beam induced phase separation leading to the formation of dark patches on the crystal surface. They have a diameter in the range of 2-5 nm (Figure 7.10). This behavior is well-known for Bi oxide compounds. Nonetheless, the simulated images (insets in Figure 7.10) fit quite well with the experimental ones and thus confirm the aforementioned structural model (cf. Figure 7.9). The agreement is good for the HRTEM image recorded along [100] and fair for that along [110].

In the latter case, the dark patches of the simulation and experimental image are at the same sites confirming the correct positions of the Bi atoms in this projection. However, the observation that some bright patches appear more intense in the experimental image than in the simulation remains inexplicable.

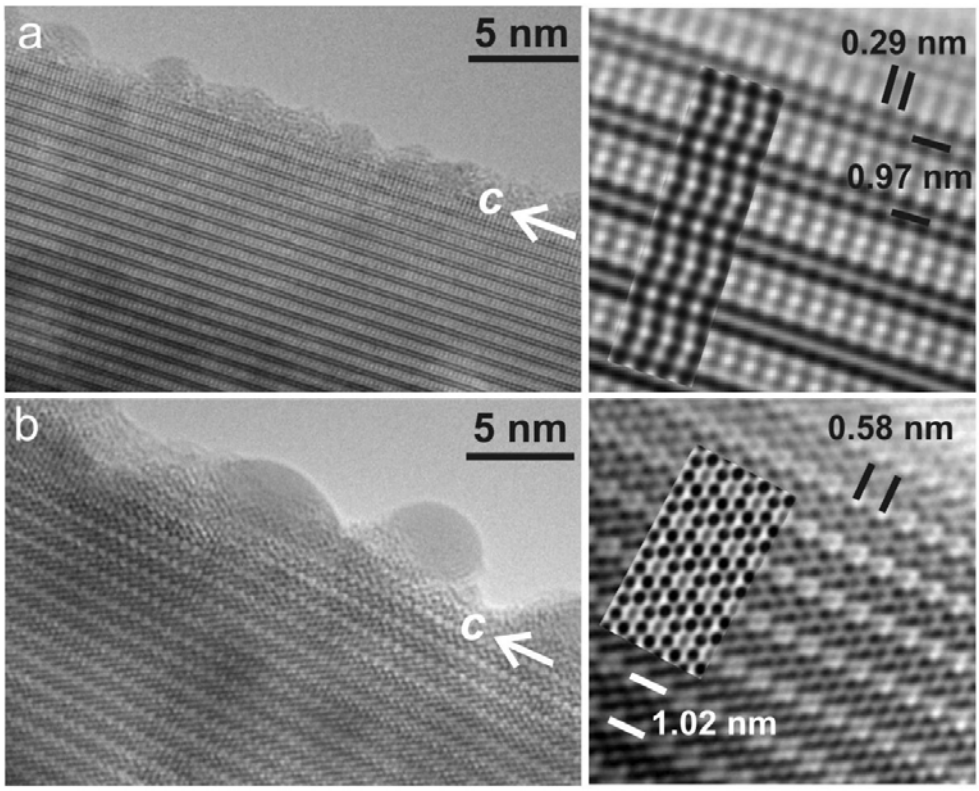

Figure 7.10. HRTEM images of nanowires recorded close to Scherzer defocus along [100] (a) and [110] (b). The *c* axis is oriented in parallel to the fiber axis. The magnified images on the right are Fourier-filtered using only the Bragg reflections for image formation. Insets show simulations with the structural data listed in Table SI-1 and the following microscope parameters used for the simulation: V = 300 kV; C_s = 1.2 mm; focus f = -40 nm (a); -30 nm (b); focus spread Δf = 10 nm; radius of the objective aperture = 10 nm^{-1}; beam half convergence = 1 mrad; crystal thickness t = 4.4 (a) and 4.6 nm (b).

7.3.3 In situ EDXRD/XAS investigations

In order to monitor the hydrothermal formation process of $Bi_6S_2O_{15}$ nanowires, ex situ quenching experiments were performed for 5, 10, 15, 20, 30, 60, or 120 min. at 160 °C. SEM images of selected quenched products are shown in Figure 7.11. Short fibers and irregular particles covered by small rods clearly occur already after only 5 min. of reaction time. This

points to a fast onset of the reaction so that the starting material is partially converted into short fibers on a time scale of minutes. Prolonged reaction times (15 min.) further increase the amount of nanowire products. After a reaction time of 1 h, the irregularly shaped α-Bi_2O_3 particles vanish almost entirely. Instead, short fibers with lengths in the micrometer range appear that grow at the cost of the bulk starting material. Several hours of treatment in water at 160 °C are sufficient to convert the starting material quantitatively into nanowires with microscale lengths.

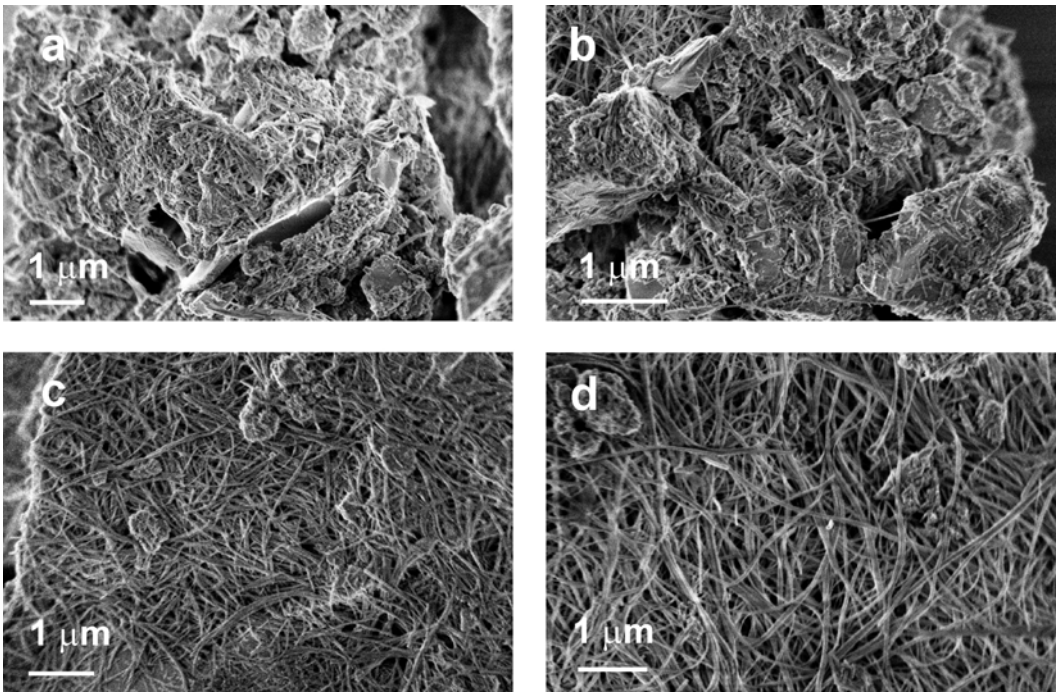

Figure 7.11. Representative SEM images of the products obtained after different reaction times: (a) 5 min; (b) 15 min; (c) 1 h; (d) 2 h.

However, the in situ EDXRD patterns recorded at different reaction times remain practically identical to the starting material α-Bi_2O_3 (cf. Figure 7.12). This observation can be explained as follows: during the measured reaction time, the products still consist of a mixture of α-Bi_2O_3 particles and $Bi_6S_2O_{15}$ nanowires and 72 h of reaction time are required to achieve a complete conversion. As the α-Bi_2O_3 particles display a higher degree of crystallinity, the intensity of their reflection completely outperforms the weaker scattering contribution of the less crystalline and highly anisotropic $Bi_6S_2O_{15}$ nanowires. Furthermore, the strongest

diffraction peak of $Bi_6S_2O_{15}$ appears at 27.899° so that it overlaps with the (012) reflection (28.00°) of α-Bi_2O_3. This renders the monitoring of the reaction progress through in situ EDXRD almost impossible. However, on the other hand, both the quenching experiments and in situ EDXRD experiments clearly show that the α-Bi_2O_3 precursor does not dissolve completely during the initial phase of the reaction.

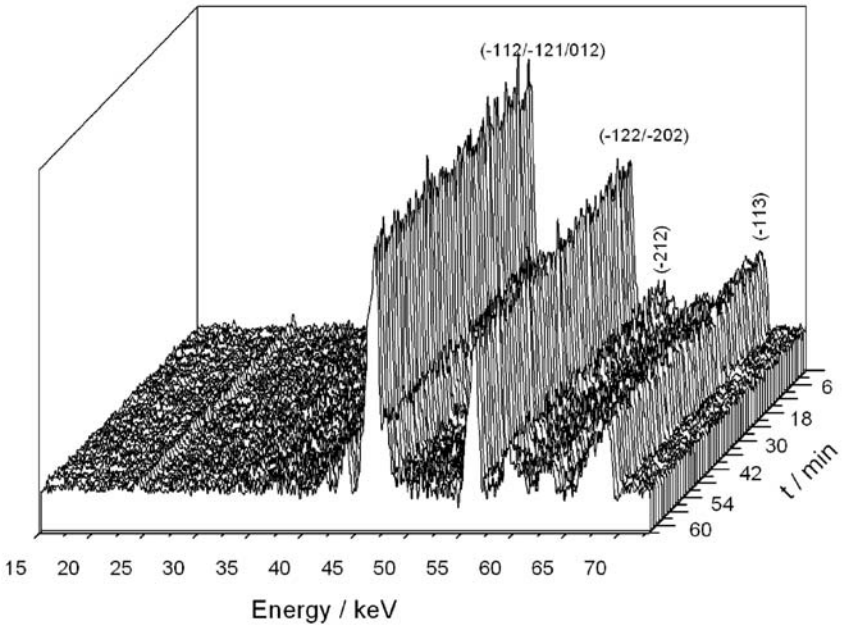

Figure 7.12. Time-resolved EDXRD pattern of the hydrothermal reaction at 160 °C.

The in situ observation of the liquid phase is essential to obtain the necessary information regarding the dissolution process of the α-Bi_2O_3 precursor during the formation process of $Bi_6S_2O_{15}$ nanowires. XAS gives access to the short-range order, which is ideally suited to monitor both crystalline and amorphous solid intermediates as well as species in solution. We used a special in situ XAS cell to study both the liquid phase and the solid/liquid interface of our hydrothermal system through QEXAFS.[17] The in situ QEXAFS spectra were recorded with a time resolution of 0.5 s. However, this time resolution was reduced to 2 s by averaging two spectra for one direction due to absorption effects of the solid phase. The QEXAFS spectra (only selected spectra are shown for clarity) at the Bi L_3-edge were taken both in the middle of the cell (liquid phase, cf. Figure 7.13) and at the bottom (mainly solid phase, Figure

7.14). Due to the inherent data intensity reduction, only the XANES region was analyzed regarding the coordination chemistry and electronic structure of the bismuth oxide-based species. The normalized spectra did not display any changes of the starting material α-Bi_2O_3 (cf. Figure 7.14). Although the liquid phase appeared to be free of bismuth-containing species at first glance, a Bi L_3-edge jump appeared after averaging over 200 spectra and increased during the reaction process (cf. Figure 7.13). The concentration of Bi in our special in situ cell autoclave was calculated to 7×10^{-5} M using a path length of 15 mm and the observed small absorption step of 0.002. This value could be verified through comparison with the Mo K-edge absorption of a calibration solution (0.1 mM Na_2MoO_4) and by relating the absorption coefficient of Bi at the Bi L_3-edge (initial Bi concentration of 0.03 M, cf. Experimental) to the absorption coefficient at the Mo K-edge: ca. 0.4 mol % Bi is dissolved during the reaction at 160 °C. After the in situ QEXAFS experiments, XRD and SEM characterizations were performed on the isolated product which shows the onset of 1D nanostructuring, but longer reaction times are required to fully convert irregular particles into nanowires in analogy to the ex situ experiments (Figure 7.11).

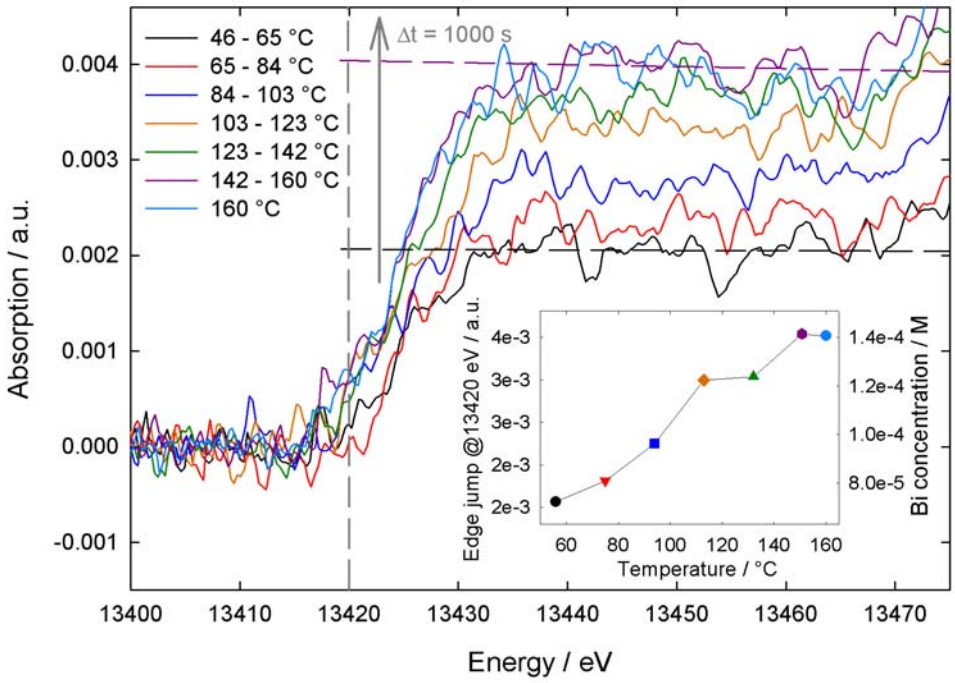

Figure 7.13. Bi L_3-edge XANES spectra recorded in QEXAFS mode (liquid phase), inset: temperature-dependent Bi concentration.

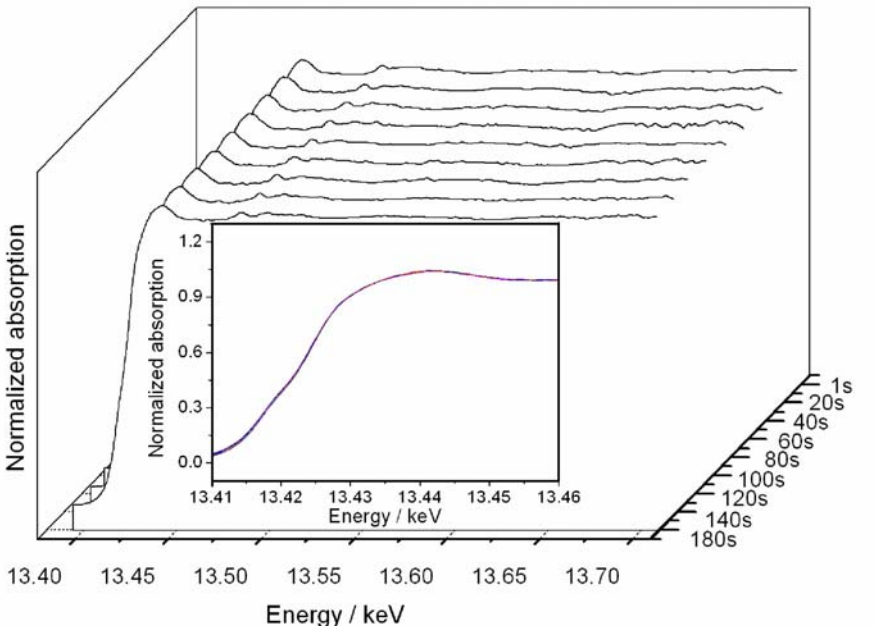

Figure 7.14. Bi L_3 edge EXAFS spectra recorded in QEXAFS mode during the hydrothermal reaction (mostly solid phase at the bottom of the in situ autoclave), inset: Bi L_3 edge XANES spectra.

The above ex situ- and in situ studies suggest in their entirety that the formation of $Bi_6S_2O_{15}$ nanowires originates at the interface of the solution and the surface of bulk α-Bi_2O_3 particles. We propose that $Bi_6S_2O_{15}$ nanowires are formed via a two-step sequence starting from a minute dissolution of the bulk α-Bi_2O_3 precursor under hydrothermal conditions, followed by $Bi_6S_2O_{15}$ rod nucleation and growth at the solid/liquid interface. Firstly, the surface of the bulk Bi_2O_3 particles slightly dissolves in water in the beginning of hydrothermal treatment. It has been demonstrated that different oxoanions, e.g. WO_4^{2-}, CrO_4^{2-} and SO_4^{2-}, can be incorporated into the Bi_2O_3 structure.[13, 14] Owing to the excess of SO_4^{2-} employed in the Bi_2O_3/K_2SO_4 hydrothermal system, the small amounts of dissolved Bi species in solution are extremely likely to react with SO_4^{2-} to form $Bi_6S_2O_{15}$ nuclei on active sites of the pristine α-Bi_2O_3 particles. The subsequent growth along the *c* axis of the $Bi_6S_2O_{15}$ unit cell results in the formation of the nanowires. The gradual transition of the bulk α-Bi_2O_3 particles into nanowires can be clearly observed from the ex situ SEM images (Figure 7.11). They illustrate how the emerging $Bi_6S_2O_{15}$ nanowires grow at the expense of the decomposing precursor

particles so that the length of the nanowires can be increased to dozens of micrometers through prolonged hydrothermal treatment. The driving force for the anisotropic growth of $Bi_6S_2O_{15}$ nanowires is likely to arise from the inherent anisotropy in the crystal structure of $Bi_6S_2O_{15}$ as no template has been used in our current route. As outlined above, the structure of $Bi_6S_2O_{15}$ contains linear $(Bi_{12}O_{14})_n^{8n+}$ columns parallel to the *c* axis as a key motif (Figure 7.9 c), which creates a tendency towards the growth of one-dimensional nanoparticles. In addition, HRTEM images confirm that $Bi_6S_2O_{15}$ nanowires display oriented growth along the *c* axis (Figure 7.10). This phenomenon is similar to the anisotropic growth of MoO_3, $LnPO_4$ and $DyPO_4$ under hydrothermal conditions.[28, 29] On the other hand, it has been reported that SO_4^{2-} can act as a capping agent that is preferentially adsorbed on the faces parallel to the *c* axis of $K_{0.33}WO_3$ nanocrystals, thereby leading to the growth of $K_{0.33}WO_3$ nanowires.[30]

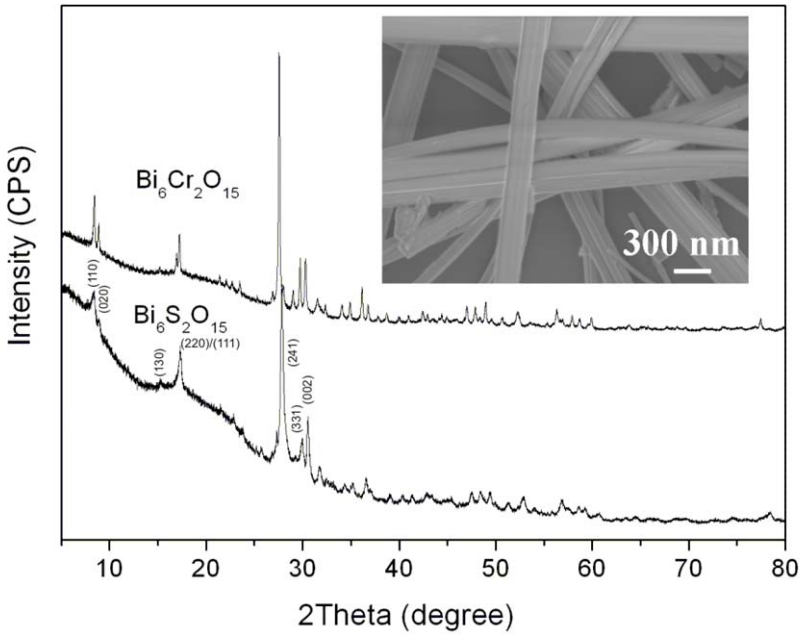

Figure 7.15. XRD patterns of $Bi_6Cr_2O_{15}$ and $Bi_6S_2O_{15}$; inset: SEM image of $Bi_6Cr_2O_{15}$.

In order to obtain further indications that SO_4^{2-} did not work as such a capping agent here, we tried to prepare $Bi_6Cr_2O_{15}$ fibers via the present route. As expected due to the structural similarity of both compounds, $Bi_6Cr_2O_{15}$ fibers could be obtained by simply replacing K_2SO_4 with K_2CrO_4 in the procedure described above. SEM images as well as the XRD of

$Bi_6Cr_2O_{15}$ fibers are shown in Figure 7.15. In comparison with the XRD patterns of $Bi_6S_2O_{15}$, all the diffraction peaks are slightly shifted to lower angles so that they can be indexed to a larger unit cell (observed lattice constants: a = 12.2951(4) Å, b = 19.8511(5) Å, c = 5.8905(2) Å, S.G. *Ccc*2). The SEM images demonstrate that the one-dimensional morphology of $Bi_6Cr_2O_{15}$ is similar to the $Bi_6S_2O_{15}$ nanowires. Their formation strongly supports that the driving force for the anisotropic growth of $Bi_6S_2O_{15}$ nanowires stems from the inherently anisotropic crystal structure of $Bi_6S_2O_{15}$ with $(Bi_{12}O_{14})_n^{8n+}$ columns. Furthermore, our results demonstrate that a comprehensive understanding of the hydrothermal reaction pathway is crucial to access other nanostructured oxides – and this is indispensable for their targeted synthesis.

7.3.4 Electrical properties of individual $Bi_6S_2O_{15}$ nanowires

Individual $Bi_6S_2O_{15}$ nanowire transistors were fabricated to investigate the electrical properties of this novel material. Figure 7.16 shows the scheme and a representative SEM image of a typical 1D $Bi_6S_2O_{15}$ nanowire-based transistor structure. The back of the low-resistance Si was used as a gate electrode. The channel width was limited by the diameter of the nanowires. Typical output and transfer characteristics of our FET with a channel length, L, of approximately 17 µm and width, W, of 100 nm were obtained according to Figure 7.16. The gate voltage V_g was increased from -5 to 20 V in steps of 5 V.

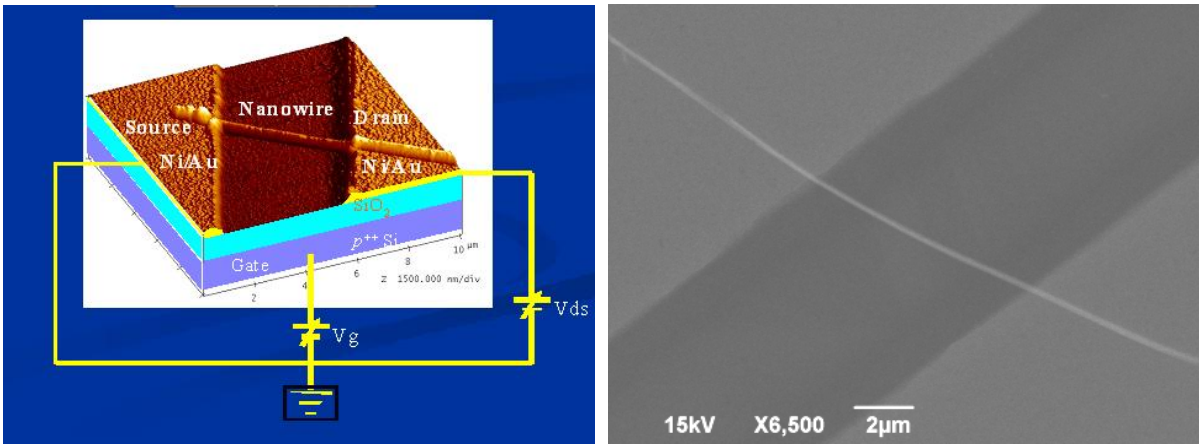

Figure 7.16. Scheme (left) and SEM image (right) of a single $Bi_6S_2O_{15}$ nanowire-based FET.

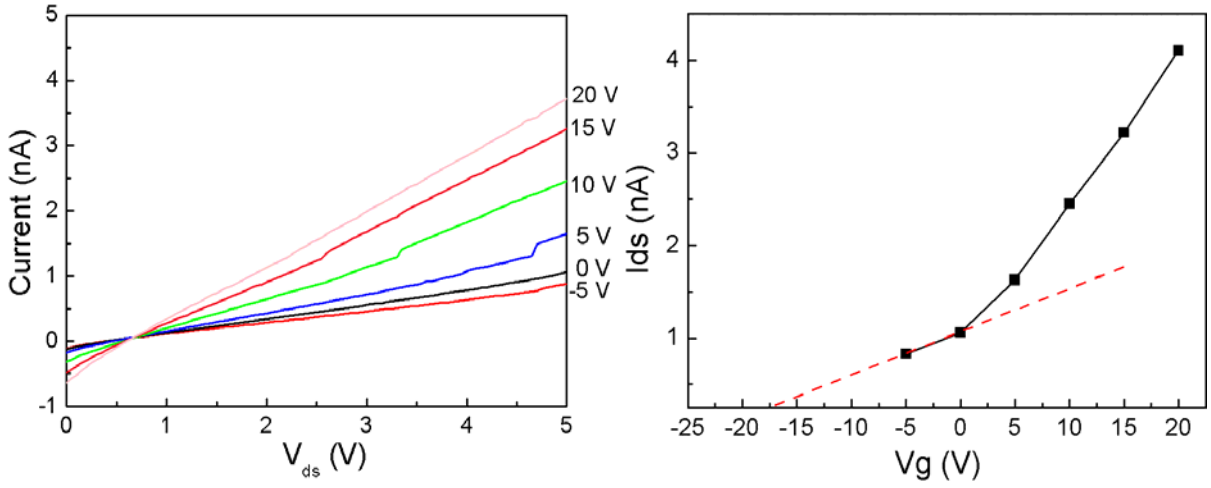

Figure 7.17. Room temperature $I - V_{ds}$ curves obtained at different gate voltages (left), and transfer characteristics taken at a drain to source voltage of 5 V (right).

The transfer characteristics at a source-drain voltage V_{ds} = 5 V are shown in Figure 7.17 (left). As the gate voltage V_g increased from -5 to 20 V, the source-drain current increased as well. This indicated that the device exhibited typical n-type transistor behavior with a low operating voltage in air.[31] Moreover, the carrier mobility in 1D channels can be expressed as follows:

$$\mu_e = (dI_d / dV_g)/(2\pi\varepsilon\varepsilon_0 V_{ds} / L \ln(2h/r)) \qquad (Eq.7.2)$$

where the transconductance $dI_d / dV_g = 4.8 \times 10^{-11} A/V$ can be extracted from the linear region (0–20 V) of Fig. 7.17 (right) at V_{ds} = 5 V. Furthermore, L (17.0 μm) and r (50 nm) are the length and radius of nanowires, whereas h (500 nm) and ε (3.9) are the thickness and dielectric constant of SiO_2 layer between the nanowire and the back gate electrode. In this way, an electron mobility of μ_e = 0.11 $cm^2/V{\cdot}s$ can be derived. From the transconductance characteristics, we obtained a threshold voltage of -17.5 V. On the other hand, the 1D carrier concentration is given as:

$$n = (V_{gt} / e)(2\pi\varepsilon\varepsilon_0 / \ln(2h/r)) \qquad (Eq.\ 7.3)$$

where V_{gt} =17.5 V is the gate threshold voltage. Therefore, the charge carrier concentration is estimated to be 7.9×10^7 cm^{-1}. The electron mobility of the obtained $Bi_6S_2O_{15}$ nanowires (0.11 $cm^2/V{\cdot}s$) is much smaller than that of SnO_2 nanowires (30 $cm^2/V{\cdot}s$)[32] and of ZnO nanowires

(3.0 $cm^2/V{\cdot}s$)[33]. These results showe that $Bi_6S_2O_{15}$ nanowires are modest oxygen ion conductors. The presence of linear column motifs in the crystal structure does not imply a high oxygen ion mobility which strongly depends on the atoms and their arrangement between the columns.[26]

7.3.5 Humidity sensing properties

Humidity sensors are very important for practical applications in environmental monitoring, industrial process control and in our daily life.[34] In general, metal oxide semiconductors display excellent water adsorption and desorption abilities and their electrical resistance variation exhibits humidity-dependent electrical characteristics.[35] In chapter 6, we have demonstrated that *Aurivillius*-type metal oxides (Bi_2MO_6; M = W, Mo) are very good potential materials for humidity sensors. In order to explore possible applications of the newly found $Bi_6S_2O_{15}$ nanowires, their humidity sensing properties were investigated at room temperature via depositing nanowires onto pre-fabricated Au interdigital electrodes. As demonstrated in chapter 6, the characteristics of humidity sensors are strongly related to the applied frequencies. Therefore, the humidity-dependent impedance of $Bi_6S_2O_{15}$ nanowire sensors was studied for different signal frequencies (100 Hz, 1 kHz, 10 kHz, 40 kHz and 100 kHz) as shown in Figure 7.18. It can be seen that impedance decreased with increasing the frequency, and the best sensitivity and linearity of the impedance vs. RH curve appeared at 1 kHz. Thus, the frequency was kept constant at 1 kHz for the following experiments. Figure 7.19 a shows the characteristic humidity hysteresis of a model humidity sensor constructed from $Bi_6S_2O_{15}$ nanowires. The upper line is corresponding to the adsorption process, while the lower one represents the desorption process: the resistance changes from about 10^7 Ω to 10^4 Ω when the RH increases from 11 % to 95 %. This resistance change of three orders of magnitude over the RH range points to a high sensitivity (three orders of magnitude) of the $Bi_6S_2O_{15}$ nanowire-based sensor. Further dynamic testing procedures were performed (cf. Figure 7.19 b), which provide more detailed information such as response, recovery time and reproducibility of the sensor. The response and recovery time, defined as the time required for

sample conductance variation to reach 90 % of the equilibrium and return to 10 % above the original conductance, were about 6 s and 40 s with RH values varying from 11 % to 85 %, respectively. The fast response and recovery behavior might arise from the 1D $Bi_6S_2O_{15}$ nanostructures with high surface areas which facilitate the absorption of water molecules on the surface of the sensors (cf. Figure 7.19 a, inset). This effect is similar to the known humidity sensors based on SnO_2 nanowires,[36] $CoFe_2O_4$ nanowires[37] and LiCl doped TiO_2 nanofibers.[38] Furthermore, it is observed that the highest and lowest resistance values varied only slightly over 5 cycles, thereby outlining the good reproducibility of the sensor. These results indicate that $Bi_6S_2O_{15}$ nanowires display a promising application potential in sensitive environmental monitoring and electronic devices for humidity control.

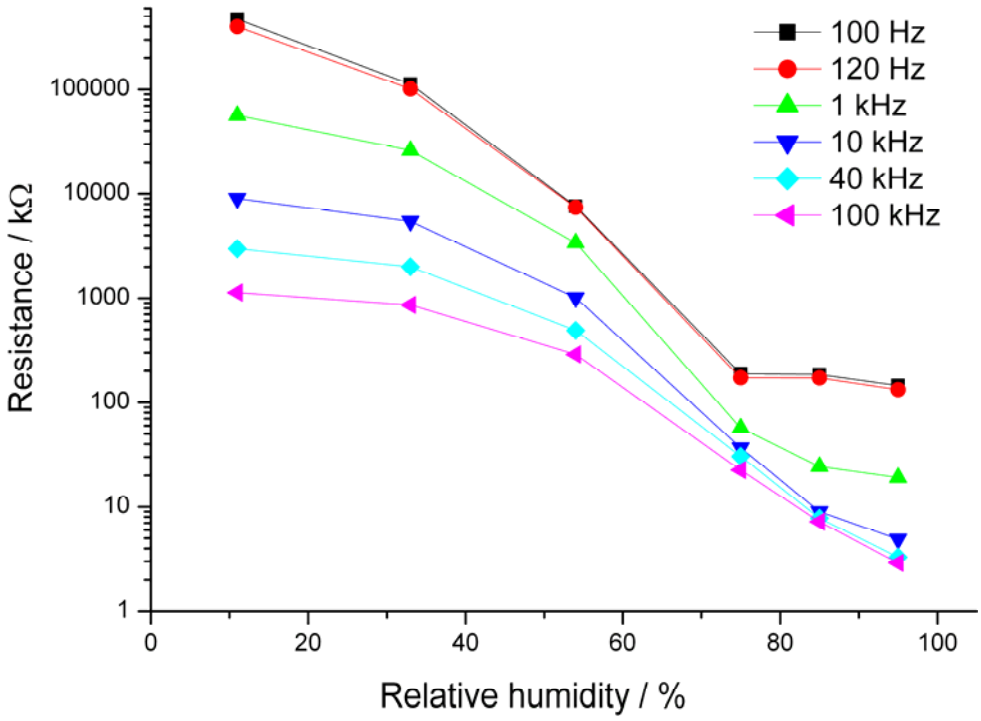

Figure 7.18. Impedance of $Bi_6S_2O_{15}$ nanowire-based sensors at different frequencies.

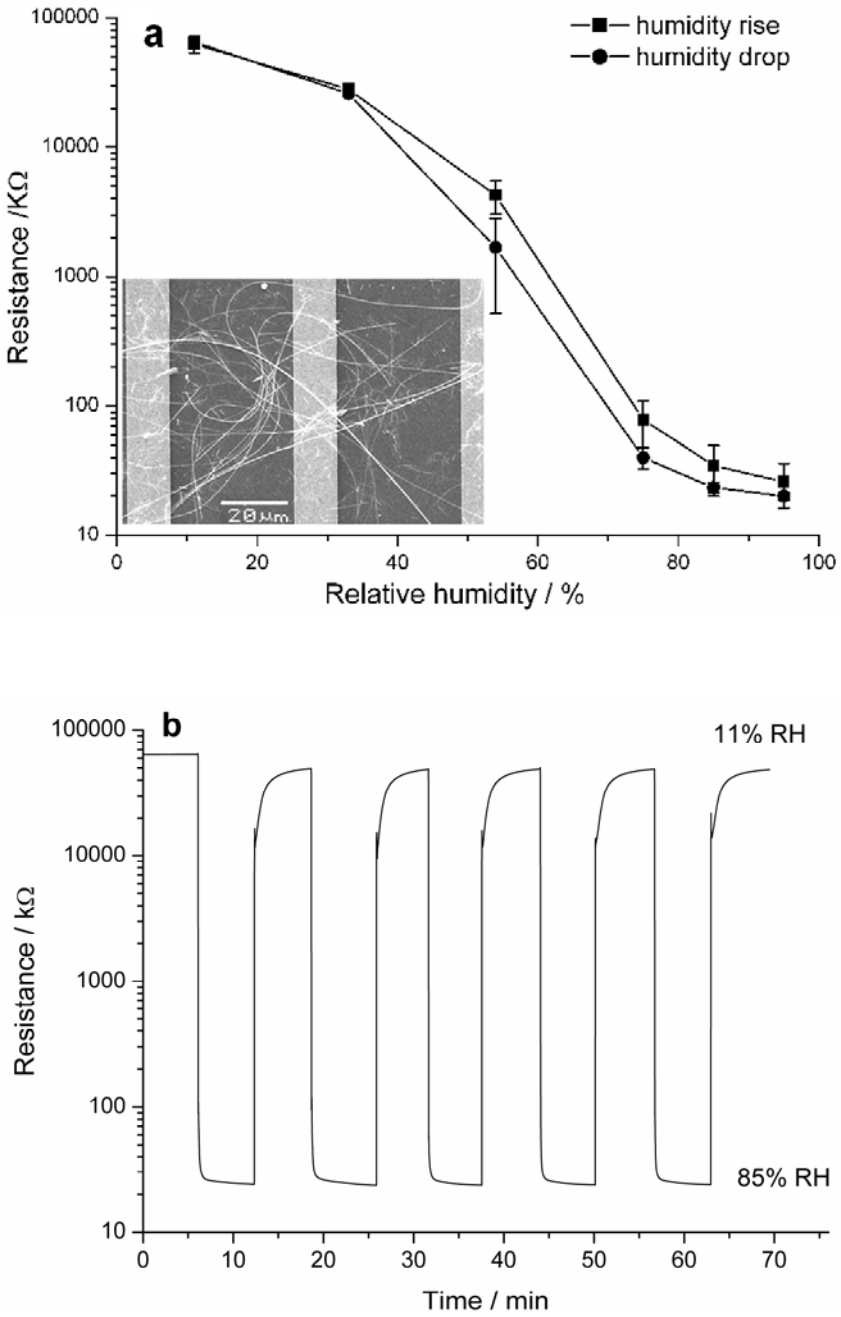

Figure 7.19. (a) Humidity hysteresis of the $Bi_6S_2O_{15}$ nanowire sensor (inset: SEM image of the nanowire sensor chip), frequency = 1 kHz; (b) characteristic response and recovery curves for 5 cycles.

7.4 Conclusion

In summary, we have developed a facile approach for to $Bi_6S_2O_{15}$ nanowires with a new structural motif that is different from the hitherto known bismuth oxide sulfates. The

hydrothermal synthesis is very straightforward, starting from commercial Bi_2O_3 and K_2SO_4 as precursors, and therefore highly suitable for industrial scale-up. Generally, the structure determination of newly emerging nanomaterials in the absence of single crystals can be a challenging task. In our case, a structural motif based on linear $(Bi_{12}O_{14})_n^{8n+}$ columns surrounded with sulfate tetrahedra was assigned to $Bi_6S_2O_{15}$ through different techniques, namely electron diffraction tilting experiments, Rietveld refinement and HRTEM investigations. Afterwards, the key steps of the hydrothermal reaction pathway were tracked down with in situ QEXAFS as a particularly powerful method. The in situ QEXAFS measurements clearly demonstrated that the bulk α-Bi_2O_3 precursor was firstly overgrown with bismuth sulfate nanowires that were continuously formed at the solid-liquid interface with only ca. 0.4 mol % Bi being dissolved so that the process takes its time to completion. The formation of $Bi_6S_2O_{15}$ nanowires is linked to the anisotropic features of the crystal structure and does not depend on the role of sulfate ions as a capping group. The facile formation of $Bi_6Cr_2O_{15}$ nanofibers from the same hydrothermal protocol indicates that the present strategy is indeed an interesting way to generate further functional bismuth oxide nanomaterials through changes in the anionic sublattice of the structure. Individual $Bi_6S_2O_{15}$ nanowire transistors were fabricated and the transistor studies revealed that $Bi_6S_2O_{15}$ is a n-type semiconductor and the charge carrier concentration was estimated to 7.9×10^7 cm^{-1}. Furthermore, our preliminary results demonstrate that sensors made of $Bi_6S_2O_{15}$ nanowires exhibit high sensitivity, quick response/recovery times and good reproducibility for humidity measurements at room temperature.

References

[1] Y. Cui, Q. Wei, H. Park, C. M. Lieber, *Science* **2001**, *293*, 1289.

[2] Z. W. Pan, Z. R. Dai, Z. L. Wang, *Science* **2001**, *291*, 1947.

[3] X. Xie, Y. Li, Z. Liu, M. Haruta, W. Shen, *Nature* **2009**, *458*, 746.

[4] M. Huang, S. Mao, H. Feick, H. Yan, Y. Wu, H. Kind, E. Weber, R. Russo, P. Yang, *Science* **2001**, *292*, 1897.

[5] Y. Xia, P. Yang, Y. Sun, Y. Wu, B. Mayers, B. Gates, Y. Yin, F. Kim, H. Yan, *Adv. Mater.*

2003, *15*, 353.

[6] M. Law, L. E. Greene, J. C. Johnson, R. Saykally, P. Yang, *Nature Mater.* **2005**, *4*, 455.

[7] E. Comini, G. Faglia, G. Sberveglieri, Z. Pan, Z. L. Wang, *Appl. Phys. Lett.* **2002**, *81*, 1869.

[8] A. Hochbaum, P. Yang, *Chem. Rev.* **2010**, *110*, 527.

[9] Y. Mao, T. J. Park, S. S. Wong, *Chem. Commun.* **2005**, 5721.

[10] C. Z. Wu, Y. Xie, *Chem. Commun.* **2010**, 5943.

[11] R. N. Vannier, G. Mairesse, F. Abraham, G. Nowogrocki, *J. Solid State Chem.* **1996**, *122*, 394.

[12] R. Punn, A. M. Feteira, D. C. Sinclair, C. Greaves, *J. Am. Chem. Soc.* **2006**, *128*, 15386.

[13] M. G. Francesconi, A. L. Kirbyshire, C. Greaves, *Chem. Mater.* **1998**, *10*, 626.

[14] T. E. Crumpton, C. Greaves, *J. Mater. Chem.* **2004**, *14*, 2433.

[15] Part of the Accelrys Materials Studio software package, Accelrys Software Inc., 2001-2009.

[16] P. Stadelmann, *Ultramicroscopy* **1987**, *21*, 131.

[17] R. Frahm, *Rev. Sci. Instrum.* **1989**, *60*, 2515.

[18] J.-D. Grunwaldt, M. Ramin, M. Rohr, A. Michailovski, G. R. Patzke, A. Baiker, *Rev. Sci. Instrum.* **2005**, *76*, 054104.

[19] T. Ressler, *J. Synchrotron Radiat.* **1998**, *5*, 118.

[20] A. Borba, A. Gomez-Zavaglia, P. N. N. L. Simoes, R. Fausto, *Spectrochim. Acta A* **2005**, *61*, 1461.

[21] C. H. Chio, S. K. Sharma, D. W. Muenow, *Spectrochim. Acta A* **2005**, *61*, 2428.

[22] J. Geng, W. Hou, Y. Lu, J. Zhu, H. Chen, *Inorg. Chem.* **2005**, *44*, 8503.

[23] F. D. Hardcastle, I. E. Wachs, *J. Solid State Chem.* **1992**, *97*, 319.

[24] G. Gattow, H. Schroeder, *Z. Anorg. Allg. Chem.* **1962,** *318*, 176.

[25] J. P. Morniroli, J. W. Steeds, *Ultramicroscopy* 1992, *45*, 219.

[26] J. Grins, S. Esmaeilzadeh, S. Hull, *J. Solid State Chem.* **2002**, *163*, 144.

[27] G. Galy, J. Hernández-Velasco, A. R. Landa-Cánovas, E. Vila, A. Castro, *J. Solid State Chem.* **2009**, *182*, 1177.

[28] G. R. Patzke, A. Michailovski, F. Krumeich, R. Nesper, J.-D. Grunwaldt, A. Baiker, *Chem. Mater.* **2004**, *16*, 1126.

[29] Y. Fang, A. Xu, R. Song, H. Zhang, L. You, J. C. Yu, H. Liu, *J. Am. Chem. Soc.* **2003**, *125*, 16025.

[30] Z. J. Gu, Y. Ma, T. Y. Zhai, B. F. Gao, W. S. Yang, J. N. Yao, *Chem. Eur. J.* **2006**, *12*,

7717.

[31] Q. H. Li, Y. X. Liang, Q. Wan, T. H. Wang, *Appl. Phys. Lett.* **2004**, *85*, 6389.

[32] Q. Kuang, C.-S. Lao, Z. Li, Y.-Z. Liu, Z.-X. Xie, L.-S. Zheng, Z. L. Wang, *J. Phys. Chem. C* **2008**, *112*, 11539.

[33] Q. H. Li, Y. X. Liang, Q. Wan, T. H. Wang, *Appl. Phys. Lett.* **2004**, *85*, 6389.

[34] J. Xu, W. Zhang, Z. Yang, S. Ding, C. Zeng, L. Chen, Q. Wang, S. Yang, *Adv. Funct. Mater.* **2009**, *19*, 1759.

[35] Y. Qiu, S. Yang, *Adv. Funct. Mater.* **2007**, *17*, 1345.

[36] Q. Kuang, C. Lao, Z. L. Wang, Z. Xie, L. Zheng, *J. Am. Chem. Soc.* **2007**, *129*, 6079.

[37] C. H. Kim, Y. Myung, Y. J. Cho, H. S. Kim, S. H. Park, *J. Phys. Chem. C* **2009**, *113*, 7085.

[38] Z. Li, H. Zhang, W. Zheng, W. Wang, H. Huang, C. Wang, A. G. MacDiarmid, Y. Wei, *J. Am. Chem. Soc.* **2008**, *130*, 5036.

8. Mixed alkali tungsten/molybdenum nanostructured oxides

8.1 Introduction

Nanostructured transition metal oxides (TMOs) are essential building blocks of modern materials chemistry and they play a crucial role in future nanotechnological applications.[1] Among the various transition metal oxides, tungsten bronzes (M_xWO_3), where M covers a wide range of cations including protons, alkali or alkaline earth metals, offer a high degree of structural flexibility.[2] Depending on the synthetic conditions, cubic, tetragonal, monoclinic, hexagonal or pyrochlore type M_xWO_3 with a different three-dimensional array of distorted (WO_6) octahedra sharing their corners can be obtained. As a consequence, they have a particularly wide spectrum of applications in electrochromic devices,[3] catalysis,[4] gas sensing,[5] large-scale static displays[6] and superconductors.[7]

The hexagonal tungstates (HTBs) are of particular interest among the M_xWO_3 systems due to their system of triangular and hexagonal channels extending along the *c* axis and the resulting intercalation chemistry. This permits the adjustment of materials properties by ion exchange and incorporation, thereby offering a wide range of potential HTB applications.[8] For example, ^{137}Cs and ^{90}Sr from radioactive waste can be removed due to the outstanding ion-exchange properties of the HTB phase.[9] The specific capacities and Li^+ cycling behavior of Li-HTBs are often superior to other tungstate phases.[10] Furthermore, the combination of two or more oxides can substantially enhance the properties of binary oxides, because ternary and higher TMOs often benefit from a "synergistic" effect. Recently, it has been reported that the substitution of molybdenum into the HTB framework can enhance the cation exchange capacity,[11] as well as the gas sensor properties[12] and the electrochromic and lithium ion transport properties.[13] These effects are likely to be further enhanced through control of the particle size and shape on the nanoscale. For this purpose, hydrothermal methods are a powerful tool due to their exceptional parameter tuning options, one-step reaction processes, low reaction temperatures and environmentally friendly handling.[14, 15] Nevertheless, hydrothermal autoclaves are mostly operated as "black boxes" due to the lack of fundamental understanding of hydrothermal kinetics and limited knowledge about the intermediate phases

occurring in solution.[16] A deeper insight into these mechanisms would enable us to exert control over the formation of solution species and thus over the resulting solid phases.

In the following, a straightforward hydrothermal route towards W/Mo-HTB oxide nanomaterials is presented. The shape of nanoscale W/Mo-HTB oxides can be expanded into a variety of morphologies by the use of alkali chloride additives. To understand the role of the alkali chlorides, these additive-assisted hydrothermal systems were monitored by in situ EDXRD investigations to elucidate their formation mechanism through a detailed study of the reaction kinetics. The mobility of alkali cations within the channels of the W/Mo-HTB host framework has been investigated by solid state NMR spectroscopy. Furthermore, the influences of these alkali cations on the local structure and on the thermal stability of W/Mo-HTB were investigated by XAS, TG and XRD. Finally, we studied the gas sensing properties of W/Mo-oxides, revealing that these oxides are potential candidates for the detection of low levels of NH_3.

8.2 Experimental

8.2.1 Synthesis

In a typical experiment, 148 mg of $(NH_4)_6[H_2W_{12}O_{40}]\cdot 3H_2O$ (AMT), 58 mg of $MoO_3\cdot 2H_2O$, 2 mmol of MCl (M = Li to Cs), and 2 mL of 25 vol% acetic acid were added to a Teflon-lined stainless-steel autoclave with a capacity of 23 mL. The autoclave was sealed, heated for 48 h at 180 ^{o}C, and subsequently cooled to room temperature. The precipitate was collected after filtration, washed with distilled water and ethanol, and dried in air.

8.2.2 Characterization

XRD analysis was conducted on a STOE STADI P diffractometer in transmission mode (flat sample holders, Ge monochromator, and Cu $K_{\alpha 1}$ radiation) operated at 40 kV and 40 mA. In situ high temperature X-ray diffraction (HT-XRD) patterns were recorded on a PANalytical X'pert diffractometer coupled with a Paar HKT-1200 high temperature XRD chamber using

Cu K_α radiation. For SEM, performed on a LEO1530 (FEG) microscope, samples were dispersed in ethanol and subsequently deposited on a silicon wafer. The specimen was investigated without conductive coating at rather low voltage (2 kV) to minimize charging effects. A JEOL-6060 electron microscope with a Bruker energy-dispersive X-ray spectrometer was employed for approximate elemental analyses. N and H analyses were conducted on a Leco CHN (S)-932 instrument. Alkali contents were determined by Mikroanalytisches Labor Pascher, Remagen, Germany. Thermal analysis was performed on a STA 449C apparatus between 50 °C and 900 °C with a heating rate of 10 ^{o}C/min in N_2 atmosphere. Platinum crucibles were used to exclude the reaction between the test sample and the crucible material. The NMR spectra were recorded at room temperature on a Bruker DRX-500-spectrometer, which has been modified for solid state measurements with MAS sample spinning up to 15 kHz (4 mm rotors) and high power ^{1}H decoupling. The NMR frequencies were 194.41 MHz for ^{7}Li (I = 3/2, QM = 0.045), 132.32 MHz for ^{23}Na (I = 3/2, QM = 0.12), 163.61 MHz for ^{87}Rb (I = 3/2, QM = 0.12), and 65.61 MHz for ^{133}Cs (I = 7/2, QM = 0.003). The Brunauer-Emmett-Teller (BET) surface area measurements were performed on a Quadrasorb SI in N_2-adsorption mode. The samples were degassed at 150 °C for 5 h under vacuum.

8.2.3 In situ EDXRD measurements

The in situ EDXRD experiments were performed at HASYLAB (Hamburg) Beamline F3, which receives white synchrotron radiation from a bending magnet with a critical energy of 16 keV and gives a positron beam energy of 4.5 GeV. An energy range from 13.7 to 72.8 keV can be observed with a maximum at about 20 keV. The diffracted beam is monitored by a nitrogen cooled solid state germanium detector. The detector angle was chosen so that all important Bragg reflections can be detected. The d-spacing range is given by E = 6.199/(d·sinθ). With a detector angle of approximately 1.90° the observable d-spacing range is 2.58 Å to 13.7 Å. The energy resolution $\Delta d/d$ is about 10^{-2} above 26 keV. The beam was collimated to 0.1 mm giving the best results. More experimental details can be found in the

literature.[17] Autoclaves with glass liners with an internal diameter of 10 mm and a volume of 7 mL were used for in situ investigations. A typical experiment (initial ratio W:Mo = 2:1) was performed starting from 148 mg AMT, 58 mg $MoO_3 \cdot 2H_2O$, 2 mmol of MCl (M = Li - Cs) and 1.5 mL of 25 % acetic acid as reactants, followed by heating to 180 °C. Data collection was started immediately after introducing the autoclave into the measurement setup.

8.2.4 XAS measurements

X-ray absorption (XAS) measurements were performed at the KMC-2 beamline at BESSY (Berlin, Germany) using the double crystal SiGe (111) monochromator, operating at 1.7 GeV. The beam intensity was stabilized by MOSTAB electronics with an accuracy of 0.3 %. The detector system consists of three ionization chambers and a reference W foil for energy calibration was used for the incident and outcoming X-ray intensity. Mo K edge spectra were recorded at the beamline X1 at HASYLAB (DESY, Hamburg, Germany) using the double crystal Si (311) monochromator. Mo foil was used for energy calibration (70 % detuning of the crystal). To guarantee the reproducibility of the experimental data, at least two spectra were recorded for each sample. Data reduction of experimental absorption spectra and EXAFS fitting and simulation were carried out using WinXAS3.2[18] and following the standard procedures. To keep the systematic error during data analysis at the same level all data were treated in the same way. The energy scale of each EXAFS scan was calibrated by assigning the first inflection point of the L_3 edge of the corresponding W foil and the K edge of Mo foil. Pre-edge background subtraction and normalization was carried out by fitting a linear polynomial to the pre-edge region and a cubic polynomial to the post-edge region of the absorption spectra. A smooth atomic background, $\mu_0(k)$, was obtained by applying a cubic polynomial. After background removal, the data were transformed into k-space. Fourier transforms of the W L_3 edge and Mo K edge $\chi(k)$ which was multiplied by k^3, were taken over similar photoelectron wavenumber ranges, typically from 2 $Å^{-1}$ to 12 $Å^{-1}$ and a Bessel window was used in the Fourier transform. The FEFF7[19] program package was used to calculate phase and amplitude factors, followed by least-squares curve fitting of the data.

8.2.5 Sensor fabrication and measurements

To fabricate thick film gas sensors with a thickness around 10 μm, 0.2 mL terpineol mixed with 5 wt% ethylcellulose and 0.04 mL acetylacetone was added to 200 mg of the respective W/Mo-HTBs to obtain a paste. The paste was coated onto a quartz slide covered by Ni interdigital electrodes. Each bar of the interdigital electrodes was 200 μm in width and the spacing between the neighbouring bars was 200 μm as well (Figure 8.1). The film was then sintered in air to remove the organic additives at 150 ^{o}C for 10 min, 350 ^{o}C for 10 min and 500 ^{o}C for 30 min, respectively, and then cooled down to the room temperature naturally. Gas sensing properties were measured using a home-built testing system, which consists of a test chamber, sensor holder with embedded heater, Agilent oscilloscope-54810A, mass flow controllers and a data acquisition system. Prior to the measurement, the gas sensor was aged for 1 h at the required temperature in Ar atmosphere. During the sensor measurements, the target gas was mixed with pure Ar using mass flow controllers to adjust the desired concentration with the total flow rate maintained at 200 sccm. The sensitivity, S, was defined as $R_{Ar}/R_{ammonia}$, where R_{Ar} is the resistance of the sensor in pure Ar gas atmosphere and $R_{ammonia}$ is the resistance in the ammonia-containing test gas atmosphere.

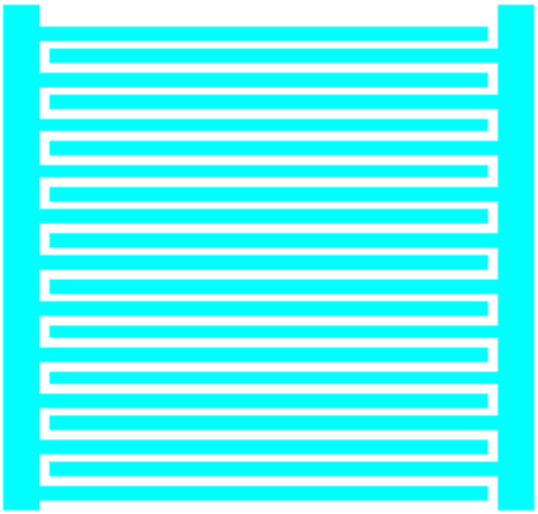

Figure 8.1. Schematic representation of Ni interdigitaling electrodes.

8.3 Results and discussion

8.3.1 Hydrothermal formation of nanostructured alkali W/Mo-HTB oxides

All products emerging from the MCl/AMT/HAc (M = Li-Cs) hydrothermal systems exhibit the hexagonal tungsten bronze (in the following: HTB) phase (JCPDS No. 85-2460) as shown in Figure 8.2, indicating that the alkali chlorides do exert a significant influence on the phases of the final products. Nevertheless, the different alkali chlorides remarkably influence the morphologies of the W/Mo-HTB oxides and they can bring forward a wide spectrum of particle shapes. The hydrothermal treatment of AMT with $MoO_3 \cdot 2H_2O$ in acetic acid at 180 ^oC affords W/Mo-HTB nanorods with diameters in the range of 20 - 30 nm and lengths around several hundred nanometers (cf. Figure 8.3). The addition of LiCl and NaCl directs the W/Mo-HTB morphology towards the similar nanorods with higher aspect ratio. Interestingly, KCl, RbCl, and CsCl as additives induce a hierarchical organization of nanorods into microshperes.

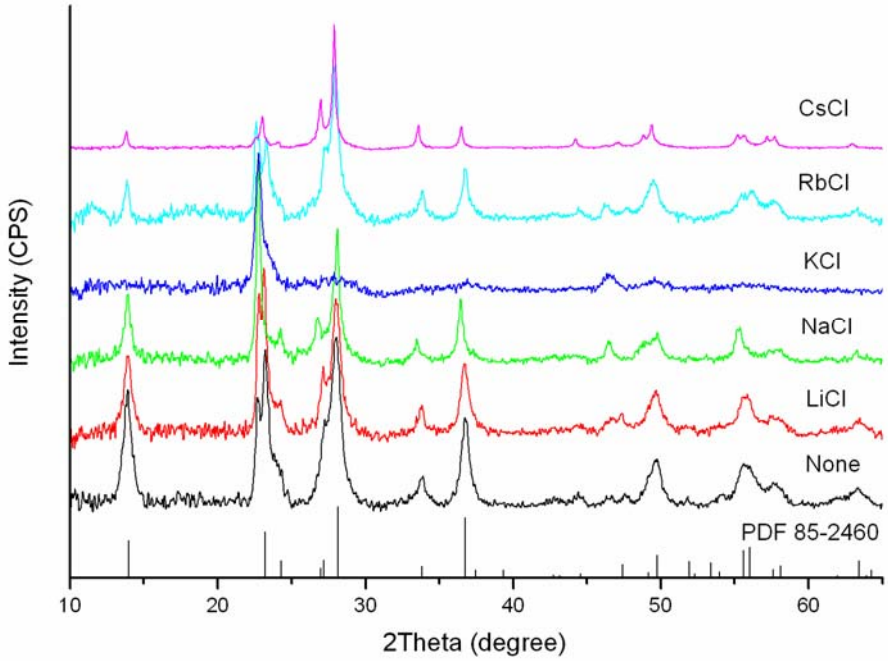

Figure 8.2. XRD patterns of alkali-free W/Mo-oxides and W/Mo-oxides with alkali chloride additives. The reference pattern of hexagonal WO_3 (JCPDS No. 85-2460) is shown at the bottom.

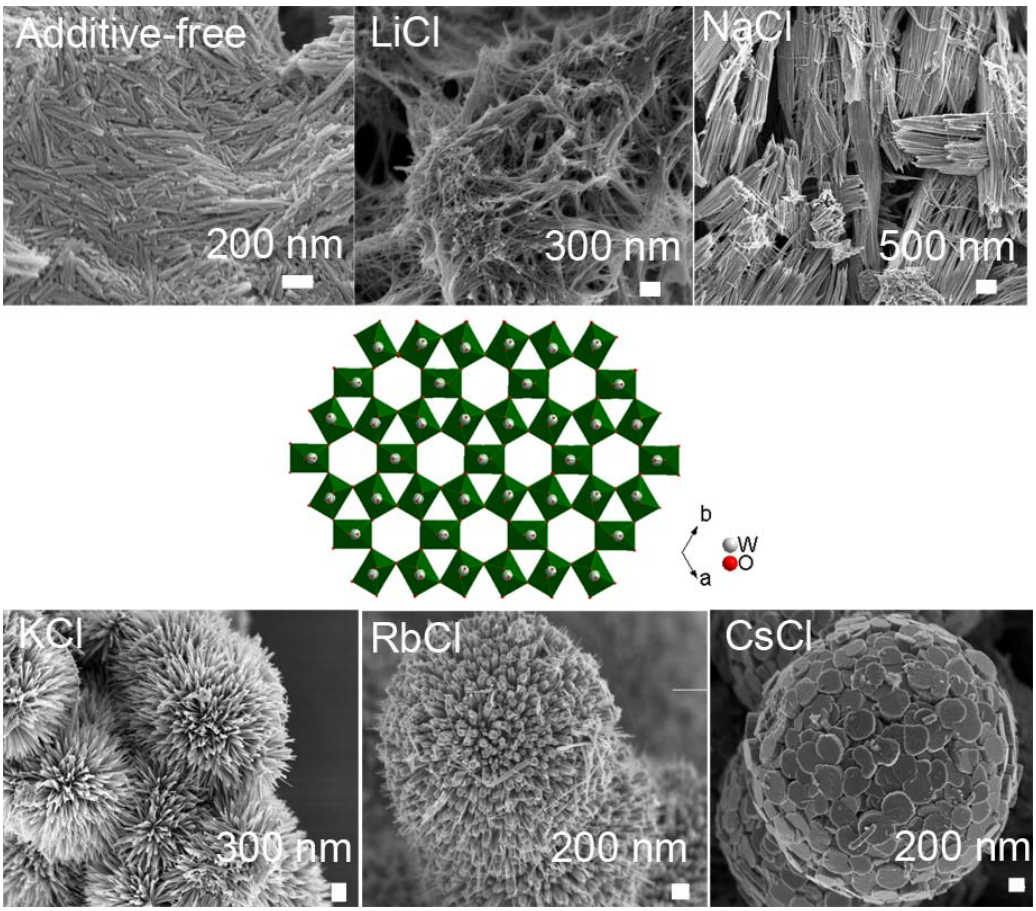

Figure 8.3. Influence of alkali chloride additives on the morphology of hydrothermally synthesized hexagonal W/Mo-HTB oxides exhibiting the characteristic channel structure motif (middle).

Table 8.1 provides a summary of the phase, composition, morphology and BET surface area of the products obtained from representative AMT/$MoO_3 \cdot 2H_2O$/MCl hydrothermal systems. The fraction of ammonium cations incorporated into the HTB framework strongly depends on the size of the alkali cations. The amount of ammonium cations determined from elemental analyses decreases from W/Mo-HTB oxide to Rb-W/Mo-HTB oxide due to the different ion exchange ability of the alkali cations. For Cs-W/Mo-HTB, no nitrogen content could be detected. The W/Mo ratios were obtained from EDXS investigations. The W/Mo ratio of all the products points to an approximately 3:1 homogeneous distribution of both elements (within the experimental error of the method) which is higher than the starting ratio of W/Mo (around 2:1). Furthermore, all the products exhibit high surface areas (between 56 and 82 m^2/g) which exceed the values of a typical $(NH_4)_{0.26}WO_3$ nanorod sample (37 m^2/g).[20]

Table 8.1. Products emerging from representative AMT/$MoO_3 \cdot 2H_2O$/MCl hydrothermal systems.

Sample	Phase	Composition	Typical morphology	BET surface area (m^2/g)
WMo	HTB	$(NH_4)_{0.24}W_{0.77}Mo_{0.23}O_3$	Nanorods	78.8
WMo_Li	HTB	$(NH_4)_{0.16}Li_{0.07}W_{0.75}Mo_{0.25}O_3$	Nanorods	64.6
WMo_Na	HTB	$(NH_4)_{0.09}Na_{0.19}W_{0.79}Mo_{0.21}O_3$	Nanorods	58.4
WMo_K	HTB	$(NH_4)_{0.04}K_{0.23}W_{075}Mo_{0.25}O_3$	Hierarchical nanostructures	82.4
WMo_Rb	HTB	$(NH_4)_{0.01}Rb_{0.24}W_{0.79}Mo_{0.21}O_3$	Hierarchical nanostructures	56.3
WMo_Cs	HTB	$Cs_{0.26}W_{0.77}Mo_{0.23}O_3$	Hierarchical nanostructures	57.3

8.3.2 Solid state NMR spectroscopy on alkali W/Mo-HTB oxides

It is well known that HTB is a metastable phase and pure HTB has not been accessed to date, because ions or molecules in the hexagonal channels are indispensable to stabilize the channel structure motif.[8] Therefore, the presence of stabilizing NH_4^+ and alkali cations in the channels of the W/Mo-HTB host frameworks is to be expected. Solid state NMR spectroscopy has been carried out in order to monitor the mobility of the alkali metal cations within the W/Mo-HTB frameworks. All incorporated alkali metals (^{7}Li, ^{23}Na, ^{87}Rb and ^{133}Cs) have half integer quadrupolar nuclear spins. Therefore, their solid state NMR spectra are dominated by the interaction of the quadrupolar moment with the electric field gradient. Chemical shift anisotropy and dipolar interactions are negligible in non-spherical symmetric environments. Furthermore, the central transition (±1/2) of non-integer spins is not affected by first order quadrupolar interactions and MAS need only remove the much smaller second order effects leading to line narrowing by approximately a factor of four in rigid systems of low symmetry. The non-central transitions of half integer quadrupolar spins are suppressed due to first order quadrupolar interactions and have therefore no influence onto the line

shape.[21] In our NMR studies the MAS line width dependency of the incorporated alkali chloride and comparison with the pure rigid chloride served as a probe for mobility. Line widths in the typical range of some kHz with high sensitivity to MAS are an indication for rigid systems. In contrast, narrow lines below 1 kHz with low sensitivity to MAS provide evidence for diffusion processes, which averages the quadrupolar interactions in the solid environment within the NMR time scale, in the rapid mode leading to line shapes even as in liquid phase. Furthermore, ^{7}Li T_1 time measurements were carried out for the lithiated systems, applying the inversion recovery method.[22] The obtained T_1 data served as an additional, sensitive probe for the dynamic behaviour of the appropriate lithium sites. Generally, quadrupolar T_1 relaxation is more efficient in dynamic systems with low symmetry, compared with rigid, symmetric systems, due to time-dependent spin lattice interactions, which occur in fluctual environments.[23]

Cs-W/Mo-HTB oxide shows a broad ^{133}Cs line (3.1 kHz) at 5 kHz MAS, -240 ppm shifted relative to CsCl (cf. Figure 8.4 a, b). Without MAS the line width increases up to 5.8 kHz, being in the typical range of a static system with lower symmetry as in pure CsCl, where the line width is 76 Hz at 5 kHz MAS and 840 Hz in the static rotor. Also the large chemical shift difference to pure CsCl indicates the absence of isolated CsCl units and is evidence for the incorporation of Cs into the W/Mo-HTB lattice.

In contrast to pure NaCl the ^{23}Na resonance of Na-W/Mo-HTB (Figure 8.4 c, d) is just slightly affected by MAS (510 Hz vs. 660 Hz with and without MAS), being additionally much sharper as in the case of NaCl without MAS (660 Hz vs. 2.6 kHz). That is in good agreement with the mobility of sodium which causes averaging effects leading to a fourfold sharper line, compared with the NaCl reference (cf. Figure 8.4 e, f). The chemical shift difference of 12 ppm relative to NaCl is not as significant as in the case of Cs relative to CsCl. Nevertheless, the line shape differences of Na-W/Mo-HTB oxide and pure NaCl (510 Hz vs. 160 Hz) at 5 kHz MAS clearly show that the sodium environment in Na-W/Mo-HTB oxide is of lower symmetry and therefore, no NaCl lattice is present.

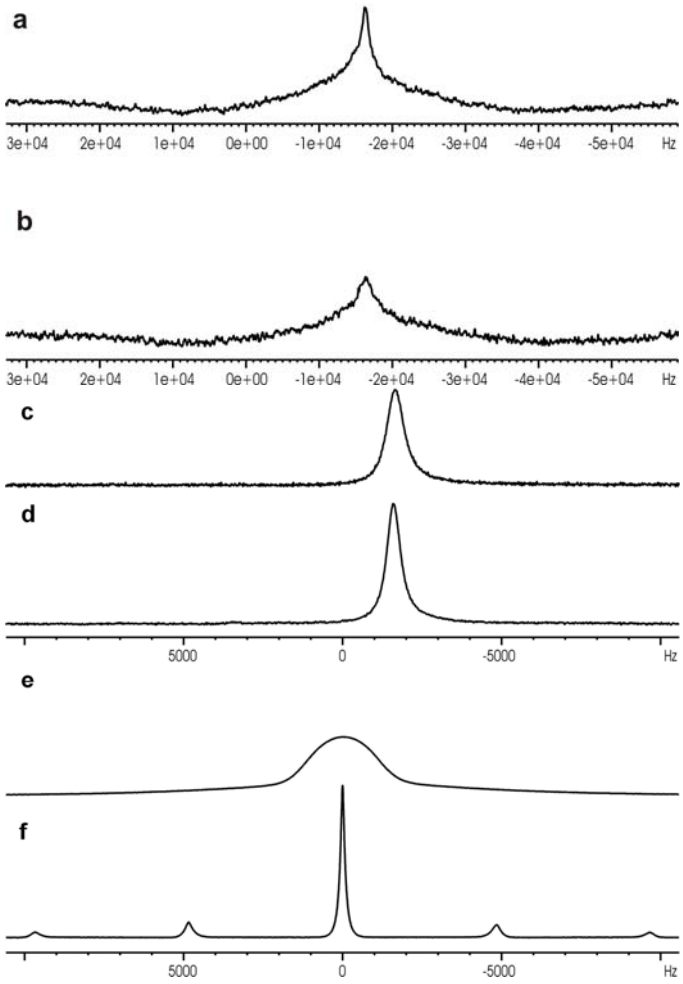

Figure 8.4. Solid state ^{133}Cs NMR spectra of Cs-W/Mo-HTB (a) with MAS, (b) without MAS and solid state ^{23}Na NMR spectra of Na-W/Mo-HTB (c) without MAS, (d) with MAS and NaCl (e) without MAS, (d) with MAS.

In contrast to the sodium and cesium species, the NMR spectra of the lithiated compounds are influenced by chemical shift anisotropy effects (csa) rather than by quadrupolar interactions. Therefore, broad rotation side band patterns are observed under MAS conditions. This is evidence for a quasi spherical symmetry with small electric field gradients at the lithium sites, resulting in just small quadrupolar interactions which are insignificant with respect to the csa effects. Li-W/Mo-HTB shows narrow ^{7}Li line widths (< 70 Hz) under MAS conditions and two lithium sites with a chemical shift difference of 1.8 ppm could be distinguished (Figure 8.5). The sharper line at lower field shows a narrow rotation side band pattern in contrast to the much broader high field signal with its large rotation side band extension. These differences are due to different environmental symmetries and site mobilities, as shown with

^{7}Li T_1 time measurements. The sharp low field signal of Li-W/Mo-HTB exhibits a T_1 time of just 481 ms, which is some orders of magnitude smaller than that one of ^{7}Li in pure LiCl (449 s). In contrast, the broad high field component of Li-W/Mo-HTB tungstate ranges with a T_1 time of 12.1 s between the values of pure LiCl and the Li- W/Mo-HTB component in the fast exchange mode.

Although ^{87}Rb has a high NMR sensitivity and a nuclear quadrupolar moment comparable with ^{23}Na and is therefore easy to detect, attempts to observe it in the WMo-HTB framework were not successful. Under MAS conditions the RbCl reference showed a ^{87}Rb line shape pattern similar to NaCl already after 4 scans, but the spectrum of Rb-W/Mo-HTB oxide did not reveal any ^{87}Rb resonance even after 80 000 scans. This may be due to a tight fixation of rubidium in a low symmetric environment, leading to strong quadrupolar couplings causing line widths which exceed the limits of the used NMR facility. Isolated RbCl units do obviously not exist in the framework, because they should lead to an intense line pattern similar to pure RbCl.

All in all, solid state NMR spectroscopy results demonstrate that the interaction of the different intercalated alkali cations results in a change of mobilities: whereas the small Li^+ cations can occupy two sites with different environments and mobilities corresponding to the trigonal and hexagonal channels along the *c* axis (Figure 8.3 middle), Na^+ cations can only be mobile in the larger hexagonal channels. Furthermore, Cs^+ cations are highly stabilizing yet less mobile. Based on the results from SEM and solid state NMR, we demonstrated that the alkali cations exert a two-fold role as internal stabilizers of the HTB phase and external shape control agents. However, it remains extremely difficult to understand how the alkali cations externally influence the morphology of the W/Mo-HTB oxides.

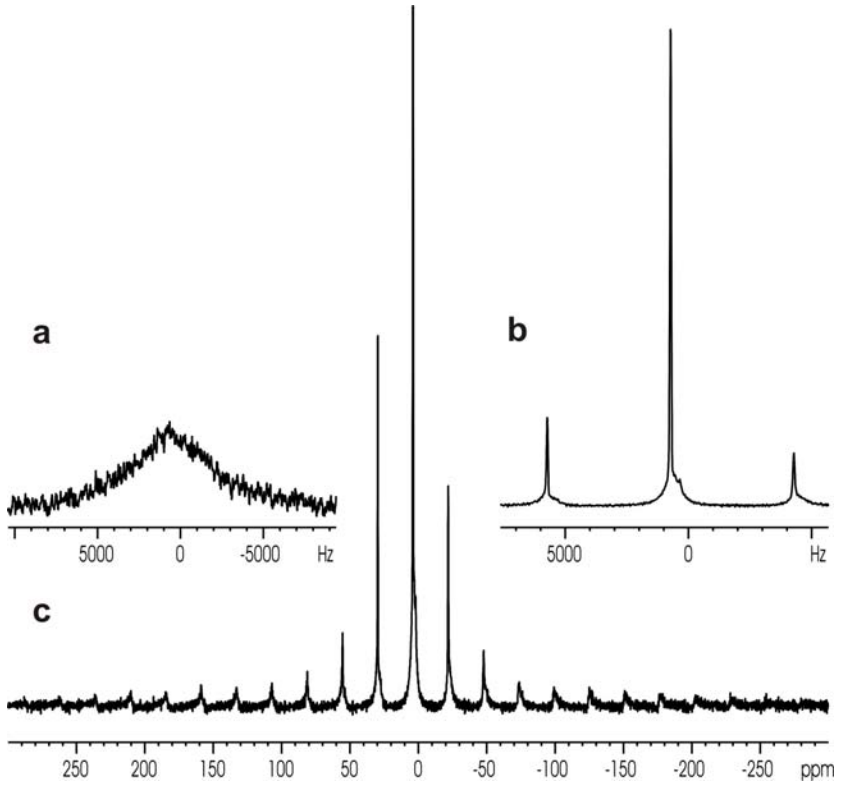

Figure 8.5. Solid state ^{7}Li NMR spectra of Li-W/Mo-HTB (a) without MAS, (b, c) with MAS.

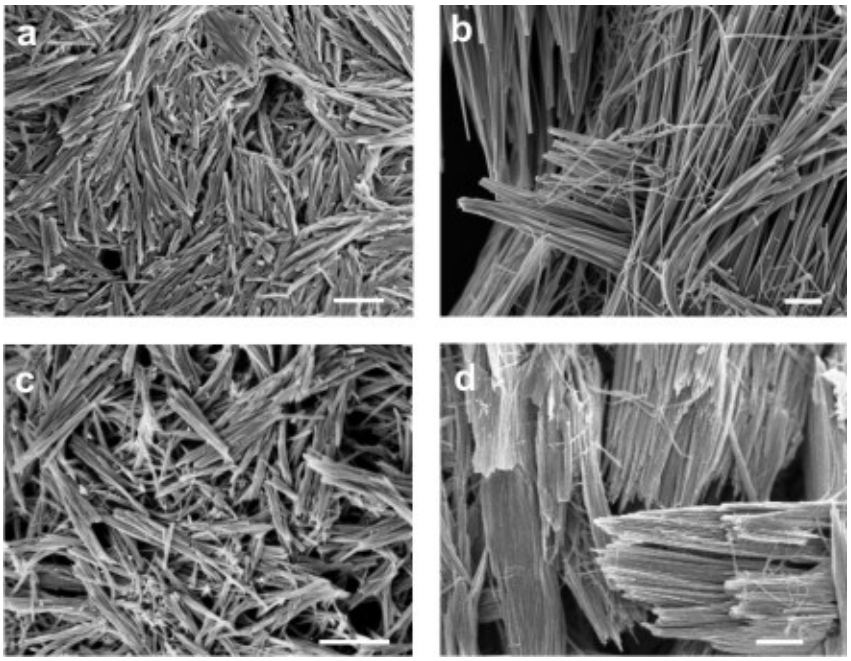

Figure 8.6. Representative SEM images (scale bar = 500 nm) of Li- and Na-W/Mo-HTB after the in situ EDXRD experiments (left column) compared to reference images of ex situ products obtained after prolonged reaction times (right column): (a-b) Li-W/Mo-HTB, (c-d) Na-W/Mo-HTB.

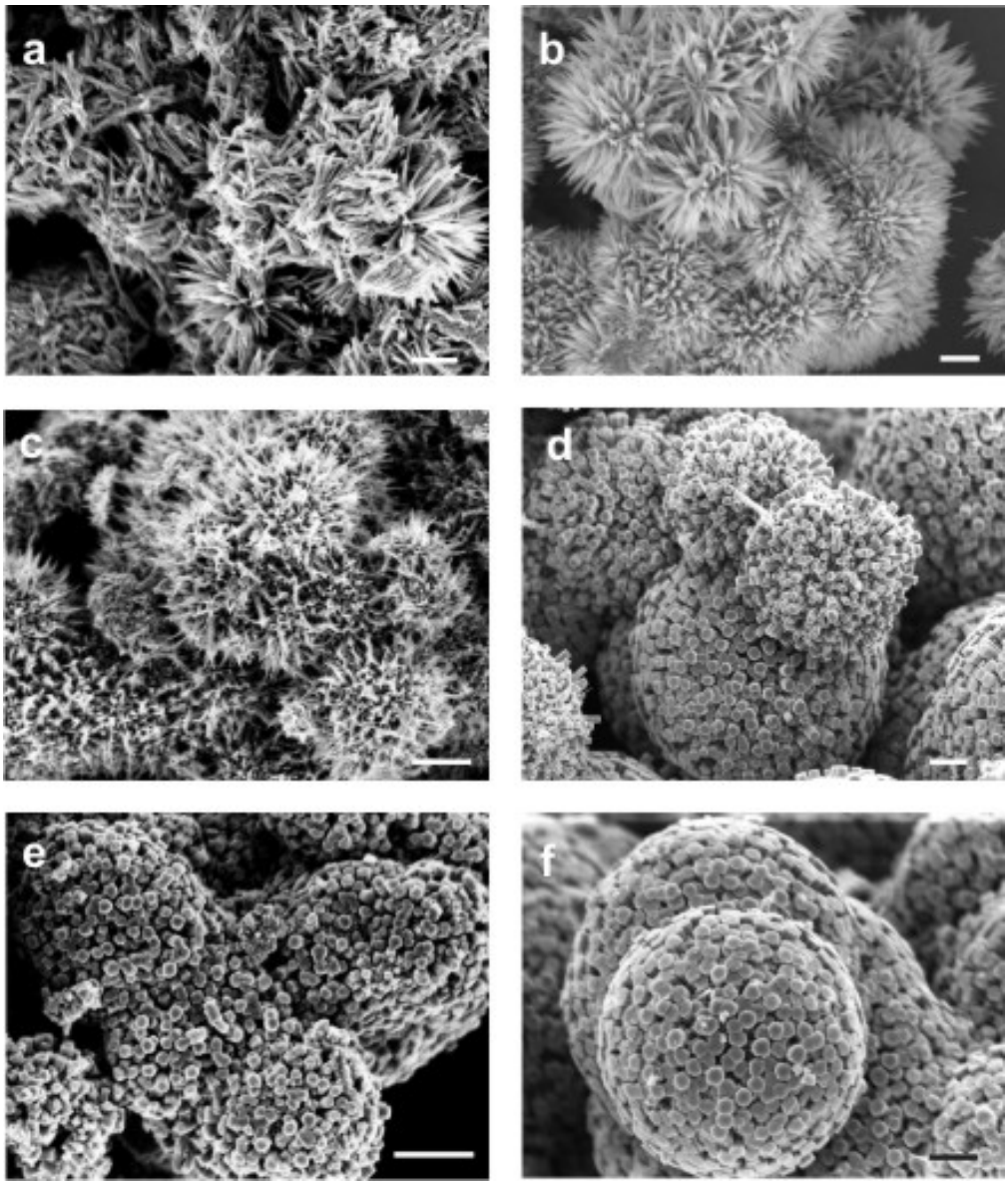

Figure 8.7. Representative SEM images (scale bar = 500 nm) of alkali-W/Mo-HTB oxides after the in situ EDXRD experiments (left column) compared to reference images of ex situ products obtained after prolonged reaction times (right column): (a-b) K-W/Mo-HTB, (c-d) Rb-W/Mo-HTB and (e-f) Cs-W/Mo-HTB.

8.3.3 In situ EDXRD investigations

With the help of in situ EDXRD measurements, we investigated the reaction kinetics of nanostructured W/Mo-HTB formation in the presence of alkali chlorides. Firstly, the kinetics and mechanisms of alkali W/Mo-HTB oxide formation were studied by monitoring the

hydrothermal reaction of AMT with $MoO_3 \cdot 2H_2O$ (W : Mo ratio = 2:1) and MCl (M = Li – Cs) at 180 °C through in situ EDXRD experiments (for details cf. section 8.2.3.). Figures 8.6 and 8.7 demonstrate that the alkali W/Mo-HTB oxides isolated after the brief in situ EDXRD investigation times already bear considerable resemblance to the fully developed materials obtained after 48 h of hydrothermal treatment. However, their XRD patterns still display broadened reflections, because the shorter in situ reaction times lead to a lower crystallinity of the products.

In the energy range chosen for in situ EDXRD analysis, several reflections of the products and W resonances (immediately visible) were monitored simultaneously (cf. Figure 8.8) and the growth rates of alkali W/Mo-HTB oxide formation were determined according to standard literature methods (details in section 1.3.1).[17] The integrated intensities of the product and intermediate reflections were normalized against the intensity of the W $K_{\alpha 1}$ resonance. For the formation of additive-free W/Mo-HTB oxide as a reference, a plot of the extent of reaction α (ratio of the normalized intensity at the reaction time t by the intensity at the time t_∞) against the reaction time t points to an isotropic crystal growth.

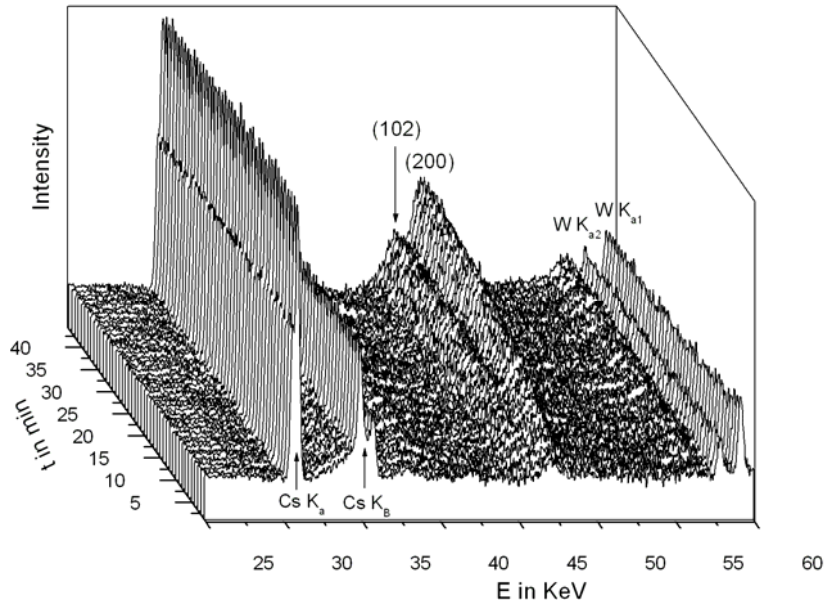

Figure 8.8. Time-resolved energy-dispersive X-ray powder pattern recorded at 180 °C in the presence of CsCl. The indices of the most intense lines of the product phase and W K_α fluorescence lines are marked.

When the reaction is performed in the presence of LiCl, the curves of $\alpha(t)$ for the decomposition of $MoO_3 \cdot 2H_2O$ and the product formation intersect exactly at $\alpha = 0.5$ as shown in Figure 8.9.

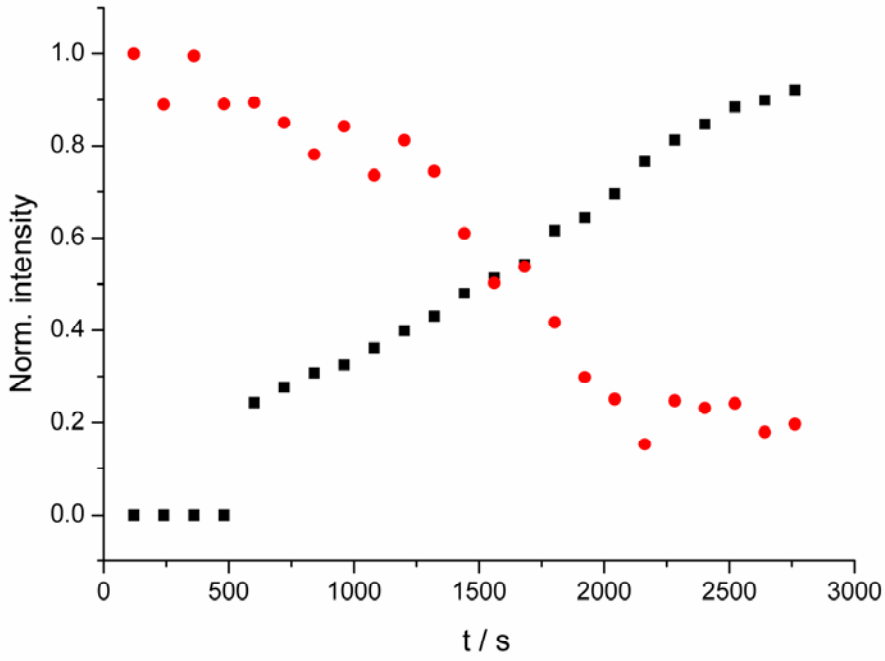

Figure 8.9. Correlation between the dissolution of AMT precursor and the formation of the HTB products in the presence of LiCl.

This indicates the dissolution of the starting material or its conversion into an amorphous state before the product nucleates and crystallizes subsequently. In fact, an intersection of the $\alpha(t)$ curves at 0.5 would not be possible if the dissolution/amorphization stage and the nucleation/crystallization steps were significantly temporally delayed so that this is clear evidence for simultaneous processes. Furthermore, supersaturation must be reached quickly during this reaction pathway. However, the induction time t_{ind} and half-life time $t_{0.5}$ strongly depend on the type of cation used for the synthesis of alkali W/Mo-HTB oxides. Figure 8.10 shows the extent of reaction α vs time t for the (200) reflection of W/Mo-HTB for different alkali ions, demonstrating that t_{ind} and $t_{0.5}$ strongly depend on the type of alkali ion. The presence of K^+, Rb^+ and Cs^+ reduces both values significantly so that the educts were dissolved too quickly to be evaluated similarly to the reaction with LiCl as an additive. When

the reaction is performed in the presence of Li^+, t_{ind} is significantly shorter than the value for the alkali-free reaction, whereas $t_{0.5}$ is only reduced by 4 min. The kinetic influence of Na^+ is even more surprising: whereas t_{ind} is slightly shorter, $t_{0.5}$ is even increased in comparison with the pristine W/Mo-HTB formation. The different growth curves observed for (a) the reactions with K^+, Rb^+, or Cs^+ and (b) the reaction without additives or with Li^+ and Na^+ suggest that the crystallization processes vary with the type of the additive. It is evident that the growth mechanism depends strongly on the type of the alkali chloride.

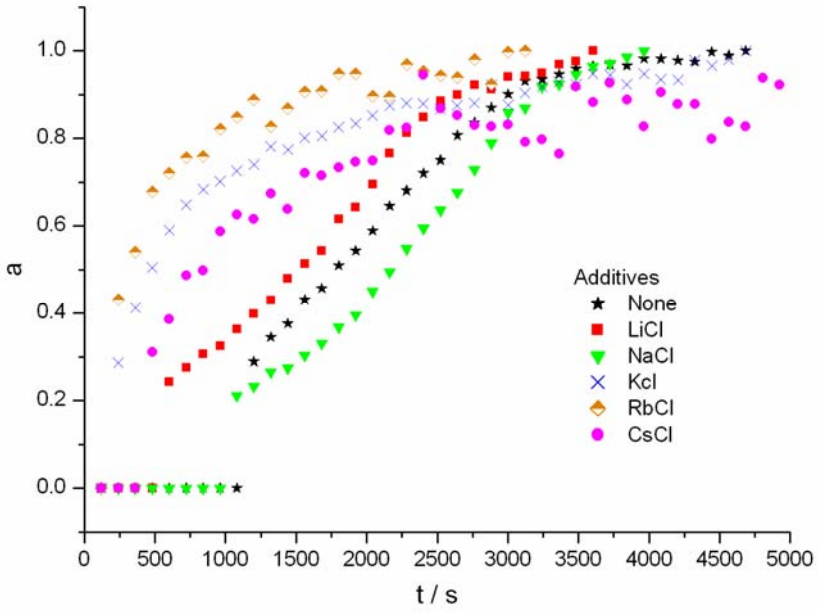

Figure 8.10. Extent of reaction α vs time *t* for the (200) reflection of W/Mo-HTB for different alkali ions.

Given that the growth mechanism of the alkali W/Mo-HTB oxides appears to vary strongly with the type of cation used, kinetic analyses were performed by fitting the experimental data to a theoretical expression relating the extent of reaction α to time.[24] A more detailed description of kinetic data evaluation can be found in the literature, together with several kinetic expressions applied to solid-state kinetics and the general shape of their curves. For data analysis, t_{ind} is subtracted from t, and $\ln[-\ln(1 - \alpha)]$ versus $\ln(t)$ is plotted in the Sharp-Hancock plot (abbreviated SH).[25] A mechanistic change in the course of the reaction is reflected in a change in the slope of the SH curve. The reaction exponent m can be evaluated

from the linear part of the curve.

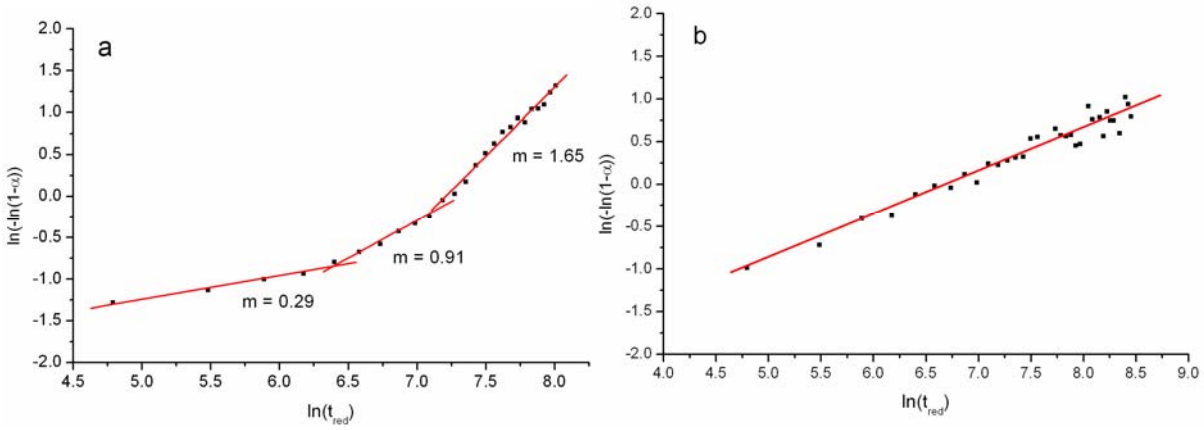

Figure 8.11. Sharp-Hancock plots of alkali-W/Mo-HTB oxide formation in the presence of (a) LiCl and (b) CsCl.

The SH plot obtained upon addition of LiCl (Figure 8.11 a) clearly shows that the growth of the Li-W/Mo-HTB oxides proceeds via different stages. The reaction exponent increases in three stages from 0.29 over 0.91 to 1.65, thereby indicating the gradual transition from diffusion control over phase boundary control to a nucleation controlled mechanism (for details cf. Table 8.2). These values for *m* are not in line with the classical established solid state kinetic models. But this does not come as a surprise, because different mechanisms can occur simultaneously and/or subsequently and the *m* value reflects an average of the processes. In addition, the situation is complicated by the fact that small amounts of a side product are formed that vanishes after prolonged hydrothermal treatment. Figure 8.11 b displays a typical SH plot in the presence of CsCl, showing that the experimental points are on a straight line for the entire reaction time. This is a clear indication that no changes in the reaction mechanism occur during the reaction progress and the value of $m \approx 0.55$ suggests that diffusion control is the prevailing mechanism. The values of *m* for all alkali cations are summed up and compared to the additive-free reactions in Table 8.3.

Table 8.2. Overview of different kinetic models used for data interpretation.[17]

Growth mode	Rate equation f(α) = *kt*	*m*
Diffusion-controlled		
$D_1(\alpha)$	$\alpha^2=0.25(t/t_{0.5})$	0.62
$D_2(\alpha)$	$(1-\alpha)\ln(1-\alpha)+\alpha=0.1534(t/t_{0.5})$	0.57
$D_3(\alpha)$ [Jander]	$[1-(1-\alpha)^{1/3}]^2=0.0425(t/t_{0.5})$	0.54
$D_4(\alpha)$ [Ginstling – Brounshtein]	$1-2\alpha/3-(1-\alpha)^{2/3}=0.0367(t/t_{0.5})$	0.57
Phase-boundary-controlled:		
$R_2(\alpha)$	$1-(1-\alpha)^{1/2}=0.2929(t/t_{0.5})$	1.11
$R_3(\alpha)$	$1-(1-\alpha)^{1/3}=0.2063(t/t_{0.5})$	1.07
First order		
$F1(\alpha)$	$[-\ln(1-\alpha)]= 0.6931(t/t_{0.5})$	1.00
Nucleation [Avrami – Erofe'ev]:		
$A2(\alpha)$	$[-\ln(1-\alpha)]^{1/2}= 0.8326(t/t_{0.5})$	2.00
$A3(\alpha)$	$[-\ln(1-\alpha)]^{1/3}= 0.885(t/t_{0.5})$	3.00

Table 8.3. Survey of kinetic data for all in situ EDXRD experiments.

Cation	t_{ind}/min	$t_{0.5}$/min	α	*m*	Growth model
None	18	30	$\alpha< 0.5$	0.40	D_2/D_3
			$\alpha>0.5$	1.39	F_1/R_3
LiCl	8	26	$0.2<\alpha<0.4$	0.29	
			$0.4<\alpha<0.6$	0.91	
			$\alpha>0.6$	1.65	R_2/A_2
NaCl	16	36	$0.3<\alpha<0.6$	1.06	$F_1/R_2/R_3$
			$\alpha>0.6$	2.33	A_2
KCl	2	8	$\alpha<0.75$	0.68	D_3
			$\alpha>0.75$	0.57	
RbCl	2	5	$\alpha>0.2$	0.55	D_3
CsCl	6	14	$\alpha>0.2$	0.55	D_3

In general, the additive-free reaction seems to be mainly controlled by diffusion ($m \approx 0.40$, $\alpha < 0.5$). For $\alpha > 0.5$, *m* increases to about 1.39, a value being more in accordance with phase boundary control and/or a nucleation controlled growth mechanism. Moreover, the growth of Na-W/Mo-HTB oxide still proceeds similarly to the pristine and Li-containing systems via two regions ranging from $0.3 < \alpha < 0.6$ and $\alpha > 0.6$, respectively. The reaction is first

dominated by a phase boundary controlled process (m = 1.06) and then continues via a nucleation controlled mechanism (m = 2.33). When NaCl is replaced by KCl, however, the value of m changes only slightly during the course of the reaction from about 0.68 in the early stages towards $m \approx 0.57$ for later reaction progress. This indicates the transition to the different mechanistic behaviour observed for RbCl and CsCl: in the presence of the larger alkali chlorides, the diffusion controlled reaction mechanism remains unchanged over the entire reaction time. The mechanistic changes observed for the range of M-W/Mo-HTBs (M = Li – Cs) point out that the formation of the mixed oxides is a far more complex process than the hydrothermal growth of the alkali W-HTBs that proceeds without cation-induced mechanistic changes.[20] For a more detailed and rigorous analysis, the experimental data were directly compared to the different models under consideration by plotting $t/t_{0.5}$ vs. α (cf. Figure 8.12, Table 8.2 and 8.3). Whereas the formation of Li-W/Mo-HTBs cannot be interpreted with any of the standard models in the early stages of the reaction, the experimental data fit with a nucleation-controlled model A_2/phase boundary controlled model R_2 (Figure 8.12 a, Table 8.3). The inset in Figure 8.11 a clearly demonstrates that the α values in the initial phase of the reaction cannot be assigned to a common model, because they display a shift between the different mechanisms (F1/R2/R3), thereby indicating a complex mechanistic evolution of the growth process. Furthermore, the limited amount of data is due to the rapid onset of the reaction that renders the observation quite challenging as has been outlined in the previous studies on the formation of MoO_3 nanorods.[26] Therefore, the overall formation of Li-W/Mo-HTBs is differentiated into several mechanistic stages as outlined by the stepwise fitting of the Sharp-Hancock plot (Figure 8.11 a). This complex influence of Li^+ in comparison with the other alkali cations might be linked to its largest hydrodynamic radius in the series.

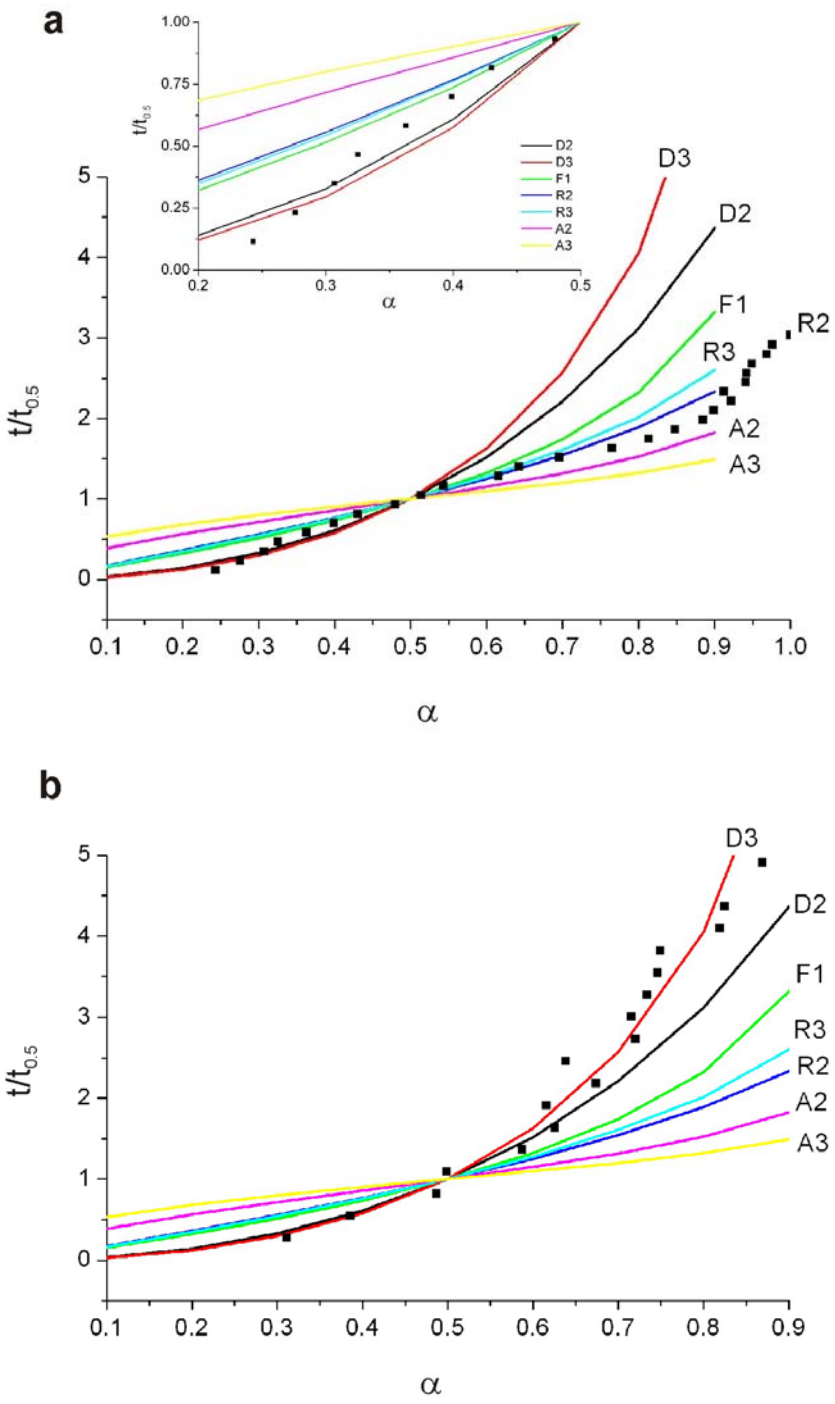

Figure 8.12. Comparison of the evolution of experimental $t/t_{0.5}$ data as a function of α (black squares) with different theoretical models for the formation of alkali-W/Mo-HTB oxides in the presence of (a) LiCl (inset: initial phase of the reaction) and (b) CsCl.

The reaction in the presence of NaCl agrees rather well with the models $F_1/R_2/R_3$ in the range of $0.3 < \alpha < 0.6$. Whilst there is no clear distinction possible between these three models, the advanced reaction ($\alpha > 0.6$) clearly fits with a nucleation controlled model A_2. The most

interesting observation, however, is the constant agreement of all data recorded for KCl, RbCl and CsCl with the three-dimensional diffusion controlled model D_3. All in all, the general morphology trend is clearly reflected in the corresponding reaction kinetics. In line with their analogous formation mechanism, the products obtained in the presence of KCl, RbCl, or CsCl exhibit in principle a similar nanostructured hierarchical organization of nanorod building blocks into cylindrical bundles that form spherical architectures. In contrast, the additive-free reaction and the hydrothermal processes in the presence of LiCl and NaCl result in the formation of nanofibers, and the complex multi-step reaction mechanisms prevent their organization into more symmetric patterns (Table 8.3). The 3D diffusion controlled growth of the hierarchically organized spherical arrangements of M-W/Mo-HTB (M = K – Cs) is thus a unique example for the correspondence of mechanism and morphology. Moreover, our in situ studies (cf. chapter 3) on the formation of morphologically related hierarchical Bi_2WO_6 nanostructures point into the same direction, because they are also formed via a diffusion-controlled mechanism with Avrami exponents around 0.5, which demonstrates that diffusion-controlled mechanisms are obviously a common denominator for the self-organization of nanoscale building blocks into hierarchical structures for chemically different hydrothermal systems. All in all, a kinetically based correlation between the type of additive, the different reaction mechanisms and the morphology of the nanoscale oxides was established: The mechanistically versatile lighter alkali chlorides give rise to overall anisotropic alkali W/Mo-HTB, whereas the heavier alkali chlorides generate isotropic hierarchical structures based on a uniform diffusion mechanism. Generally, the complete prediction of structures and morphologies resulting from complex hydrothermal oxide systems remains an almost insurmountable endeavor that requires novel and comprehensive insight into nucleation processes, additive-surface interactions and reaction mechanisms for each individual system, because there are no generally applicable theoretical models available at the moment. We hereby demonstrate that the strategy of steering hydrothermal processes through readily available inorganic additives in combination with their kinetic/mechanistic understanding is a versatile and practical approach towards controlled synthesis and materials design.

8.3.4 Local structure of W/Mo-HTB oxides

Although the reaction kinetics of nanostructured W/Mo-HTB oxide formation in the presence of alkali chlorides could be understood through in situ EDXRD studies, little is known about the coordination states of Mo in the W/Mo-HTB framework. Especially the influence of different alkali cations that are present in the hexagonal channels on the local environment and oxidation state of W and Mo atoms remain poorly understood; however, these factors are of great importance for the applications of W/Mo-HTB materials.

Although the phase of the products could be assigned with laboratory X-ray powder diffraction methods, their accuracy is not sufficient to elucidate the detailed local environments of the different cations. The small particle size together with the low degree of crystallinity of the M-W/Mo-HTBs (M = Li to Rb) led to very broad FWHM values (full width at half maximum) that rendered Rietveld refinements impossible. XAS methods were the appropriate choice for the present study, because the determination of the coordination and oxidation state of a target element with XANES/EXAFS does not require the presence of a crystalline material.[27] This wide applicability of XAS furthermore facilitates the assignment of local environments to dopant elements in solid solutions, such as the Mo atoms incorporated into the HTB framework.

Figures 8.13 a and b show the W L_3 and Mo K edge XANES/EXAFS spectra recorded on the entire W/Mo-oxide series (cf. Table 8.3). The XAS spectra at the W L_3 edge show a single large peak (white line) above the edge which corresponds to a transition of 2p3/2 electrons towards the 5d state.[28] The edge position is usually strongly related to the oxidation state of the absorber ion with lower oxidation states leading to lower energies. As the W L_3 absorption edge energies for all W/Mo-oxide samples remained practically constant at 10204 eV, the presence of alkali cations within the channels does not seem to affect the oxidation state of the tungsten atoms in an obvious manner. However, the intensity of the white line increased with the size of the alkali cation from 1.76 for the alkali-free W/Mo-oxide reference sample to 1.96 for Rb-W/Mo-HTB. Recently, *T. Pauporte* et al. have suggested that the white line height increased with declining condensation degree (the structural arrangement at a middle distances) of W species.[29] Interestingly, the incorporation of alkali cations with increasing

ionic radii reduced the condensation level of the W species within the W/Mo-HTB oxides. On the other hand, all XAS investigations at the Mo K-edge (cf. Figure 8.13 b) had a characteristic weak pre-edge feature around 19995 eV prior to the sharp absorption rise at around 20000 eV in common that is due to the dipole-forbidden transition from 1s to the *n*d (*n* = 3 or 4) level (by dipole selection rules).[30] The intensity of the pre-edge peak is generally higher for tetrahedrally coordinated Mo(VI) than the values observed for an octahedral environment. A comparison of a representative W/Mo-HTB oxide sample with $NaMoO_4$ as a reference for tetrahedrally coordinated Mo(VI) clearly showed that the HTB compound has a less intense pre-edge peak and a more pronounced feature on the ascending part of the curve (denoted with A and B in Figure 8.14). This indicates that all the Mo atoms in the W/Mo-HTB samples are octahedrally coordinated. In contrast to the constant +VI oxidation state of W observed for all the samples, the position of the Mo K edge shows a clear dependence on the incorporated alkali cation that points to a higher redox flexibility of the Mo centers. Whereas the Mo K edge positions for the pristine W/Mo-HTB oxide, Li-W/Mo-HTB and Na-W/Mo-HTB remain constant at 20010 eV, the values for K-W/Mo-HTB and Rb-W/Mo-HTB are shifted to lower energies at 20009 eV and 20007 eV, respectively, thereby pointing to a lower oxidation state of Mo in the corresponding samples. These valence changes can be quantified by evaluating the XAS edge positions using references with different valences V (Mo metal (z(V) = 0), MoO_2 (z(V) = +4) and MoO_3 (z(V) = +6)) and the linear relationship between the Mo valence and the Mo K edge energy shift (E) can be expressed as follows (Figure 8.15):[31]

$$z\,(\mathrm{V}) = -0.000724 + 0.51658\,f(\mathrm{E}). \qquad (Eq.\ 8.1)$$

The average valence of Mo in W/Mo-HTB, Li-W/Mo-HTB and Na-W/Mo-HTB was determined to +5.7 on this basis and the values for K-W/Mo-HTB and Rb-W/Mo-HTB were calculated to +5.2 and +4.1, respectively, on the basis of the above linear function. As the hexagonal channels may contain both NH_3 and NH_4^+,[8] a more accurate determination of the sample compositions beyond these trends is a demanding task, because it would also include a full discussion of possible oxygen vacancies. We have tried to determine the NH_3/NH_4^+ ratio

by means of solid state NMR, but given that these attempts were not sucessful, we prefer to limit the stoichiometric accuracy to the tentative values given in Table 8.1.

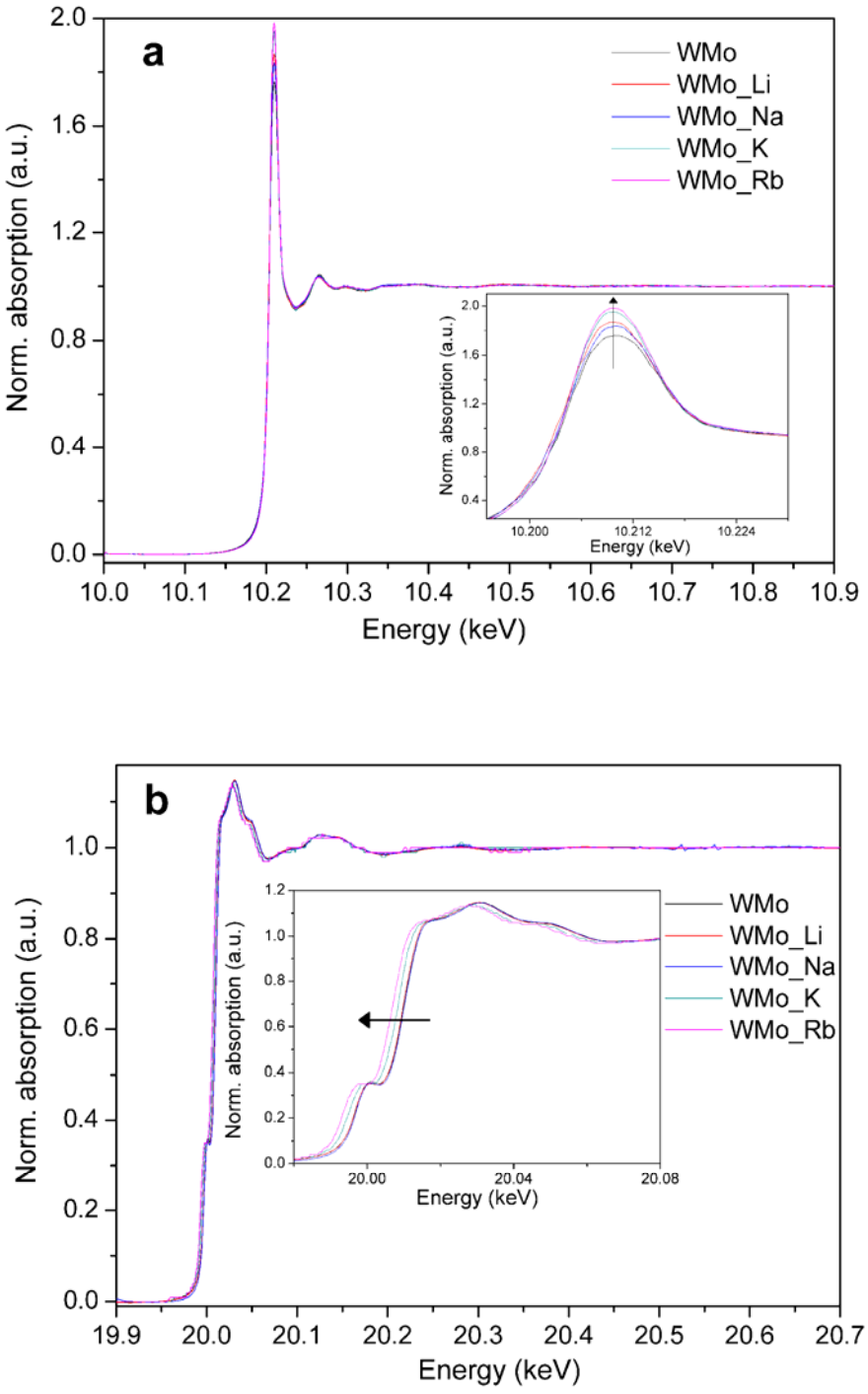

Figure 8.13. (a) Normalized W L_3-edge EXAFS spectra (inset: W L_3-edge XANES spectra) and (b) normalized Mo K-edge EXAFS spectra (inset: Mo K-edge XANES spectra of the WMo-oxide series prepared with different alkali chlorides).

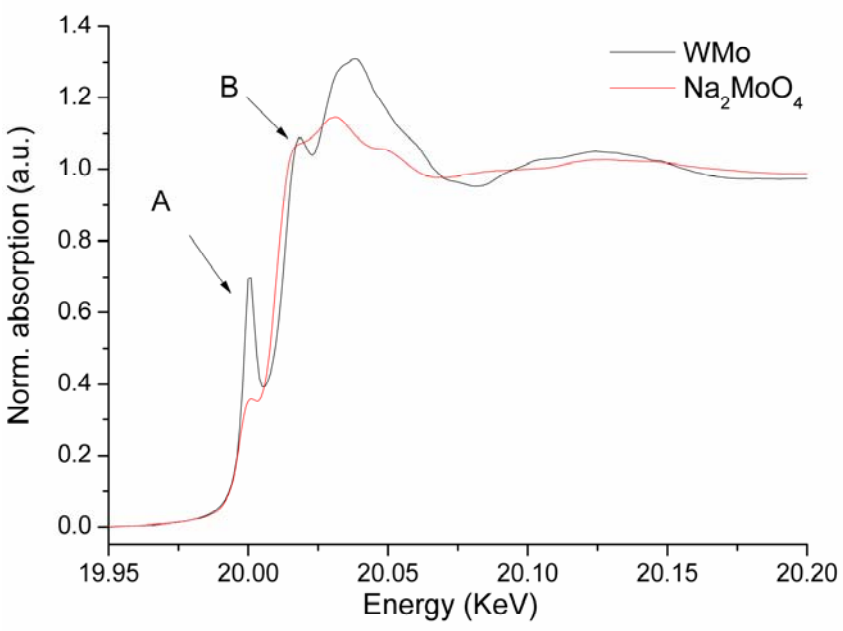

Figure 8.14. Mo K-edge XANES of WMo-HTB oxide compared with Na_2MoO_4 as a reference for tetrahedrally coordinated Mo(VI).

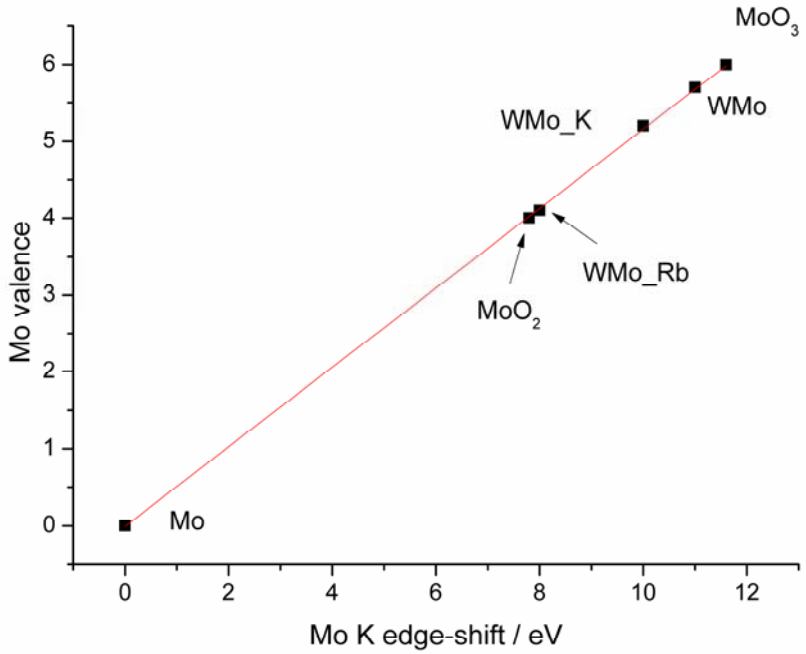

Figure 8.15. Linear relationship of average valence and Mo K-edge positions.

The above valence trends shed an interesting light on the different response of W and Mo towards the incorporation of alkali cations into the channel structure: whereas the Mo centers display versatile redox properties, the oxidation state of W is not affected by the ion-exchange

process. Previous studies have already shown that Mo(VI) is more easily reduced in the HTB framework than W(VI).[32]

More detailed information about the coordination numbers and bond distances of the W and Mo atoms can furthermore be obtained from curve-fitting analyses of the W L_3 and Mo K edge EXAFS spectra, respectively (for according typical Fourier transformed spectra (FT, without phase correction cf. Figure 8.16). The close resemblance of the FT spectra recorded at the W L_3 and Mo K edge is a good prerequisite for the facile replacement of W with Mo in the channel walls of the HTB structure. The first peak appears at 0.8 - 2.2 Å and can be assigned to the first coordination shell consisting of six oxygen atoms, whilst the following peak in the region from 2.2 to 3 Å arises from multiple scattering (MS). The W/Mo-W/Mo coordination shell is finally reflected in the third backscattering contribution (from 3 to 4.3 Å).[29] Although the key structure motif of hexagonal WO_3 has already been determined from powder X-ray diffraction data in 1979,[33] the lack of suitable single crystals rendered the complete structural elucidation quite difficult so that the occurrence of two subsets of W-O distances was suggested. This hypothesis was revised in a recent attempt to fit the EXAFS spectra recorded at the W L_3 edge of hexagonal WO_3: as two W-O distances turned out to be insufficient to obtain a good fit, the authors proposed to use three different W-O distances instead.[34] These findings also apply for our current measurements that can best be fitted with a set of three W/Mo-O distances. The fit was performed in *r*-space and the prefactor S_0^2 was fixed at 0.8 (for typical fit results cf. Figure 8.16 as well as Tables 8.4 and 8.5). Firstly, the coordination sphere of the Mo atoms bears a close resemblance to that of tungsten as the majority species and the mean Mo-O distances appear to be slightly shorter that the corresponding W-O values (for details cf. Table 8.4 and 8.5). A clear-cut relationship between the individual bond lengths and the type of the incorporated alkali cation could not be established.

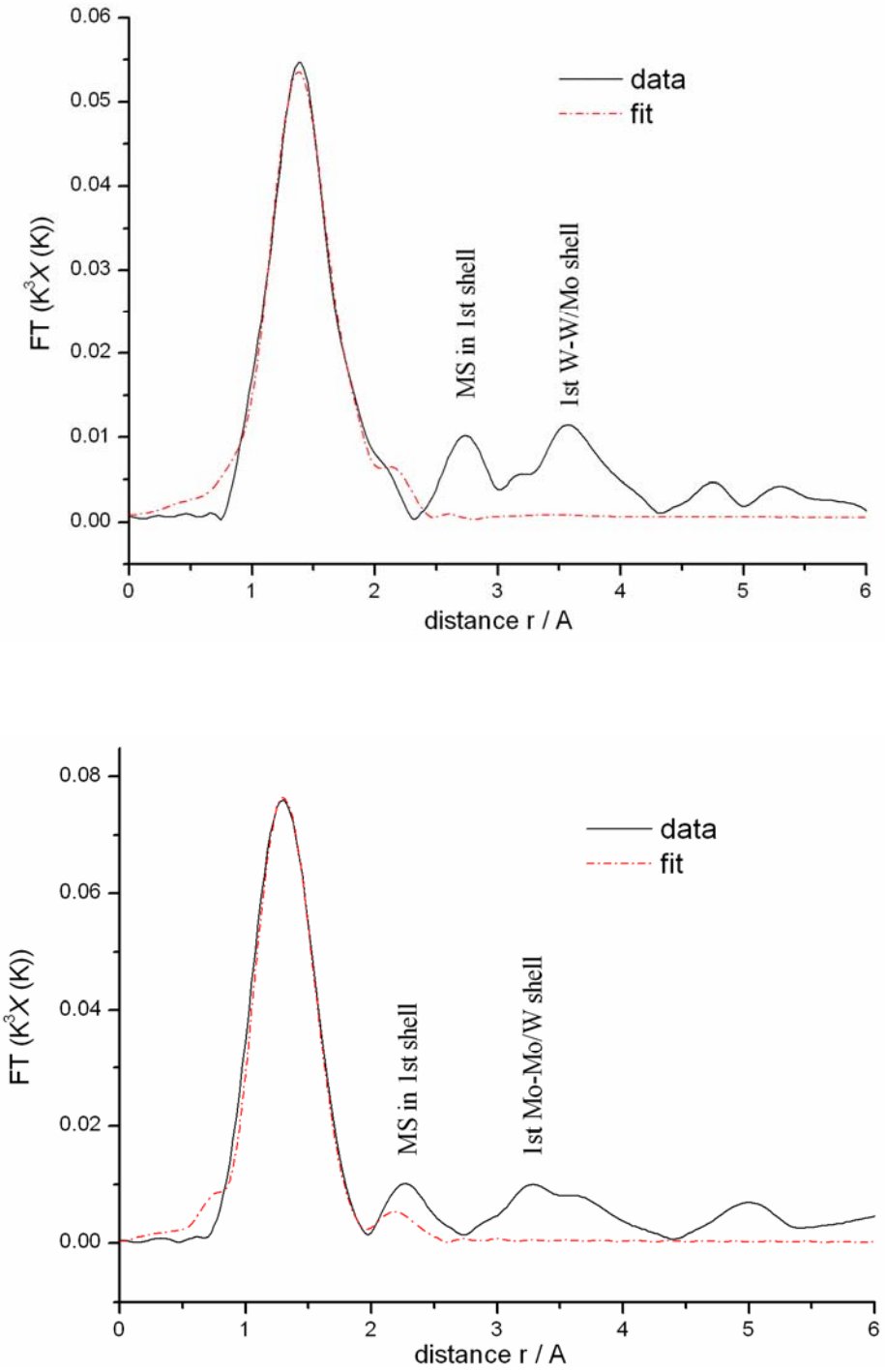

Figure 8.16. Typical first-shell fit of W/Mo-HTB, considering the first oxygen coordination (up) recorded at W L_3-edge and (bottom) recorded at Mo K-edge.

Table 8.4. Structural parameters determined by fitting of EXAFS spectra at the W L_3-edge of M-W/Mo-HTBs (W-O bonds).*

Samples	CN	R / Å	δ^2 / Å^2	ΔE / eV	Residual
W/Mo-HTB	2.3	1.73	0.004	12.2	7.0
	1.9	1.83	0.004	12.4	
	1.8	2.06	0.004	12.5	
Li-W/Mo-HTB	2.2	1.74	0.004	12.1	8.8
	2.6	1.87	0.010	12.2	
	1.2	2.10	0.002	12.2	
Na-W/Mo-HTB	2.7	1.75	0.006	12.2	9.9
	1.4	1.81	0.004	12.2	
	1.9	2.06	0.006	12.3	
K-W/Mo-HTB	2.4	1.74	0.003	12.4	7.0
	1.8	1.89	0.006	12.5	
	1.8	2.07	0.003	12.6	
Rb-W/Mo-HTB	2.0	1.73	0.002	12.9	6.6
	2.4	1.87	0.006	13.1	
	1.6	2.09	0.003	13.2	

*CN is the coordination number with the overall number 6, R is the distance of the first oxygen coordination shell, δ^2 is the Debye-Waller factor, ΔE is the energy shift and Residual is the factor assigning the goodness of fit.

Table 8.5 Structural parameters determined by fitting of EXAFS spectra at the Mo K-edge of M-W/Mo-HTBs (Mo-O bonds).

Samples	CN	R / Å	δ^2 / Å^2	ΔE / eV	Residual
W/Mo-HTB	2.5	1.69	0.002	-6.6	5.8
	1.3	1.80	0.005	8.9	
	2.2	2.11	0.005	9.6	
Li-W/Mo-HTB	2.0	1.72	0.001	9.1	5.8
	2.2	1.78	0.003	-12	
	1.8	2.11	0.003	12	
Na-W/Mo-HTB	2.2	1.73	0.001	11.9	4.6
	2.3	1.80	0.004	-12	
	1.5	2.11	0.003	12	
K-W/Mo-HTB	2.1	1.73	0.001	12	5.0
	2.1	1.79	0.003	-12	
	1.8	2.09	0.005	12	
Rb-W/Mo-HTB	2.0	1.71	0.001	9.3	7.3
	2.4	1.78	0.004	-12	
	1.6	2.10	0.005	12	

8.3.5 Thermal stability of W/Mo-HTB oxides

As sensor fabrication often involves continuous heating processes, the sensing material under consideration has to be stable with respect to structure, composition and, if possible, morphology. This renders thermal stability investigations of the W/Mo-oxides an indispensable prerequisite for their potential use in gas sensors. The M-W/Mo-HTB series (M = Li – Rb) was thus investigated with TG methods and representative results are shown in Figure 8.17. The Cs-W/Mo-HTB are excluded in the following studies, because they frequently contain small amount of pyrochlore side products. This renders their phase pure synthesis rather demanding. The alkali-free W/Mo-HTB underwent a mass loss of 3.0 % below 300 °C that is probably due to residual amounts of H_2O or acetic acid. In the next stage

(300 to 520 °C), further release of NH_3 and H_2O led to a mass loss of 2.5 % (note that the nitrogen content obtained from elemental analyses is 1.5 %). No further mass loss upon raising the temperature to 750 °C was observed and at higher temperatures, the evaporation of MoO_3 sets in as had been previously reported.[35] The TG curves of Li-, Na- and K-W/Mo-HTB basically followed the same trend with different mass losses for H_2O and NH_3, respectively, that agreed well with the elemental analyses (Table 8.1). Rb-W/Mo-HTB, however, exhibits a different thermal behaviour, because an additional mass loss peak (0.44 %) was observed at 550 °C with a corresponding thermal effect that remains to be investigated in detail: for the evaporation of Rb-containing species, the temperature appears to be too low, so that this phenomenon may arise from more firmly bound water molecules in the channels that are only removed upon stronger heat treatment or it could be traced back to loss of other species involving oxygen.

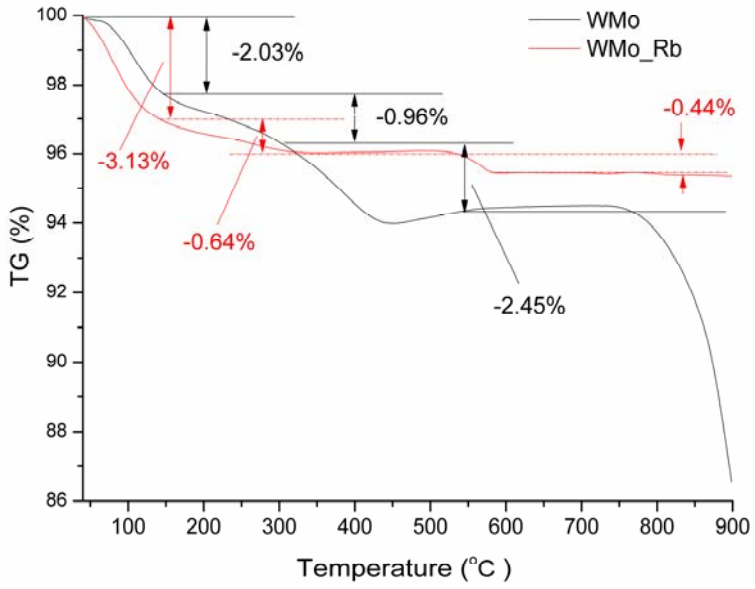

Figure 8.17 TG analysis of W/Mo-HTB and Rb-W/Mo-HTB oxides

Moreover, the structural changes accompanying the thermal treatment were monitored with the help of in situ powder XRD. Figure 8.18 shows the temperature-dependent in situ XRD patterns of W/Mo-HTB and Rb-W/Mo-HTB. At ca. 435 °C, W/Mo-HTB displayed the onset of a phase transition into a modification of lower symmetry as can be seen from the splitting

of the (111) and (112) reflections together with the appearance of new reflections.

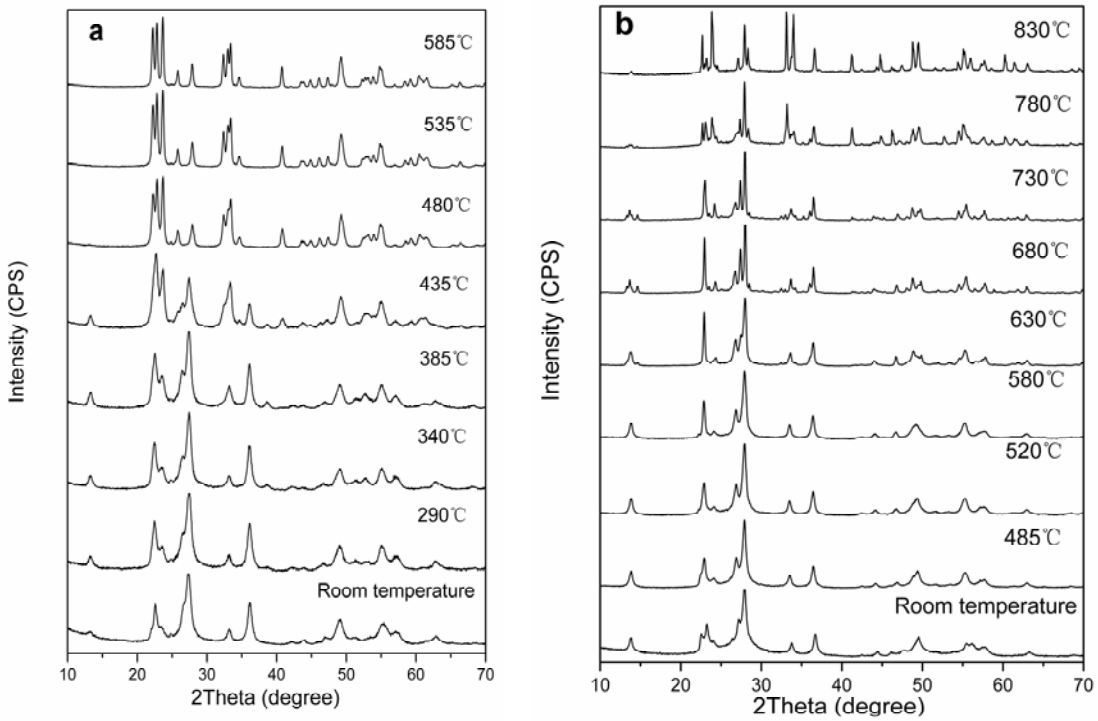

Figure 8.18 In situ PXRD patterns of (a) W/Mo-HTB and (b) Rb-W/Mo-HTB oxide

The XRD patterns recorded at 480 °C permitted its identification as monoclinic $W_{0.71}Mo_{0.29}O_3$ (JCPDS No. 76-1279: S. G. $P2_1/n$, a = 7.446 Å, b = 7.424 Å, c = 7.613 Å, β = 91.24°). Interestingly, the Rb-containing HTB framework displayed a much higher thermal stability up to around 580 °C and a further temperature raise led to the formation of a mixed oxide phase with a hitherto unassigned structural motif. Generally, the thermal resistance of the HTB framework is a function of the incorporated cations that are indispensable to maintain the open structural motif: not only is the hexagonal form of WO_3 metastable at room temperature with respect to the monoclinic and orthorhombic modifications, but it has also not been accessed yet in pure form without any stabilizing ions or molecules.[8] Therefore, the collapse of the alkali-free as well as of the Li-, Na- and K-W/Mo-HTB frameworks goes hand in hand with the observed mass loss of the NH_4^+ ions that are obviously essential to keep up the structural motif (Figures 8.17 and 8.18). However, their role can be taken over by the larger Rb^+ cation that exerts a stronger stabilizing effect than its smaller analogues Li^+, Na^+

and K^+ so that the Rb-W/Mo-HTB oxides contain the lowest amounts of NH_4^+ among the series (Table 8.1). Concerning the formation of Na-HTBs, a minimum value of 160 ppm Na^+ in the precursor has been reported to be essential for the above-mentioned structural stabilization effect.[8] The remaining amounts of the smaller cations (Li^+, Na^+, K^+) after heat treatment are obviously insufficient to sustain the hexagonal framework, whereas the Rb-W/Mo-HTBs contain enough Rb^+ to withstand treatment in air up to 580 °C (cf. Figures 8.17 and 8.18).

EDXS determinations of the residual alkali amounts after heat treatment at 500 °C for 1 h demonstrated that these values were in the same range of the initial contents prior to heating. In the case of thermally treated Li-W/Mo-HTBs, the effect of the thermally induced phase changes was monitored with solid state NMR investigations (for details cf. below and Figure 8.21). All samples heated to 500 °C were structurally characterized afterwards in more detail with ex situ powder XRD (cf. Figure 8.19). The alkali-free W/Mo-HTB as well as the Li- and Na-containing compounds were almost quantitatively converted into a monoclinic phase with a structural motif corresponding to that of $W_{0.71}Mo_{0.29}O_3$ (JCPDS No. 76-1279, cf. above). The intermediate ionic radius of K^+ prevents the complete collapse of the HTB structure so that it is partially retained besides the monoclinic phase as can be seen from Figure 8.19. Rb-W/Mo-HTB, however, remains structurally unaltered at 500 °C as to be expected from the in situ XRD screening (Figure 8.18). In addition to the consequences of the thermal treatment for the structure and composition of the HTBs, the morphological changes were also investigated: SEM images of the pristine W/Mo-HTBs as well as of the Li- and Na-containing analogues demonstrated that the nanorods emerging from hydrothermal synthesis (cf. Figure 8.3) aggregated into larger and less anisotropic particles at 500 °C with individual sizes ranging from several tens of nanometers to several hundred nanometers (Figure 8.20).

As the K-W/Mo oxide product formed after heating is biphasic, its morphology is a mixture of rods and irregularly shaped particles (Figure 8.20 d). Most importantly, the structural stability of Rb-W/Mo-HTBs goes hand in hand with morphological resistance so that the hierarchical arrangement of nanorods withstands the thermal treatment at 500 °C as can be seen from Figures 8.20 e and f. In summary, the choice of the stabilizing cation is decisive for

the thermal materials properties of W/Mo-HTBs and Rb-W/Mo-HTBs turned out to be the most promising candidates for the application in sensors at high operational temperatures.

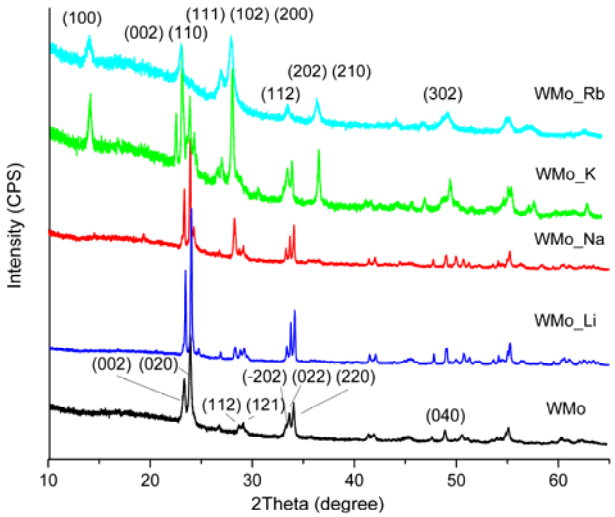

Figure 8.19. PXRD patterns of the WMo-oxide series after heat treatment at 500 ^{o}C.

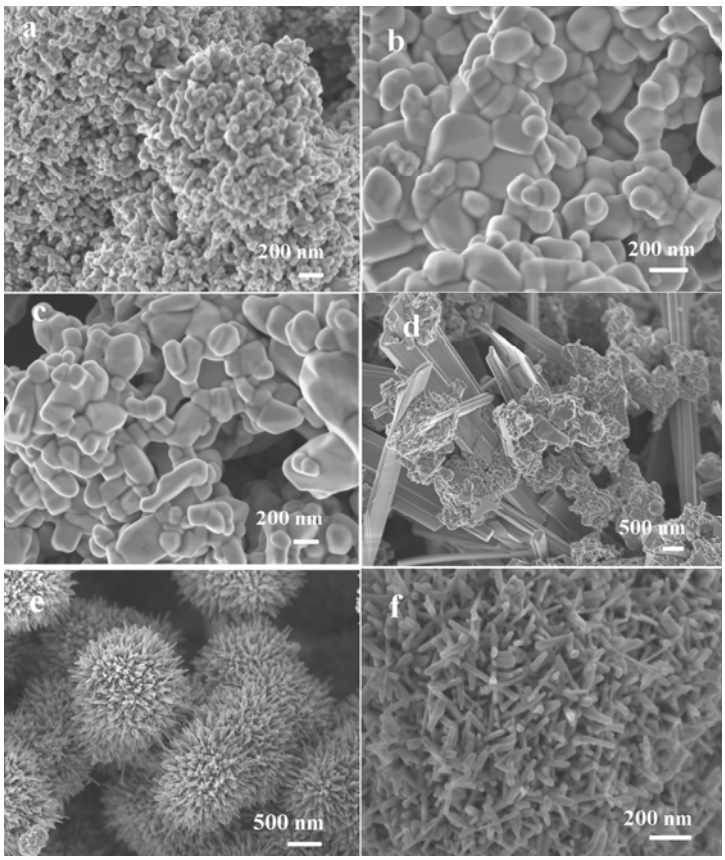

Figure 8.20. Representative SEM images of the WMo-oxide series after heat treatment at 500 ^{o}C for 1 h: (a) W/Mo; (b) Li-W/Mo oxide; (c) Na-W/Mo oxide; (d) K-W/Mo oxide; (e) Rb-W/Mo-HTB; (f) Rb-W/Mo-HTB recorded at higher magnification.

In section 8.3.2, the mobility of Li^+ within the channels of the W/Mo-HTB host framework has been investigated by solid state ^7Li NMR spectroscopy. Our preceding solid state ^7Li NMR spectroscopy investigations on the mobility of Li^+ within the W/Mo-HTB host framework showed that it depends on the channel types – trigonal or hexagonal – that can in principle both the occupied. After the heat treatment at 500 °C, the Li^+ cations are situated in the structurally different environment of the above mentioned monoclinic W/Mo-phase (cf. Figure 8.19). We thus applied ^7Li NMR spectroscopy as another complementary technique to differentiate the present W/Mo-oxide types with respect to their application-oriented properties by monitoring the effect of thermal treatment on the Li^+ mobility and environment in the Li-W/Mo-oxide samples. A comparison of the HTB spectra prior to heating and those of the monoclinic Li-containing phase is shown in Figure 8.21 together with a schematic representation of the different structural features of the host lattice. Whereas the major structural changes only exerted a slight influence on the ^7Li solid state NMR, the ^7Li MAS spectrum of the monoclinic mixed oxide still showed an extensive side band pattern (Figure 8.21 e) that is comparable with the results of the pristine Li-W/Mo-HTB sample (Figure 8.21 b). This implies the presence of quasi spherical symmetry with dominating chemical shift anisotropy (CSA) effects and just small quadrupolar interactions, as had been already observed on the untreated sample (cf. above). However, the sharpening of the static ^7Li powder pattern from 5.8 kHz to 2.0 kHz after the heating process can be interpreted as a first indication of an accompanying increase of the Li^+ mobility that was further confirmed through a solid state ^7Li-T_1 time measurement. Generally, the obtained T_1 data are an additional, sensitive probe for the dynamic behavior of the respective lithium sites. After treatment of the Li-W/Mo-oxide at 500 °C, the T_1 time displayed a more than three-fold decrease from 481 ms to 144 ms. Furthermore, the presence of only one isotropic shift in the MAS spectra indicated the presence of a single site for Li^+ remaining after the thermally induced phase transition: other than the dual channel system of the HTBs (Figure 8.21 c), the monoclinic W/Mo-oxide host framework offers only one tunnel type to be occupied by the Li^+ cations (Figure 8.21 f).

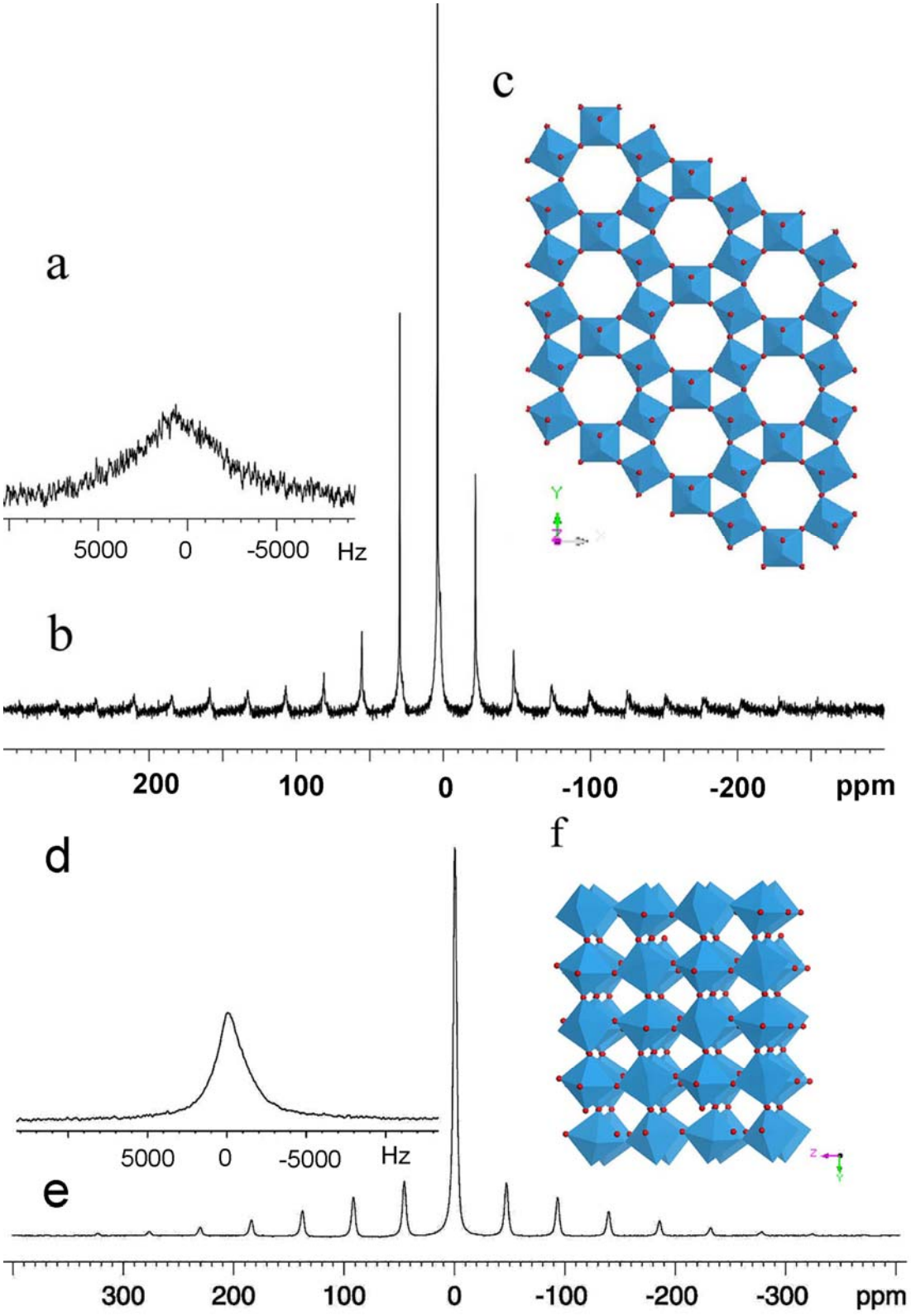

Figure 8.21 Solid state ^{7}Li NMR spectra of Li-W/Mo-HTB (a) without MAS, (b) with MAS, (c) structural motif of hexagonal tungstates, compared to that of Li-W/Mo oxide after heat treatment (d) without MAS, (e) with MAS, (f) schematic structure representation of monoclinic $W_{0.71}Mo_{0.29}O_3$

8.3.6 Ammonia sensing properties of W/Mo-oxides

The sensitivity of tungsten trioxide towards a variety of gases such as NO_2, O_3, H_2S, H_2 and NH_3, has been reported in a variety of studies.[5, 37] Among them, WO_3 is weakly sensitive towards NH_3 in comparison with a superior sensitivity in detecting NO_2 gas.[38]

The temperature-dependent sensitivity of the W/Mo-oxide series towards NH_3 as a test gas was therefore monitored and Figure 8.22 displays the results for the different sensor types obtained with 100 ppm NH_3 diluted in pure Ar. Here, the sensitivity S was defined as the relative resistance: $S = R_{Ar}/R_{ammonia}$. The resistance of all W/Mo-oxide based sensors generally decreased in the presence of NH_3 which is a characteristic feature of *n*-type semiconductors.[38] It is well accepted that the gas response of semiconductor gas sensors is attributed to the chemical sorption of oxygen on the oxide surface and the subsequent reaction between adsorbed oxygen and test gas, which brings the resistance change.

The adsorbed oxygens are present on the surface of the metal oxides:

$$O_{2\ (g)} + e^- \rightarrow O_2^-{}_{(ads)} \qquad (Eq.\ 8.2)$$

$$O_2^-{}_{(ads)} + e^- \rightarrow 2O^-_{(ads)} \qquad (Eq.\ 8.3)$$

And the reaction for sensing ammonia is thus given by:

$$2NH_3 + 3O^-_{(ads)} \rightarrow N_2 + 3H_2O + 3e^- \qquad (Eq.\ 8.4)$$

As expected from equation (*Eq. 8.4*), the resistance of the WMo_series material decreases once they contact with ammonia.

As mentioned above, this trend does not apply for the Cs-W/Mo-oxide member of the series: its different and more complex sensing behaviour is still under investigation and will be reported elsewhere. The discontinous and non-linear resistance change with temperature among the series is also typical of oxide sensors[39] and it arises from the type of chemisorption on the surface: whilst lower temperatures do not provide sufficient energy for chemisorption, the desorption rate outweighs the adsorption rate again at considerably higher temperatures. This results in maximum sensitivities at medium temperatures (275 °C) for all oxides under investigation so that they display a lower operating temperature than pure WO_3 nanofibers at 350 °C.[40] When operated at the optimized temperature of 275 °C, all alkali-containing oxide samples exhibit higher sensitivities than the alkali-free W/Mo-oxide and,

irrespective of the actual structure motif, the overall sensitivity of the oxide materials increases with the size of the alkali cations, i.e. $S_{Rb\_WMo} > S_{K\_WMo} > S_{Na\_WMo} > S_{Li\_WMo}$ (cf. Table 8.6).

As structural stability and a high surface area are key requirements for sensor materials, the Rb-W/Mo-HTB is of the highest interest among the investigated compounds and this corresponds with its highest sensitivity of 11.1 among the series that exceeds the lowest value observed for alkali-free W/Mo-oxide (1.2) almost by a factor of ten. The same trends apply for the sensitivity as a function of the gas concentration at 275 °C (Figure 8.23): the sensitivities increase rapidly towards a saturation value at higher concentrations. These data can be well fitted with the power law for semiconductor oxides according to the following equation:

$$S = 1 + A_g(P_g)^{\beta} \qquad (Eq.\ 8.5)$$

where P_g is the target gas partial pressure, which is proportional to the gas concentration, A_g is a prefactor, and β is the exponent of P_g.

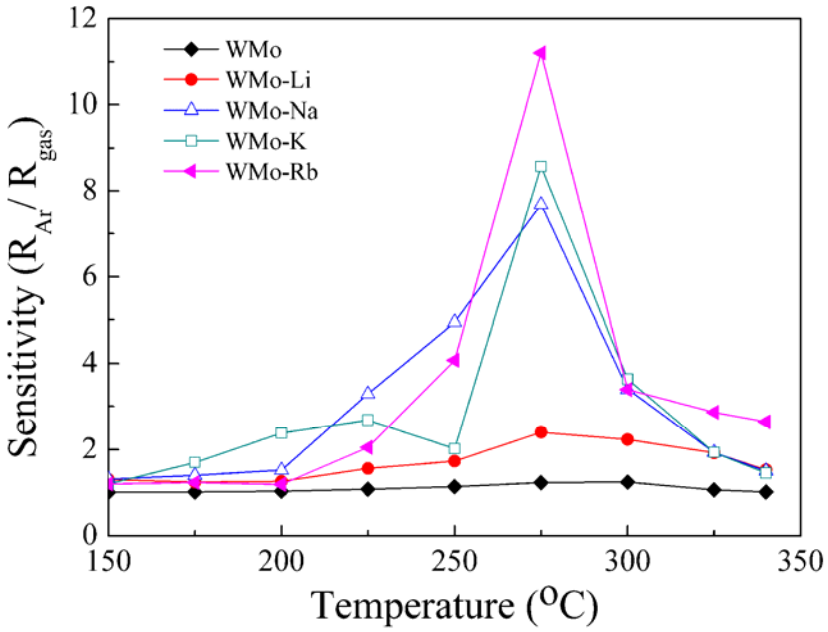

Figure 8.22. Sensitivity S vs. operation temperature for NH_3 sensing (100 ppm) of gas sensors based on the W/Mo-oxide series.

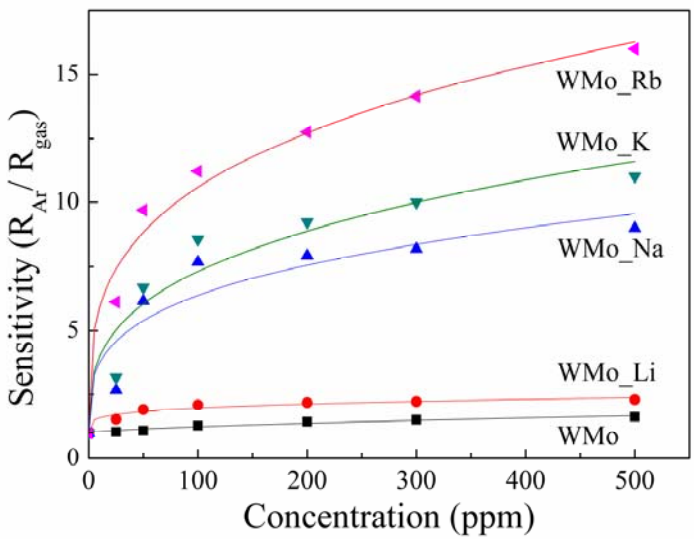

Figure 8.23. Sensitivities vs. different NH_3 concentrations at an operating temperature of 275 ^oC.

The sensing response of the Rb-WMo-HTB oxide layer towards 25 ppm NH_3 is shown in Figure 8.24. The film showed a decrease in resistance on exposure to NH_3, which is characteristic for an *n*-type semiconductor. Furthermore, the response time was quite fast with 228 s for 25 ppm NH_3, but the recovery time was much longer (12 min.). In general, the gas sensor based on films exhibited a longer recovery time in comparison with their response time due to difficulties in the gas desorption process.

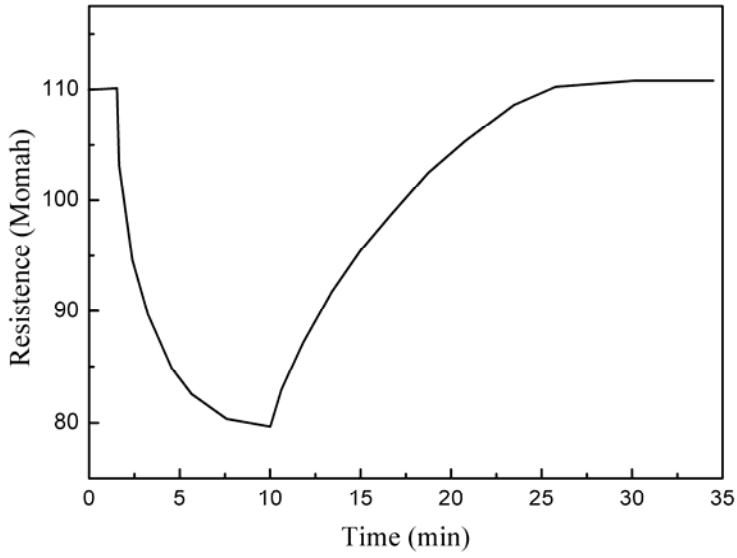

Figure 8.24. Sensing response curves of Rb-W/Mo-HTB towards 25 ppm NH_3 at 275 ^oC.

Table 8.6. Values of *S* at 275 °C towards 100 ppm NH_3 of the WMo-series gas sensors.

Sample	WMo	WMo_Li	WMo_Na	WMo_K	WMo_Rb
S	1.2	2.1	7.7	8.6	11.1

The present results clearly show that the sensitivity of W/Mo-oxides towards NH_3 can be remarkably enhanced through the structural incorporation of additional cations (cf. Table 8.6). However, several parameters, especially structure, composition and morphology and thermal stability of the product have to be optimized and the phase change of the M-W/Mo-HTB oxides (M = Li – K) during sensor preparation has to be taken into consideration. With respect to these stability criteria, Rb-W/Mo-HTB oxides are the most promising sensor candidate emerging from the present study, because all other oxides undergo a complete or partial phase transition into a monoclinic W/Mo-oxide modification during the annealing process at 500 °C that is required to remove the organic additives for the completion of the sensor fabrication. As the gas sensitivity increases with the amount of HTB phases remaining in the oxide components after thermal treatment, it is reasonable to conclude that the W/Mo-HTB oxide type displays a higher sensitivity towards NH_3 than the monoclinic modification. This hypothesis agrees well with recent reports on WO_3 that confirm a better NH_3 sensing performance of the binary nanoscale HTBs in comparison with monoclinic WO_3 particles.[41] Moreover, the number of conducting electrons determines the quantity of the chemisorbed oxygen on the surface and affects the sensing process. It is well known that the electronic properties of tungsten bronzes are strongly related to their crystal structure. For example, it was demonstrated that the resistivity of hexagonal potassium bronze is significantly lower than that of tetragonal $K_{0.58}WO_3$.[42] In the course of our study, pristine W/Mo-oxide exhibited the largest intrinsic resistance in air atmosphere, thereby indicating an insufficient amount of conducting electrons on the surface (cf. Figure 8.25). As a result, the alkali-free W/Mo sample shows the lowest sensitivity towards NH_3 gas. Figure 8.25 furthermore shows that the order of resistance ($R_{WMo\text{-}Li} > R_{WMo\text{-}Na} > R_{WMo\text{-}K}$) corresponds to the observed sensitivities ($S_{WMo\text{-}Li} < S_{WMo\text{-}Na} < S_{WMo\text{-}K}$) along the lines of the above discussion. Rb-W/Mo-HTB, however, exhibited the highest sensitivity together with relatively larger intrinsic

resistance. This can be attributed to its unique morphology compared with the remaining members of the W/Mo-oxide series: as shown in Figure 8.20, Rb-W/Mo-HTB retained its hierarchical arrangement of nanorods with a remarkable high surface area after heat treatment at 500 °C, whereas the other W/Mo-oxides showed intense agglomeration effects. The high surface area of Rb-W/Mo-HTB enhances the number of absorption sites for NH_3 sensing, which in turn improves the sensing properties. This is in line with a recent study that identified the surface area as the most influential parameter in the comparison of the NO_2 sensing properties of different tungsten oxide modifications.[43] The present results furthermore illustrate the importance of selecting the appropriate cationic stabilizer for the hexagonal HTB channels to render them sufficiently stable for technical applications.

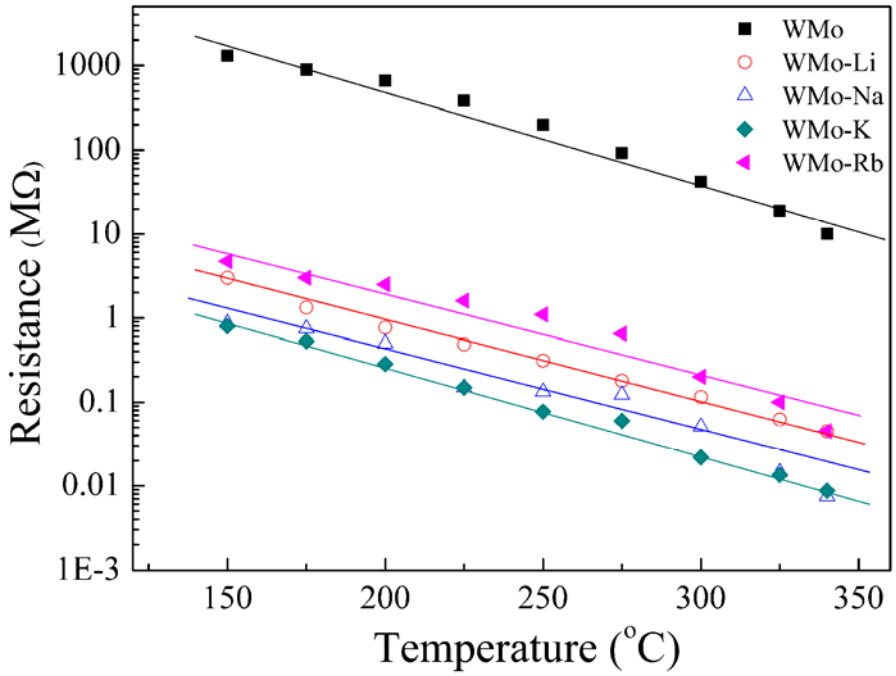

Figure 8.25. Temperature-dependent resistivity among the W/Mo-oxide sensor series.

8.4 Conclusions

In conclusion, the complex mechanistic role of alkali halides as morphology-directing agents in the hydrothermal formation of nanostructured W/Mo-HTB oxides was investigated with in

situ EDXRD methods. For the first time, a kinetically based correlation between the type of additive, the different reaction mechanisms and the morphology of the nanoscale oxides was established: the mechanistically versatile lighter alkali chlorides give rise to overall anisotropic alkali-W/Mo-HTB oxides whereas the heavier alkali chlorides generate isotropic hierarchical structures based on a uniform diffusion mechanism. We hereby demonstrate that the strategy of steering hydrothermal processes through readily available inorganic additives in combination with their kinetic/mechanistic understanding is a versatile and practical approach towards controlled synthesis and materials design.

Moreover, the local environment and oxidation state of W and Mo in HTBs with different alkali cations was investigated with XANES/EXAFS methods. It was found that Mo is more easily reduced than W in the HTB framework structure. The oxidation state of Mo decreased from +5.7 to +4.1 with increasing radius of the incorporated alkali cation. The thermal stability of M-W/Mo-HTBs also strongly depends on the type and amount of alkali cations. The hexagonal W/Mo-HTB, Li-W/Mo-HTB and Na-W/Mo-HTB phases changed into a $W_{0.71}Mo_{0.29}O_3$ monoclinic phase through heat treatment at 500 ^{o}C, whereas K-W/Mo-HTB was transformed into a mixture of hexagonal and monoclinic phases. In contrast, Rb-W/Mo-HTB can maintain both the hexagonal structure and its hierarchically nanostructured morphology up to 580 °C. In addition, Rb-W/Mo-HTB displayed a high sensitivity towards NH_3 in comparison with the remaining W/Mo-oxides of the series.

References

[1] (a) C. N. R. Rao, F. L. Deepak, G. Gundiah, A. Govindaraj, *Prog. Solid State Chem.* **2003**, *31*, 5; (b) G. R. Patzke, F. Krumeich, R. Nesper, *Angew. Chem. Int. Ed.* **2003**, *42*, 972.

[2] (a) O. Zivkovic, C. Yan, M. J. Wagner, *J. Mater. Chem.* **2009**, *19*, 6029; (b) J. D. Guo, K. P. Reis, M. S. Whittingham, *Solid State Ionics* **1992**, *305*, 53.

[3] (a) M. Shibuya, M. Miyauchi, *Chem. Phys. Lett.* **2009**, *473*, 126; (b) W. Han, M. Hibino, T. Kudo, *Solid State Ionics* **2000**, *128*, 25.

[4] L. Francke, E. Durand, A. Demourgues, A. Vimont, M. Daturi, A. Tressaud, *J. Mater. Chem.* **2003**, *13*, 2330.

[5] (a) J. Polleux, A. Gurlo, N. Barsan, U. Weimar, M. Antonietti, M. Niederberger, *Angew. Chem. Int. Ed.* **2006**, *45*, 261; (b) X. L. Li, T. J Lou, X. M. Sun, Y. D. Li, *Inorg. Chem.* **2004**, *43*, 5442.

[6] M. S. Whittingham, In *Solid State Devices*; Chowdari, B. V. R., Radhakrishnan, S., Eds.; World Scientific: Singapore, **1988**.

[7] A. Shengelaya, S. Reich, Y. Tsabba, K. A. Müller, *Eur. Phys. J. B* **1998**, *12*, 13.

[8] I. M. Szilagyi, J. Madarasz, G. Pokol, P. Kiraly, G. Tarkanyi, S. Saukko, J. Mizsei, A. L. Toth, A. Szabo, K. Varga-Josepovitso, *Chem. Mater.* **2008**, *20*, 4116.

[9] C. S. Griffith, F. Sebesta, J. V. Hanna, P. Yee, E. Drabarek, M. E. Smith, V. Luca, *J. Nucl. Mater.* **2006**, *358*, 151.

[10] K. P. Reis, A. Ramanan, M. S. Whittingham, *J. Solid State Chem.* **1992**, *96*, 31.

[11] C. S. Griffith, V. Luca, *Chem. Mater.* **2004**, *16*, 4992.

[12] O. Merdrignac-Conanec, P. T. Moseley, *J. Mater. Chem.* **2002**, *12*, 1779.

[13] B. Xue, J. Peng, Z. F. Xin, Y. M. Kong, L. Li, B. Li, *J. Mater. Chem.* **2005**, *15*, 4793.

[14] K. Byrappa, T. Adschiri, *Prog. Cryst. Growth Ch.* **2007**, *53*, 117.

[15] K. Byrappa, T. Adschiri, *Handbook of Hydrothermal Technology*, Noyes, Park Ridge, N. J., **2001**.

[16] R. I. Walton, D. O'Hare, *Chem. Commun.* **2000**, 2283.

[17] L. Engelke, M. Schaefer, M. Schur, W. Bensch, *Chem. Mater.* **2001**, *13*, 1383.

[18] T. Ressler, *J. Synchrot. Radiat.* **1998**, *5*, 118.

[19] M. Newville, *J. Synchrot. Radiat.* **2000**, *8*, 322.

[20] A. Michailovski, R. Kiebach, W. Bensch, J.-D. Grunwaldt, A. Baiker, S. Konmarneni, G. R. Patzke, *Chem. Mater.* **2007**, *19*, 185.

[21] C. A. Fyfe, *Solid State NMR for Chemists*, Guelph, Ontario, Canada, **1983**.

[22] B. Cowan, *Nuclear Magnetic Resonance and Relaxation*, Cambridge University Press, New York, **1997**.

[23] A. Abragam, *Principles of Nuclear Magnetism*, Clarendon Press, Oxford, **1986**.

[24] (a) M. Avrami, *J. Chem. Phys.* **1939**, *7*, 1103 ; (b) M. Avrami, *J. Chem. Phys.* **1940**, *8*, 212. (c) M. Avrami, *J. Chem. Phys.* **1941**, *9*, 177.

[25] (a) J. D. Hancock, J. H. Sharp, *J. Am. Ceram. Soc.* **1972**, *55*, 74; (b) B. M. Mohamed, J. H. Sharp, *J. Mater. Sci.* **1997**, 1595.

[26] A. Michailovski, J.-D. Grunwaldt, A. Baiker, R. Kiebach, W. Bensch, G. R. Patzke, *Angew. Chem. Int. Ed.* **2005**, *44*, 5643.

[27] J. J. Rehr, R. C. Albers, *Rev. Mod. Phys.* **2000**, *72*, 621.

[28] S. Yamazoe, Y. Hitomi, T. Shishido, T. Yanaka, *J. Phys. Chem. C* **2008**, *112*, 6869.

[29] T. Pauporte, Y. Soldo-Olivier, R. Faure, *J. Phys. Chem. B* **2003**, *107*, 8861.

[30] A. M. Beale, G. Sankar, *Chem. Mater.* **2003**, *15*, 146.

[31] T. Ressler, J. Wienold, R. E. Jentoft, T. Neisius, *J. Catal.* **2002**, *210*, 67.

[32] C. Genin, A. Driouiche, B. Gerand, M. Figlarz, *Solid State Ionics* **1992**, *53-56*, 315.

[33] B. Gerand, G. Nowogrocki, J. Guenot, M. Figlarz, *J. Solid State Chem.* **1979**, *29*, 429.

[34] J. Moscovici, A. Rougier, S. Laruelle, A. Michalowicz, *J. Chem. Phys.* **2006**, *125*, 124505.

[35] A. Michailovski, F. Krumeich, G. R. Patzke, *Chem. Mater.* **2004**, *16,* 1433.

[36] J. Pfeifer, C. Balazsi, B. A. Kiss, B. Pecz, A. L. Toth, *J. Mater. Sci. Lett.* **1999**, *18*, 1103.

[37] I. M. Szilagyi, L. S. Wang, P. I. Gouma, C. Balaszsi, J. Madarasz, G. Pokol, *Mater. Res. Bull.* **2009**, *44*, 505.

[38] B. B. Cao, J. J. Chen, X. J. Tang, W. L. Zhou, *J. Mater. Chem.* **2009**, *19*, 2323.

[39] K. Zheng, L. Gu, D. Sun, X. Mo, G. Chen, *Mater. Sci. Eng. B* **2010**, *166*, 104.

[40] G. Wang, Y. Ji, X. Huang, X. Yang, P. Gounma, M. Dudley, *J. Phys. Chem. B* **2006**, *110*, 23777.

[41] L. Wang, J. Pfeifer, C. Balazsi, P. I. Gouma, *Mater. Manu. Process* **2007**, *22*, 773.

[42] R. Fan, X. H. Chen, Z. Gui, S. Y. Li, Z. Y. Chen, *Mater. Lett.* **2001**, *49*, 214

[43] Z. Liu, M. Miyauchi, T. Yamazaki, Y. Shen, *Sens. Actuators B* **2009**, *140*, 514-519.

Summary

The future of our modern society will depend on how we handle our most urgent issues, namely the depletion of natural water and energy resources. At present, it is becoming increasingly clear that oxide nanomaterials can play a very important role in the development of clean energy sources and in all fields of environmental safety and protection that are essential to ensure a constant quality of life. This calls for synthetic approaches that are capable of producing nanomaterials on a large scale and simultaneously permit the control of relevant materials properties, such as structure, size, particle morphology and chemical composition. The present thesis demonstrates that inorganic hydrothermal routes in combination with their kinetic/mechanistic understanding through in situ EDXRD/XAS methods are a very promising and practical approach towards the targeted production of complex oxide nanomaterials with a high environmental application potential.

We have successfully synthesized $BiVO_4$ nanoparticles (chapter 2), hierarchical Bi_2WO_6 and $Bi_2W_{0.75}Mo_{0.25}O_6$ nanostructures (chapter 3 and 4), $Bi_6S_2O_{15}$ nanowires (chapter 7) and M-W/Mo-HTB oxides (M = Li to Cs, chapter 8) using readily available inorganic materials as precursors or additives under hydrothermal reaction conditions. The synthesis of M-W/Mo-HTB oxide is one of the most interesting and representative examples for the efficient use of inorganic additives as morphology control agents: the addition of LiCl and NaCl directs the W/Mo-HTB oxides into fibrous structures, whereas KCl induces an arrangement of these nanofibers into spherical patterns. RbCl and CsCl as additives support a hierarchical organization of nanorods on three levels into microspheres. Furthermore, we developed a novel inorganic hydrothermal coating approach towards hierarchical Bi_2WO_6/TiO_2 heterostructures (chapter 5). Our route is of general relevance, because the substrate oxides can be exchanged to access other heterostructured materials, such as $BiVO_4/TiO_2$ or Bi_2MoO_6/TiO_2. However, the most challenging task in the development of inorganic hydrothermal routes is the optimization of their manifold reaction parameters, such as temperature, pH, concentration, choice of precursors and additives. This may lead to time-consuming screening procedures so that the appropriate parameter window for the preparation

of nanostructured target oxides can be difficult to find. This is mainly due to a lack of mechanistic knowledge concerning the hydrothermal formation processes of oxide materials. The development of in situ techniques opens up the unique opportunity to understand the hydrothermal growth mechanisms of oxide nanomaterials through their direct monitoring. Therefore, we have studied the hydrothermal formation mechanisms of hierarchical Bi_2WO_6 and $Bi_2W_{0.75}Mo_{0.25}O_6$ nanostructures (chapter 3 and 4), $Bi_6S_2O_{15}$ nanowires (chapter 7) and nanostructured M-W/Mo-HTB oxides (chapter 8) with a combination of in situ EDXRD and XAS techniques. The in situ EDXRD results show that the growth mechanism of hierarchically structured Bi_2WO_6 microspheres is temperature independent in the studied temperature range (150 - 180 ^oC). Nevertheless, the reaction mechanism for this hydrothermal system is pH-dependent. The reaction under strongly acidic conditions (pH 1.1) is diffusion controlled with Avrami exponents of ca. 0.5. When the pH value is raised to 4.0, the Avrami exponent increases accordingly to 0.77 with the accelerated reaction kinetics. This is the reason for the decay of Bi_2WO_6 micro-architectures into their nanosheet building blocks at higher pH values. Moreover, our in situ studies on the formation of morphologically related hierarchical M-W/Mo-HTB oxides (M = K to Cs) point into the same direction, because they are also formed via a diffusion-controlled mechanism with Avrami exponents around 0.55. Our results demonstrated that diffusion-controlled mechanisms are probably a common denominator for the self-organization of nanoscale building blocks into hierarchical structures that excel through enhanced gas sensing or photocatalytic properties in comparison with less complex morphologies of the same compounds. The newly formed $Bi_6S_2O_{15}$ nanowires, however, follow a different mechanistic pathway, because they are formed via a two-step sequence starting from a minute dissolution of the bulk Bi_2O_3 precursor under hydrothermal conditions, followed by $Bi_6S_2O_{15}$ nucleation and growth along the *c* axis at the solid/liquid interface. All in all, we have successfully demonstrated that combined in situ EDXRD/XAS approaches are highly efficient tools to elucidate how different parameters influence the hydrothermal growth process of oxide materials and to obtain insights into hydrothermal formation mechanisms.

The structural characterization of oxide nanomaterials can turn into another remarkable

challenge, especially when the diffraction data of hitherto unknown phases are affected by small particle sizes and anisotropic morphologies. In the course of this thesis, we have successfully determined the crystal structure of $Bi_6S_2O_{15}$ nanowires through a skilful combination of tilt electron diffraction, Rietveld refinement and HRTEM investigations (chapter 7). The crystal structure of $Bi_6S_2O_{15}$ can be described as $(Bi_{12}O_{14})_n^{8n+}$ columns surrounded with sulfate tetrahedra and these anisotropic structural features are a driving force for the above-mentioned nanowire growth. Moreover, the local structure of M-W/Mo-HTB oxides was studied by XANES/EXAFS techniques (chapter 8). It was found that Mo is more easily reduced than W in the HTB framework. The oxidation state of Mo decreased from +5.7 to +4.1 with increasing radii of the alkali cations incorporated into the HTB framework.

Moreover, we investigated the potential applications of the obtained oxide nanomaterials in the areas of photocatalysis and gas and humidity sensors. We demonstrated how the visible light driven photocatalytic activity of bismuth containing V/W/Mo-oxides can be enhanced through three different strategies: firstly, this goal was obtained by decreasing the particle size (chapter 2), next, the electronic structure of the target compounds was adjusted (chapter 4) and finally the photocatalytic performance was improved through the synthesis of heterostructures (chapter 5). Furthermore, our results revealed that the *Aurivillius* type oxides Bi_2WO_6 and Bi_2MoO_6 (chapter 6) as well as the $Bi_6S_2O_{15}$ nanowires (chapter 7) have a promising application potential for the fabrication of effective, stable and low-cost humidity sensors, whereas nanostructured Rb-W/Mo-HTB oxide is a good candidate for NH_3 sensing.

All in all, this thesis illustrates how a three-step approach (synthesis optimization – mechanistic studies – materials applications) paves the way to the comprehensive development of oxide nanomaterials for the most relevant technologies of the future.

Zusammenfassung

Die Zukunft unserer modernen Gesellschaft hängt entscheidend davon ab, wie wir unsere dringendsten Probleme auf breiter Ebene lösen, zu denen insbesondere die Verknappung der natürlichen Wasser- und Energieressourcen gehören. Es zeichnet sich deutlich ab, dass oxidische Nanomaterialien eine entscheidende Rolle bei der Entwicklung einer nachhaltigen Energieversorgung und in allen Gebieten von Umweltschutz und –sicherheit (z. B. Abwasserreinigung oder Sensorik) spielen werden und somit dazu beitragen können, die Standards unserer Lebensqualität zu erhalten. Dies erfordert die Entwicklung grosstechnischer Synthesemethoden für Oxid-Nanomaterialien, die gleichzeitig eine Kontrolle über deren entscheidenden Eigenschaften erlauben, zu denen Struktur, Partikelgrösse und –morphologie sowie chemische Zusammensetzung zählen. In der vorliegenden Arbeit wird aufgezeigt, dass anorganische Hydrothermalsynthesen in Kombination mit ihrer mechanistischen Untersuchung durch in situ EDXRD/XAS-Methoden ein vielversprechender und praxisnaher Weg sind, um gezielt auch komplexe nanostrukturierte Oxide mit einem hohen Anwendungspotential in den oben genannten Bereichen herzustellen.

Auf der synthetischen Ebene wird anhand der hydrothermalen Produktion von $BiVO_4$-Nanopartikeln (Kapitel 2), hierarchisch strukturiertem Bi_2WO_6 und nanostrukturiertem $Bi_2W_{0.75}Mo_{0.25}O_6$ (Kapitel 3 und 4) sowie von $Bi_6S_2O_{15}$-Nanofasern (Kapitel 7) und M-W/Mo-HTB-Oxiden (M = Li – Cs, Kapitel 8) die Effizienz und Vielseitigkeit einfacher anorganischer Ausgangsstoffe als Prekursoren oder Additive illustriert.

Die Synthese der M-W/Mo-HTB Oxidserie ist dabei ein besonders interessantes Beispiel für den Einsatz anorganischer Additive zur Kontrolle der entstehenden Morphologie der nanostrukturierten Produkte: der Zusatz von LiCl und NaCl fördert das Wachstum von faserigen W/Mo-HTB-Oxiden, während in Gegenwart von KCl ihre Organisation in sphärische Einheiten beginnt. Dieser hierarchische Selbstorganisationsprozess von Nanorods auf drei Ebenen ist mit RbCl und CsCl als Additiven voll ausgeprägt.

Darüber hinaus entwickelten wir eine neue anorganische Beschichtungsstrategie zur hydrothermalen Herstellung von hierarchisch aufgebauten Bi_2WO_6/TiO_2-Heterostrukturen

(Kapitel 5). Diese Syntheseroute ist von generellem Interesse, da sie auf verschiedene oxidische Substrate angewandte werden kann und so andere Komposite, wie $BiVO_4/TiO_2$ oder Bi_2MoO_6/TiO_2, zugänglich sind.

Dennoch bleibt die Optimierung hydrothermaler Prozesse eine Herausforderung, da sie viele simultane Parameter umfasst, zu denen Temperatur, pH-Wert, Konzentration und Auswahl von Prekursoren und Additiven etc. zählen. Dies zieht oft zeitaufwendige Screening-Prozesse nach sich, so dass es schwierig sein kann, das geeignete Parameterfenster für die Präparation eines gewünschten Oxid-Nanomaterials zu finden. Erschwerend kommt hier noch der Mangel an mechanistischem Wissen über fundamentale hydrothermale Bildungsprinzipien oxidischer Materialien hinzu.

Daher eröffnet die Entwicklung von in situ-Techniken die einzigartige Möglichkeit, hydrothermale Mechanismen durch die direkte Beobachtung des Wachstums von Oxiden zu ermitteln. Auf dieser Grundlage haben wir eine Kombination von in situ EDXRD und XAS-Techniken angewendet, um die hydrothermalen Bildungsprozesse von hierarchisch strukturiertem Bi_2WO_6 und nanostrukturiertem $Bi_2W_{0.75}Mo_{0.25}O_6$ (Kapitel 3), von $Bi_6S_2O_{15}$ Kapitel 7) und von nanoskaligen M-W/Mo-HTB-Oxiden (Kapitel 8) zu untersuchen. So zeigen z. B. die in situ EDXRD-Resultate zum Wachstumsmechanismus hierarchisch strukturierter Bi_2WO_6-Mikrosphären, dass dieser im betrachteten Temperaturintervall (150 – 180 °C) temperaturunabhängig ist, aber stark durch den pH-Wert beeinflusst wird. Die Reaktion unter stark sauren Bedingungen (pH 1.1) ist diffusionskontrolliert mit einem Avrami-Exponenten von ca. 0.5. Mit steigendem pH-Wert (4.0) nimmt auch dieser Wert auf 0.77 zu, da die Reaktionskinetik beschleunigt wird und darin liegt die Begründung für den Zerfall der Bi_2WO_6-Mikroarchitekturen in ihre nanoskaligen Komponenten bei höheren pH-Werten. In situ-Studien zur Bildung der morphologisch ähnlichen hierarchisch-sphärischen M-W/Mo-HTB-Oxide (M = K – Cs) weisen ebenfalls auf einen diffusionskontrollierten Mechanismus mit Avrami-Exponenten um 0.55 hin. Unsere Untersuchungen deuten also an, dass verschiedene Selbstorganisation nanoskaliger Einheiten in sphärische Architekturen, die sich durch interessante sensorische und katalytische Eigenschaften auszeichnen, mechanistisch korreliert sind.

Anders jedoch verläuft das Wachstum von $Bi_6S_2O_{15}$-Nanofasern, die über einen zweischrittigen hydrothermalen Bildungsweg entstehen: zuerst gehen geringe Mengen des Bi_2O_3-Prekursors in Lösung, dann setzt ein Nukleationsprozess von $Bi_6S_2O_{15}$ ein, gefolgt vom Wachstum entlang der *c*-Achse an der fest/flüssig-Grenzfläche. Gesamthaft wird deutlich, dass man mit Hilfe von kombinierten in situ EDXRD/XAS-Strategien auf effiziente Weise deutliche Einblicke in verschiedene hydrothermale Oxidsysteme erhalten und die jeweils ablaufenden Bildungsmechanismen vergleichen kann.

Eine weitere Herausforderung ist die strukturelle Charakterisierung bislang unbekannter Nanomaterialien, besonders, wenn die Qualität der erhaltenen Beugungsdaten durch kleine und stark anisotrope Teilchendimensionen verringert wird. Dies wird im Rahmen dieser Arbeit für die Strukturbestimmung der $Bi_6S_2O_{15}$-Nanodrähte gezeigt, die nur mit einer anspruchsvollen Kombination aus Elektronenbeugungsmethoden, Rietveld-Verfeinerungen und HRTEM-Untersuchungen (Kapitel 7) gelang. Die Kristallstruktur von $Bi_6S_2O_{15}$, das einen neuen Typ von Bismutoxysulfaten repräsentiert, enthält $(Bi_{12}O_{14})_n^{8n+}$-Stränge als zentrales Strukturelement, die von SO_4^{2-}-Tetraedern umgeben sind und als anisotrope Triebkraft das Wachstum der Nanodrähte fördern. In struktureller Hinsicht beschäftigten wir uns auch mit der lokalen Koordinationsumgebung der Mo- und W-Zentren in den M-W/Mo-HTB-Oxiden, die mit Hilfe von XANES/EXAFS-Techniken untersucht wurde (Kapitel 8). Die Ergebnisse zeigen, dass der Oxidationszustand von Mo von +5.7 auf +4.1 abnimmt, wenn Alkalikationen mit steigendem Radius in das HTB-Gerüst eingebaut werden.

Darüber hinaus sind die Anwendungsmöglichkeiten der erhaltenen Oxid-Nanomaterialien in den Bereichen der Photokatalyse (für mögliche Abwasserreinigung) und der Gas- sowie Feuchtigkeitssensorik ein zentraler Punkt dieser Arbeit. Am Beispiel von Bi-V/W/Mo-Oxiden zeigten wir, wie die photokatalytische Aktivität unter Einfluss von sichtbarem Licht mit drei Strategien verändert werden kann: zunächst geschah dies durch eine Verringerung der Partikelgrösse (Kapitel 2), des weiteren führte die gezielte Veränderung der elektronischen Struktur zum gewünschten Ergebnis (Kapitel 4) und schlussendlich konnten die katalytischen Eigenschaften durch die Bildung von Heterostrukturen verbessert werden (Kapitel 5).

Im Bereich der Sensorik erwiesen sich die *Aurivillius*-Oxide Bi_2WO_6 und Bi_2MoO_6 (Kapitel

6) als sowie die $Bi_6S_2O_{15}$-Nanodrähte (Kapitel 7) als vielversprechend für die effiziente und kostengünstige Herstellung stabiler Feuchtigkeitssensoren, während die nanostrukturierten Rb-W/Mo-HTB-Oxide aussichtsreiche Kandidaten für die Entwicklung von NH_3-Sensoren sind.

Zusammenfassend illustriert die vorliegende Arbeit, wie eine umfassende Strategie in drei Schritten (Syntheseoptimierung – mechanistische Studien – Materialanwendungen) den Weg zu oxidischen Nanomaterialien für die technologischen Herausforderungen der Zukunft weisen kann.

Ying Zhou

Institute of Inorganic Chemistry, University of Zurich, Switzerland
Phone: +41 44 63 54697 e-mail: ying.zhou@aci.uzh.ch

Personal Information

• married, male, P. R. China, born on 24th March 1981

Education

PhD studies in Chemistry, Institute of Inorganic Chemistry, University of Zurich, Switzerland, 06/2007-now

M.Sc. in Materials Science, Shanghai Institute of Optics and Fine Mechanics, Chinese Academy of Sciences, P. R. China, 09/2004-05/2007

B.Eng. in Inorganic Materials Science and Engineering, Central South University, P. R. China, 09/2000-06/2004

Research Experience

PhD Thesis, Institute of Inorganic Chemistry, University of Zurich 06/2007-now

- Combination of in situ EDXRD and XAS methods to investigate the hydrothermal formation mechanism of oxide nanomaterials
- Hydrothermal synthesis, structure and morphology characterization of oxide nanomaterials
- Environmental applications of selected oxide nanomaterials

Master Thesis, Chinese Academy of Sciences 09/2005-05/2007

- Inorganic materials used in write-once Blu-ray recording

Internship, Philips Research East Asia 10/2005-01/2006

- Robust recording optical drives

Bachelor Degree Project, Central South University 02/2004-06/2004

- Preparation of ultrafine nickel powder by polyol method and its thermodynamic study

Posters and Oral Presentations

1. **Y. Zhou**, N. Pienack, W. Bensch, G. R. Patzke, *Morphology Control and Hydrothermal Formation Mechanism of Hexagonal W/Mo-Oxides: In Situ Investigations*. 12th European Conference on Solid State Chemistry, University of Munster, Germany, Sept. 20-23, 2009.
2. **Y. Zhou**, A. Heel, G. R. Patzke. *Bismuth Oxide Nanomaterials: Morphology Control and Photocatalytic Activity*. Vortragstagung der Wöhler-Vereinigung für Anorganische

Chemie, München, Germany, Oct. 8-10, 2008.

3. G. R. Patzke, **Y. Zhou**, E. F. C. Chimamkpam, F. Hussain. *Oxide-based Functional Materials: From Nanorods to Bio-inorganic Hybrids*. Sixth International Conference on Inorganic Materials, Dresden, Germany, Sept. 28-30, 2008.

4. **Y. Zhou**, K. Vuille, A. Heel, G. R. Patzke. *Functionalized Hierarchical Bi_2WO_6 Flowers with a TiO_2 Coating: A Straightforward Chemical Route*. NanoEurope 2008, St.Gallen, Switzerland, Sept. 16-17, 2008.

5. G. R. Patzke, **Y. Zhou**, *Targeted Synthesis of Nanostructured Oxide Materials,* 2007 MRS Fall Meeting, Boston, America, Nov. 26-30 2007.

6. G. R. Patzke, **Y. Zhou**, T. Fox, R. Kiebach, W. Bensch, J.-D. Grunwaldt, A. Baiker. *Controlled Hydrothermal Pathways to (W, Mo)-Oxides.* The 11th European Conference on Solid State Chemistry, Caen, France, Sept. 11-13, 2007.

Workshops

1. XAFS for Beginners, MAX-lab synchrotron source, Lund, Sweden, Sept. 1-10, 2008.

2. Energy Dispersive X-ray Absorption Spectroscopy: Scientific Opportunities and Technical Challenges, ESRF, Grenoble, France, Feb. 2-5, 2009.

3. 6th Workshop on Structural Analysis of Aperiodic Crystals, University of Bayreuth, Bayreuth, Germany, Mar. 5-8, 2009.

4. PHARE 2009: Crystal Structure Solution and Refinement from Powder Data, Martina Franca, Italy, Apr. 15-17, 2009.

5. 2009 Swiss Workshop on Materials with Novel Electronic Properties, Les Diablerets, Switzerland, Aug. 26-28, 2009.

Honors

06/2010	T. S. Kê Research Fellowship
05/2010	Chinese Government Award for Outstanding Self-Financed Students Abroad
04/2010	2010 SCNAT/SCS Chemistry Travel Award
01/2009	Sino-Swiss Science and Technology Cooperation (SSSTC) Student Exchange Grant
06/2007	Excellent graduate of Shanghai
05/2007	“YongLing Liu” Scholarship of Chinese Academy of Sciences
12/2006	“Shanghai-Applied Materials R&D Fund” Scholarship
06/2004	Excellent graduate of Hunan Province
12/2003	Chinese National Scholarship
02/2003	Oustanding Scholarship of Hunan Province
12/2002	“HaiHang” Scholarship